



TECHNISCHE UNIVERSITÄT MÜNCHEN

Ingenieur fakultät Bau Geo Umwelt

Lehrstuhl für Statik

# **Numerical and Experimental Modeling for Shape Optimization of Offshore Structures**

**Daniel Markus**

Vollständiger Abdruck der von der Ingenieur fakultät Bau Geo Umwelt der Technischen Universität München zur Erlangung des akademischen Grades eines

**Doktor-Ingenieurs**

genehmigten Dissertation.

Vorsitzender:

Univ.-Prof. Dr.-Ing. habil. Fabian Duddeck, TU München

Prüfer der Dissertation:

1. Univ.-Prof. Dr.-Ing. Kai-Uwe Bletzinger
2. Prof. Dr. Peter Frigaard, Aalborg Universitet, Dänemark
3. Univ.-Prof. Dr. sc. tech. Peter Rutschmann

Die Dissertation wurde am 25.09.2014 bei der Technischen Universität München eingereicht und durch die Ingenieur fakultät Bau Geo Umwelt am 24.03.2015 angenommen.



Schriftenreihe des Lehrstuhls für Statik TU München

Band 28

**Daniel Markus**

**Numerical and Experimental Modeling for  
Shape Optimization of Offshore Structures**

München 2015

Veröffentlicht durch:

Kai-Uwe Bletzinger  
Lehrstuhl für Statik  
Technische Universität München  
Arcisstraße 21  
D-80333 München

Telefon: +49 89 289 22422  
Telefax: +49 89 289 22421  
E-Mail: [kub@tum.de](mailto:kub@tum.de)  
Internet: [www.st.bgu.tum.de](http://www.st.bgu.tum.de)

ISBN: 978-3-943683-35-6

© Lehrstuhl für Statik, TU München



## Abstract

The development of innovative technologies in the ocean energy sector has introduced new challenges in modeling design relevant offshore conditions as part of ongoing efforts to optimize structures and devices. These challenges are approached in this thesis through the development and application of numerical and experimental methods. Many of these methods and findings are applicable in the design of offshore structures in general. However, a particular focus has been put on a previously unsolved problem in ocean engineering: The shape optimal design of bottom mounted structures subjected to combined wave-current loading. In engineering practice, the problem is specifically encountered in the design of tidal turbine foundations.

In the process of analyzing and solving this problem, several advancements in Computational Fluid Dynamics are presented. These include new simulation techniques that allow for ocean modeling considering wave-current interaction, a reduced modeling approach that significantly decreases computational costs, an automated optimization framework that allows for efficient design space exploration, and a benchmark validation problem that is readily reproducible. In addition, a new experimental approach to generating stable wave-current laboratory conditions is introduced, which can be efficiently implemented into flumes operating with a current pump and a horizontal wave maker.

Furthermore, the verified and validated methods are applied to investigations of the intricacies of wave-current flows and their implications to loads on offshore structures. These investigations reveal several key findings regarding load increase as a result of the interaction between waves and currents, ideal shape characteristics for design relevant offshore conditions, and measures to control horizontal and vertical loads on offshore structures.

Finally, the methods and findings are collectively applied to the development of a design procedure for a new generation of gravity base foundations. Substantial improvements of the design's hydrodynamic performance are revealed, compared to previous prototype structures. Overall, the newly developed foundation concept demonstrates the capabilities of the introduced methods as a powerful tool in the design process of offshore structures.

## Zusammenfassung

Die Entwicklung innovativer Strukturen zur Nutzung von Meeresenergie stellt Ingenieure vor immer neue Herausforderungen. Von zentraler Bedeutung ist dabei die sorgfältige Modellierung von Offshore-Bedingungen als Basis der Analyse und Optimierung von Strukturen und Anlagen. In dieser Arbeit werden numerische und experimentelle Methoden entwickelt, die diesen Anforderungen gerecht werden sollen. Die Methoden und Erkenntnisse können auf eine Vielzahl praxisrelevanter Aufgaben beim Entwurf von Offshore-Bauten angewendet werden. Ein besonderer Fokus dieser Arbeit liegt auf der Formoptimierung von Fundamenten für Gezeitenturbinen unter Strömungs- und Wellenbelastung.

Im Rahmen der Arbeit werden zahlreiche Neuerungen im Bereich Computational Fluid Dynamics vorgestellt. Diese umfassen neue Simulationsmethoden zur Modellierung der Wellen-Strömungs-Interaktion, reduzierte Modellierungsansätze zur Verringerung von Rechenzeiten, ein automatisiertes Optimierungsverfahren zur Untersuchung des Entwurfsraums und die Definition eines reproduzierbaren Benchmark-Validierungsproblems. Außerdem wird ein neuer experimenteller Versuchsaufbau vorgestellt, der sowohl eine stabile Erzeugung von Wellen-Strömungs-Bedingungen ermöglicht, als auch eine einfache Installation in bestehenden Labors gewährleistet.

Die verifizierten und validierten Methoden werden zur Erforschung grundlegender Vorgänge in Wellen-Strömungs-Bedingungen und deren Auswirkung auf Offshore-Lasten angewendet. Hieraus lassen sich Erkenntnisse über Lastzunahmen durch die Interaktion zwischen Wellen und Strömungen ableiten. Die lastabhängigen Formeigenschaften werden beschrieben und klassifiziert und Maßnahmen zur Beeinflussung von horizontalen und vertikalen Strukturlasten aufgezeigt.

Als Anwendung werden die Methoden und Erkenntnisse zur Entwicklung eines Entwurfsverfahrens einer neuen Generation von Schwergewichtsfundamenten herangezogen. Verglichen mit bislang errichteten Prototypen weist die neue Struktur erhebliche Verbesserungen der hydrodynamischen Eigenschaften auf. Insgesamt demonstriert die Entwicklung der neuen Struktur die Leistungsfähigkeit der vorgestellten Methoden beim Entwurf von Offshorebauten. Die gewonnenen Erkenntnisse dienen der Entwicklung und Verbesserung zukunftsweisender Technologien im Bereich der Meeresenergie.

---

## Acknowledgments

The research presented in this thesis goes far beyond the commitment of a single person. It has been greatly influenced and inspired by a number of dedicated persons. First of all, I would like to express my sincere gratitude to Prof. Kai-Uwe Bletzinger, my research supervisor, for giving me the opportunity and the necessary freedom to grow as a researcher and for his great support and trust throughout all phases of my PhD. Very special thanks to Prof. Peter Frigaard, who has guided me throughout my experimental research and has given me the opportunity to spend an immensely valuable and very enjoyable six months at Aalborg University. I will always keep my time in Denmark in great memory. I would further like to express my gratitude to Prof. Peter Rutschmann for his work as part of the examination committee and for the helpful comments and suggestions. I thank Prof. Fabian Duddeck for his contribution as chairman of the committee. I would also like to express my sincere gratitude to the financial supporters that have made this work possible. I greatly benefited from the funding of the German National Academic Foundation (Studienstiftung des deutschen Volkes), the TUM International Graduate School of Science and Engineering (IGSSE), and the Marine Renewables Infrastructure Network (MARINET).

I am very grateful to Roland Wüchner, whose tireless dedication in the department has greatly contributed to finding the financial support that made my PhD possible in the first place. I also very much enjoyed and appreciated our countless scientific discussions. My colleagues at the department I would like to thank for the good times spent together, particularly during our daily coffee break discussions that were often controversial and always very enjoyable. Particularly I would like to thank my office mates Electra Stavropoulou and Majid Hojjat, who not only gave me guidance and support, but very quickly became friends. We always managed to make our office a fun place to be and I will never forget the many great hours spent together during and after work. Many thanks to my colleague and friend Robert Schmidt for the great after-work evenings spent in Munich. Furthermore, much appreciation goes to Stefan Sicklinger, for equipping our department with a fantastic computation infrastructure that I greatly benefited from. Special thanks goes to Andreas Kelder, who began working at the department as a student and very quickly

became a valuable discussion partner, a great help in my research, and a good friend. I also thank him very much for the nice cover design and his dedication in formatting many figures shown in this thesis.

I thank all members of the Department of Civil Engineering at Aalborg University who warmly welcomed me to Denmark and made my stay so memorable. In particular, I thank Amélie Têtu for introducing me to the department and to her wonderful family. I cannot stress enough the influence of Francesco Ferri, who supported me throughout my experimental work in Aalborg and greatly contributed to the achievements we made in the lab. I truly enjoyed working with you and above all, very much appreciate the hours I got to spend together with you, Valeria and Miral. I also feel very fortunate to have had the pleasure of working with Morten Jakobsen, who not only became a great partner in research, but also in running, and in experiencing Aalborg city life. My deep appreciation goes to the AAU lab technicians, who greatly contributed to the realization of the experimental setups. In particular I thank Kim Borup, Niels Drustrup, Nikolaj Holk, Morten Olsen, and Kurt Sørensen.

Very special thanks goes to Christian Dehlinger, who as senior director at Ed. Züblin AG initiated and inspired this wonderful research project. I also very much appreciate the contribution of Jochen Röhm, who very successfully and with much dedication laid the groundwork for my research and supported me thereafter. Furthermore, I am grateful for the many technical discussions I held with Tomás Arana, for his advice, and for an open ear whenever I approached him. My thanks also goes to Holger Wahrmund for his support and motivation.

Thank you very much Ulrich Pfisterer, my good friend and supporter in all phases of life. I greatly value our friendship and know that I can always count on you. I thank Lisa Röhr, for helping me edit this thesis and for her many delightful visits to Munich. In much appreciation and with gratitude I thank my family, for their continuous encouragement, support, motivation, and love. Finally, I wish to especially thank Melanie Hoehl, for her unfaltering support, for always believing in me, and for being the amazing person she is. It feels wonderful knowing you by my side.

---

# Contents

---

<b>Nomenclature</b>	<b>ix</b>
Acronyms . . . . .	ix
Latin Symbols . . . . .	xi
Greek Symbols . . . . .	xvi
<b>1 Introduction and Motivation</b>	<b>1</b>
<b>2 Numerical Wave-Current Modeling</b>	<b>7</b>
2.1 Introduction and Overview . . . . .	7
2.2 Governing Equations . . . . .	9
2.3 Turbulence Model . . . . .	10
2.4 Free Surface Model . . . . .	11
2.5 Offshore Conditions Model . . . . .	14
2.5.1 Modeling Strategies . . . . .	14
2.5.2 Wave Model . . . . .	15
2.5.3 Wave-Current Model . . . . .	19
2.6 Initial and Boundary Conditions . . . . .	22
2.6.1 Initial Conditions . . . . .	23
2.6.2 Inlet Boundary . . . . .	24
2.6.3 Outlet Boundary . . . . .	26
2.6.4 Bottom Boundary and other Wall Boundaries . . . . .	27
2.6.5 Top Boundary . . . . .	28
2.6.6 Side Boundary . . . . .	28
2.7 Solution Schemes and Software Description . . . . .	29

---

2.8	Model Verification . . . . .	30
2.8.1	Test Case Description . . . . .	30
2.8.2	Test Case Results . . . . .	32
2.9	Conclusions and Summary . . . . .	36
<b>3</b>	<b>Load Analysis</b>	<b>37</b>
3.1	Introduction and Overview . . . . .	37
3.2	Assessment of Wave-Current Fluid Kinematics . . . . .	39
3.3	Load Analysis of Basic Shapes . . . . .	41
3.3.1	Test Case Setup . . . . .	42
3.3.2	Test Case Results . . . . .	44
3.4	Load Analysis of Prototype SeaTurtle . . . . .	50
3.4.1	Project Description . . . . .	50
3.4.2	Discretization . . . . .	53
3.4.3	Load Investigation . . . . .	55
3.4.4	Shape Investigation . . . . .	58
3.5	Conclusions and Summary . . . . .	61
<b>4</b>	<b>Reduced Modeling</b>	<b>63</b>
4.1	Introduction and Overview . . . . .	63
4.2	Virtual Free Surface (VFS) Model . . . . .	65
4.2.1	Model Description . . . . .	65
4.2.2	Model Assessment . . . . .	67
4.3	Correction Method . . . . .	70
4.3.1	Basic Concept . . . . .	70
4.3.2	Mathematical Formulation . . . . .	71
4.3.3	Model Implementation . . . . .	72
4.3.4	Model Assessment . . . . .	74
4.4	VFS Wave-Current Model . . . . .	75
4.4.1	Flow Kinematics . . . . .	76
4.4.2	Wave Length . . . . .	80
4.5	Model Verification . . . . .	84
4.6	Model Performance . . . . .	90
4.7	Conclusions and Summary . . . . .	91
<b>5</b>	<b>Shape Optimization</b>	<b>95</b>
5.1	Introduction and Overview . . . . .	95
5.2	Optimization Framework . . . . .	99
5.3	Horizontal Force Analysis . . . . .	105
5.3.1	Single-Variable Optimization . . . . .	106

---

5.3.2	Multiple Variables Optimization . . . . .	114
5.4	Vertical Force Analysis . . . . .	119
5.4.1	Foundation Base Modeling . . . . .	120
5.4.2	Single Variable Optimization . . . . .	126
5.4.3	Multiple Variables Optimization . . . . .	133
5.5	Conclusions and Summary . . . . .	137
<b>6</b>	<b>Experimental Wave-Current Modeling</b>	<b>141</b>
6.1	Introduction and Overview . . . . .	141
6.2	Wave-Current Filter . . . . .	143
6.3	Experimental Filter Setup . . . . .	146
6.4	Filter Analysis . . . . .	148
6.4.1	Current Scenario . . . . .	148
6.4.2	Wave Scenario . . . . .	152
6.4.3	Wave-Current Scenario . . . . .	157
6.5	Conclusions and Summary . . . . .	159
<b>7</b>	<b>Experimental Validation</b>	<b>161</b>
7.1	Introduction and Overview . . . . .	161
7.2	Benchmark geometry specification . . . . .	164
7.3	Experimental Benchmark Setup . . . . .	166
7.3.1	Flume . . . . .	166
7.3.2	Load Measurement . . . . .	168
7.3.3	Models . . . . .	170
7.3.4	Flow Measurement . . . . .	171
7.4	Numerical setup . . . . .	172
7.5	Benchmark Results . . . . .	174
7.5.1	Flow kinematics . . . . .	174
7.5.2	Two-Dimensional Current Forces . . . . .	178
7.5.3	Two-Dimensional Wave Forces . . . . .	183
7.5.4	Two-Dimensional Wave-Current Forces . . . . .	186
7.5.5	Three-Dimensional Forces . . . . .	190
7.6	Conclusions and Summary . . . . .	196
<b>8</b>	<b>Advanced Foundation Design</b>	<b>199</b>
8.1	Introduction and Overview . . . . .	199
8.2	Foundation Description . . . . .	200
8.3	Optimization . . . . .	203
8.4	Assessment . . . . .	205
8.5	Conclusions and Summary . . . . .	210

<b>9 Conclusions and Outlook</b>	<b>211</b>
<b>Bibliography</b>	<b>217</b>



---

# Nomenclature

---

## Acronyms

**ADCP** Acoustic Doppler Current Profiler

**ADV** Acoustic Doppler Velocimeter

**BEM** Blade Element Momentum

**CFD** Computational Fluid Dynamics

**DV** Design Variable

**FV** Finite Volume

**GBF** Gravity Base Foundation

**LATOS** Load Analysis Tool for Offshore Structures

**LES** Large Eddy Simulation

**LOLA** Local Linear Approximation

**LSM** Level Set Method

**MAC** Marker and Cell

**NN** Neural Network

**NRMSD** Normalized Root-Mean-Square Deviation

**NWCT** Numerical Wave-Current Tank

**PISO** Pressure Implicit with Splitting of Operators

**PSD** Point Symmetric Diffuser

**RANS** Reynolds-averaged Navier-Stokes

**RMS** Root Mean Square

**RSD** Relative Standard Deviation

**SED** Sequential Experimental Design

**SQP** Successive Quadratic Programming

**SUMO** Surrogate Modeling

**URANS** Unsteady Reynolds-averaged Navier-Stokes

**VFS** Virtual Free Surface

**VOF** Volume of Fluid

**WCI** Wave-Current Interaction

## Latin Symbols

$A$  Structure cross-sectional area with horizontal surface normal perpendicular to the flow direction

$a$  Diffuser average flow height

$A_p$  Structure projected cross-sectional area with horizontal surface normal parallel to the flow direction

$A_s$  Structure surface area

$a_D \dots d_D$  Damping function polynomial coefficients

$b$  Structure base width

$B_j$  Dimensionless Fourier coefficients

$c$  Central diffuser height

$c_0$  Semivariogram intercept

$c_1$  Semivariance as  $h_m$  goes to infinity

$c_2$  Variogram data point correlation scalar

$C_\mu$  Wall function model constant

$C_d$  Drag coefficient

$C_m$  Inertia coefficient

$c_w$  Wave celerity

$D$  Amount of filter damping

$d$  Water depth

$E$  Wall function model constant

$F_b$  Blending function

$F_i$  Total force acting on the structure

$F_{mhs}$  Mean hydrostatic force

$g_i$  Gravitational acceleration vector

$g_i^{nb}$  Local neighborhood point gradient

$H$  Wave height

$h$  Structure height

$h_{vfs}$  VFS height

$h_d$  Diffuser inlet and outlet height

$h_e$  Experimental semivariance approximation distance

$h_m$  Model semivariance distance

$h_p$  Structure base plate height

$H_{ref}$  Reference wave height

$I$  Turbulence Intensity

$k$  Turbulent kinetic energy

$k_w$  Wave number

$L$  Wave length

$l$  Turbulence length scale

$L_{\Delta}$  Wave length deviation from true value

$L_i$  LOLA weighting vector

$LV_i$  LOLA-Voronoi weighting vector

$M_{mhs}$  Mean hydrostatic moment

$M_{ot}$  Overturning moment

$N$  Subset function

- $n_i$  Normal vector
- $n_d$  Number of design variables
- $n_{nb}$  Number of neighborhood points
- $n_s$  Number of selected sample points
- $n^*$  Number of new sample points
- $O$  Optimization objective
- $o_i$  Discrete objective value vector
- $O_{kg}$  Objective approximation based on kriging
- $o_i^{nb}$  Neighborhood point objective values
- $o_i^*$  New objective values
- $P$  Mean pressure
- $p_a$  Atmospheric pressure
- $\tilde{P}$  Adjusted pressure field
- $p_{i,j}$  Structure point coordinates with  $i$  equal to the point number and  $j$  indexing the dimensions of the point
- $p_{\kappa,i}$  Polynomial function correction vector
- $P_p^{vfs}$  Probed wave peak pressure value based on the VFS model
- $P_p^{vof}$  Probed wave peak pressure value based on the VOF model
- $p_s$  Voronoi sample points
- $Q$  Experimental design
- $q_j^c$  Candidate point for the sample point matrix
- $q_{i,j}$  Set of sample points
- $q_j^l$  Lower side constraint
- $q_{i,j}^{nb}$  Set of neighborhood points

$q_{i,j}^*$  New set of sample points

$q_j^u$  Upper side constraint

$r$  Geometric variable enforcing the structure area constraint

$R_i$  Residual vector

$s$  Gap size

$T$  Wave period

$t$  Time

$U_i$  Mean velocity vector

$u'_i$  Fluctuating velocity vector

$U_{wall}$  Flow velocity parallel to the wall

$U_a$  Depth averaged current velocity

$U_i^c$  Current velocity vector

$U_i^\Delta$  Change in velocity due to wave-current interaction

$\tilde{U}_i$  Adjusted velocity field

$U_i^{in}$  Velocity vector pointing into the domain

$U_i^{inl}$  Inlet boundary velocity vector

$U_i^{inl,c}$  Inlet current velocity boundary vector

$U_i^{inl,w}$  Inlet wave velocity boundary vector

$U_i^{out}$  Velocity vector pointing out of the domain

$U_{p,i}^w$  Probed wave peak velocity values

$U_{p,i}^{wci}$  Probed WCI peak velocity values

$U_s$  Current surface velocity

$u_\tau$  Friction velocity

$U_i^{vfs}$  VFS boundary velocity vector

$U_i^{vfs,c}$  VFS current velocity boundary vector

$U_i^{vfs,w}$  VFS wave velocity boundary vector

$U_i^w$  Wave velocity vector

$\bar{U}_1^w$  Mean horizontal wave velocity

$U_i^{wci}$  Wave-current interaction velocity vector

$V$  Structure volume

$V_i$  Voronoi weighting vector

$v_i$  Design variables vector

$v_i^l$  Design variables lower bound

$v_i^u$  Design variables upper bound

$w$  Structure width

$W_i$  Kriging model weights

$x, z$  Fixed coordinate system with origin at the mean sea level; for the numerical simulations  $x = 0$  is defined at the domain inlet

$\hat{x}, \hat{z}$  Moving coordinate system with origin at the mean sea level and  $\hat{x} = 0$  defined at the location of the propagating wave crest

$x', z'$  Local structure coordinate system with  $z'$ -coordinate origin at the sea bottom and  $x'$ -coordinate origin at the structure center

$y_{wall}$  Wall distance

$y^+$  Dimensionless wall distance

$\tilde{z}$  z-coordinate normalized with the water depth to the range 0 to  $-1$

## Greek Symbols

$\alpha$  Phase parameter

$\beta$  Turbulence model constant

$\beta_c$  Current exponent

$\beta^*$  Turbulence model constant

$\gamma$  Turbulence model constant

$\gamma_m$  Model semivariogram

$\gamma_e$  Experimental semivariogram

$\delta$  Iteration loop tolerance

$\epsilon$  Turbulent dissipation

$\zeta$  Weighting factor equal to 1 or -1

$\eta$  Free surface height

$\kappa_i$  VFS model WCI correction vector

$\kappa_{wall}$  Wall function model constant

$\lambda$  VFS model correction factor

$\lambda_s$  Kriging equation slack variable

$\mu$  Dynamic viscosity

$\mu_{eff}$  Effective dynamic viscosity

$\mu_t$  Turbulent dynamic viscosity

$\nu$  Kinematic viscosity

$\rho$  Fluid density

$\sigma_{exp}$  Standard deviation of experimental results

$\sigma_k$  Turbulence model constant

$\sigma_\omega$  Turbulence model constant



$\sigma_{\omega_2}$  Turbulence model constant

$\sigma_P$  Pressure standard deviation

$\tau_{wall}$  Wall shear stress

$\phi$  Structure inclination angle

$\psi$  Stream function

$\omega$  Turbulent frequency



---

# Chapter 1

## Introduction and Motivation

---

In the past decades, the types of developed and installed offshore structures has greatly diversified. Until the early 1990s, a major focus in ocean engineering was directed towards oil and gas applications. With the design of the world's first offshore wind farm completed near Vindeby, Denmark in 1991 (Breton and Moe, 2009) offshore structures for the renewable energy sector steadily gained in importance. At the turn of the century, offshore devices designed to extract energy from the oceans entered a pre-commercial phase. Testing of full scale tidal turbine prototypes in Kvalsund, Norway and Lynmouth, England began in 2003 (Faez Hassan et al., 2012). At the same time, the world's first offshore wave energy converter was grid connected in Nissum Bredning, Denmark (Kofoed et al., 2006). A number of devices have since passed proof of concept studies that demonstrated their capabilities and potential. This has led to a new phase in the development of the technologies, which aims at further improving existing devices in order to establish large scale commercial offshore parks. As part of this phase, optimization based on numerical and experimental modeling has started to play a central role in the search of solutions to new design challenges in offshore engineering. This thesis undertakes the analysis, development, and validation of these models while applying them to offshore engineering related optimization tasks.

To some extent, knowledge and experience gained in decades of research and development in the offshore oil and gas industry could be applied in the early design stages of new ocean engineering technologies. However, these young technologies introduced a variety of previously not encountered design challenges, motivating the exploration of new research topics. Particularly when this research aims at optimizing a technology, the unique characteristics and specifications of individual design problems need to be considered, in order to unveil the full optimization potential. In the presented thesis, the design problem is the shape optimization of tidal turbine gravity base foundations. Furthermore, many of the findings and conclusions drawn from the research are applicable to a much broader application range. Particularly, this pertains to tasks involving efficient numerical and experimental modeling of waves, currents and wave-current interaction, load analysis and optimization of offshore structures, and the validation of force computation and shape optimization in ocean conditions.

In addition to investigating these fundamental aspects of ocean engineering, the research aims at providing a practical contribution to the development and establishment of new generation tidal turbines. The principal functionality of this technology is to convert kinetic energy of streaming water into electrical energy. This is typically achieved by placing fully submerged turbines in regions of the oceans consisting of high tidal velocities. The great advantages of using tidal currents as a source of energy are the long term predictability of the expected energy extraction, and the low influence of daily weather conditions on power generation. In these regards, tidal turbines hold a unique status in the renewable energy sector. The technology was tested thoroughly in recent years, with a number of successful deployments of first generation tidal turbine prototypes that operated at a capacity of around 300 kW, while some second generation designs dispatched over 1 MW of power (Faez Hassan et al., 2012). During this design phase, wide spread research efforts were undertaken in order to support the development of the technology.

A large part of this research has focused on topics related to energy resource assessment and turbine design. As pointed out by Blunden and Bahaj (2007), tidal stream resource assessments have been carried out at least since the 1970s, including publications by Heronimus et al. (1974) and Lissamen and Radkey (1979). As the development of the turbines advanced, various private consultants also carried out desktop studies assessing tidal resources, as noted and referenced by Grabbe

---

et al. (2009). In addition, numerical models were developed to aid in the selection of suitable sites for power extraction (e.g. Evans, 1987; Garrett and Cummins, 2004, 2005; Karsten et al., 2008; Blanchfield et al., 2008; Blunden, 2009; Yang et al., 2013). Simultaneously, a great number of experimental and numerical research projects were carried out targeting various aspects of tidal turbine development. Among others, these studies include research focusing on the following turbine related topics:

- Hydrodynamic blade design (e.g. Batten et al., 2006, 2008; Bahaj et al., 2007)
- Tidal turbine wakes (e.g. Turnock et al., 2011; Batten et al., 2013; Masters et al., 2013; Tedds et al., 2014)
- Fatigue loads (e.g. McCann, 2007; Milne et al., 2011)
- Blade materials (e.g. Uzawa et al., 2008; Davies et al., 2013)
- Turbine array interactions (e.g. O’Doherty et al., 2009; Vennell, 2012; Funke et al., 2014)
- Turbine noise emissions (e.g. Wang et al., 2007; Halvorsen et al., 2011)

While the list of literature related to tidal resources and turbine design is quite exhaustive, very little research has been presented regarding tidal turbine support structures. The lack of research in this particular area is somewhat surprising, considering that in offshore wind farm projects the foundation costs make up between 15 % and 40 % of the total costs (Sun et al., 2012). Similarly, the realization of profitable tidal turbine parks relies heavily on innovative and efficient foundation solutions, which take into account the unique environment encountered at tidal turbine sites. In particular, this environment involves offshore conditions with high tidal velocities, reducing the time windows during which an installation of the structures is practical. Another unique characteristic of sites suitable for an efficient operation of tidal turbines are the properties and conditions of the sea floor. As a result of high flow velocities, there is usually very little, if any sediment (Owen, 2007). The rocky substrate that is consequently encountered complicates the installation of foundations that enter the sea floor.

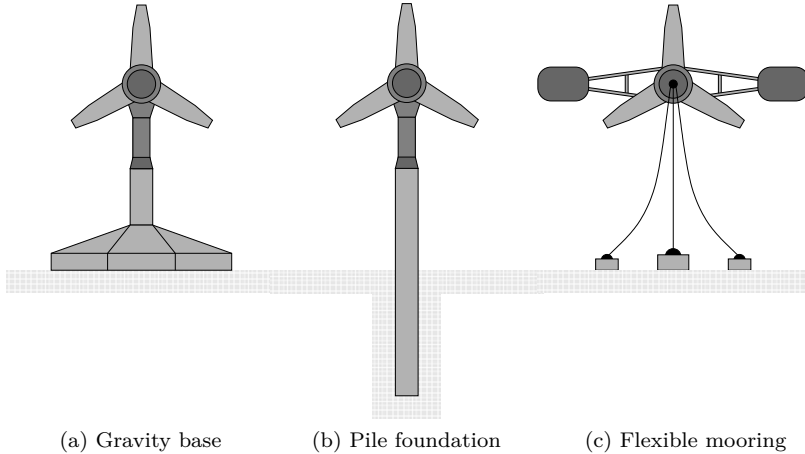


Figure 1.1: Classification of typical tidal turbine foundation types.

Some foundation solutions that take into account these special conditions have very recently been researched and published. Among these, one focus has been on pile foundations such as monopiles, tripods, and jacket foundations. These foundations consist of a single or multiple piles that have to be drilled into the sea floor (Fig. 1.1b). During initial pile installations for tidal turbine prototypes, significant difficulties arose with seakeeping of the installation vessels. This problem was addressed through the development of the so called Dive Drill, a drilling template that is lowered to the sea floor and connected to the ship through an umbilical handling system, allowing for some motion of the vessel during installation (Spagnoli and Weixler, 2013). Pile foundations are particularly advantageous in terms of the load analysis during the design process, because the geometric simplicity of the structure allows for a computation of forces using simple and well documented methods. The drilling noise emissions during installation and the relatively high material costs for the steel piles are considered to be the main drawbacks of this foundation technology.

Alternatively, tidal turbines can be secured using flexible mooring in combination with floater sections (Fig. 1.1c). Research on this foundation type was recently carried out by Sanchez (2013), including the introduction of an experimental-based methodology to analyze tethered systems. The basic concept of this foundation type is to induce a buoyant lift force on the turbine through floater bodies, while

---

anchoring the structure to the sea floor using mooring lines. As a result of this setup, material costs are reduced and there are no limitations concerning the water depth. However, Sanchez also concluded that during operation of the devices high stresses in the mooring lines occur, requiring frequent substitution and therefore higher maintenance costs.

Finally, a Gravity Base Foundation (GBF) can be utilized to support tidal turbines (Fig. 1.1a). The functional principle of this foundation concept is to transfer all structural forces to the sea floor exclusively through friction between the foundation base and the substrate. Drilling or mooring procedures during installation are thus avoided. Instead, the integrity of the structure is safeguarded through the weight of the foundation. Concrete is often chosen as material for the foundation to supply the required weight. This choice reduces the material costs significantly, compared to steel structures. As analyzed by Vølund (2005), the material costs for concrete gravity base foundations are approximately half of the costs of a comparable steel monopile. It is therefore of little surprise that according to the European Marine Energy Centre (EMEC), 63 % of the 58 tidal turbine devices under development in 2012 utilized GBFs, while pile foundations and foundations with flexible mooring only constituted 14 % and 23 %, respectively (Sanchez, 2013).

The design of these GBFs for tidal turbines has largely been carried out based on engineering intuition and previous experience from the offshore wind sector. Detailed research concerning favorable concrete foundation shapes to reduce loads in the expected marine environment was thus far lacking. This is likely due to the fact that an analysis of a complex geometry in a combined wave-current environment requires the application and enhancement of highly complex modeling techniques. However, if such methods are unveiled and utilized, there is large potential to optimize the massive bluff bodies used as GBFs, such that the load on the structure is reduced. This allows for the utilization of smaller and lighter foundations, which results in lower material, transportation, and installation costs. Considering the large contribution of these costs to the overall tidal turbine expenses, the development of methods for shape optimal design of GBFs has the potential of triggering significant advancements of the technology.

The development and application of these methods is presented in this thesis. In Chapter 2, a Numerical Wave-Current Tank (NWCT) is introduced that allows for reliable simulation of wave-current offshore conditions using Computational Fluid Dynamics (CFD). Included in the

chapter is the description and verification of a novel methodology that allows for the generation of combined wave-current scenarios under consideration of the interaction between the wave and the current field. This method is applied to load simulations of bottom mounted structures in [Chapter 3](#). A particular focus is set on demonstrating the importance of analyzing wave-current flows in a single simulation, and identifying the difference to a simplified superposition of results from individual wave and current simulations. Furthermore, the NWCT is applied to determine the loading on a prototype GBF for a tidal turbine installed near Jindo Island, South Korea. Following, a new reduced modeling approach for efficient offshore wave-current CFD simulation is derived and tested in [Chapter 4](#). The purpose of the model is to reduce computational requirements for offshore CFD simulations of fully submerged structures, thereby enabling cost-effective optimization studies. Such studies are then carried out in [Chapter 5](#), which introduces an optimization framework that is used to determine optimal shape characteristics of GBFs in waves, currents, and combined wave-current scenarios.

In addition to numerical considerations, this thesis introduces and applies experimental techniques developed for testing of structures in wave-current environments. A newly designed and evaluated experimental modeling approach to generate stable wave-current flow conditions is described in [Chapter 6](#). The experimental setup is applied to an elaborate experimental investigation of bottom mounted structure shapes in [Chapter 7](#), in order to validate the attained optimization results. At the same time, the study establishes a simple benchmark for testing of related numerical and experimental models. Finally, the introduced models and confirmed findings are collectively applied to the design of a new and improved GBF for tidal turbines in [Chapter 8](#). It is shown that the new design results in significantly reduced critical loads on the structure, compared to the initially analyzed prototype structure.

Overall, this thesis provides a comprehensive framework for the development of a new generation of efficient tidal turbine GBFs. The numerical and experimental methods derived for this purpose are suitable to address related shape optimization tasks of offshore structures. Thereby, this research is meant to support solving some of the new challenges introduced by the development of renewable energy technologies in offshore engineering.



---

## Chapter 2

# Numerical Wave-Current Modeling

---

### 2.1 Introduction and Overview

Throughout ocean engineering, offshore structure design has frequently been carried out using cylindrical supports that have found applications in the construction of tension-leg platforms and monopile structures. Environmental forces on these support members of prismatic shape can efficiently be calculated using simplified semi-empirical equations, such as the well known Morison equation introduced by [Morison et al. \(1950\)](#). However, these methods presume that geometry specific shape parameters are available for the structure of interest. These parameters are typically determined experimentally and have, for example, been summarized by [Sarpkaya \(2010\)](#) and [Bartrop et al. \(1991\)](#) for a variety of simple shapes.

In addition to pile-structures, complex three dimensional geometries have started to gain importance in the ocean energy sector. GBFs for tidal turbines are one example of such structures, which are subjected to a complex flow field. These support structures consist of a three dimensional bluff body, for which shape parameters used in semi-empirical approaches are often not documented. Furthermore,

it is usually not economical to determine these shape parameters experimentally in the early design stages of an offshore project, because the design may still be subject to fundamental alterations. Experiments are typically conducted in a much later phase of the project, when the general design concept has been established. However, even at the outset of an offshore project, engineers rely heavily on accurate environmental force estimations when making the first fundamental design choices. This calls for an efficient and economical methodology capable of capturing realistic offshore conditions that can be evaluated in combination with complex geometries.

Particularly in the early stages of a project, numerical methods based on CFD are powerful tools to gain access to complicated flow fields. A description of a modeling strategy to carry out CFD-based offshore simulations in a Numerical Wave-Current Tank (NWCT) is presented in this chapter. The numerical tank combines the solution of water wave problems introduced by [Fenton \(1988\)](#) with the multiphase Volume of Fluid (VOF) method established by [Hirt and Nichols \(1981\)](#). The methodology allows for the simulation of offshore environments based on the numerical solution of the Unsteady Reynolds-averaged Navier-Stokes (URANS) equations. Numerical wave tanks have become a popular tool for offshore engineering applications. However, the simulations are often carried out without justification of the individual model choices and without an awareness of the consequences of these choices. In this chapter, the different components of the numerical tank are selected and evaluated carefully, with a particular focus on choosing the most suitable configuration to capture design relevant marine environments encountered by offshore structures.

In many cases, the design of offshore structures is governed by severe loads resulting from the combination of a site specific maximum current and an extreme wave scenario. This gives rise to a phenomenon referred to as wave-current interaction, which leads to a modification of the overall fluid kinematics. Capturing the interaction process is particularly difficult when the flow becomes rotational, as is the case when simulating non-uniform ocean currents. Under such conditions, some fundamental assumptions underlying established wave theories commonly used for offshore applications are violated. In this chapter, a novel methodology is presented that overcomes this problem by capturing the interaction within a CFD simulation, allowing for an extension of commonly utilized numerical wave tanks to incorporate a non-uniform current.

In order to evaluate the capabilities of the NWCT to accurately model realistic conditions throughout the water column, the proposed methodology is verified with respect to fluid particle kinematics developing in the computational domain. Overall, the aim is to evaluate the proposed methodology and to assess its potential to be used in the design process of offshore structures.

Part of the work presented in this chapter has been published in the International Journal of Offshore and Polar Engineering (Markus et al., 2013b) and in the Proceedings of the twenty-second International Conference of Offshore and Polar Engineering (Markus et al., 2012). It is presented here with explicit written consent from the publishers.

## 2.2 Governing Equations

The basic principle of the NWCT is to describe fluid particle kinematics by simulating a physical flow field based on the numerical solution of the Navier-Stokes equations. The complexity of the transient fluid flow encountered at offshore sites calls for a methodology that is capable of efficiently describing high Reynolds numbers turbulent flows. Large Eddy Simulation (LES) is increasingly finding application in industrial problems. However, the method still requires considerable computational resources. In order to capture the velocity fluctuations throughout the regions of wave development, an LES simulation requires a fine mesh resolution. This is particularly problematic in open water flows, where a large computational domain is typically necessary in order to eliminate the influence of the various boundaries. Alternatively, a time averaged solution of the turbulent fluid problem based on the Reynolds-averaged Navier-Stokes (RANS) equations significantly reduces required computer resources. However, a steady solution of the Navier-Stokes equations is inadequate to describe the unsteady flow field generated by ocean waves. The transient characteristic of the flow can be captured by retaining the rate of change of the fluid properties in the RANS equations, which is referred to as unsteady RANS (URANS). The URANS equations comprise of the following averaged continuity equation and averaged system of momentum equations:

$$\frac{\partial U_i}{\partial x_i} = 0 \quad (2.1)$$

$$\frac{\partial U_i}{\partial t} + \frac{\partial}{\partial x_j}(U_i U_j) = -\frac{1}{\rho} \frac{\partial P}{\partial x_i} + \nu \frac{\partial^2 U_i}{\partial x_j^2} - \frac{\partial}{\partial x_j}(\overline{u'_i u'_j}) + g_i \quad (2.2)$$

where  $U_i$  and  $u'_i$  are the mean and fluctuating velocity components, respectively,  $P$  is the mean pressure,  $\rho$  is the density of the fluid,  $\nu$  is the kinematic viscosity and  $g_i$  is the gravitational acceleration. The URANS approach is particularly suitable for numerical offshore simulations, as it captures the transient behavior of the flow at manageable computational costs.

### 2.3 Turbulence Model

When modeling realistic offshore environments, the investigated flow fields are typically highly turbulent. These conditions require a physically meaningful modeling of the Reynolds stresses  $\overline{u'_i u'_j}$  of Eq. 2.2. In many applications, it is common practice to model the Reynolds stresses of highly turbulent flows using the  $k$ - $\epsilon$  model initially introduced by [Launder and Spalding \(1974\)](#). This method performs well in many physical fluid problems, particularly in the free stream regions of the flow. Problems arise in the near wall regions, where the model definition leads to an unphysical development of turbulent viscosity that needs to be damped out. [Wilcox \(1988\)](#) introduced an alternative approach based on the turbulence frequency  $\omega$ . The definition of the turbulence parameters in the  $k$ - $\omega$  model is such that wall damping functions can be avoided. However, problems arise in the free stream, where  $k$  and  $\omega$  tend towards zero, resulting in an undefined turbulent viscosity. The particular application of a numerical wave tank is sensitive to both regions: the free stream, where a physical wave motion should be captured, and the near wall regions, where the pressure on the structure is relevant. In order to account for these conditions, a combination of both models is preferable, as proposed by [Menter \(1993\)](#). The  $k$ - $\omega$  SST model blends the  $k$ - $\epsilon$  model applied to the free stream with the  $k$ - $\omega$  model used in the near wall regions, thus capitalizing on the advantages of both models and making it particularly useful for a numerical simulation of offshore environments.

The transport equations for the turbulent kinetic energy  $k$  and the

specific dissipation  $\omega$  are defined by Menter as follows:

$$\frac{\partial \rho k}{\partial t} + \frac{\partial \rho U_j k}{\partial x_j} = P_k - \beta^* \rho \omega k + \frac{\partial}{\partial x_j} \left[ (\mu + \sigma_k \mu_t) \frac{\partial k}{\partial x_j} \right] \quad (2.3a)$$

$$P_k = \mu_t \frac{\partial U_i}{\partial x_j} \left( \frac{\partial U_i}{\partial x_j} + \frac{\partial U_j}{\partial x_i} \right) - \frac{2}{3} \rho k \delta_{ij} \frac{\partial U_i}{\partial x_j} \quad (2.3b)$$

$$\begin{aligned} \frac{\partial \rho \omega}{\partial t} + \frac{\partial \rho U_j \omega}{\partial x_j} &= \gamma P_\omega - \beta \rho \omega^2 + 2\rho(1 - F_b) \sigma_\omega \frac{1}{\omega} \frac{\partial k}{\partial x_j} \frac{\partial \omega}{\partial x_j} \\ &+ \frac{\partial}{\partial x_j} \left[ (\mu + \sigma_\omega \mu_t) \frac{\partial \omega}{\partial x_j} \right] \end{aligned} \quad (2.4a)$$

$$P_\omega = \rho \frac{\partial U_i}{\partial x_j} \left( \frac{\partial U_i}{\partial x_j} + \frac{\partial U_j}{\partial x_i} \right) - \frac{2}{3} \rho \omega \delta_{ij} \frac{\partial U_i}{\partial x_j} \quad (2.4b)$$

where  $\mu$  denotes the dynamic viscosity of the fluid and  $\mu_t$  is the coefficient of turbulent viscosity.  $F_b$  in Eq. 2.4 is equal to one in the near wall region and equal to zero in the free stream. The function takes on intermediate values in the wake region, ensuring a smooth transition. The model constants applied in the near wall region correspond to those customary applied in the  $k$ - $\omega$  model ( $\sigma_k = 0.5$ ,  $\sigma_\omega = 0.5$ ,  $\beta = 0.075$ ,  $\beta^* = 0.09$ ,  $\gamma = 0.5532$ ) while in the free stream region the constants are defined in accordance with the  $k$ - $\epsilon$  model ( $\sigma_k = 1.0$ ,  $\sigma_\omega = \sigma_{\omega_2} = 0.856$ ,  $\beta = 0.0828$ ,  $\beta^* = 0.09$ ,  $\gamma = 0.4403$ ).

## 2.4 Free Surface Model

Gravity waves are characterized by orbital fluid particle paths and a fluctuating free surface profile. Such a fluctuation of a free surface is not explicit in the URANS equations, requiring further modeling steps to simulate the vertical velocity oscillations throughout the water column. Methods that focus on capturing the free surface can be classified into two distinct general categories, based on the utilized frame of reference:

- interface-tracking techniques
- interface-capturing techniques

Interface-tracking techniques follow the surface elevation using a Lagrangian moving mesh, which is boundary fitted and updated as the free surface evolves. Methods that fall into this category include the Height Function Method and Line Segment Method, described in detail by Nichols and Hirt (1971, 1973), Hirt et al. (1975), and Nichols (1975). The methods have small storage requirements and typically render low calculation times. However, as pointed out by Hirt and Nichols (1981), the major disadvantage of interface-tracking techniques is the difficulty to represent intersecting surfaces or surfaces that fold. These scenarios may occur when analyzing more complex wave phenomena.

As an alternative, interface-capturing techniques have been developed, which are based on an Eulerian stationary mesh that extends beyond the free surface. The surface is captured indirectly by defining different regions for the water and air phase of the domain, and by identifying the interface between these regions. Among the earliest developments in this field is the Marker and Cell (MAC) method introduced by Harlow and Welch (1965) and later extended by Harlow et al. (1976) and Chen et al. (1997). The basic idea of the method is to spread massless marker particles over the water phase of the domain, which are specified to move with the fluid velocity at their location. The free surface is identified at the interface between regions with and without particles. The method allows for a representation of intersecting and folding surfaces, and has been used in various applications (e.g. Christensen and Deigaard, 2001; Popinet and Zaleski, 2002; Bidoae et al., 2003). However, the introduction of marker particles into the simulation inevitably increases computational storage requirements, which may be impractical when analyzing large domain offshore applications.

The Level Set Method (LSM) introduced by Osher and Sethian (1988) is an alternative Eulerian approach to capturing the free surface, which is more efficient in terms of the required computational storage. As a result, the method has been used for the evaluation of various applications in the offshore engineering sector (e.g. Zhang et al., 2012; Kamath et al., 2013; Iafrazi et al., 2014). The basic idea of the LSM is to define a transport equation in the form of a weighted distance function. When this function is evaluated, the sign of non-zero distance values determines whether each point is in the air or water phase of the domain, while a zero value, the so called zero level set, defines the free surface. A detailed description of the LSM can be found in

Sethian (1999). The principal drawback of the level set method is that it inherently does not satisfy conservation of mass. Therefore, highly accurate schemes for the solution of the level set equation or alternatively, re-initialization schemes are necessary, as described by Salih and Moulic (2013).

An interface-capturing technique that is inherently mass conserving, while also requiring relatively little computational storage compared to the MAC method, is the VOF method introduced by Hirt and Nichols (1981). Since its introduction, the method has been widely researched leading to an abundance of further developments (e.g. Rider and Kothe, 1998; Rudman, 1998; Gueyffier et al., 1999; Welch and Wilson, 2000; Pilliod Jr and Puckett, 2004; Garrioch and Baliga, 2006). The VOF method is well established as part of CFD simulations in offshore engineering applications and was also chosen as a free surface model for the NWCT described in this thesis. The underlying concept of the VOF method is to describe the different fluid regions in terms of a scalar quantity  $\alpha$ , defining the phase at each point of the domain. This is achieved by introducing an additional transport equation that is solved as part of the CFD problem:

$$\frac{\partial \alpha}{\partial t} + U_i \frac{\partial \alpha}{\partial x_i} = 0 \quad (2.5)$$

In the NWCT,  $\alpha$  is set equal to one in areas containing the water phase and equal to zero in those containing the air phase. Regions where  $0 < \alpha < 1$  contain the free surface of the fluid flow. Because the method follows regions, rather than surfaces, difficulties regarding intersecting or folding surfaces are avoided (Hirt and Nichols, 1981). Therefore, VOF based free surface capturing of complex wave scenarios, including a simulation of breaking waves, is generally possible. It should be noted that an accurate resolution of the free surface requires local grid refinement in the free surface region, when utilizing mesh based numerical methods to solve the VOF-CFD problem (Ferziger and Perić, 2002). Mesh refinement also avoids numerical problems of attaining mass conservation which, depending on the formulation, may arise when the free surface containing cells are too coarse.

A variety of further methods have been developed to model free surface flows, but the aforementioned approaches are the most commonly utilized methods in ocean engineering related research and are implemented in a variety of commercial and open source software packets.

## 2.5 Offshore Conditions Model

### 2.5.1 Modeling Strategies

Incorporating offshore conditions into CFD computations has been successfully approached using various modeling strategies that allow for a simulation of waves. As described by [Saripilli et al. \(2014\)](#), the different approaches can be categorized into three general groups:

- inlet mesh displacement methods
- internal wave generation methods
- inlet velocity boundary field methods

The first method closely follows the general concept of physical wave-makers utilized in laboratory testing. Typical marine laboratory facilities consist of a flap or plunger type wave maker, which is set into motion in order to generate the desired offshore conditions. Similarly, a mesh displacement model can be used as part of CFD simulations in order to generate fluid motion in the inlet region of the domain. This approach was, for example, utilized in numerical studies carried out by [Kim et al. \(2001\)](#), [Lal and Elangovan \(2008\)](#), [Finnegan et al. \(2013\)](#), and [Anbarsooz et al. \(2013\)](#). Mesh displacement methods as a means to generate wave conditions are particularly suitable for validation studies, because they allow for a close modeling of comparative laboratory conditions. However, the displacement model results in an overall increase of the computational costs compared to a fixed mesh approach and is therefore seldom used to model full-scale conditions.

An alternative approach was developed by [Larsen and Dancy \(1983\)](#) and [Lin and Liu \(1999\)](#) based on an internal wave generation method that uses a mass source of the continuity equations inside the computational domain to generate wave motion. The method was further developed based on Boussinesq type equations in research documented by [Lee and Suh \(1998\)](#) and [Lee et al. \(2001\)](#). Internal wave generation models have been developed for the simulation of various wave conditions, including linear and nonlinear chromatic waves, irregular waves, and solitary waves. Examples of related research include [Lin and Karunarathna \(2007\)](#), [Choi and Yoon \(2009\)](#), [Hafsia et al. \(2009\)](#), and [Ha et al. \(2013\)](#).



Finally, wave conditions can be simulated using inlet velocity field methods, by specifying the wave kinematics directly as a time varying boundary field at a stationary inlet boundary of the domain. The velocity field is typically derived from potential theory and specified as a Dirichlet boundary condition at the inlet boundary. This method was first utilized by [Lin and Liu \(1998\)](#) as part of a two-dimensional numerical wave tank, and later adapted in three-dimensional simulations carried out by [Li and Fleming \(2001\)](#) as well as [Apsley and Hu \(2003\)](#). The method has since been applied extensively to model a great variety of flow problems, as documented by [Wu et al. \(2008\)](#), [Li and Lin \(2010\)](#), [Zhao et al. \(2010\)](#), and [Chen \(2013\)](#), to name a few. One advantage of the approach lies in the possibility to define the wave conditions directly in the wave equations in terms of the wave height and period, which avoids a translation of the offshore data to a flap or piston motion, as required by mesh displacement methods. Because inlet velocity boundary field methods do not require mesh-motion to generate the wave conditions, the methods are also more efficient in terms of computational costs. In addition, the definition of the wave as part of the boundary conditions allows for a segregated approach, using separate and exchangeable components for wave generation and the fluid computation. It allows for a definition of the wave field without having to alter the fundamental fluid dynamics equations, as required by internal wave generation methods. For these reasons, the approach is also chosen as part of this thesis, as described in detail in [Section 2.5.2](#). A novel CFD modeling strategy that extends the capabilities of Numerical Wave Tanks to incorporate an underlying non-uniform current, is introduced in [Section 2.5.3](#).

## 2.5.2 Wave Model

Several theories have been developed to describe non-linear ocean waves. The most popular approach for practical offshore applications is the solution of the wave problem developed as a power series, as introduced by [Stokes \(1847\)](#). Although a broad spectrum of different wave heights and lengths is covered by this approach, the theory breaks down in shallow waters, as analyzed by [Fenton \(1979\)](#). Furthermore, in offshore applications, a solution is frequently not attained for intermediate water depths, if the wave height is near the breaking limit. These cases are often caused by extreme scenarios and are therefore design relevant.

As an alternative, [Korteweg and de Vries \(1895\)](#) derived a theory based on a Jacobian elliptical function, referred to as Cnoidal theory. [Fenton \(1979\)](#) was able to derive a fifth order solution that can be used to model shallow water waves, but noted that Cnoidal theory also tends to break down for high waves.

Instead of following a purely analytical approach for solving the boundary value problem of a non-linear wave, [Dean \(1965\)](#) introduced a numerical procedure known as stream function theory. It allows for a simultaneous calculation of the non-linear equations, instead of solving the problem successively based on a previously calculated lower order theory. The method has performed well in comparison to laboratory wave studies, as analyzed by [Le Mehaute et al. \(1968\)](#) and extended by [Dean \(1974\)](#). Therein, the stream function approach gave an overall better fit to measured data than the predicted results from Stokes and Cnoidal theory.

[Rienecker and Fenton \(1981\)](#) further extended the approach of Dean's stream function model. Rather than using Dean's least square error method to solve the non-linear equations, Newton's method is used to solve the system, making the calculation numerically more efficient. The approach is commonly referred to as the Fenton model and will subsequently be denoted as such. The range of application of the Fenton model is broader than that of both the Stokes and Cnoidal theory ([Demirbilek and Vincent, 2002](#)), allowing for the generation of a wide spectrum of realistic offshore conditions. This was verified in a previous study carried out by [Markus \(2009\)](#), which specifically analyzed the theory in regard to its applicability for extreme conditions typically encountered at offshore sites. Using the Fenton model, it was possible to attain results for extreme wave scenarios close to the breaking limit, where the fifth order Stokes model had previously broken down. Because these conditions are frequently design relevant, the Fenton model was deemed to be most suitable for the wave scenarios analyzed as part of in this thesis.

After the initial introduction of the Fenton model in 1981, it was further developed by [Fenton \(1985, 1988\)](#), as well as [Fenton and McKee \(1990\)](#). The description of the methodology in this thesis is limited to an overview of the fundamental model equations, while the complete derivation of the wave theory is found in the listed references. The Fenton model assumes an incompressible potential flow. This allows for a formulation of the wave problem in the form of Laplace's equation, written in terms of the stream function  $\psi$ , whose contour lines describe

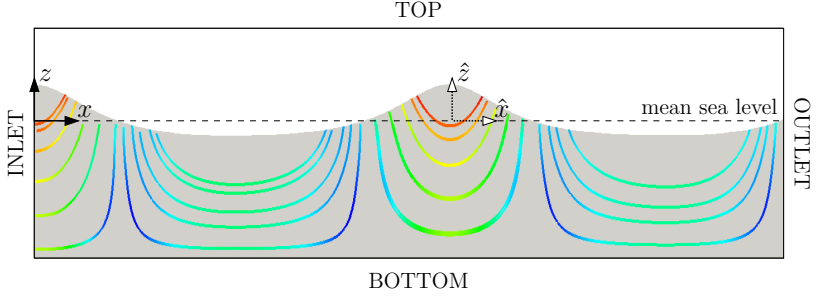


Figure 2.1: Coordinate system definition and NWCT domain specifications with simulated wave stream line visualization.

the streamlines in the flow:

$$\nabla^2 \psi = \frac{\partial^2 \psi}{\partial x^2} + \frac{\partial^2 \psi}{\partial z^2} = 0 \quad (2.6)$$

It is assumed that the wave is traveling in the  $x$ -direction, while the  $z$ -coordinate is defined at the still water level, pointing upwards, as shown in Fig. 2.1. A solution of the wave problem is attained by solving Eq. 2.6 together with appropriate boundary conditions. An application of the boundary conditions can be simplified through a coordinate transformation from the fixed reference frame  $(x, z)$  to a moving frame  $(\hat{x}, \hat{z})$ , which propagates with the wave at celerity  $c_w$ :

$$\hat{x} = x - c_w t \quad (2.7a)$$

$$\hat{z} = z \quad (2.7b)$$

This transformation removes the time-dependency of the problem and allows for a definition of the boundary conditions solely in terms of spatial derivatives. The boundary conditions applied as part of the wave model can be summarized as follows:

- *bottom boundary condition*, assuming that the sea floor located at water depth  $d$ , defined as the distance from the mean sea level to the sea floor, is impermeable:

$$\frac{\partial \psi}{\partial \hat{z}} = 0 \quad \text{at} \quad \hat{z} = -d \quad (2.8a)$$

- *kinematic boundary condition*, assuming that particles located on the surface  $\eta$  of a wave traveling with celerity  $c_w$  remain on the surface at all times:

$$\left(\frac{\partial\psi}{\partial\hat{z}} - c_w\right)\frac{\partial\eta}{\partial\hat{x}} + \frac{\partial\psi}{\partial\hat{x}} = 0 \quad \text{at} \quad \hat{z} = \eta \quad (2.8b)$$

- *dynamic boundary condition*, assuming a constant atmospheric pressure  $p_a$  on the surface of the wave:

$$\frac{1}{2}\left[\left(\frac{\partial\psi}{\partial\hat{z}} - c_w\right)^2 + \left(\frac{\partial\psi}{\partial\hat{x}}\right)^2\right] + g\eta = p_a \quad \text{at} \quad \hat{z} = \eta \quad (2.8c)$$

Fenton's solution method to solve the boundary-value problem defined by Eqs. 2.6 and 2.8 uses a Fourier series approximation of  $\psi$  of order  $N$ , in terms of the wave number  $k_w$ :

$$\psi = -\bar{U}_1^w(\hat{z} + d) + \sqrt{\frac{g}{k_w^3}} \sum_{j=1}^N B_j \frac{\sinh(jk_w(d + \hat{z}))}{\cosh(jk_w d)} \cos(jk_w \hat{x}) \quad (2.9)$$

Here  $\bar{U}_1^w$  is defined as the mean value of the horizontal fluid velocity for a constant value of  $\hat{z}$  taken over one wavelength, while  $B_j$  are the dimensionless Fourier coefficients. The governing Eq. 2.9 is combined into a system of nonlinear equations together with the boundary conditions defined in Eq. 2.8, as well as a set of simple equations defining relationships between the known parameters (e.g. wave height  $H$ , wave period  $T$ , water depth  $d$ , etc.). Thereby, the boundary conditions are evaluated at  $N$  points equidistantly distributed over half the wave length. Fenton proposed solving the system of equations iteratively in steps of wave height using Netwon's method, based on an initial solution derived from linear wave theory.

The horizontal wave velocity  $U_1^w$  and vertical velocity  $U_3^w$  of the wave velocity vector  $U_i^w$  can then be determined directly from Laplace's equation (Eq. 2.6) using the following relationships:

$$U_1^w(\hat{x}, \hat{z}) = \frac{\partial\psi}{\partial\hat{z}} = -\bar{U}_1^w + \sqrt{\frac{g}{k_w}} \sum_{j=1}^N j B_j \frac{\cosh(jk_w(d + \hat{z}))}{\cosh(jk_w d)} \cos(jk_w \hat{x}) \quad (2.10a)$$

$$U_3^w(\hat{x}, \hat{z}) = -\frac{\partial\psi}{\partial\hat{x}} = \sqrt{\frac{g}{k_w}} \sum_{j=1}^N jB_j \frac{\sinh(jk_w(d + \hat{z}))}{\cosh(jk_w d)} \sin(jk_w \hat{x}) \quad (2.10b)$$

Finally, the surface elevation  $\eta$  can be calculated by interpolating the Fourier series that passes through  $\eta_m$ , which are the elevation results computed as part of the solution procedure at the  $N$  points over half the wave length.

$$\eta(\hat{x}) = \frac{1}{k_w} \sum_{j=1}^N F_j \cos(jk_w \hat{x}) \quad (2.11a)$$

$$F_j = \frac{2}{N} \left( \frac{1}{2} \eta_0 + \sum_{m=1}^{N-1} \eta_m \cos\left(\frac{jm\pi}{N}\right) + \frac{1}{2} \eta_N \cos(j\pi) \right) \quad (2.11b)$$

In order to specify the wave solutions given in Eqs. 2.10 and 2.11 as a boundary condition at the stationary inlet of the CFD domain, a back-transformation from the moving frame  $(\hat{x}, \hat{z})$  to the fixed frame  $(x, z)$  is required, using Eq. 2.7. This leads to the following solution of the wave problem, which can be used as part of a boundary condition at an arbitrary constant inlet  $x$ -coordinate:

$$U_1^w(z, t) = -\bar{U}_1^w + \sqrt{\frac{g}{k_w}} \sum_{j=1}^N jB_j \frac{\cosh(jk_w(d + z))}{\cosh(jk_w d)} \cos(jk_w(x - c_w t)) \quad (2.12a)$$

$$U_3^w(z, t) = \sqrt{\frac{g}{k_w}} \sum_{j=1}^N jB_j \frac{\sinh(jk_w(d + z))}{\cosh(jk_w d)} \sin(jk_w(x - c_w t)) \quad (2.12b)$$

$$\eta(t) = \frac{1}{k_w} \sum_{j=1}^N F_j \cos(jk_w(x - c_w t)) \quad (2.13)$$

The velocities perpendicular to the direction of wave propagation ( $U_2^w$ ) are considered to be constant and equal to zero.

### 2.5.3 Wave-Current Model

In order to fully analyze design relevant offshore conditions, an investigation of a maximum wave scenario in combination with an

extreme current scenario is often necessary. This is particularly true in regard to tidal stream generators, where large currents and extreme waves frequently coexist. Modeling the fluid flow under these conditions is not a trivial task due to the assumption of an irrotational flow underlying virtually all wave theories used in offshore engineering practice, including the stream function approach described in [Section 2.5.2](#). Therein, the assumption of irrotationality is made in the derivation of the Laplace form given in [Eq. 2.6](#). When modeling combined wave-current problems, this assumption is typically considered to be fulfilled in the simplest case of a uniform current, for which the flow is assumed to remain irrotational. However, the introduction of a depth varying current gives rise to a shear flow, in which the fluid encounters rotational particle motion. For instance, tidal flows are typically represented by a depth varying exponential velocity profile  $U_i^c$  of the following form:

$$U_1^c(z, t) = U_s \left( \frac{d + z}{d + \eta(t)} \right)^{\beta_c} \quad (2.14)$$

where  $U_s$ ,  $\beta_c$ , and  $d$  denote the site specific surface velocity, current exponent, and undisturbed water depth, respectively. The resulting rotational shear flow is characterized by high velocity gradients in the lower regions of the water column, which is particularly relevant when analyzing offshore support structures.

Extensive research has been carried out to analyze rotational wave-current interaction in order to allow for the incorporation of non-uniform currents. For waves on a current with an exponential distribution of vorticity, [Abdullah \(1949\)](#) was able to derive the dispersion relation and the ensuing wave kinematics. Furthermore, [Dalrymple \(1977\)](#) obtained a numerical solution of a nonlinear wave traveling on a current satisfying  $1/7$  power law vorticity. For an arbitrary distribution of vorticity, [Thomas \(1990\)](#) analyzed the interaction between currents and non-linear waves. More recently, [Liu et al. \(2012\)](#) investigated the interaction between a non-uniform shear current and waves based on the homotopy analysis method. Clearly, a thorough theoretical basis has been established to gain insight into the behavior of wave-current flows. However, at this point these theories are not commonly utilized for offshore applications, for which offshore engineering standards still primarily suggest established irrotational wave theories. An alternative approach is therefore introduced in

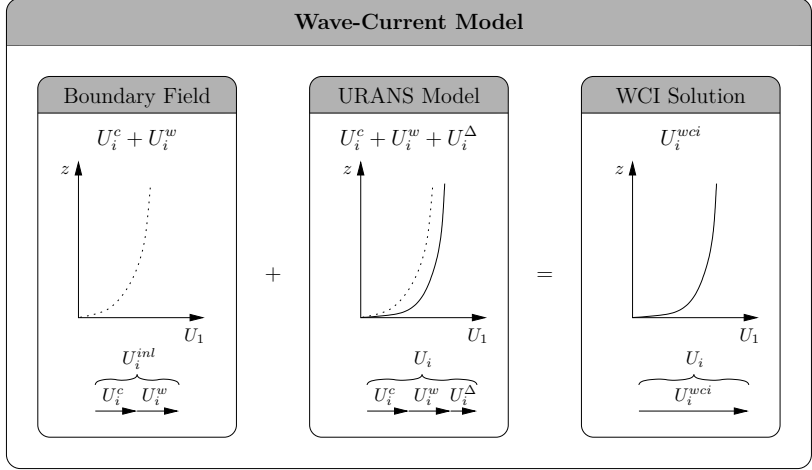


Figure 2.2: Schematic overview of the wave-current model.

this thesis, as summarized in Fig. 2.2. The idea is to utilize the established and thoroughly tested irrotational Fenton model introduced in Section 2.5.2 as a boundary condition for the fluid problem, and to capture the Wave-Current Interaction (WCI) as part of the CFD simulation.

Much like the approach followed in the case of the wave model, the wave-current offshore conditions are again introduced into the CFD model following the inlet boundary field method described in Section 2.5.1. However, rather than specifying a field that incorporates the wave-current interaction solution, a simple linear superposition of the wave and current equations is applied as a boundary model. In this thesis this translates to a superposition of Eqs. 2.12 and 2.14, resulting in the following wave-current velocity equations  $U_i^{w+c}$ , which

are specified as an inlet boundary condition  $U_i^{inl}$ :

$$U_1^{w+c}(z, t) = -\bar{U}_1^w + \sqrt{\frac{g}{k_w}} \sum_{j=1}^N j B_j \frac{\cosh(jk_w(d+z))}{\cosh(jk_w d)} \cos(jk_w(x - c_w t)) + U_s \left( \frac{d+z}{d+\eta(t)} \right)^{\beta_c} \quad (2.15a)$$

$$U_3^{w+c}(z, t) = \sqrt{\frac{g}{k_w}} \sum_{j=1}^N j B_j \frac{\sinh(jk_w(d+z))}{\cosh(jk_w d)} \sin(jk_w(x - c_w t)) \quad (2.15b)$$

The interaction between the wave and the current is then resolved as part of the CFD computation, without any further modeling steps. The result is an altered velocity field  $U_i^{wci}$  in the CFD domain that incorporates the change in velocity  $U_i^\Delta$  due to the interaction between the wave and the current. The advantage of this approach is that it allows for a simple combination of widely used and well established irrotational wave-models with an arbitrary current distribution, while still fully capturing the viscous effects of the flow problem. The introduced method of modeling combined wave-current scenarios is verified in [Section 2.8](#).

The approach of using sophisticated CFD models in order to correct simplified boundary conditions was also followed by [Chen \(2013\)](#), who defined three-dimensional irregular storm waves based on linear wave theory at the boundary, to then capture the non-linear characteristic of the extreme waves in the CFD model. The methodology allowed for successful simulations of irregular, strongly non-linear wave events.

## 2.6 Initial and Boundary Conditions

In order to solve the introduced model equations, it is necessary to define initial internal field conditions for  $U_i$ ,  $P$ ,  $\alpha$ ,  $k$  and  $\omega$ , as well as boundary conditions at the inlet, outlet, bottom, top, and side boundaries of the CFD domain. These conditions are described in this section. A summary of the boundary conditions is given in [Fig. 2.3](#).



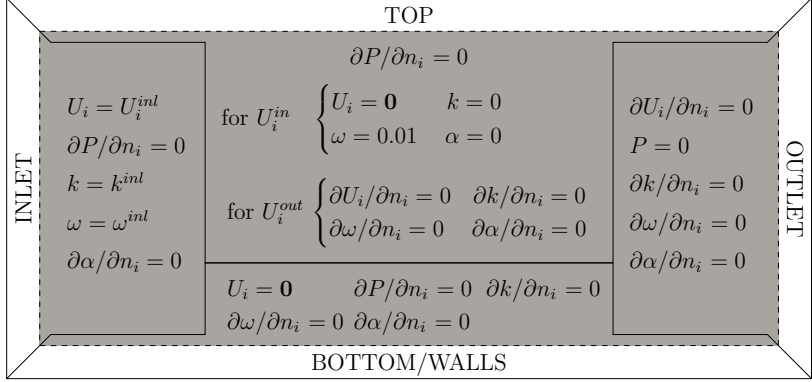


Figure 2.3: Summary of boundary conditions. The superscript  $^{inl}$  refers to the Dirichlet conditions specified for the inlet wave, current, or wave-current boundary.  $U_i^{in}$  and  $U_i^{out}$  correspond to velocity vectors pointing in and out of the domain, respectively. The SIDE boundary conditions are problem dependent, and documented in [Section 2.6.6](#).

### 2.6.1 Initial Conditions

A uniform and constant distribution of the initial pressure field  $P$  and initial turbulence fields  $k$  and  $\omega$  is specified. In the case of the pressure distribution, a zero-field is initially assumed. For  $k$  and  $\omega$  the initial turbulence values can be approximated based on measured turbulence intensities and characteristic length scales using simplified forms from the literature (e.g. [Versteeg and Malalasekera, 2007](#)). The scalar field  $\alpha$  is initially defined depending on the location of the cell node  $z$ -coordinates with respect to the still water level:

$$\alpha = 1 \quad \forall \quad z \leq \eta(t = 0) \quad (2.16a)$$

$$\alpha = 0 \quad \forall \quad z > \eta(t = 0) \quad (2.16b)$$

In the case of a pure wave simulation, the velocity vector  $U_i$  is initiated as a zero vector throughout the domain. For pure current and combined wave-current scenarios, [Eq. 2.14](#) is used to define the  $U_1$  component of the velocity field for all nodes with a  $z$ -coordinate below the still water level. The  $U_1$  velocity component of nodes above the

still water level as well as the  $U_2$  and  $U_3$  velocity components of all nodes in the domain is initially set equal to zero.

### 2.6.2 Inlet Boundary

The velocity boundary at the inlet of the domain is modeled using a Dirichlet boundary condition for  $U_i$  corresponding to the modeled offshore conditions. Depending on the scenario of interest (pure wave, pure current, or combined wave-current), the inlet boundary field  $U_i^{inl}$  takes on the following forms:

$$U_i^{inl} = \begin{cases} U_i^w & \text{for pure wave scenarios} \\ U_i^c & \text{for pure current scenarios} \\ U_i^w + U_i^c & \text{for combined wave-current scenarios} \end{cases} \quad (2.17)$$

Using the wave solution given in [Eq. 2.12](#), the wave vector  $U_i^w$  is defined as follows:

$$U_i^w = \begin{bmatrix} U_1^w(z, t) \\ 0 \\ U_3^w(z, t) \end{bmatrix} \quad \forall \quad z \leq \eta(t) \quad (2.18a)$$

$$U_i^w = \begin{bmatrix} 0 \\ 0 \\ 0 \end{bmatrix} \quad \forall \quad z > \eta(t) \quad (2.18b)$$

Similarly, the current vector  $U_i^c$  is defined using [Eq. 2.14](#):

$$U_i^c = \begin{bmatrix} U_1^c(z, t) \\ 0 \\ 0 \end{bmatrix} \quad \forall \quad z \leq \eta(t) \quad (2.19a)$$

$$U_i^c = \begin{bmatrix} 0 \\ 0 \\ 0 \end{bmatrix} \quad \forall \quad z > \eta(t) \quad (2.19b)$$

If desired, it would also be possible to include a non-zero velocity boundary condition in the air phase region of the inlet boundary (at  $z > \eta(t)$ ) for each scenario, to incorporate a wind profile into the simulation.

As described in [Section 2.6.1](#), the still water level is used to define the initial conditions of the phase field  $\alpha$ . If the fully developed

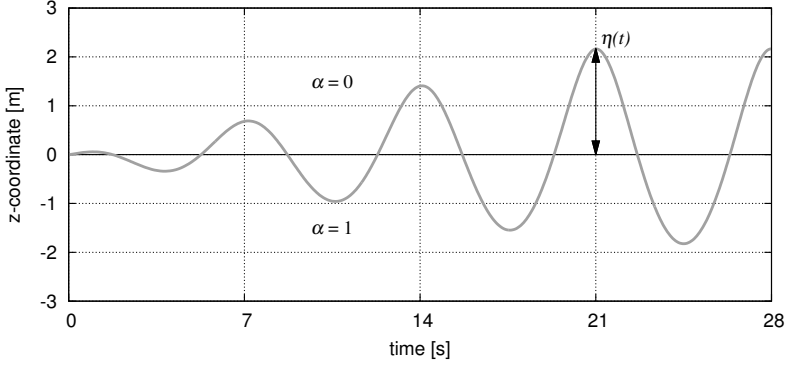


Figure 2.4: Incremental wave stepping with 3 build-up waves shown exemplarily for a 4 m target wave with 7 s period in 35 m water depth.

wave solution of Eq. 2.12 is specified as a boundary condition, phase-discrepancies between the inlet boundary and adjacent cell regions may occur at the onset of the simulation. To avoid such discrepancies, and possibly instabilities in the numerical calculation of the flow problem, a gradual buildup of the wave field is initiated. This is achieved by applying a wave stepping procedure over a specified time frame. As part of this procedure, the wave height is increased at each time step and the nonlinear wave-problem is recomputed, starting from the still water level and ending at the target wave height. The result is a smooth wave buildup as shown in Fig. 2.4, which allows for a stable generation of the specified wave conditions.

The boundary condition for the pressure  $P$  at the inlet is defined in the form of a Neumann boundary condition:

$$\left. \frac{\partial P}{\partial n_i} \right|_{inl} = 0 \quad (2.20)$$

where  $n_i$  is the cell face normal vector. This specification for the pressure boundary avoids inconsistencies with the defined velocity boundary condition (Hirsch, 2007). In the Navier-Stokes equations, velocity and pressure fields are coupled. A non zero pressure gradient at the inlet boundary could therefore result in an increase or decrease of the velocity field, inconsistent with the specified velocity

boundary condition, which in turn may lead to numerical instabilities. Furthermore, specifying Dirichlet boundary conditions for both the velocity and the pressure would over-constrain the problem. These problems are avoided when using the specified combination of a Dirichlet velocity condition with a Neumann pressure condition at the inlet boundary.

The boundary conditions for  $k$  and  $\omega$  are defined in the form of Dirichlet boundary conditions using simplified forms from the literature (e.g. [Versteeg and Malalasekera, 2007](#)), in the same manner as the definition of the initial conditions for these turbulence parameter.

### 2.6.3 Outlet Boundary

It is assumed that the outlet boundary of the domain is positioned at a location where the flow is approximately unidirectional and fully developed. Under such conditions, it is customary in CFD practice to specify a zero gradient velocity boundary condition together with a Dirichlet pressure boundary (e.g. [Jasak, 1996](#); [Versteeg and Malalasekera, 2007](#)). This outflow boundary condition has been the source of some discussion in the literature. Concerns regarding its mathematical intricacies have been raised by [Gresho \(1991\)](#). However, the work acknowledges the success of the boundary condition in CFD simulations and its advantages in terms of computational efficiency. As recently pointed out by [Tu et al. \(2007\)](#), these open boundary conditions continue to be preferable due to their simplicity and efficiency. The outlet boundary conditions for  $k$  and  $\omega$  are specified using a zero gradient condition, as recommended by [Versteeg and Malalasekera \(2007\)](#). A zero gradient outlet condition is also applied for  $\alpha$ .

To reduce wave reflections, the outlet boundary is preceded by a numerical damping zone in the NWCT. Here, mesh stretching is utilized in order to damp the wave numerically, thus reducing outlet reflections at low computational costs. It should be noted that reflections are not particularly crucial for the scenarios analyzed in this thesis. When modeling extreme waves for the design of offshore structures, the simulation is completed after a single target wave has surpassed the structure. Therefore, an outlet distance equal to the wavelength multiplied by the number of preceding buildup waves is sufficient to ensure boundary independent results. Wave reflections begin influencing results in long term simulations, which may, for example, be of interest when analyzing irregular sea states. Under

such conditions, a variety of different approaches have been developed to reduce reflections from the outlet boundary. For instance, the development of open boundary conditions has been pursued by several researchers, including but not limited to [Orlanski \(1976\)](#), [Engquist and Majda \(1977\)](#), [Chapman \(1985\)](#), and [Poinsot and Lele \(1992\)](#). These conditions allow for the developing kinematics in the domain to pass through the outlet without influencing the interior solution. A review of general literature on the topic is given by [Givoli \(1991, 2004\)](#). Another option is the introduction of an artificial damping zone, also referred to as a sponge layer, in the outlet region of the domain (e.g. [Israeli and Orszag, 1981](#); [Larsen and Dancy, 1983](#)). Active wave absorption in the form of a piston-like Neumann condition is also conceivable, as described by [Clément \(1996\)](#). When analyzing load cases influenced by outlet reflections, such methods may be used to improve the efficiency and quality of the computation. Because the research presented in this thesis focuses on the simulation of individual extreme scenarios, the details of different damping strategies are not further analyzed.

#### 2.6.4 Bottom Boundary and other Wall Boundaries

The bottom boundary condition and all other structure boundaries defined in the domain have to fulfill the characteristics of the modeled wall boundary, namely the zero velocity (no slip) and impermeability conditions of the boundary.

For low-Reynolds flows and for highly refined wall boundaries this can be achieved by simply introducing a zero velocity Dirichlet condition for  $U_i$  in combination with a zero gradient Neumann condition for  $P$  ([Breuer, 2002](#)). The turbulence parameters  $k$  and  $\omega$  as well as the phase parameter  $\alpha$  at the bottom boundary are also specified in the form of a zero gradient condition. However, the flows encountered in ocean engineering practice are typically of a high Reynolds number. For such flows, it is customary to apply wall functions that relate the turbulence parameters  $k$  and  $\omega$  to the local wall shear stress and mean velocity ([Versteeg and Malalasekera, 2007](#)). A variety of different wall functions for turbulent flow simulations have been developed (e.g. [Schumann, 1975](#); [Werner and Wengle, 1993](#); [Wilcox, 1998](#); [Moin, 2002](#)). When modeling high-Reynolds flows in the NWCT, the wall function formulation according to [Launder and Spalding \(1974\)](#) is utilized. It defines the logarithmic mean velocity profile in the vicinity of the wall as a function of the turbulent kinetic energy  $k$ :

$$\frac{U_i C_\mu^{1/4} \sqrt{k}}{u_\tau^2} = \frac{1}{\kappa_{wall}} \ln \left( E \frac{C_\mu^{1/4} y_{wall} \sqrt{k}}{\nu} \right) \quad (2.21)$$

where  $u_\tau$  is the friction velocity and  $y_{wall}$  is the wall distance. The model constants are defined as  $C_\mu = 0.09$ ,  $\kappa_{wall} = 0.42$  and  $E = 9.8$ . When analyzing wall bounded turbulent flows, [Salas et al. \(1999\)](#) found that the wall function formulation of [Launder and Spalding \(1974\)](#) outperforms approaches based on the universal law of the wall. The model has thus found wide application in the computation of industrial flow problems.

### 2.6.5 Top Boundary

At the top boundary, an inlet/outlet back flow boundary condition is specified for  $U_i$ ,  $k$ ,  $\omega$ , and  $\alpha$ . Here, a zero gradient condition is applied to the variable if the velocity vector at the boundary points out of the domain. If the velocity vector points into the domain, an inflow condition is established in the form of a Dirichlet condition. For the inflow condition, the velocity and turbulence values are set equal to zero to model the entrainment of an inactive fluid from the surrounding environment, under the assumption that the top boundary is located sufficiently far from the wave surface profile. Likewise,  $\alpha$  is also defined as zero for the inflow condition, implying an entrainment of the air phase at the top boundary. The top boundary condition for  $P$  is set equal to zero gradient.

### 2.6.6 Side Boundary

The boundary conditions for the sides of the domain are problem dependent. For simulations in a two-dimensional NWCT, the boundary conditions for all variables are set equal to zero gradient on the side boundaries. These boundary conditions can also be applied for three-dimensional flow problems, when modeling full scale offshore conditions. Alternatively, cyclic boundary conditions may be applied, enforcing equivalent values of the variables on corresponding cell phases of the front and back side of the domain. Regarding the avoidance of boundary effects on a structure defined in the center of the domain, cyclic boundary conditions may allow for a smaller domain width compared to an application of zero gradient conditions. When carrying

out validation studies comparing results from NWCT-simulations to experimental tests, the physical dimensions of the flume or basin are typically also used for the dimensioning of the CFD domain. In these cases, a physical wall boundary is usually defined on the sides of the domain, according to the description given in [Section 2.6.6](#).

## 2.7 Solution Schemes and Software Description

The introduced models chosen specifically for the simulation of offshore conditions are combined into the NWCT. The fundamental system of equations consists of the continuity equation ([Eq. 2.1](#)), the three momentum equations ([Eq. 2.2](#)), the two turbulence model equations ([Eqs. 2.3](#) and [2.4](#)), and the phase transport equation ([Eq. 2.5](#)), with the unknown variables  $P$ ,  $U_i$ ,  $k$ ,  $\omega$ , and  $\alpha$ . The system of partial differential equations is solved numerically using the Finite Volume (FV) method. As part of this discretization scheme, the individual terms of the equations are evaluated as fluxes at the surface of the individual cells. The flux entering one volume is equal to that leaving the adjacent volume, independent of the number of faces enclosing the control volume. This inherently satisfies conservation of mass and allows for a simple implementation of arbitrary polyhedral elements and mixed meshes. The discretized problem is solved using the initial conditions and boundary conditions described in [Section 2.6](#), including the introduced wave and current models ([Eq. 2.17](#)). The schemes utilized in the solution process of the simulations consist of higher-order upwind differencing schemes. As part of the wave and wave-current simulations, first order implicit Euler time integration is carried out.

The results presented in this thesis are computed using the open source software package OpenFOAM version 2.1. The program consists of a parallel computing URANS code that utilizes the Pressure Implicit with Splitting of Operators (PISO) method in the solution process ([Issa, 1986](#)), a segregated approach for which operations on pressure and velocity are carried out decoupled at each iterative solution step. Phase-fraction based interface capturing is used as part of the incorporated VOF method with the addition of an artificial compression term at the surface interface, as introduced by [Rusche \(2002\)](#).

In addition, the in-house control and monitoring script Load Analysis Tool for Offshore Structures (LATOS) was developed and

applied. LATOS is a script language based software that is programmed around the functionalities of OpenFOAM. Incorporated into LATOS is a boundary field generator for offshore conditions, a reduced modeling method (Chapter 4), and an interface to a MATLAB based optimization framework (Chapter 5).

## 2.8 Model Verification

In order to apply the introduced NWCT to a realistic analysis of offshore structures, it is crucial to accurately capture the flow kinematics in regions of interest in the defined numerical domain. Therefore, a detailed analysis of the development of fluid particle motion is carried out. In particular, the aim is to verify the newly proposed approach of modeling combined wave-current flows using the methodology introduced in Section 2.5.3.

### 2.8.1 Test Case Description

For the verification test case, a wave-current simulation with a uniform current profile is used to analyze the capability of the NWCT. The scenario is selected because the assumption of an irrotational flow field for the calculation of an analytical reference solution is plausible for such conditions.

The parameters used to define the wave conditions are summarized in Tab. 2.1a. Based on these values, the boundary conditions for the velocity and phase fields are calculated. In addition, boundary conditions for the turbulence parameters are defined based on recorded data from offshore sites. A turbulent kinetic energy of  $0.0864 \text{ m}^2/\text{s}^2$  is specified at the inlet while the turbulence frequency is set to  $0.21467 \text{ 1/s}$ . This corresponds to a turbulence intensity of 6% and a turbulent length scale of 2.5 m. A sensitivity study was carried out in order to analyze the influence of the turbulence boundary data. It was found that an accurate simulation of the velocity field is not particularly sensitive to the choice of the turbulence frequency at the boundary. A variation of  $\omega$  corresponding to turbulent length scales ranging from 0.1 m to 20 m resulted in a difference of 2% or less in peak values. In addition, the sensitivity of the results to the selected  $k$  value was analyzed. A distortion of the velocity profile was observed for specified inlet values corresponding to a turbulence intensity of 10% and higher. This is



Table 2.1: Verification study test case specifications.

(a) Boundary condition data		(b) Domain and mesh data	
Parameter	Value	Parameter	Value
current velocity	2 m/s	domain length	700 m
current exp. $\beta_c$	0	domain height	55 m
water depth $d$	35 m	free surface mesh size	0.3 m
wave height $H$	4 m	water region mesh size	0.5 m
wave period $T$	7 s	air region mesh size	1.8 m
wave build-up	14 s	number of cells	100,000

likely the result of additional dissipation caused by the increase in turbulence.

The FV discretization of the computational domain is carried out using a Cartesian mesh. Tab. 2.1b summarizes the most relevant mesh parameters. A relatively long domain length is selected in order to analyze the development of the wave as it travels through the tank. Because the chosen offshore scenarios lead to a wave length of about 100 m, the length of the domain was selected such that a comparison of fluid kinematics after multiple wave lengths is possible. Applications of the NWCT to the simulation of an offshore structure under extreme load scenarios can be carried out using a significantly shorter domain length. For a wave of wavelength 100 m simulated in conjunction with two preceding build-up waves, an outlet distance of 200 m from the structure would be adequate to guarantee reflection independent results.

The computational mesh is optimized with consideration of the significance of different domain regions. Cells located in regions of a constant water phase are defined with a maximum edge length of 0.5 m, with mesh refinement towards the bottom and the air boundaries. The motion of the fluid kinematics in cells of constant air phase has no particular significance in this application, apart from acting as a buffer zone allowing for a fluctuation of the sea level. Therefore, the mesh is coarsened in the regions close to the top boundary of the domain. It should be noted that the mesh set up is defined for offshore environments with characteristics comparable to those presented in Tab. 2.1a. When modeling significantly smaller waves, the mesh should

be refined accordingly in order to capture the relevant fluctuations.

For the analyzed offshore environments, it is assumed that the wave is constant in the third spatial direction. This is consistent with offshore engineering practice, where site specific data is usually not available to generate a three-dimensional wave field. For the presented verification test case, it is therefore sufficient to carry out a two-dimensional simulation.

For waves traveling on a current that is uniform over the water depth, a theoretical solution of the flow problem can be calculated by solving the irrotational Fenton model, as explained by [Fenton \(1988\)](#). Using this reference solution, the simulated fluid motion in the NWCT is verified.

## 2.8.2 Test Case Results

The simulated results probed at three depths throughout the water column are compared to the theoretical Fenton wave solution in [Figs. 2.5](#) and [2.6](#). The profiles attained as part of the CFD simulation closely match the predicted theoretical results. In addition, the accuracy of the NWCT is assessed in [Tab. 2.2](#), which gives the simulated and theoretical maximum and minimum velocity values. In the lower regions of the water column, peak velocities deviate by a maximum value of  $0.0136 \text{ m/s}$ , while in the upper regions, the largest calculated difference is  $0.0283 \text{ m/s}$ . Considering the magnitude of the peak and trough velocities, the results are remarkably close to the theoretical prediction.

It can be shown that the adjustment of the wave-current velocity field takes place within a relatively short distance from the domain inlet. [Fig. 2.7](#) shows the distribution of the horizontal velocity component of the developed flow field over the first 200 m of the numerical tank. Within half a wave length, the simulated distribution matches the predicted theoretical results. The two profiles coincide as the wave travels deeper into the domain.

In addition to the evaluation of results two wave lengths from the inlet, the particle kinematics was also analyzed at an inlet distance of three and four wave lengths. It was found that the results are consistent with those attained further upstream in the numerical tank. Even after four wave lengths (400 m from the inlet boundary), the fluid motion does not deviate significantly from the kinematics attained in the upstream region of the tank.

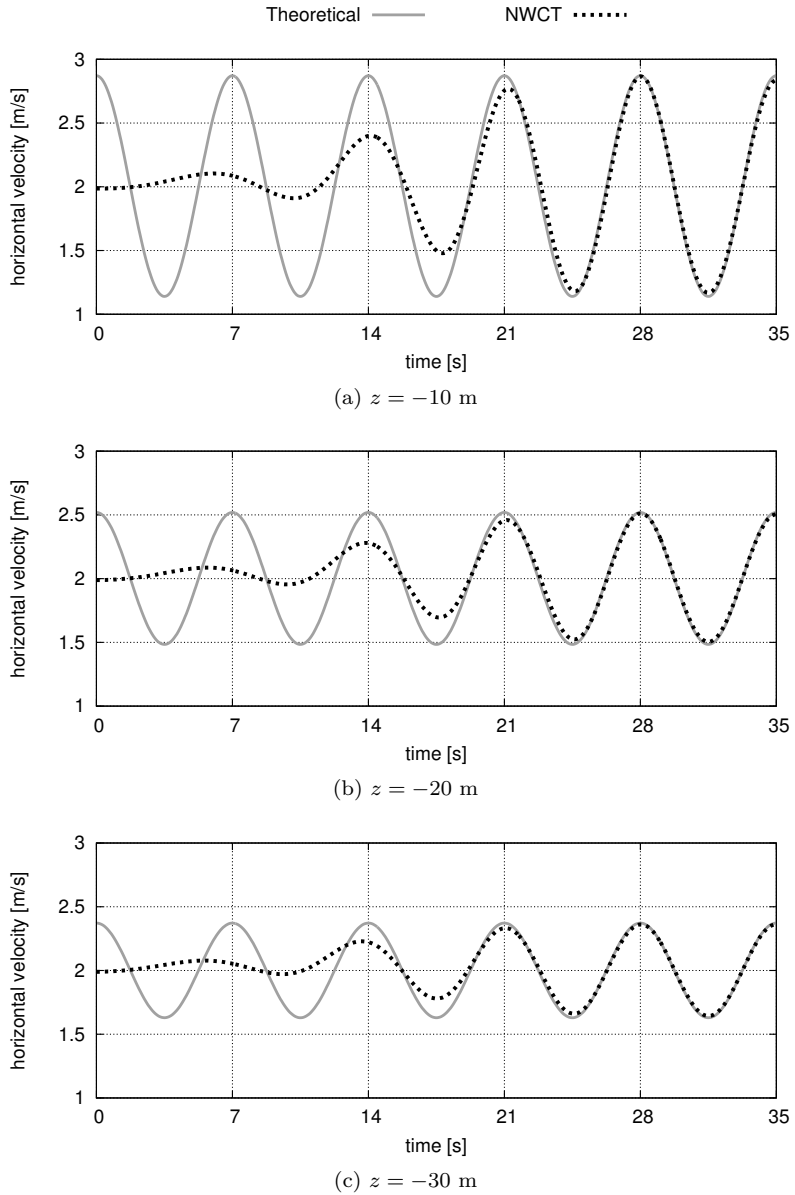


Figure 2.5: Comparison of horizontal velocities at various water depths measured at a distance of 203.5 m from the inlet (2 wave lengths).

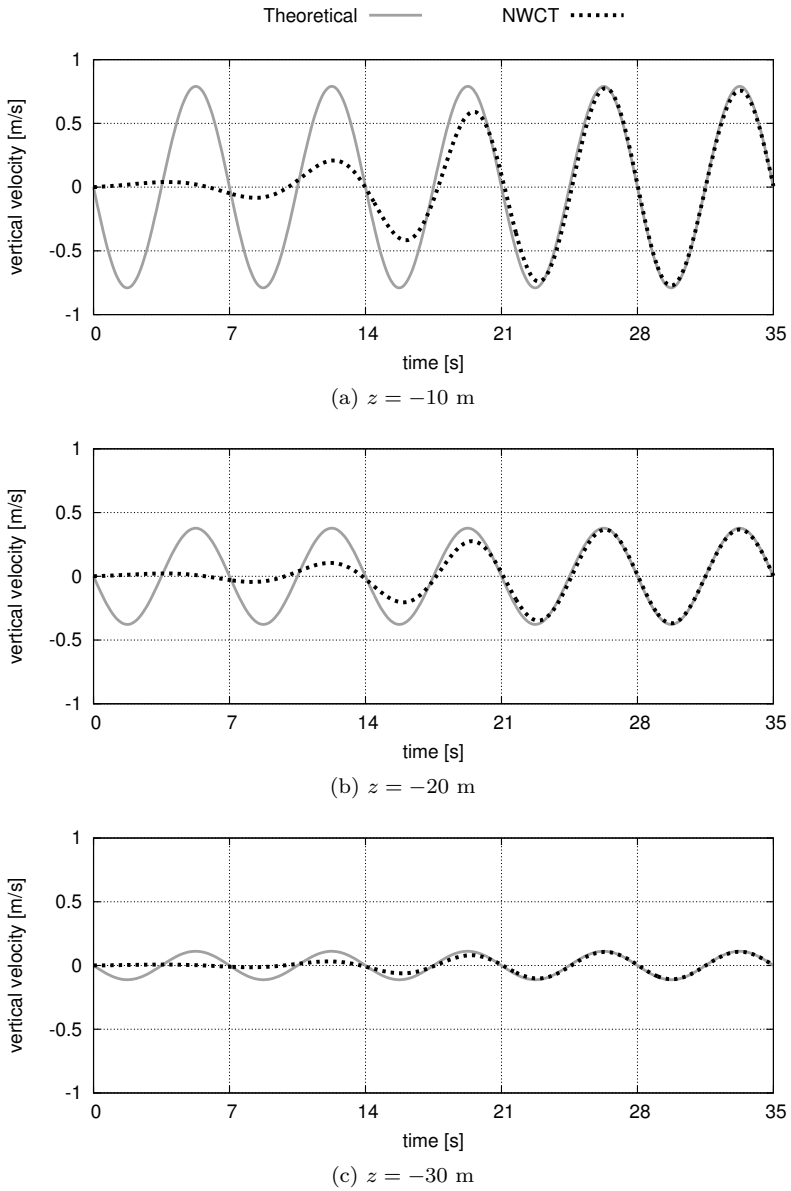


Figure 2.6: Comparison of vertical velocities at various water depths measured at a distance of 203.5 m from the inlet (2 wave lengths).

Table 2.2: Validation of fluid particle kinematics at a distance of 203.5 m from the inlet (2 wave lengths).

$z$ [m]	Extremum	$t$ [s]	Theoretical [m/s]	Simulated [m/s]	$\Delta$ [m/s]
-10	hor. max	42.00	2.8714	2.8652	0.0062
	ver. max	40.25	0.7903	0.7714	0.0189
	hor. min	45.50	1.1397	1.1680	-0.0283
	ver. min	43.75	-0.7903	-0.7729	-0.0174
-20	hor. max	42.00	2.5195	2.5109	0.0086
	ver. max	40.25	0.3774	0.3669	0.0105
	hor. min	45.50	1.4838	1.5044	-0.0206
	ver. min	43.75	-0.3774	-0.3687	-0.0087
-30	hor. max	42.00	2.3719	2.3629	0.0090
	ver. max	40.25	0.1115	0.1077	0.0038
	hor. min	45.50	1.6293	1.6429	-0.0136
	ver. min	43.75	-0.1115	-0.1078	-0.0037

In order to verify that the calculated increase in fluid particle velocities can truly be contributed to the interaction between the wave and the current, an additional test was carried out. The same wave was again simulated in combination with a uniform current. However, in this simulation, the inlet boundary condition was not defined as a linear superposition of the fluid velocities of the wave and the current. Instead, the interaction was already incorporated into the inflow condition, based on the theoretical solution calculated with the Fenton model. In this case, it was found that the wave travels through the domain without an increase in horizontal or vertical fluid velocities. Therefore, it is reasonable to conclude that when a linear superposition of velocities is used as an inlet condition, the change in fluid kinematics occurring in the tank can truly be contributed to the interaction between the wave and the current.

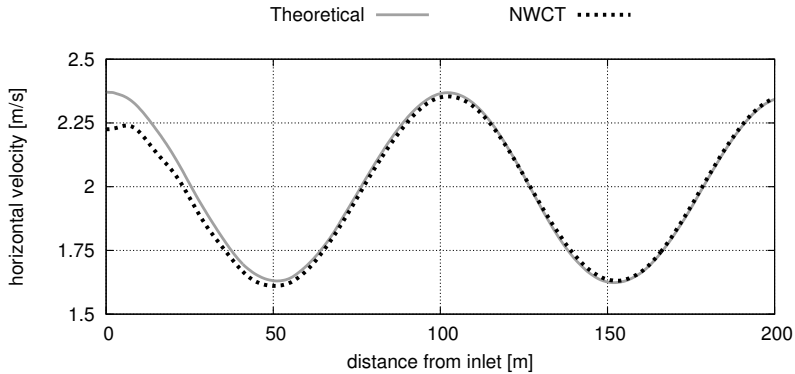


Figure 2.7: Horizontal velocity comparison of the developed flow field at  $z = -30$  m and  $t = 42$  s over a distance of 200 m from the inlet.

## 2.9 Conclusions and Summary

The aim of this chapter was to establish a NWCT that can be used to simulate realistic marine environments. Various models were carefully chosen and combined into a methodology specifically configured to simulate offshore conditions. The methodology utilizes CFD to calculate a numerical solution of the unsteady RANS equations in combination with a two equation turbulence model and the VOF method. The inlet boundary data is calculated using the Fenton model to generate a non-linear wave field. This allows for a multiphase simulation with a free surface wave profile.

A methodology was introduced that extends the numerical wave tank to incorporate a current profile of arbitrary distribution. This is achieved by gradually projecting the wave solution onto an initial current profile at the inlet boundary of the computational domain. The interaction between the wave and the current is then captured within the CFD simulation.

The method was verified in a test case simulation that compared wave-current velocity kinematics computed with the NWCT to a theoretical reference solution. A good agreement of the results was attained with regards to the distribution and peak values of horizontal and vertical velocities. Overall, it was shown that the presented approach is suitable to assist in an efficient analysis of structures subjected to complex offshore conditions, as carried out in [Chapter 3](#).

---

## Chapter 3

# Load Analysis

---

### 3.1 Introduction and Overview

The NWCT introduced in [Chapter 2](#) can generally be applied to simulations of various offshore structures. In this chapter, the method is utilized to investigate support structures of tidal turbines. In recent years, a number of tidal turbine prototypes and pre-commercial devices have been successfully developed and tested. In order to push the technology into a commercial phase, elaborate research projects have focused on the optimization of the devices and advancements in the methods used in the development. Many of these projects have relied on sophisticated numerical methods to carry out extensive studies of complex flow problems. This has led to considerable progress in turbine design, in particular regarding the blades and the generator efficiency. For instance, [McCann et al. \(2008\)](#) carried out a numerical investigation of the power performance of tidal stream devices, taking into account the turbulent characteristics of the flow. A numerical analysis of the wake of horizontal axis turbines was conducted by [Gant and Stallard \(2008\)](#) in order to gain insight into the influence of device proximity on the net power output. Furthermore, [Ruopp and Ruprecht \(2011\)](#) introduced an automated blade optimization technique based on a genetic optimization algorithm, allowing for improvements of the

overall blade design.

While diverse studies of the turbine design have been carried out and published, research concerning design relevant loading on the structures is still very limited. This is particularly problematic when designing the support structure of an offshore device because an accurate consideration of extreme load scenarios is indispensable to ensure the stability of the overall structure. Such load scenarios have been investigated thoroughly with regard to offshore wind structures. Examples include numerical investigations of wave induced loading on offshore substructures carried out by [Chella et al. \(2012\)](#) as well as [Bredmose and Jacobsen \(2011\)](#). These investigations primarily focused on the effect of wave loading, which is reasonable considering that most offshore wind parks are located in areas with moderate current velocities. However, in the case of tidal turbines, the extreme wave scenario is combined with a maximum current scenario in the definition of extreme loads. This approach accounts for the possibility of extreme weather conditions with large waves occurring at the time of maximum tidal velocities. This load combination typically involves a tidal flow for which fluid velocities exceed  $3\text{ m/s}$ . Under these conditions, the drag forces resulting from the current begin to have a significant impact, in addition to the wave induced loads on the structure.

In engineering practice, wave and current loads are still often regarded separately and the resulting fields are superimposed to estimate the combined loading. This allows for the implementation of simplified methods, such as the calculation of wave loads based on potential theory. However, this approach neglects the interaction phenomenon between the wave and the current. The influence of this simplification on the accuracy of the computed overall loads on the structure is questionable, but has not been investigated and documented thoroughly. In order to address this topic, combined wave-current offshore conditions are analyzed in this chapter. The aim is to investigate to what extent the wave-current conditions influence the total loads on tidal turbine foundations, compared to a linear superposition of a pure wave and pure current scenario. The numerical methods introduced in [Chapter 2](#) are used in order to carry out the investigation. This allows for the treatment of complex three-dimensional structures, which is particularly relevant when analyzing structures for which form parameters are not readily available.

In a first step, the fluid kinematics of combined wave-current flows



and the ensuing implications for force computations are analyzed. Following, the numerical methods are applied to a two-dimensional study of hydrodynamic wave and current loads on various geometries. Finally, the methodology is applied to the project SeaTurtle, a tidal turbine prototype constructed off the coast of South Korea's Jindo Island.

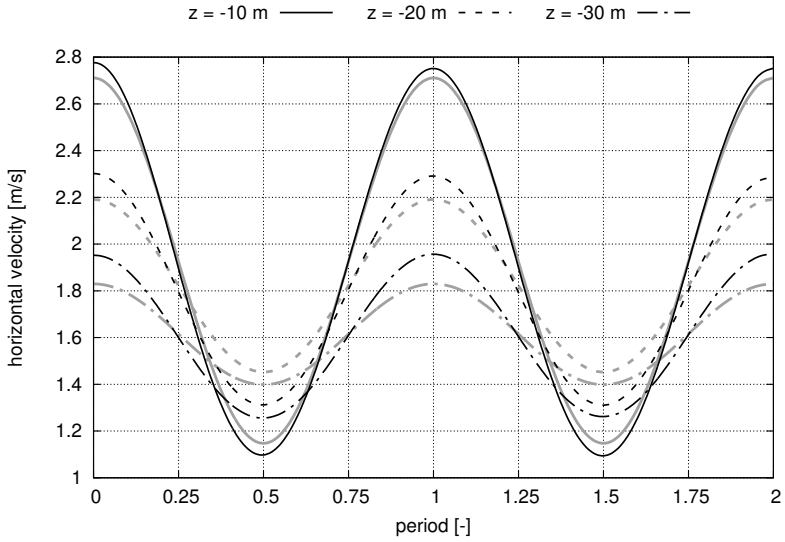
Part of the work presented in this chapter has been published in *Ocean Engineering* (Markus et al., 2013c). It is presented here with explicit written consent from the publisher.

### 3.2 Assessment of Wave-Current Fluid Kinematics

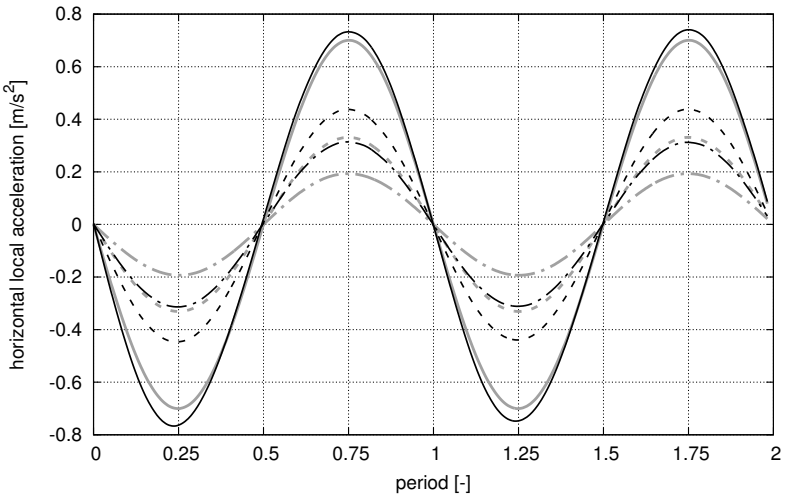
The methodology proposed in [Section 2.5.3](#) to capture wave-current kinematics using the NWCT is utilized in order to analyze realistic offshore conditions encountered in regions suitable for tidal turbines. A test scenario is defined consisting of a 4 m high wave with a period of 7 s superimposed with an exponential current distribution with  $U_s$  and  $\beta_c$  equal to 2 m/s and 0.11, respectively. The boundary conditions for the turbulence parameters are defined analogue to the specifications of [Section 2.8.1](#), based on recorded data from offshore sites. The simulation is carried out for a water depth of 35 m using the domain discretization summarized in [Tab. 2.1b](#) on [page 31](#).

The calculated velocity profiles are plotted in [Fig. 3.1a](#). Given are the linearly superimposed current and wave velocity fields as well as the computed WCI-solution determined as part of the CFD-simulation. The difference in fluid kinematics in the near surface region of the water column is relatively small. Here, the calculated difference in peak velocities is less than 2.5 %. However, when analyzing the results attained near the sea floor, a more significant difference in particle kinematics becomes apparent. In this region, a linear superposition of the wave and current velocities leads to an underestimation of the maximum horizontal velocities of up to 6 %.

The described maximum wave velocities are of particular interest when modeling geometries and wave conditions for which the drag force is dominant. However, the contribution of the maximum wave loads on tidal turbines is largely caused by inertia forces. These forces can be defined in terms of the local fluid accelerations, as for example discussed by [Sarpkaya \(2010\)](#) and [Sumer and Fredsøe \(2006\)](#). A comparison



(a) Velocity



(b) Acceleration

Figure 3.1: Comparison of fluid kinematic between results simulated considering WCI (black curves) and linearly superimposed results without WCI (grey curves).

of the calculated local accelerations with and without wave-current interaction is given in Fig. 3.1b. Here, wave-current interaction results in an increase in peak accelerations ranging from approximately 5 % near the free surface to over 35 % near the sea floor. Once again, the deviation is particularly high in the lower regions of the water column. This phenomena is a result of the depth varying wave velocity field. Compared to the near surface regions, the wave motion is significantly smaller in the near sea floor region, which in turn leads to a larger influence of the current field and an increased change in fluid particle kinematics. The significant increase in particle acceleration in the near sea floor region suggests that an increase in the total forces on bottom mounted structures is to be expected when considering combined wave-current loading compared to a linear superposition of the individual load cases.

### 3.3 Load Analysis of Basic Shapes

The established hypothesis regarding an increase in structural loading due to wave-current interaction is verified in this section. A test case is presented that includes a two-dimensional study of different geometries subjected to a pure wave, pure current, and combined wave-current scenario. Based on simulations carried out using the NWCT, the structural loads are determined directly from the CFD pressure and velocity fields computed with the NWCT. The total force  $F_i$  acting on the structure is defined in terms of a pressure force contribution and a viscous force contribution as an integral over the structure surface area  $A_s$ :

$$F_{tot} = \int_{A_s} P n_i dA_s + \int_{A_s} \tau_{wall} dA_s \quad (3.1a)$$

$$= \int_{A_s} P n_i dA_s + \int_{A_s} \mu \left( \frac{\partial U_{wall}}{\partial y_{wall}} \right)_{y_{wall}=0} dA_s \quad (3.1b)$$

where  $\tau_{wall}$  is the wall shear stress according to Pope (2000) and  $U_{wall}$  is the flow velocity parallel to the wall. When modeling turbulent flows, the effective viscosity  $\mu_{eff}$  rather than the fluid viscosity  $\mu$  is used in the computation of the viscous force term, in order to consider the influence of the modeled turbulent viscosity  $\mu_t$  on the overall forces:

$$\mu_{eff} = \mu + \mu_t \quad (3.2)$$

Using this adjustment, the discretized form of Eq. 3.1 is written as a sum over the number of boundary cell nodes  $N$  of the structure:

$$F_{tot} = \sum_{j=1}^N P n_i A_{s,j} + \sum_{j=1}^N \mu_{eff} \left( \frac{\partial U_{wall}}{\partial y_{wall}} \right)_{y_{wall}=0} A_{s,j} \quad (3.3)$$

with  $A_{s,j}$  denoting the face surface area of the structure adjacent boundary cells.

### 3.3.1 Test Case Setup

The structural load analysis incorporates an investigation of three geometries as defined in Tab. 3.1. The two-dimensional shapes are chosen to resemble a wide range of plausible alternatives for tidal turbine GBFs with distinct representative flow patterns. An equivalent cross-sectional area  $A$  with horizontal surface normal perpendicular to the flow direction is specified for each shape. This implies that all structures would consist of an identical horizontal load resistance due to frictional force activated between the base of the foundation and the sea floor. In addition, the same height  $h$  is selected for all geometries in order to ensure that each structure is subjected to the same undisturbed flow environment. The base width  $w$  of the structures is adjusted to fulfill the requirement of equivalent cross-sectional areas. The previously analyzed offshore scenario of Section 3.2 is used as a load case for the force investigation. In addition, a pure wave and pure current scenario is defined, as given in Tab. 3.2.

As part of the FV discretization, a hexa-dominated mesh with refinement at the wall boundaries is generated for each geometry. The high velocities resulting from the real-size offshore scenario motivate the use of wall functions at the structure boundaries in order to allow for manageable computational costs. The use of wall functions requires the generation of a mesh resulting in a dimension-less wall distance  $y^+$  in the range  $30 < y^+ < 300$ , which ensures that the first row of cell centers is positioned within the log-law layer of the boundary flow. The requirement is satisfied in the shape study by refining the mesh to a wall distance of  $2 \cdot 10^{-3}$  m. Overall, the computational domain

is defined with a total length of 650 m and a height of 55 m. The structures are positioned approximately 150 m from the inlet. Each discretization consists of approximately 200,000 cells of which 99.2 % are of hexahedral shape and the remaining 0.8 % of triangular shape.

Table 3.1: Geometry parameters

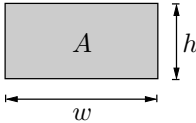
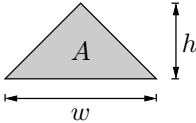
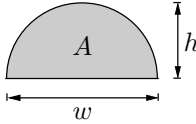
Shape	Section Area $A$ [m <sup>2</sup> ]	Height $h$ [m]	Width $w$ [m]
	200.00	10.00	20.00
	200.00	10.00	40.00
	200.00	10.00	25.46

Table 3.2: Load case parameters

Load Case	Water Depth $d$ [m]	Wave Period $T$ [s]	Wave Height $H$ [m]	Surface Velocity $U_s$ [m/s]	Velocity Exponent $\beta_c$ [-]
wave	35	7	4.00	-	-
current	35	-	-	2.00	0.11
wave & current	35	7	4.00	2.00	0.11

### 3.3.2 Test Case Results

The NWCT is utilized to simulate pure current, pure wave, and combined wave-current loading using the setup of [Section 3.3.1](#).

[Fig. 3.2](#) shows the calculated maximum horizontal loads attained for each individual structure. Generally, a smooth redirection of the flow field and a small dead water zone behind the shape are considered to have a favorable impact on the drag forces on a structure, when considering pure current load cases. It is therefore of no surprise that the highest loads for the pure current scenario are attained for the rectangular shape, while the loading is significantly smaller for the triangular and elliptical geometries.

In contrast to the pure current load states, the inertia driven maximum wave loads on the individual structures are less intuitive. While the rectangular shape for this particular load case also results in the largest forces, the smallest wave loads are actually attained for the triangular shape. The results suggest that the maximum horizontal wave loads are mainly driven by the surface orientation and the distribution of the horizontal cross-sectional length (or area in a three-dimensional-case) over the height of the structure. A reduction of the object area (or volume in a three-dimensional case) in the upper regions of the water column seems to result in a decrease in the overall inertia forces. This is plausible considering that the wave induced forces exhibit larger accelerations at the top of the water column compared to the lower regions.

Independent of the shape of the structure, the combined wave-current simulation results in a significant increase of the overall forces compared to a linear superposition of the pure wave and pure current load case. The effect is clearly observed in [Fig. 3.3](#), which shows the linear superposition of the individual wave and current results normalized with respect to the corresponding wave-current solution. As can be seen, the wave-current simulation results in an increase of the maximum horizontal forces ranging from 25% to 28%. This clearly supports the hypothesis of [Section 3.2](#), which suggests that the change in fluid particle kinematics due to wave-current interaction should lead to a considerable increase in the hydrodynamic forces on a structure situated on the sea floor. A comparison of the velocity contour plots resulting from the combined wave-current scenarios is given in [Fig. 3.4](#).

In addition to the consideration of resultant horizontal forces, a

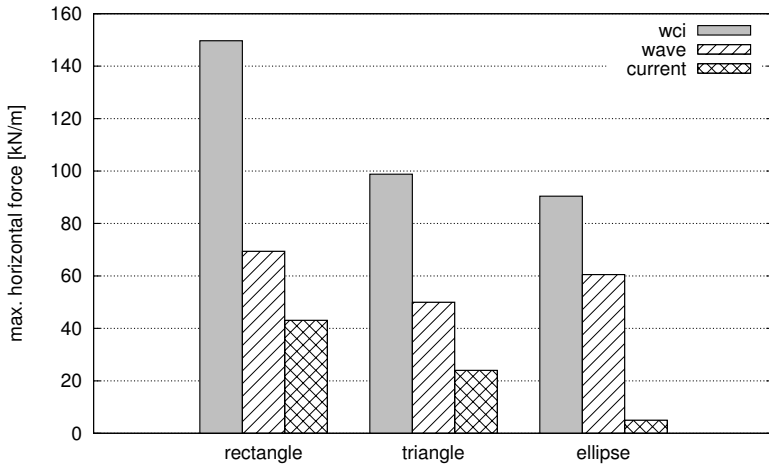


Figure 3.2: Maximum horizontal loads on each two-dimensional structure resulting from the three load cases.

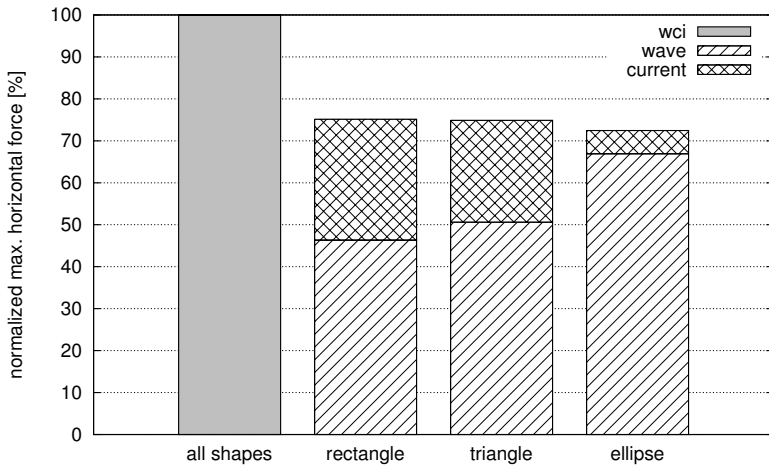
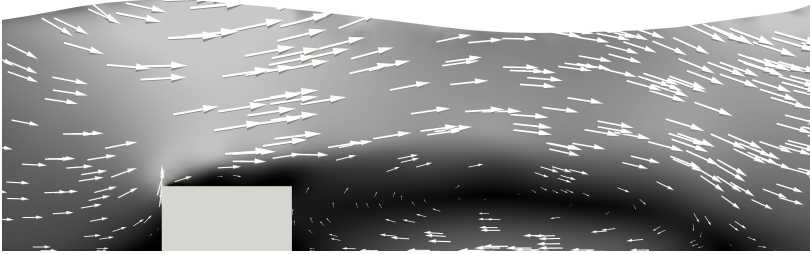
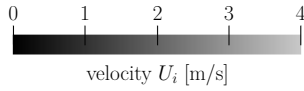
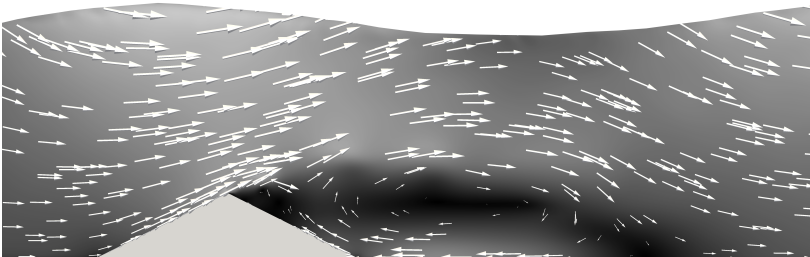


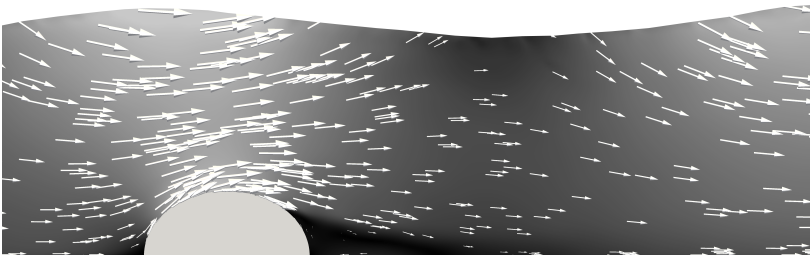
Figure 3.3: Linear superposition of the pure wave and pure current loads normalized with the corresponding combined wave-current results.



(a) Rectangular shape



(b) Triangular shape



(c) Elliptical shape

Figure 3.4: Comparison of velocity contours and velocity vector distributions for the wave-current simulations.



detailed load distribution of the forces over the height of each structure at the time of maximum loading is given in Fig. 3.5. The distributions are attained by piecewise summing up the pressure and the viscous stress over height-increments of each structure. The load curves show a significant difference between a linear superposition of the wave and current forces (solid grey lines) and the WCI solution (solid black lines). For the rectangular structure, the WCI scenario results in an increase in loading over the entire height of the structure. This increase is also encountered throughout large parts of the triangular and elliptical structures. An interesting observation is made for the top 20% of the elliptical structure load curve. As can be seen, the curve of the linearly superimposed results coincides approximately with the WCI curve in this region. The point at which both curves begin to deviate is approximately at the height of the flow separation point for the WCI and pure current scenario. Therefore, in the case of the analyzed elliptical structure, the difference of WCI loads compared to a linear superposition appears to be significantly smaller in the attached flow region of the structure.

The load history over one period at  $1/3$  and  $2/3$  of the structure height is given for each structure in Fig. 3.6. The previously analyzed peak loads correspond to the time of maximum loading at  $3/4$  of the period. An absolute increase in loading of the WCI scenario (black curves) compared to a linear superposition (grey curves) occurs at both the peak and trough of each load curve. For the analyzed scenarios the orientation of the current is constant in time and in the direction of wave propagation. As a consequence, larger absolute peak values are attained for the WCI and combined wave-current results, because at the time of trough loading the wave results in forces that are directed in the opposite direction as those resulting from the current. The only exceptions are the load curves corresponding to  $2/3$  of the height of the elliptical structure (dashed lines in Fig. 3.6c). At this height, the current results in a negative load component for the elliptical structure. As a consequence, larger absolute trough values are attained in the load history. It should however be noted that this region of the structure has a relatively small contribution to the overall loads so that for the whole structure, the peak load is once again more critical in terms of absolute horizontal loading.

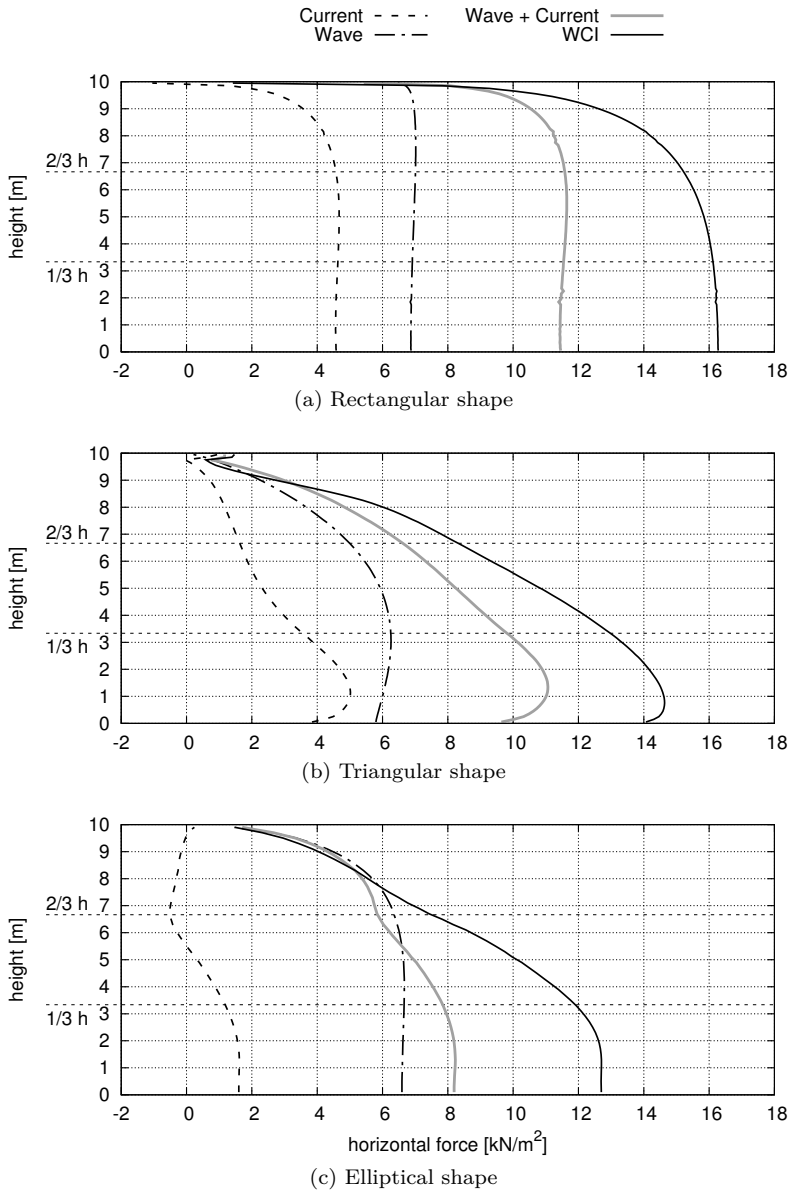


Figure 3.5: Load distribution at the time of max. horizontal loading over the height  $h$  of each structure.

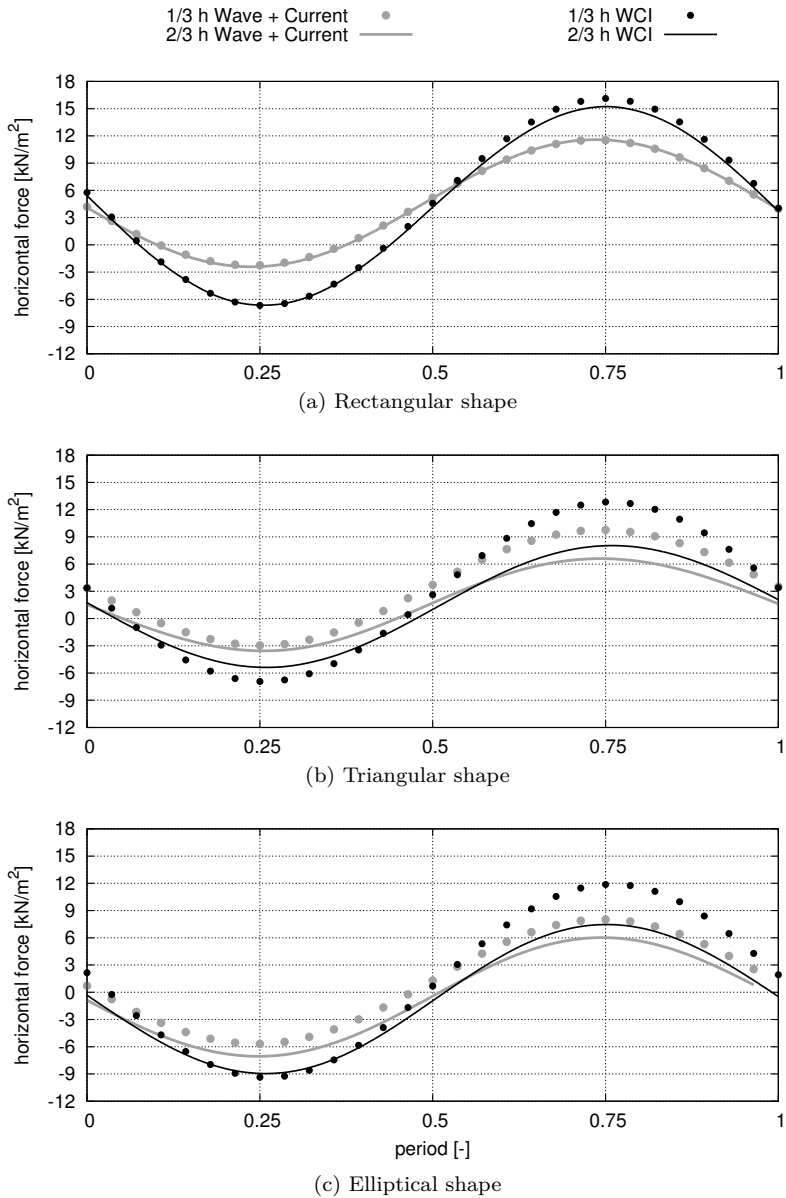


Figure 3.6: Pointwise load history at  $1/3 h$  and  $2/3 h$  over one period of loading.

## 3.4 Load Analysis of Prototype SeaTurtle

Building on the findings of the load analysis of two-dimensional basic foundation shapes, the NWCT is applied as part of the structural analysis for a prototype tidal turbine built near Jindo Island, South Korea. An analysis of the support structure is carried out by investigating the extreme load condition, which is defined as the combination of a maximum wave and current field traveling in the same direction. Particular focus is put on investigating the combined wave-current scenarios in comparison to a separate simulation of the wave and current fields.

### 3.4.1 Project Description

The SeaTurtle project describes a tidal park to be constructed near the South Jeolla Province of South Korea in the Yellow Sea. In a first step, a prototype structure was commissioned by the project owner RENETEC, consisting of a 110 kW tidal turbine developed by VOITH Hydro. The support structure was designed by Ed. Züblin AG and analyzed as part of this thesis. A numerical investigation of the support structure was carried out by applying the NWCT in order to gain insight into the structural loads under combined wave-current impact. The results are presented in this section. A GBF was selected for the project, taking into account the rocky substrate of the offshore site. Under these conditions, ramming methods were declared unsuitable and the more elaborate drilling procedures were feared to cause stabilization problems of the offshore vessel at high current velocities, as discussed by [Markus et al. \(2011\)](#).

The foundation was designed in a ramp-like shape, allowing for a redirection of the current flow field while reducing wave induced inertia loads in the upper regions of the foundation. [Fig. 3.7](#) shows the GBF and the tidal turbine designed as part of the SeaTurtle project. The dimensions of the support structure are given in [Fig. 3.8](#).

Site specific offshore data was acquired using an Acoustic Doppler Current Profiler (ADCP). Based on this data, velocity distributions, turbulence levels, and the boundary layer shape were determined, as described in detail by [Daus et al. \(2011\)](#). A maximum wave scenario was derived from 50-year wave conditions and a maximum current scenario was provided in order to define the critical load conditions. Based on the data, three load cases are defined, as shown in [Tab. 3.3](#).



Figure 3.7: Prototype support structure and 110kW tidal turbine [RENETEC, Voith Hydro].

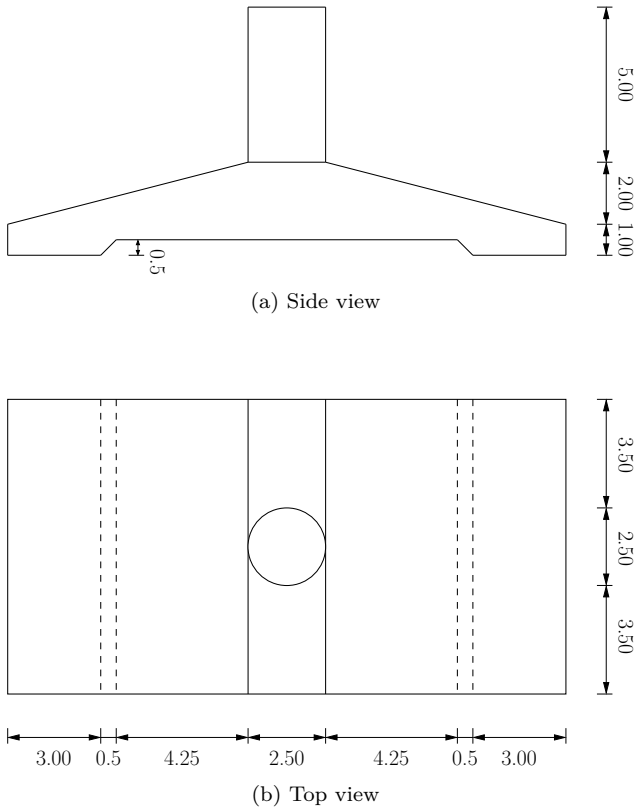


Figure 3.8: SeaTurtle support structure. All dimensions are in meters.

Table 3.3: Load case parameters project SeaTurtle

Load Case	Water Depth $d$ [m]	Wave Period $T$ [s]	Wave Height $H$ [m]	Surface Velocity $U_s$ [m/s]	Velocity Exponent $\beta_c$ [-]
wave	35	7	6.80	-	-
current	35	-	-	3.80	0.11
wave & current	35	7	6.80	3.80	0.11

Furthermore, the collected data provided insight into the stream directions encountered at the offshore site. It was determined that a maximum deviation of  $55^\circ$  from the main flow direction should be taken into account. Two scenarios are therefore considered: zero degree flow conditions for which the flow fields are aligned with the lengthwise axis of the structure and a  $55^\circ$  misalignment of the flow direction from the structure axis.

### 3.4.2 Discretization

Taking advantage of the flexibilities of the FV method regarding the type of polyhedral elements used in the computational domain, a hybrid mesh model is used for the SeaTurtle simulations, consisting of a structured outer domain and an unstructured inner domain. In the outer region, the structured hexahedral mesh consists of a Cartesian grid with refinement in the near surface region and mesh coarsening at the domain outlet. Arbitrary structures can efficiently be included in the unstructured inner domain using a hex core, tetrahedral mesh with prism layers at the wall boundaries. The two domains are connected using pyramidal elements. A schematic overview of the hybrid mesh model is given in Fig. 3.9.

Fig. 3.10 shows part of the mesh that incorporates the three-dimensional SeaTurtle foundation. Prism layers are used to refine the structure boundaries in order to ensure  $y^+$  values in the range  $30 < y^+ < 300$ . The overall domain size is 470 m x 140 m x 50 m and includes approximately 5 million cells. A mesh study was carried out in order to verify the hybrid mesh model. For this purpose, a high quality block structured mesh consisting of over 10 million cells was generated for both the  $0^\circ$  and  $55^\circ$  structure orientation. Pure

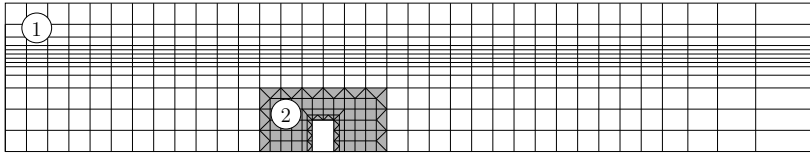


Figure 3.9: Hybrid mesh model. Region 1: Structured hexahedral mesh. Region 2: Unstructured, hex core, tetrahedral mesh.

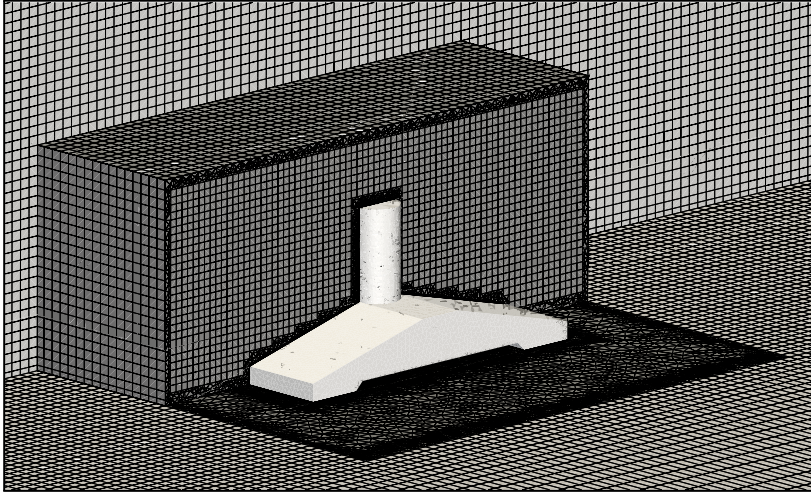


Figure 3.10: Hybrid mesh consisting of a cartesian block structured outer domain and unstructured inner domain.

current simulations carried out for the  $0^\circ$  angle of attack resulted in drag force deviations of 2.5% between the structured and hybrid mesh. For the  $55^\circ$  flow direction, a deviation of 3.5% was determined. These deviations are considered acceptable for practical engineering applications. It should also be noted that the structured mesh used for the pure current simulation consisted of a coarse mesh in the outer regions of the domain. For a wave analysis, these regions would have to be refined in order to accurately capture the wave kinematics, resulting in a further increase in the number of cells and computation cost. This is particularly problematic considering that a dynamic wave analysis requires a computation of multiple wave periods. Therefore, even highly parallelized simulations would result in unreasonable computational costs when utilizing the structured mesh. In comparison, the hybrid mesh model is deemed to be highly efficient, taking into consideration comparatively low mesh generation and computation times as well as satisfactory results attained in the mesh study.



### 3.4.3 Load Investigation

The NWCT is applied to a three-dimensional, dynamic analysis of the SeaTurtle support structure. CFD velocity contour results are shown for the combined wave-current scenario in Fig. 3.11. All results presented in this section are related to the ramp shaped support structure. Although the ramped foundation and concrete cylinder were simulated together, the loading of the cylinder was analyzed separately, and is not addressed in this thesis. Resulting peak loads for the previously introduced load cases are summarized in Fig. 3.12 for both flow field directions. As expected, drag loads resulting from the pure current scenario increase significantly when the flow field deviates from the zero degree flow direction, due to the large dead water zone developing behind the structure. Interestingly, the inertia loads resulting from the pure wave scenario are of similar magnitude for both flow directions. This further supports the hypothesis that the peak wave loads of structures located on the sea floor are sensitive to the volume distribution in the vertical direction (which is identical for both flow directions), while a change in the projected area seems to have a minor influence on the maximum inertia loads.

A rotation of the flow field by  $55^\circ$  also results in a reaction force component perpendicular to the flow direction for the pure current simulation. The magnitude of this force is approximately 17% of the total horizontal load. In contrast, the pure wave load scenario results in horizontal loads perpendicular to the flow field equal to only 2% of the total horizontal load, when the flow direction is altered. This leads to the conclusion that both direction and magnitude of the maximum wave induced horizontal loads do not seem to be influenced significantly by a deviation of the flow field.

Fig. 3.13 compares the peak load attained in the combined wave-current simulation with a linear superposition of the pure wave and pure current loads. As can be seen, the combined computation results in significantly higher loads for both flow directions. The peak load increase is of a similar magnitude as the results presented as part of the two-dimensional study in Section 3.3.2. Overall, the results raise awareness of the error that may result from a simplified approach of investigating extreme load cases on tidal turbines, by superimposing separately computed wave and current loads. In the analyzed SeaTurtle project, such a procedure would have resulted in an underestimation of the extreme loads by over 30%.

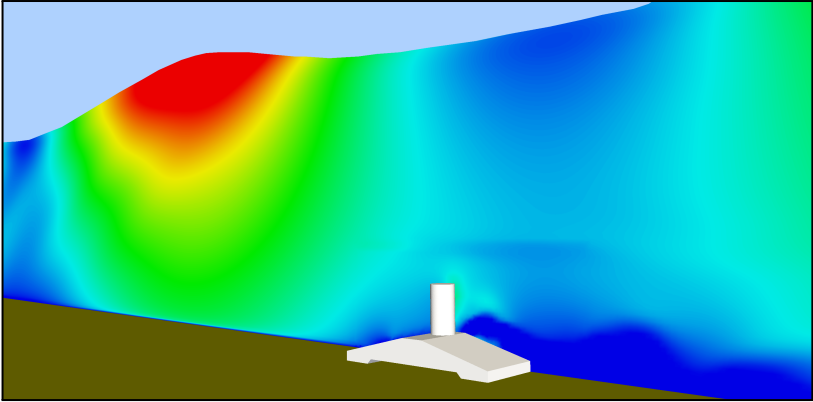
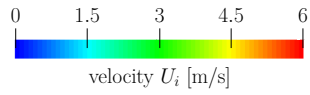
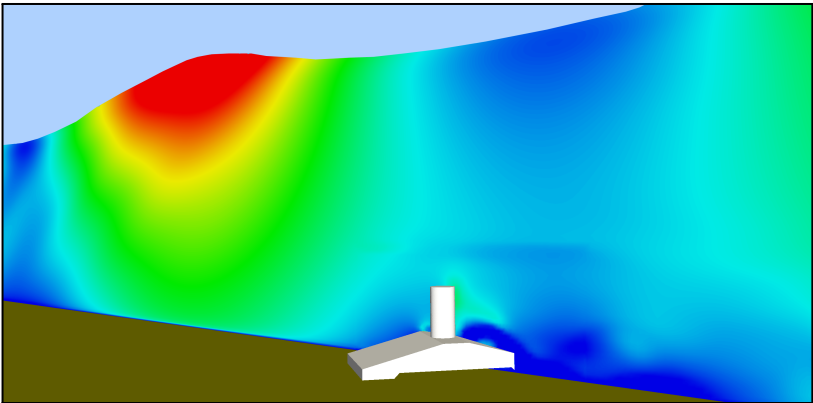
(a)  $0^\circ$  flow field direction(b)  $55^\circ$  flow field direction

Figure 3.11: SeaTurtle simulation velocity contour plots.

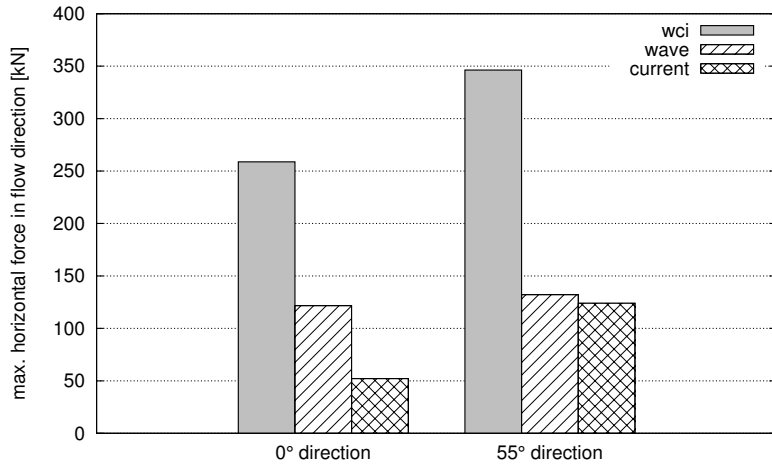


Figure 3.12: SeaTurtle maximum horizontal loads for both flow directions resulting from the three load cases.

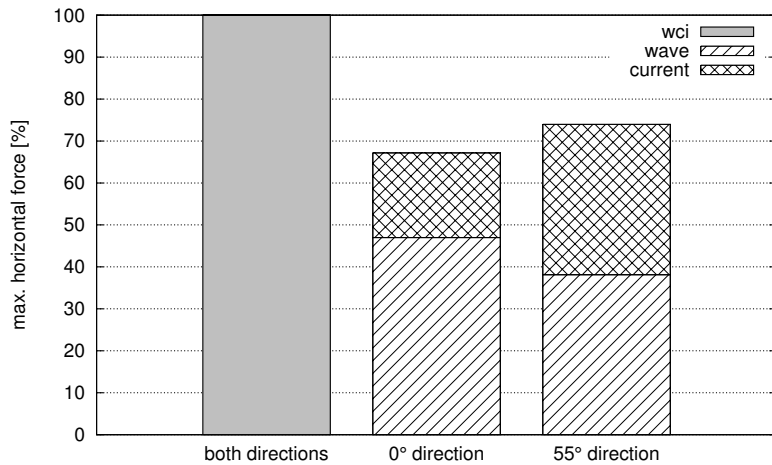


Figure 3.13: SeaTurtle linear superposition of the pure wave and pure current load case normalized with respect to the according combined wave-current result.

### 3.4.4 Shape Investigation

In addition to the peak load investigation of the structure, the hydrodynamic properties of the foundation shape are analyzed. In order to gain insight into the influence of the structural shape on the load contributions, dimensionless shape parameters are computed for the individual load cases. The dimensions of the analyzed structure are much smaller than the wave length of the considered load cases. Under such conditions, a widely used approach to estimate drag and inertia loads is the utilization of the semi-empirical Morison equation (Morison et al., 1950):

$$F_1(t) = 0.5 \rho C_d A_p U_1(t) |U_1(t)| + \rho C_m V \frac{\partial U_1}{\partial t} \quad (3.4)$$

where  $A_p$  represents the projected cross-sectional area of the body with horizontal surface normal parallel to the flow direction and  $V$  is the water volume displaced by the body.  $C_d$  and  $C_m$  are the drag and inertia coefficients, respectively. The force and velocity values at discrete time intervals are obtained from the flow simulations. For stability reasons, explicit and partially explicit time marching schemes are typically applied with time steps below one millisecond, particularly when using a fine mesh resolution and high velocity magnitudes. As a consequence, a reasonably accurate solution of the velocity time derivative can be computed from the discrete CFD velocity results. Using the force and velocity data as well as the geometric constants  $A_p$  and  $V$ , a least square approximation is carried out over one wave period in order to compute the dimensionless shape parameters  $C_d$  and  $C_m$ . The approach has been widely used in experimental studies and was found to provide reliable shape parameters (Venugopal et al., 2009).

Tab. 3.4 lists the computed foundation shape parameters. It should be noted that the  $C_d$  value for the pure wave scenario is disregarded because the drag contribution for this particular scenario is negligible. Analyzing the columns of the table, it can be seen that the shape parameters for all scenarios decrease when the wave and the current are simulated together, compared to the individual load cases. For rectangular cylinders this phenomenon was also observed by Vengatesan et al. (1999), who experimentally investigated combined wave-current loads for two different cylinder aspect ratios. The increase in the loading on the structures is thus a phenomenon predominantly caused

Table 3.4: Foundation shape parameters

Load Case	$C_d$		$C_m$	
	0°	55°	0°	55°
wave	-	-	1.23	1.32
current	0.50	0.74	-	-
wave & current	0.42	0.65	1.05	1.12

by the change in the physical flow field, while the results suggest that the altered load case has a favorable impact on the shape parameters.

A comparison of the CFD force development with forces calculated using the Morison equation is shown in Fig. 3.14. The Morison results are based on the shape parameters and particle kinematics computed with the NWCT. An overall good agreement is attained for the wave and WCI load cases subjected to both the 0° and 55° load direction.

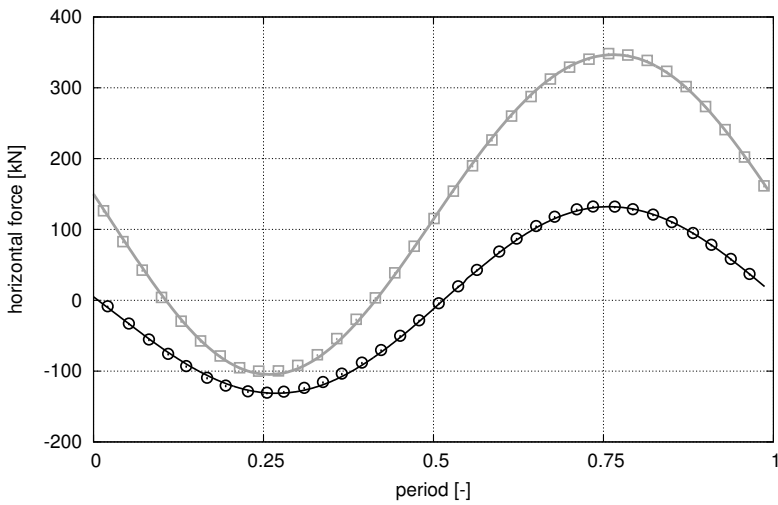
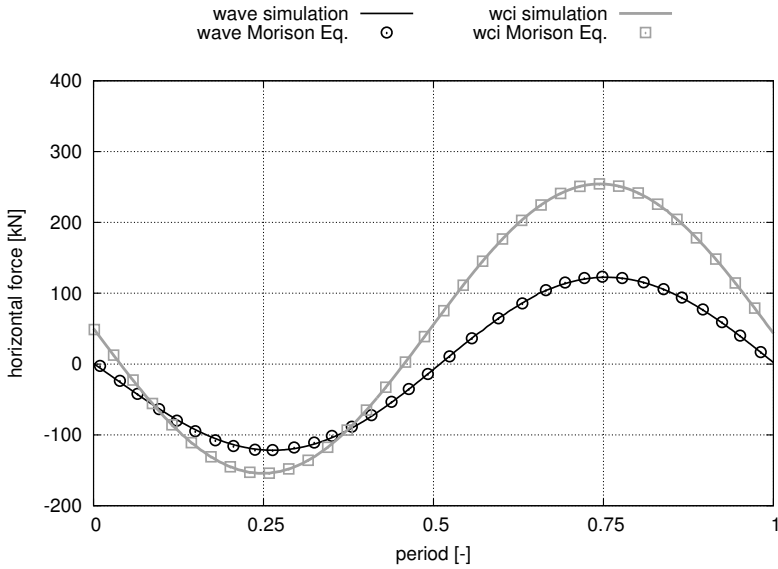


Figure 3.14: Comparison of CFD results with forces calculated with the Morison equation using the  $C_d$  and  $C_m$  values given in Tab. 3.4.

## 3.5 Conclusions and Summary

The aim of this chapter was to analyze extreme load scenarios subjected to tidal turbine foundations. Of particular interest was the investigation of how a combined consideration of waves and currents affects the overall loading on the structures, compared to a linear superposition of the individual load cases.

The NWCT was used to compare the fluid kinematics of the combined wave-current problem with a linear superposition of the individual load cases. When applied to realistic offshore conditions encountered at sites suitable for tidal turbines, the wave-current simulation resulted in a significant increase in local particle accelerations in the lower regions of the water column (approximately 30%). Following, a structural load analysis was carried out in order to determine how the forces on a structure are influenced by the altered flow field. In a first step, a two-dimensional study of three basic shapes was presented. The results of the combined simulation showed a significant load increase compared to a linear superposition of wave and current loads, ranging from 25% to 28%.

Finally, the NWCT was applied as part of the project SeaTurtle, which involved the design of a prototype GBF for a tidal turbine. A pure wave, a pure current and a combined wave-current load case were analyzed for two different flow directions. Once again, significantly higher wave-current loads were attained than those computed as a linear superposition of the pure wave and pure current load case. An investigation of the structure shape parameters showed a decrease of the calculated  $C_d$  and  $C_m$  values when the wave and the current were simulated together. This suggests that the load increase is a phenomenon that is largely a result of the altered physical flow field. Furthermore, the simulations indicate that the inertia loads of structures located on the sea floor are mainly influenced by the volume distribution of the structure in the vertical direction, rather than the projected area encountered by the flow.

Overall, the presented study demonstrated the capabilities of the NWCT to simulate wave-current load scenarios. It allowed for a detailed investigation of the offshore conditions encountered by tidal turbines. The major conclusion drawn from the study is that a physically accurate simulation of combined wave-current conditions results in drastically higher structural forces than a linear superposition of pure wave and pure current scenarios.





---

## Chapter 4

# Reduced Modeling

---

### 4.1 Introduction and Overview

The simulations carried out in [Chapter 3](#) demonstrated the capabilities of the numerical methods implemented into the NWCT. A wide range of valuable information can be drawn from the results and directly applied in the design of offshore structures. Taking advantage of modern computational resources, the presented simulations were carried out within a reasonable amount of time. However, the computational times may become quite restrictive in parameter studies and optimization procedures that require multiple CFD simulations of various structure variations.

For such design tasks, simplified methods can be applied that are computationally more efficient. For instance, [Batten et al. \(2006\)](#) investigated the hydrodynamics of tidal turbines using Blade Element Momentum (BEM) theory and a linear vorticity stream function panel method. Furthermore, [Whelan et al. \(2009\)](#) introduced a correction for a blade element code, taking into account the free surface and blockage when modeling tidal turbines. [Bai et al. \(2013\)](#) coupled the blade element method with a three-dimensional Navier-Stokes code in order to analyze the relationship between power extraction and the turbine array layout. In addition to the pure current scenarios investigated

in the aforementioned studies, [Whelan et al. \(2007\)](#) analyzed the interaction of a linear, regular wave train with the rotor array using BEM theory. [Batten et al. \(2006\)](#) considered combined wave-current loads on tidal turbine blades, applying the quasi-static BEM theory in combination with an added mass force modeling. In this work, the fluid velocities of the wave were derived from linear wave theory and added to a uniform stream velocity.

Hydrodynamic optimization problems involving waves have been approached by [Birk \(2009\)](#) making use of linear potential theory, thereby drastically reducing the computational costs in comparison to Navier-Stokes codes. [Kandasamy et al. \(2011\)](#) introduced a multifidelity optimization strategy, performing several potential flow computations of a catamaran hull followed by an evaluation of the optimized shape using a URANS model. However, potential flow codes can only be applied reliably if the viscous effects do not have a significant influence on the results. This is not generally the case for applications involving combined wave-current flows.

There is a large discrepancy between elaborate free surface CFD methods as implemented into the NWCT, and less extensive approaches such as the BEM model or the potential theory approach. VOF based CFD methods provide in-depth flow field information at the cost of high computational times. Conversely, the simplified approaches are computationally efficient, but exclude viscous effects, thereby rendering limited and sometimes insufficient information of the flow field. In order to close the gap between these approaches, a novel reduced modeling strategy in the form of a Virtual Free Surface (VFS) model is introduced in this chapter, which is designed to capture the general flow characteristics of the NWCT at significantly lower computational costs. The VFS method is based on a Navier-Stokes approach including viscosity and turbulence, but excluding elaborate free surface considerations. The method has been developed to allow for efficient optimization studies that focus on an analysis of fully submerged structures and flow field studies of regions that are not in contact with the free surface. As examples, offshore tidal turbine development, pipeline analysis, and scour protection studies can be named.

In this chapter, the VFS model is outlined in detail, including a theoretical overview, an assessment of the methodology, and a model correction method for pressure field sensitive applications. A wave-current interaction model is introduced, which allows for a

modeling of non-uniform currents in combination with waves. The models are verified as part of an elaborate design study of a GBF for tidal turbines. Overall, the aim is to establish a novel methodology for efficient wave-current CFD simulations of fully submerged structures, which can be applied to a variety of applications ranging from blade evaluations to structural force analysis.

Part of the work presented in this chapter has been published in Coastal Engineering (Markus et al., 2014a) and in the Proceedings of the thirty-second International Conference on Ocean, Offshore and Arctic Engineering (Markus et al., 2013a). It is presented here with explicit written consent from the publishers.

## 4.2 Virtual Free Surface (VFS) Model

### 4.2.1 Model Description

The basic idea of the VFS model is to reduce the multiphase VOF model included in the NWCT to a single phase URANS model, while maintaining the offshore flow characteristics. This is achieved by replacing the physical free surface with a virtual free surface boundary condition. To do so, the NWCT domain given in Fig. 2.1 on page 17 is reduced to incorporate only the water region, by limiting the vertical dimension of the computational domain to the virtual free surface height  $h_{vfs}$ , specified at a  $z$ -coordinate that is below the wave trough height throughout the simulation. In the process, the top boundary is replaced by a VFS boundary (Fig. 4.1). All other boundaries, including the sides of the domain, are treated as described in Section 2.6, apart from the phase field  $\alpha$ , which is eliminated from the model.

The characteristics of the current and wave are retained in the reduced model by introducing a Dirichlet velocity field at the VFS boundary corresponding to the current and wave solutions of Eqs. 2.14 and 2.15 at  $z = -h_{vfs}$ . Contrary to the inlet boundary condition, the  $x$ -coordinate in the wave formulation of Eqs. 2.12 and 2.15 is not constant at the VFS, but corresponds to the  $x$ -coordinates of the VFS boundary cell nodes. Overall, the VFS velocity boundary field  $U_i^{vfs}$  is defined in the following form:

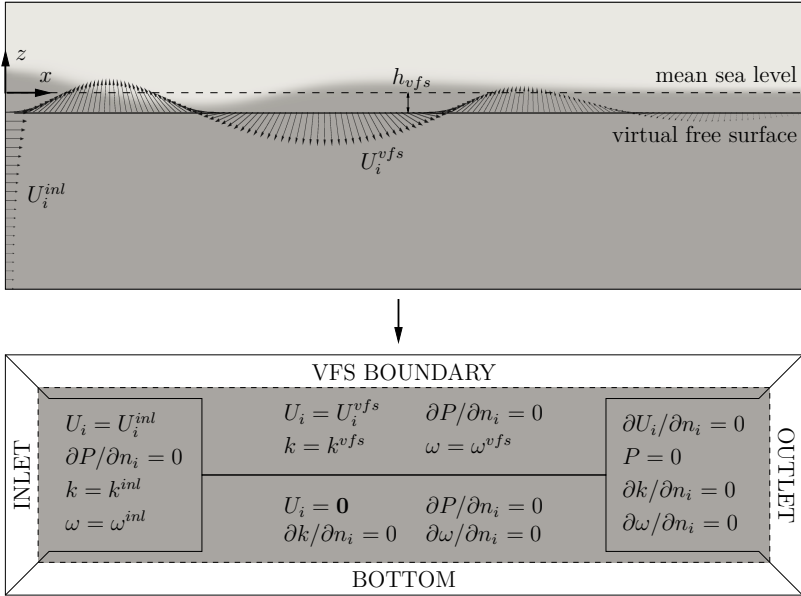


Figure 4.1: VFS model. Top: The background contour shows the physical phase distribution eliminated by the VFS modeling approach. Arrows correspond to specified velocity boundary fields at the inlet (superscript  $inl$ ) and VFS (superscript  $vfs$ ). Bottom: VFS boundary conditions. The SIDE boundary conditions are problem dependent and documented in [Section 2.6.6](#).

$$U_i^{vfs} = \begin{cases} U_i^w(z = -h_{vfs}) & \text{for pure wave scenarios} \\ U_i^c(z = -h_{vfs}) & \text{for pure current scenarios} \\ U_i^{wci}(z = -h_{vfs}) & \text{for combined wave-current scenarios} \end{cases} \quad (4.1)$$

For a wave traveling on a uniform current, the combined wave-current boundary field  $U_i^{wci}$  can be determined directly from the Fenton wave model. Incorporating a non-uniform current into the VFS wave simulation under consideration of WCI requires a number of further modeling steps, as described in [Section 4.4](#).

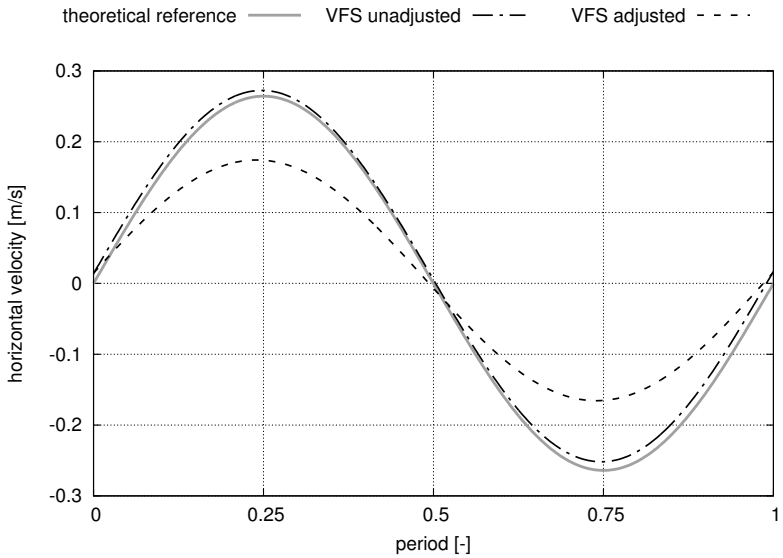
Analogue to the inlet treatment described in [Section 2.6.2](#), the boundary condition for  $P$  at the VFS is defined in the form of a Neumann condition, while boundary conditions for  $k$  and  $\omega$  are specified using Dirichlet boundary conditions ([Fig. 4.1](#)).

A final simplification is carried out as part of the VFS-NWCT, by eliminating the gravitational source term  $g_i$  in [Eq. 2.2](#) on [page 10](#). In the VOF-CFD computation, this term dictates the hydrostatic component of the pressure solution. For wave and wave-current simulations, this component fluctuates together with the modeled free surface. Because the free surface fluctuations are eliminated in the VFS model, the hydrostatic pressure field throughout the VFS model domain is constant in time and known a priori. The gravitational source term is therefore not included in the model equations and the hydrostatic pressure component is simply added to the total pressure solution in a post-processing step.

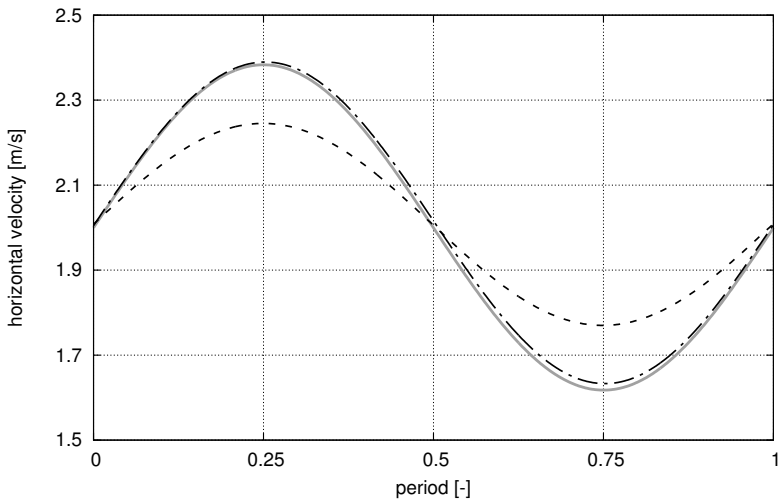
### 4.2.2 Model Assessment

The behavior of the VFS model is analyzed in this section. A test wave scenario is defined consisting of a wave with  $H = 4$  m,  $T = 7$  s, and  $d = 45$  m. In addition, a wave-current scenario is analyzed, for which the specified wave is combined with a uniform current ( $U_s = 2$  m/s and  $\beta_c = 0$ ). For both scenarios, the boundary field  $U_i$  at the inlet and VFS boundary is defined using the Fenton nonlinear wave model. A two-dimensional wave is assumed with a constant zero velocity perpendicular to the wave field.

The accuracy of the velocity solution computed with the VFS model at mid-height of the domain approximately one wave length from the inlet is analyzed in [Fig. 4.2](#). For both the pure wave and wave-current scenario the initial VFS model solution (labeled VFS unadjusted), match well with the theoretical reference solution determined using non-linear wave theory. The accurate velocity distribution computed with the VFS model is a result of the zero gradient pressure boundary condition at the VFS boundary that is consistent with the specified Dirichlet velocity boundary condition. However, the pressure boundary condition does not reflect the fluctuating pressure gradient of the wave field. As a result of this modeling choice, the initial VFS model pressure solution (labeled VFS unadjusted) deviates from the theoretical pressure solution, as shown in [Fig. 4.3](#).

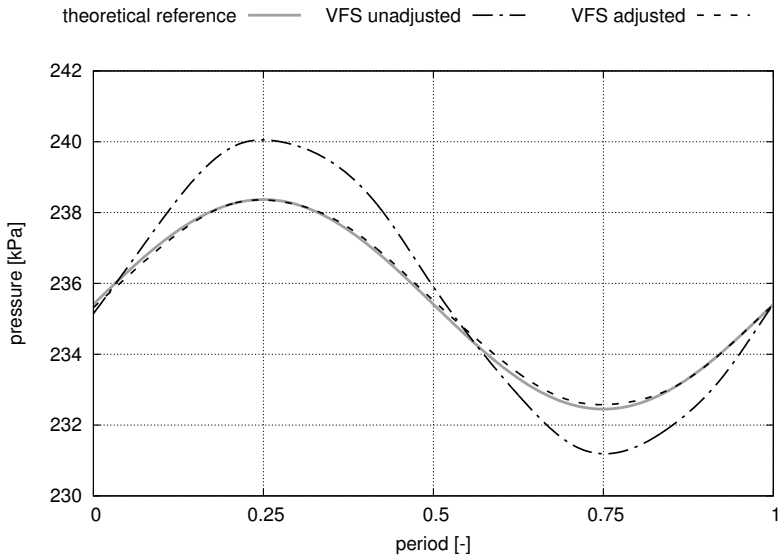


(a) Pure wave

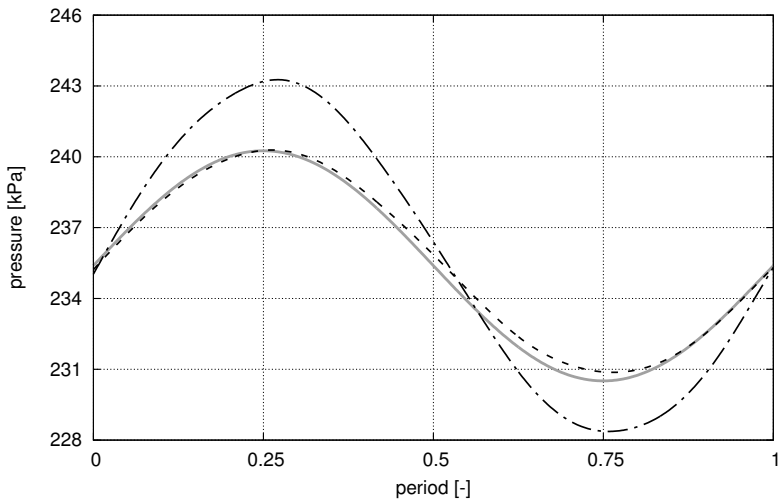


(b) Combined wave-current

Figure 4.2: VFS model velocity results at mid-height of the domain approx. 1 wave length from the inlet vs. theoretical reference solutions.



(a) Pure wave



(b) Combined wave-current

Figure 4.3: VFS model pressure results at mid-height of the domain approx. 1 wave length from the inlet vs. theoretical reference solutions.

For certain applications the computation of a realistic velocity distribution is sufficient. One example is the thrust estimation of a tidal turbine using an actuator disk, an application that was, for example, further investigated by Arnold in [Markus et al. \(2014a\)](#). In such cases, the VFS may be applied without further adjustment steps. However, when structural forces are of interest, the computation of an accurate pressure solution is crucial. [Idelsohn et al. \(1999\)](#) described an approach that prescribed an analytical solution of a wave pressure field as a Dirichlet boundary condition on a reference free surface. This procedure was further discussed and successfully applied to ship hydrodynamics by [García and Oñate \(2003\)](#). However, the approach requires a pressure solution, which is not always available. This is particularly true in the case of waves in combination with a non-uniform current, a scenario typically defined in terms of the velocities. In order to maintain a Dirichlet velocity boundary field at  $U_i^{inl}$  and  $U_i^{vfs}$ , a pressure field correction method to the VFS model is introduced in the following section.

## 4.3 Correction Method

### 4.3.1 Basic Concept

The correction method focuses on adjusting the VFS model for applications for which the pressure solution dictates the accuracy of the computation. In particular, this concerns structural load calculations with a significant inertia force contribution. This force component results from wave loading in ocean engineering applications. The peak forces during extreme wave loading occur approximately at the instance at which the wave accelerations are maximum and the wave velocities are approximately equal to zero in the vicinity of the structure. At this instance, the contribution of the wave induced wall shear stresses  $\tau_{wall}$  computed from the velocity field  $U_{wall}$  in [Eq. 3.1](#) on [page 41](#), are negligible. The correction model takes advantage of this characteristic.

The fundamental idea is to adjust the velocity boundary field at the inlet and VFS boundary so that a correct pressure solution is attained. This is possible because velocity and pressure are coupled in CFD simulations. The adjustment of the velocity field is carried out using a multiplicative correction factor  $\lambda$  that is applied to the entire velocity boundary field. The overall influence of multiplying the



field by a factor is minor in boundary regions consisting of low or zero velocities. This implies that the alteration is of minor consequence regarding the ensuing viscous forces at time instances resulting in peak forces, because here the wave velocities are at a minimum. Therefore, if the modeled VFS pressure field is corrected, reasonably accurate peak loads on the structure are attained, despite the alterations of the wave velocities. The derivation of  $\lambda$  is formulated in the following section.

### 4.3.2 Mathematical Formulation

In order to adjust the velocity field such that the desired pressure solution is attained, the relationship between velocity and pressure is required. An analytical solution for this relationship under consideration of all intricacies of the flow is not available, but an approximation can be derived from the momentum equation (Eq. 2.2). Considering that the wave problem of interest is dominated by inertial effects, it is assumed that the rate of change in the momentum equation is dominant compared to the convective and the diffusive terms. Neglecting these terms results in the following approximation for the pressure-velocity relationship:

$$\frac{\partial U_i}{\partial t} = -\frac{1}{\rho} \frac{\partial P}{\partial x_i} \quad (4.2)$$

Multiplying both sides of Equation 4.2 by a scalar constant  $\lambda$  leads to the following relationship under the assumption that  $\lambda$  is constant in time and space:

$$\lambda \frac{\partial U_i}{\partial t} = -\frac{\lambda}{\rho} \frac{\partial P}{\partial x_i} \quad (4.3a)$$

$$\frac{\partial \lambda U_i}{\partial t} = -\frac{1}{\rho} \frac{\partial \lambda P}{\partial x_i} \quad (4.3b)$$

Eq. 4.3b implies that an adjusted pressure value

$$\tilde{P} = \lambda P \quad (4.4)$$

corresponds to an adjusted velocity vector

$$\tilde{U}_i = \lambda U_i \quad (4.5)$$

After rearranging Eq. 4.4 to make  $\lambda$  the subject of the formula and substituting into Eq. 4.5, the following formulation is attained:

$$\tilde{U}_i = \lambda U_i = \frac{\tilde{P}}{P} U_i \quad (4.6)$$

Eq. 4.6 indicates how the velocity vector  $U_i$  has to be altered using the correction factor  $\lambda$  in order to attain the adjusted velocity vector  $\tilde{U}_i$  that corresponds to the adjusted pressure value  $\tilde{P}$ .

### 4.3.3 Model Implementation

The formulation given in Eq. 4.6 is used in order to adjust the velocity boundary fields  $U_i^{inl}$  and  $U_i^{vfs}$  such that a corrected pressure solution is attained with the VFS model. This requires a solution for  $\tilde{P}$ , which is determined using a VOF based NWCT simulation during which the pressure field in the VOF domain is probed at the location  $z = -h_{vfs}$ . The correction factor  $\lambda$  is then derived by computing the ratio of the wave trough pressure values  $P_p^{vof}$  and  $P_p^{vfs}$  determined at  $z = -h_{vfs}$  with the VOF model and VFS model, respectively:

$$\lambda = \frac{P_p^{vof}}{P_p^{vfs}} \quad (4.7)$$

Because it is assumed that  $\lambda$  is constant in time and space, it may be used to adjust the entire velocity boundary field at the inlet and VFS boundary when analyzing pure wave scenarios. When a current is incorporated into the VFS model,  $\lambda$  is only applied to the wave boundary fields  $U_i^{inl,w}$  and  $U_i^{vfs,w}$ , because the current boundary fields  $U_i^{inl,c}$  and  $U_i^{vfs,c}$  satisfy the zero gradient condition and should therefore not be altered:

$$\tilde{U}_i^{inl} = U_i^{inl,c} + \lambda U_i^{inl,w} \quad (4.8a)$$

$$\tilde{U}_i^{vfs} = U_i^{vfs,c} + \lambda U_i^{vfs,w} \quad (4.8b)$$

Excluding the current velocities in the adjustment operation is further necessary because the current results in a drag force component on the structure that is heavily dependent on the true velocity field. A derivation of a combined wave-current VFS boundary field including an arbitrary current profile is described in Section 4.4.

Because Eq. 4.2 is only an estimation of the pressure-velocity relationship, the procedure is applied iteratively until the pressure solution is within the desired tolerance  $\delta$ , as outlined in Fig. 4.4. It

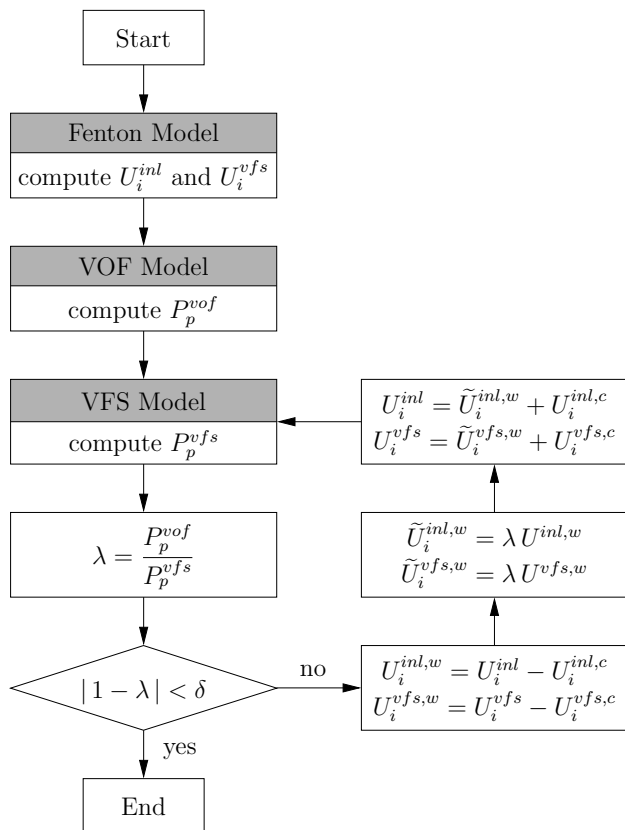


Figure 4.4: General schematic overview of the VFS pressure correction model. For pure wave simulations, the inlet and VFS current boundary fields  $U_i^{inl,c}$  and  $U_i^{vfs,c}$  are simply set equal to zero.

may seem contradictory that a VOF simulation is required as part of the correction method in order to determine the correct pressure values  $\tilde{P}$ . However, this VOF computation can be carried out in an empty channel, under the assumption that the VFS velocity field is not influenced by a structure modeled in the domain. Computationally, this is significantly more efficient than a VOF simulation of the problem involving a structure with wall refinement. Furthermore, the reference VOF simulation is generally carried out in a two-dimensional framework, while the correction parameter can afterwards be used for efficient three-dimensional VFS simulations of structures subjected to a wave constant in the  $y$ -direction. The advantages of the method in terms of computational costs are however felt most strongly in optimization problems, where a variety of structures are subjected to the same wave field. Here, results from a single VOF boundary adjustment simulation can be used to analyze a multitude of different shape variations.

#### 4.3.4 Model Assessment

The correction method is applied to generate an adjusted boundary field for the pure wave and combined wave-current scenarios analyzed in [Section 4.2.2](#). The development of the difference  $|1 - \lambda|$  computed during each boundary adjustment iteration is shown in [Fig. 4.5](#). A perfect match between the computed VFS and VOF trough pressure values is reached when  $\lambda = 1$  and the difference becomes zero. After the first iteration the difference is reduced to approximately 0.02 for both the wave and wave-current scenario. A second correction iteration reduces the difference further, to approximately 0.0003. Various test simulations were carried out for a great variety of different wave and wave-current scenarios. For all tested cases the difference reduced to below 0.001 within two correction iterations. The rapid decline of the deviation indicates that the estimation of the velocity-pressure relationship of [Eq. 4.2](#), used in the derivation of  $\lambda$ , is quite accurate. The resulting adjusted pressure field at the mid-height of the channel approximately one wave length from the inlet are given in [Fig. 4.3](#) (labeled VFS adjusted). A good agreement between the adjusted VFS pressure solution and the theoretical reference solution is attained for both the pure wave and combined wave-current solution. The corresponding adjusted velocity solution is shown in [Fig. 4.2](#).

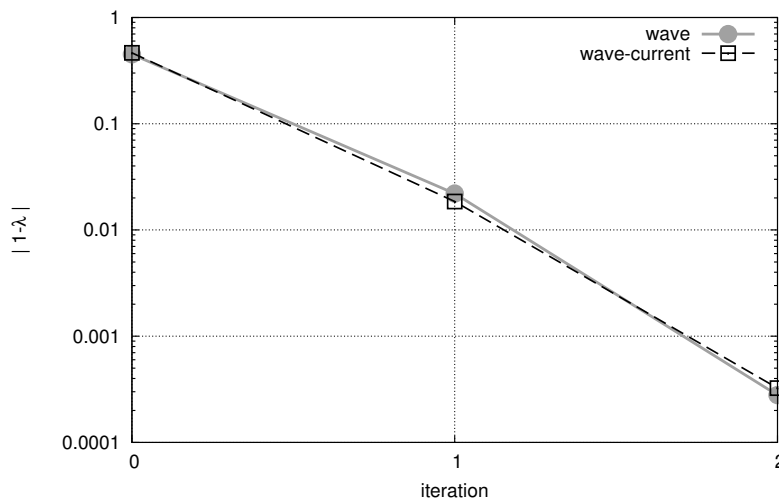


Figure 4.5: Correction factor development for the simulated pure wave and combined wave-current scenarios.

## 4.4 VFS Wave-Current Model

In [Section 4.2.2](#), an example of a combined wave-current simulation was given that considered a uniform current, constant over the water depth. Under these conditions, a solutions of the combined wave-current problem can be computed using standard irrotational wave theories such as the Fenton model. The problem is significantly more complex when considering a shear flow in combination with a wave. As described in [Section 2.5.3](#), it is possible to resolve the interaction between the wave and the current as part of a VOF simulation, after linearly superimposing the wave and current field at the inlet of the computational domain. However, in the VFS model the flow field can not develop freely, but is subject to the VFS boundary condition throughout the domain. A correct WCI solution is thus only attained in the VFS domain if the WCI solution is incorporated into the boundary condition. A derivation of the WCI boundary condition for waves propagating on an arbitrary non-uniform current is presented in this section.

### 4.4.1 Flow Kinematics

In a first step, it is assumed that the correct WCI solution can be expressed as the sum of the pure current solution and an altered wave solution, which accounts for the change in the wave kinematics due to the underlying current:

$$U_i^{wci} = U_i^c + \kappa_i(z) U_i^w \quad (4.9)$$

where  $\kappa_i$  denotes a correction vector as a function of  $z$ . For simplicity, the correction vector is assumed to be constant in time but varying over the height of the domain, taking into account the varying wave to current velocity ratio throughout the water depth. Rearrangement of Eq. 4.9 yields the following expression:

$$\kappa_i(z) = \frac{U_i^{wci} - U_i^c}{U_i^w} \quad (4.10)$$

Abiding to the wave field assumption of a constant zero velocity boundary field in the  $y$ -direction made throughout this thesis,  $\kappa_2$  is assumed to be zero. Due to the assumption of a correction vector  $\kappa_i$  constant in time, it is again sufficient to compute the correction vector using the peak velocity values  $U_{p,i}^w$ , and  $U_{p,i}^{wci}$ . However, because the degree of interaction varies over the water depth, the velocities are attained as a function of  $z$ , rather than at a single point coordinate:

$$\kappa_i(z) = \frac{U_{p,i}^{wci}(z) - U_i^c(z)}{U_{p,i}^w(z)} \quad (4.11)$$

The WCI velocity solution of Eq. 4.11 can once again be computed at discrete points over the height of the channel using a VOF based NWCT computation, while the corresponding pure wave and pure current solutions are derived directly from the Fenton model. Based on these values,  $\kappa_i$  can be computed for each discrete probe location. It may be desirable to define  $\kappa_i$  in the form of a continuous function, in order to attain a formulation that is independent of the point coordinates. For this purpose, a polynomial function vector  $p_{\kappa,i}$  is defined:

$$p_{\kappa,i}(\tilde{z}) = p_{\kappa,1}\tilde{z}^m + p_{\kappa,2}\tilde{z}^{m-1} + \dots + p_{\kappa,m}\tilde{z} + p_{\kappa,m+1} \quad (4.12a)$$

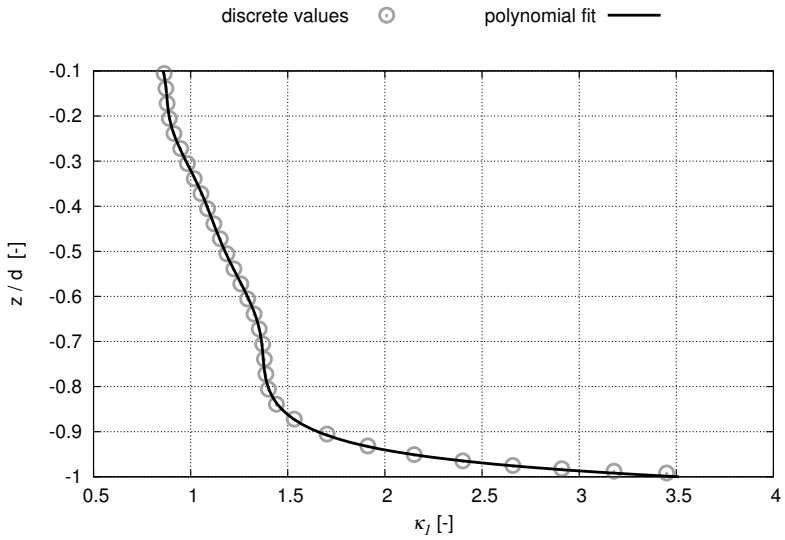
$$\tilde{z} = \frac{z}{d} \quad (4.12b)$$

To avoid bad conditioning of the polynomial, the coordinate  $\tilde{z}$  is used, which is normalized with the water depth to the range 0 to  $-1$ , corresponding to the mean sea level and sea floor, respectively. The coefficients  $p_{i,m}$  are found by fitting Eq. 4.12 to the  $N$  discrete  $\kappa_i$  values in a least squares sense, by minimizing the residual vector  $R_i$ :

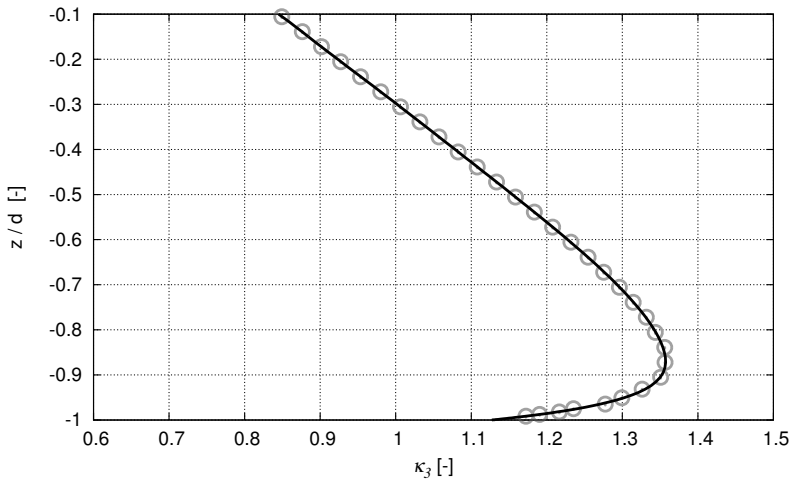
$$R_i^2 = \sum_{j=1}^N [\kappa_{i,j} - (p_{\kappa,1}\tilde{z}_j^m + p_{\kappa,2}\tilde{z}_j^{m-1} + \dots + p_{\kappa,m}\tilde{z}_j + p_{\kappa,m+1})]^2 \quad (4.13)$$

Numerical test simulations showed that a polynomial of degree  $m = 10$  gives a good fit to the data of interest, without any noteworthy oscillations of the resulting curve. The number of discrete  $\kappa_i$  values  $N$  is governed by the mesh resolution and corresponds to the number of cell nodes along the  $z$ -coordinate. The nodes in the immediate vicinity of the bottom wall are disregarded in the polynomial fit, due to the discrepancy of the zero value velocity bottom boundary condition in the CFD model and the slip boundary condition in the wave solution, which results in large deviations between the two models and oscillations of the polynomial function. The discrepancy between the slip bottom boundary condition in the wave model and the no slip condition in the CFD simulation is a modeling choice that is of minor consequence because the horizontal velocities computed in the near bottom region are very small. Therefore, numerical instabilities at the boundary typically do not ensue. Disregarding the near bottom values in the polynomial fit is also uncritical, because velocities in the near wall region are close to zero and thus the multiplicative correction in these regions is of minor consequence.

The methodology is applied to a wave-current field with  $H = 4$  m,  $T = 7$  s,  $d = 45$  m,  $U_s = 2$  m/s and  $\beta_c = 0.11$ . The discrete  $\kappa_i$  values computed using the VOF based WCI solution and the Fenton wave solution are given in Fig. 4.6, together with the corresponding polynomial fit. In addition, Fig. 4.7 shows the peak velocities over the water column before and after  $\kappa_i$  is applied, in comparison with the reference VOF-WCI solution. A good agreement of the velocity distribution is observed when utilizing the wave-current correction procedure. As before, the procedure relies on a VOF simulation in the derivation of the correction vector. However, once again only one two-dimensional, empty channel computation is necessary to adjust the boundary fields.



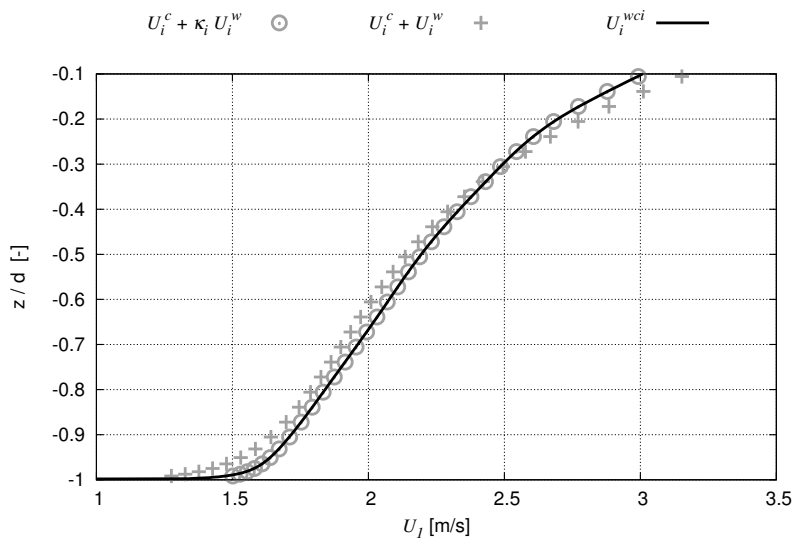
(a) Horizontal WCI correction factor



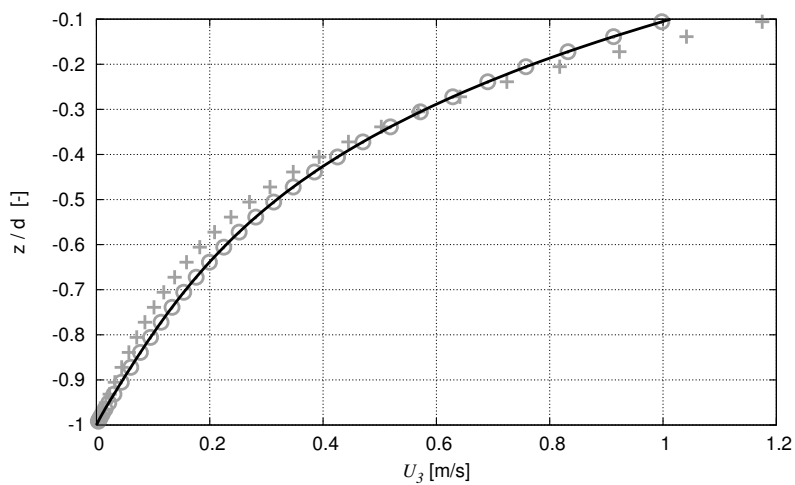
(b) Vertical WCI correction factor

Figure 4.6: WCI correction factor distributions for a wave-current scenario with  $H = 4$  m,  $T = 7$  s,  $d = 45$  m,  $U_s = 2$  m/s and  $\beta_c = 0.11$ .





(a) Horizontal velocity



(b) Vertical velocity

Figure 4.7: Velocities before and after applying  $\kappa_i$  for a wave-current scenario with  $H = 4$  m,  $T = 7$  s,  $d = 45$  m,  $U_s = 2$  m/s and  $\beta_C = 0.11$ .

### 4.4.2 Wave Length

Before the adjusted WCI velocities can be used as inlet and VFS boundary conditions for wave-current VFS simulations, the wave length  $L$  of the adjusted wave-current field needs to be determined. At this point, the wave solution  $U_i^w$  of Eq. 4.9 still incorporates the wave length of the pure wave scenario, which is altered by applying  $\kappa_i$  during the correction procedure. When utilizing  $L$  of the pure wave scenario in the computation of wave-current boundary conditions, numerical instabilities in the form of velocity and pressure oscillations occur in the CFD simulation. This is illustrated in Fig. 4.8a, which shows pressure spheres plotted throughout the domain for the previously analyzed wave-current scenario propagated 1.5 wave lengths into the channel. The radius of the spheres is scaled with respect to the corresponding pressure value, implying that sphere-free areas indicate zero-pressure regions. The zero-pressure Dirichlet boundary condition is satisfied at the outlet, but pressure fluctuations result in an incorrect non-zero pressure field in regions of the domain that have not been reached by the wave field. In addition, the pressure values in the domain are highly skewed, resulting in under and overshoots of peak and trough pressures, respectively. The solution for the same wave-current scenario when defined using the correct wave length is shown in Fig. 4.8b. A

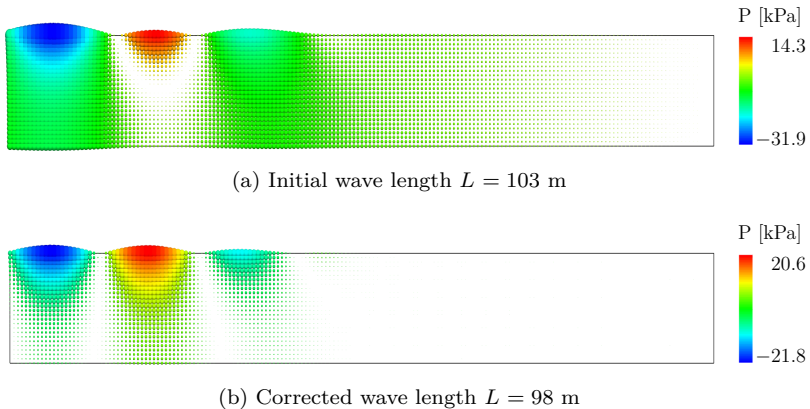


Figure 4.8: Pressure comparison for a wave-current field propagated 1.5 wave lengths into the domain.

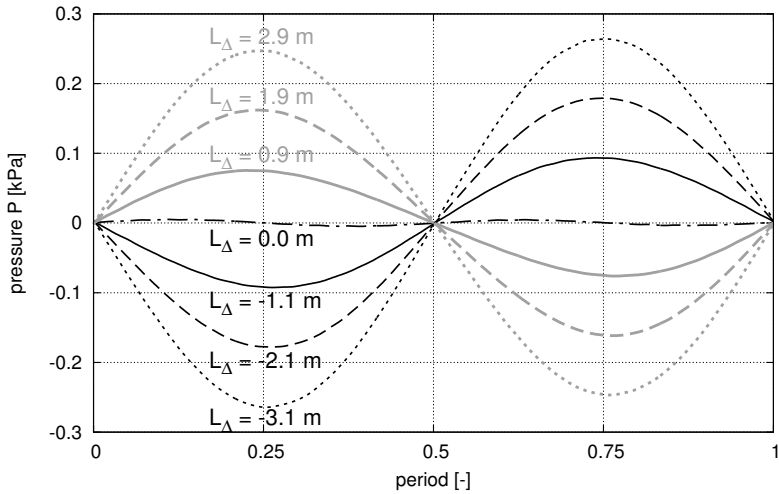
zero-pressure field is attained in regions of the domain that have not been infiltrated by the wave field. Also, physically accurate, near symmetric peak and trough pressure values are computed.

By comparing results of the wave-current scenario simulated using various wave lengths, it can be shown that there is a relationship between the magnitude of unphysical pressure fluctuations, and the degree of wave length overestimation or underestimation. Overestimating the wave length  $L$  by  $L_\Delta$  will result in the near outlet fluctuations plotted in Fig. 4.9a. This also holds true if the wave length is underestimated, although the pressure fluctuations are in antiphase to those attained with an overestimated wave length. The magnitude of the fluctuation may be quantified by computing the standard deviation of the pressure. The plot given in Fig. 4.9b is attained if the standard deviation  $\sigma_P$  for the analyzed wave lengths is weighted with a factor  $\zeta$  equal to 1 or  $-1$ , depending on the phase of the fluctuations:

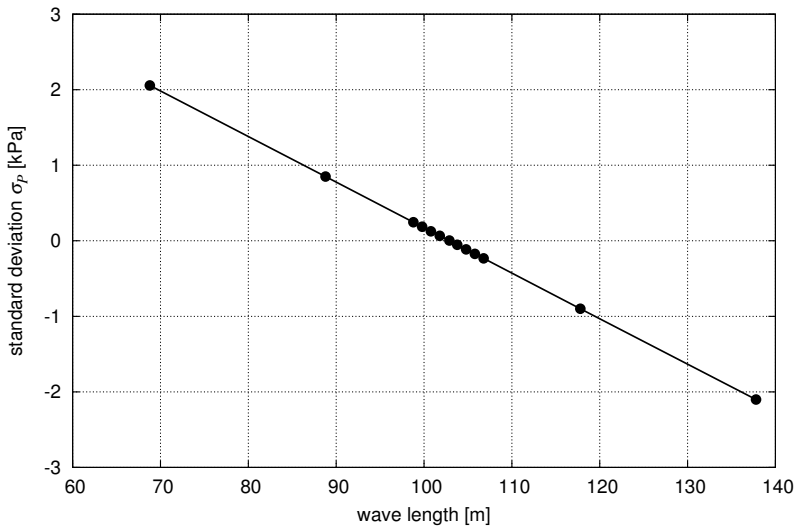
$$\sigma_P = \zeta \sqrt{E[P^2] - (E[P])^2} \text{ with } \zeta = \begin{cases} 1 & \text{for in phase fluctuation} \\ -1 & \text{for antiphase fluctuation} \end{cases} \quad (4.14)$$

As demonstrated in Fig. 4.9b, there is a linear relationship between the weighted standard deviation and the chosen wave length. This relationship may be used in order to numerically compute the wave length of the corrected wave-current velocity field, by carrying out two empty channel VFS simulations with different initial guesses for  $L$ . Based on the weighted standard deviation results, the correct wave length, with a standard deviation equal to zero, can easily be interpolated.

After the wave length  $L$  corresponding to the  $\kappa_i$ -corrected wave-current field is determined, Eq. 4.9 can be applied to generate stable VFS wave-current boundary conditions. The velocity results for a simulation of the analyzed wave-current conditions is given in Fig. 4.10. Throughout the water column the results match well with a reference solution computed using the VOF model. For pressure field sensitive application the pressure correction methodology outlined in Fig. 4.4 is applied by simply defining the corrected WCI boundary conditions as initial fields for  $U_i^{inl}$  and  $U_i^{vfs}$ , rather than computing them with the Fenton model.

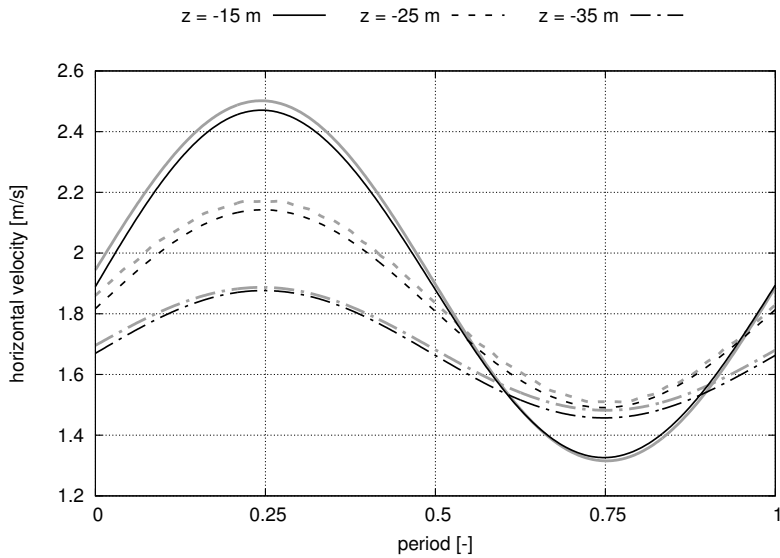


(a) Pressure development

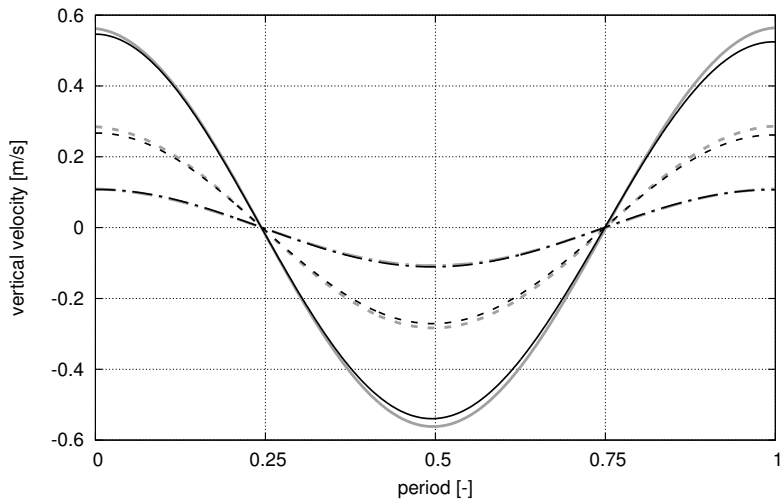


(b) Weighted standard deviation

Figure 4.9: Pressure development and weighted standard deviation over one period at mid-height of the domain in the near outlet region.



(a) Horizontal velocity



(b) Vertical velocity

Figure 4.10: VFS-WCI velocity results (grey curves) vs. VOF reference solution (black curves) at a distance of 1 wave length from the inlet.

## 4.5 Model Verification

In order to test and verify the VFS-NWCT, a design study is carried out that focuses on the sensitivity of maximum horizontal forces to geometry variation of a structure located on the sea floor. As shown in Fig. 4.11a, this geometry is parameterized by the point coordinates  $p_{i,j}$ , where the index  $i$  refers to the point number and  $j$  indexes the dimensions of the point in terms of the local structure coordinate system  $(x', z')$ . In this coordinate system, the  $x'$ -coordinate origin (with index  $j = 1$ ) is defined at the center of the structure, and the  $z'$ -coordinate origin (with index  $j = 3$ ) at the sea bottom. The shape is varied using the inclination angle  $\phi$  as the only design variable. The location of point  $p_{1,j}$  is fixed and  $p_{2,1} = p_{4,1}$ . In addition, a vertical symmetry axis is defined passing through  $p_{1,j}$ . Finally, constraints are introduced into the study that enforce an identical structural height  $h = 4$  m and an equivalent in-plane cross-sectional area  $A = 32$  m<sup>2</sup> for all geometry variations. This leads to the angle dependent point coordinates defined in Tab. 4.1 in terms of the inclination length  $r$ . The shape evolution is shown in Fig. 4.11b. In the study,  $\phi$  is varied in 1° increments from 1° to 26°. The virtual free surface height  $h_{v,fs}$  is defined 1 m below the physical wave trough.

The load cases analyzed in the VFS verification study are defined in Tab. 4.2. In a first step, simulations are carried out incorporating the pure wave scenarios of Tab. 4.2a at  $d = 45$  m. The resulting horizontal wave loads for each  $\phi$ -variation are shown in Fig. 4.12a with the maximum and average VFS deviations from the VOF reference solution given in Tab. 4.3a. A very good match is attained particularly for the smaller wave heights. Load case H1 results in a maximum deviation of 1.8% between the VOF and VFS results. A larger deviation is observed for higher waves, although the maximum recorded deviation for load case H3 is still below 5%. The increase in the deviations for larger wave heights may be explained by local flow field considerations. In the vicinity of a bottom mounted structure, significant alterations of the wave velocity field develop, compared to an undisturbed wave field (Grilli et al., 2003). As the wave height is increased, the penetration depth of the wave increases, resulting in a smaller minimum distance between the structure and the sea elevation during one wave cycle. As a consequence, the altered near structure flow field begins to influence the surface velocity field. This influence is not captured by the VFS model, resulting in a deviations increase from the reference solution.

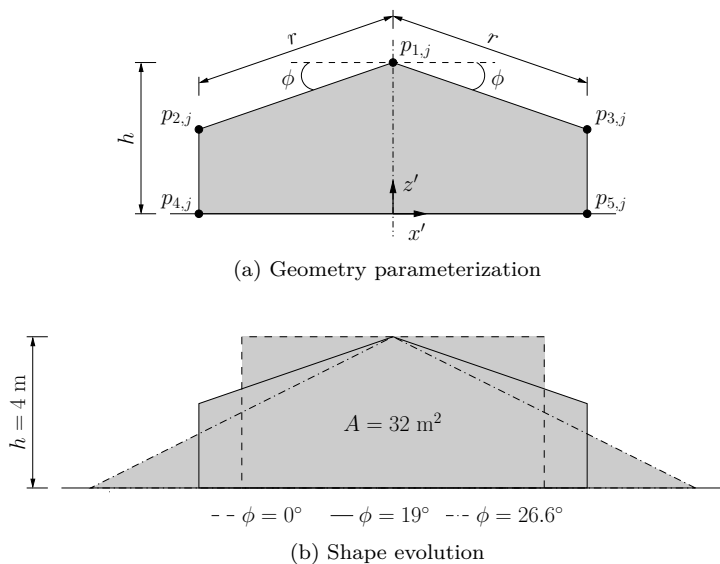


Figure 4.11: Geometry specifications of the design study structure.

Table 4.1: Test case point coordinates

point	$x'$ -coordinate	point	$z'$ -coordinate
$p_{1,1}$	0	$p_{1,3}$	$h$
$p_{2,1} = -p_{3,1}$	$-r \cos \phi$	$p_{2,3} = p_{3,3}$	$h - r \sin \phi$
$p_{4,1} = -p_{5,1}$	$-r \cos \phi$	$p_{4,3} = p_{5,3}$	0

$$r = \frac{h \cos \phi - \sqrt{(h \cos \phi)^2 - A \cos \phi \sin \phi}}{\cos \phi \sin \phi}$$

Table 4.2: Load case data.

(a) Wave			(b) Current		
case	$H$ [m]	$T$ [s]	case	$U_s$ [m/s]	$\beta_c$ [-]
H1	4.0	7.0	C1	2.0	0.11
H2	7.0	9.5	C2	4.0	0.11
H3	10.0	11.0	C3	6.0	0.11

Table 4.3: Maximum and average horizontal force deviations.

(a) Const. depth, varying wave				(b) Const. wave, varying depth			
case	depth [m]	max. [%]	ave. [%]	case	depth [m]	max. [%]	ave. [%]
H1	45	1.8	0.6	H1	55	1.5	0.7
H2	45	3.2	2.4	H1	45	1.8	0.6
H3	45	4.3	2.4	H1	35	5.1	3.4

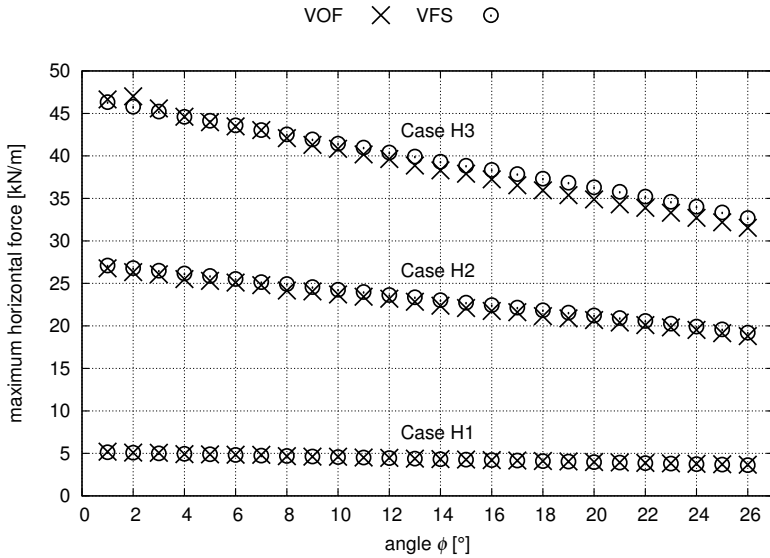
  

(c) Const. current, varying wave				(d) Const. wave, varying current			
case	depth [m]	max. [%]	ave. [%]	case	depth [m]	max. [%]	ave. [%]
H1C1	45	4.0	1.9	H1C1	45	4.0	1.9
H2C1	45	5.9	2.9	H1C2	45	15.4	6.5
H3C1	45	7.3	3.3	H1C3	45	21.5	8.9

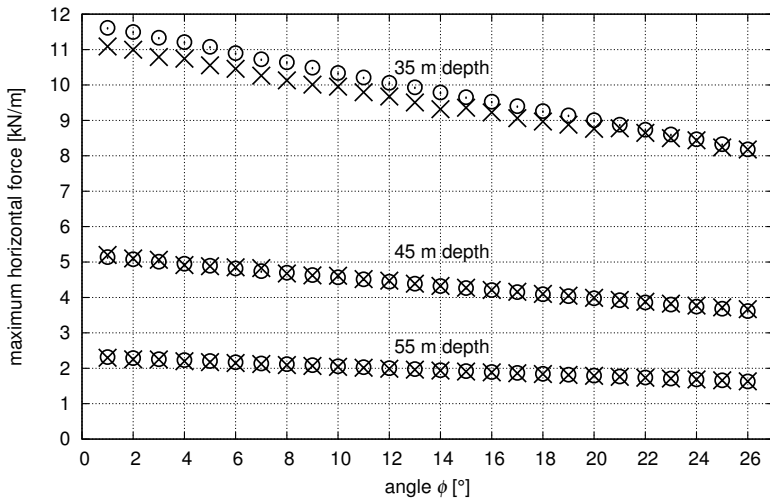
In addition, load case H1 is analyzed at different water depths (35 m, 45 m, and 55 m). The resulting forces are plotted in Fig. 4.12b with the deviations from the VOF reference solution recorded in Tab. 4.3b. Excellent agreement is attained for water depths of 55 m and 45 m with a maximum deviation of 1.5% and 1.8%, respectively. As the water depth is reduced to 35 m, the maximum deviations increase to 5.1%. This can be contributed to the increased influence of the bottom boundary and the structure on the overall wave field, which violates the assumption of an undisturbed VFS wave profile.

In addition to the pure wave tests, the VFS model is applied to two sets of wave-current interaction scenarios, defined by combining the wave load cases of Tab. 4.2a with the current load cases of Tab. 4.2b. The first set comprises of the H1 wave load case in combination with the three current load cases. Additionally, the load cases in a second set are defined using the current load case C1 in combination with the three wave load cases. The resulting maximum force values are given in Fig. 4.13 with model deviations documented in Tabs. 4.3c and 4.3d. The deviations increase as the magnitude of the velocities of the wave or current field is increased. This is once again due to the alterations



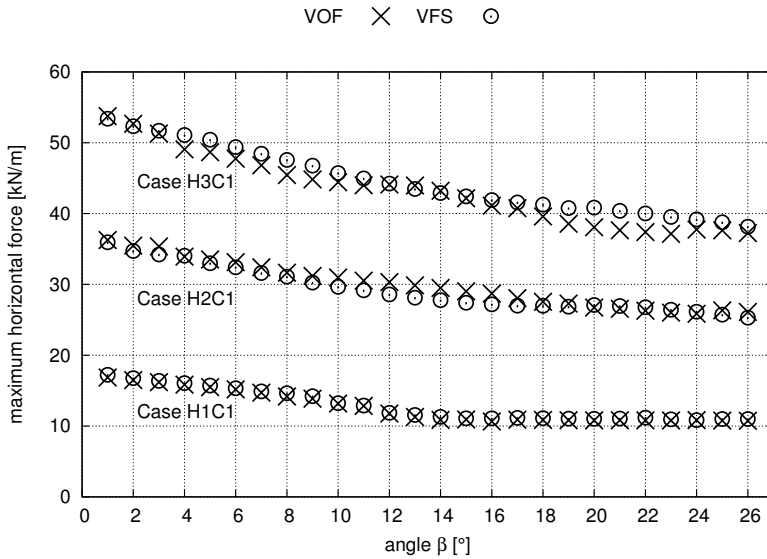


(a) Wave variations for depth 45 m

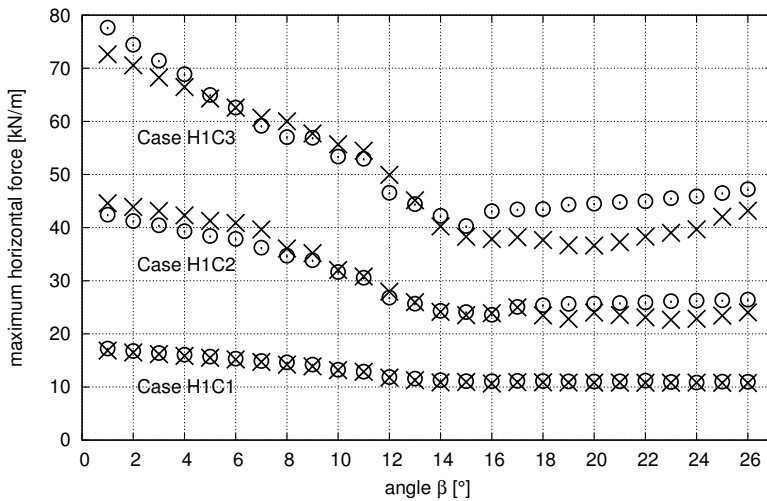


(b) Depth variations for wave H1

Figure 4.12: Pure wave load case VFS model verification using VOF reference solutions.



(a) Wave variations for current C1



(b) Current variations for wave H1

Figure 4.13: Wave-current load case VFS model verification using VOF reference solutions.

of the flow field caused by the structure. The presence of the structure in the channel results in a vertical velocity component and a vertical nonzero pressure gradient as the flow is redirected over the obstacle, causing an upwelling of the surface elevation over the structure. At higher current velocities, both vertical velocity and the nonzero pressure gradient at the structure propagate further towards the top and begin to stand in conflict with the zero gradient pressure boundary condition specified at the VFS boundary. The consequences of these conditions are particularly prominent in load case H1C3. This load case has the highest current velocity and a maximum percentage deviation of 21.5% between the VFS and VOF model. However, even under such extreme conditions, the qualitative distribution of the horizontal forces shown in Fig. 4.13b gives a good indication of the shape of the force function. This is particularly beneficial for the application of the VFS model in design studies or optimization problems.

Finally, the results of the wave length model introduced in Section 4.4.2 are analyzed. In terms of the maximum horizontal loads on a structure, the time derivative of the flow field velocities (local derivative) is a highly dominant factor when analyzing pure wave cases. In these cases, the spatial derivative, governed by the wave length, is of minor importance. However, the contribution of the spatial derivative is more significant in combined wave-current scenarios. Therefore, it is desirable to predict the wave length accurately for these scenarios. As shown in Tab. 4.4, the maximum deviation between the wave lengths computed for the VFS boundary conditions and the VOF reference solution is less than 5% for all tested scenarios. This is quite remarkable considering the complexity of the wave-current flow, which is simulated in the VFS model using adjusted boundary condition based on a simple polynomial correction function.

Table 4.4: Wave length comparison

case	VOF [m]	VFS [m]	$\Delta$ [%]
H1C3	136.0	138.7	2.0
H1C2	133.0	132.5	0.4
H1C1	105.5	100.4	4.8
H2C1	169.0	169.3	0.2
H3C1	204.5	212.3	3.8

## 4.6 Model Performance

Eliminating the physical free surface from the overall approach has several advantages with regard to a reduction of the computational costs. First of all, additional numerical solution steps necessary in order to solve the free surface model equations are not required. Furthermore, sidestepping the free surface treatment has the advantage of avoiding mesh refinement in the free surface region of the computational domain. Such a refinement is necessary in order to maintain the accuracy of the free surface methods. Insufficient mesh refinement may lead to inaccuracies in the computation of the free surface location, free surface normal vector, local curvature, and free surface tension forces. In addition to the discretization in space, the transient characteristic of wave and wave-current problems requires an adequate time discretization. In this regard, the spatial discretization of the free surface region has an influence on the chosen time step size, as excessive spatial refinement lowers the stability limit of explicit or partially explicit time-marching schemes. The stability limit is further affected by the physical characteristics of the wave-current problem, for which the maximum velocities occur in the free surface region. Mesh refinement in combination with large velocities requires the utilization of small time steps in order to attain stable solutions with explicit or partially explicit codes. The avoidance of free surface refinement in the VFS model approach therefore also allows for the utilization of a coarser time discretization. Overall, these considerations result in a significant reduction in computational costs.

The quantitative gain in efficiency depends on many factors, such as the utilized time integration schemes, the stability of the numerical schemes, the degree of free surface refinement, and the magnitude of the velocity boundary conditions. Therefore, a general rule concerning the gain in efficiency cannot be established. However, the performed verification studies give a good indication of the efficiency benefits of the reduced modeling technique.

In the design study carried out in [Section 4.5](#), the maximum Courant Number was set to 1.0 when the reference VOF model was used. Under this condition, all VOF simulations for the studied geometries and boundary conditions ran stable, while an increase of the Courant Number resulted in numerical instabilities. When utilizing the VFS model, stable simulations can be carried out at much higher Courant Numbers. Here, the time step is mainly limited by a reasonable time

discretization of the wave period, ensuring that the general behavior of the velocity fluctuations is captured. This was guaranteed by setting the time step to 0.1 s. For the highest velocity wave case analyzed in the study, this time step resulted in a Courant Number of approximately 7, without encountering numerical instabilities. For this particular case, the computation cost of the VOF model is approximately 15 times higher than that of the VFS simulation.

This efficiency gain was even exceeded in simulations carried out by Arnold (Markus et al., 2014a), who used the VFS model in simulations carried out with the software Ansys CFX. The solver implemented into the program is based on a fully implicit, parallel solution of the URANS equations. Using the fully implicit stable method, the number of time steps could be reduced to 40 per wave period for the VFS simulations. In comparison, 100 time steps per wave period were required in corresponding VOF simulations in order to reduce the numerical damping of the waves to an acceptable level. Overall, the increased time step and the avoidance of mesh refinement in the free surface region, lead to a reduction of the computational costs by a factor of approximately 40, when using the VFS model in combination with the fully implicit method.

## 4.7 Conclusions and Summary

In order to reduce the computational costs of wave and current CFD simulations, a single phase Virtual Free Surface model was introduced that allows for an efficient simulation of fully submerged structures. As part of the method, a VFS boundary is defined that simulates the wave field in the form of velocity boundary conditions, thereby avoiding the necessity of capturing the surface, as is customary in traditional free surface approaches. The approach has a number of advantages in terms of computational efficiency:

- Surface refinement to accurately capture the waves becomes obsolete, thereby reducing the number of cells in the domain.
- The comparatively coarse mesh in regions of the highest wave velocities and current velocities allows for the utilization of larger time steps while still fulfilling the stability limit of explicit or partially explicit time-marching schemes.

- A discretization of an air phase in the domain can be avoided altogether, further reducing the number of cells.

For velocity field sensitive applications involving waves and uniform currents, the VFS velocity boundary field may be used directly as part of the simulation. However, it was shown that the application of the VFS boundary conditions gives rise to pressure field deviations. For pressure field sensitive applications and for simulations involving a depth varying current, further modeling steps were introduced. These can be outlined as follows (*italic text* refers to information that is only relevant when modeling waves with a depth varying current):

1. A free surface CFD simulation is carried out using a predefined inlet wave boundary field. *For wave-current simulations, the boundary field is initially generated by linearly superimposing the wave and current solution.* During simulation, pressure and velocity values are probed in the domain.
2. *For combined wave-current flows, the WCI correction vector  $\kappa_i$  is computed based on the probed velocity values.*
3. A horizontal VFS boundary is introduced in the vicinity of the free surface and a VFS wave velocity boundary field is generated.
4. The VFS model is applied consecutively while probing the pressure values. The results are used together with the free surface reference pressure to define the correction factor  $\lambda$ .
5. *For combined wave-current flows, the VFS wave length is computed by iteratively applying the VFS model and monitoring the near outlet pressure fluctuations.*
6. The final boundary field is computed based on the calculated correction parameters.

The VFS model was successfully tested in an extensive verification study. It was shown that in empty channel simulations the developing velocity field of the VFS model closely follows the theoretical solution. After following the outlined correction procedure for pressure sensitive applications, a good match of the pressure field was also attained. In addition, the VFS model was verified with regard to the forces on a bottom mounted structure. Results from VOF based simulations

served as a reference solution. A wide range of pure wave and combined wave-current scenarios were included in the investigation. The following key conclusions were drawn from the verification simulations:

- A good agreement between the models was achieved for pure wave simulations, with deviations ranging from 1.5% to 5.1%. Larger deviations occurred in the combined wave-current force computations. This is a result of changes in the wave-current field in the vicinity of the boundary, not taken into account by the VFS model.
- In all studies, an excellent match of the general trends resulting from geometry and flow condition variations was captured with the VFS model.
- In terms of efficiency, the VFS simulations were observed to be roughly 1-2 orders of magnitude faster than the VOF reference calculations.

Overall, the VFS model allows for an efficient analysis of the effect of flow field and geometry alterations as part of elaborate parameter and optimization studies of fully submerged structures.





---

## Chapter 5

# Shape Optimization

---

### 5.1 Introduction and Overview

The VFS method introduced in [Chapter 4](#) allows for efficient CFD simulation of offshore environments. This allows for a time-effective analysis of shape optimization problems, which would involve highly restrictive computational times using a VOF based approach. In this chapter, the method is applied as part of a thorough shape optimization study of GBFs subjected to wave and current conditions. The aim is to provide insight into how bottom mounted bluff bodies should ideally be shaped to render minimum forces under the unique loading encountered at offshore sites. This highly complex and previously unsolved design problem was introduced by the development of tidal turbines, which heavily rely on innovative support structure designs to allow for an economical implementation of the devices.

A great wealth of knowledge in the field of optimal shape design has been collected in automotive engineering and aeronautics. However, these fields almost exclusively consider time invariant inflow conditions, while a physical phenomena comparable to ocean wave motion is not encountered. The closest topic related to the design problem at hand is the shape optimization of ship hulls in marine environments. It is a field with a strong research background for which the full

spectrum of optimization methods has been and continues to be utilized. This concerns both zero order and gradient based methods, as outlined in this section. A detailed account of the classification and fundamental description of optimization techniques in general is found in the literature (e.g. Vanderplaats, 1984; Mohammadi et al., 2001; Thévenin and Janiga, 2008; Griva et al., 2009; Hazra, 2009).

Early automated hull shape optimization based on CFD simulations dates back to publications by Wyatt and Chang (1994), Janson and Larsson (1996), Tahara and Himeno (1998) and Campana et al. (1999), to name a few. Ever since, a great variety of approaches have been followed to improve ship hulls. Gradient based approaches using steepest decent, conjugate gradient, and sequential quadratic programming schemes were for instance utilized by Peri et al. (2001) and Tahara et al. (2004). More recently, adjoint-based shape optimization was applied to ship hull design as documented in Stück and Rung (2011) and Rung et al. (2012). In addition, zero order approaches of all varieties have been applied to hull design. These include evolutionary strategies (e.g. Grigoropoulos and Chalkias, 2010; Zakerdoost et al., 2013), genetic algorithms (e.g. Dejhalla et al., 2002; Tahara et al., 2008), particle swarm optimization (e.g. Pinto et al., 2007; Hart and Vlahopoulos, 2010), neural networks (e.g. Besnard et al., 2007; Chen and Ye, 2009), and simulated annealing (e.g. Kosmas and Vlachos, 2012). Furthermore, response surface modeling based on Kriging has been utilized in combination with CFD simulations to allow for an efficient exploration of the design space (e.g. Kim et al., 2011; Tahara et al., 2011).

Ship hull optimization and GBF design share some general similarities regarding the characteristics of the considered marine loading and the objective of the problem. However, there are several fundamental differences that greatly influence the overall optimization approach:

- The objective in optimal hull design is often tied to an economical context, with the aim to minimize drag during cruising speed, rather than during extreme weather conditions. Contrary, the forces on GBFs during average operating conditions are typically of minor relevance, while the design of the structures is dictated mainly by extreme load cases.
- Every ship serves a specific functionality, which typically relates to the transportation of goods or people. The constraints imposed

during hull design are directly tied to this functionality. In the case of GBFs, the functionality and the resulting constraints are entirely different, leading to a new optimization problem.

- The steady flow simulated in hull optimization studies typically represents the ship motion relative to the still water, rather than a current flow subjected to a still structure. The fundamental difference lies in the shape of the fluid velocity profile, which is constant over depth in the case of ship motion, and incorporates a boundary layer flow when considering a current profile.
- For the same offshore conditions, the kinematics at the water surface differ considerably from the flow motion encountered near the sea floor. As shown in [Section 3.2](#), this is particularly true regarding the interaction between the wave and the current, which is depth dependent. Consequently, the same offshore conditions result in different flow environments for a ship on the surface compared to a structure on the sea floor
- An entirely contrasting objective is followed regarding the role of the vertical forces on the body. In ship design, floatability needs to be maintained in the optimization process. Conversely, the shape of a GBF should ideally initiate a downward force on the structure during loading.
- In the design of ship hulls, the first CFD based optimization studies drew from a great wealth of prior knowledge and experience, resulting from decades of experimental testing and ship building. These provided a good initial design for the shape to be optimized. In the case of GBFs for tidal turbines such prior knowledge is largely lacking.

As a result of these differences, the findings from many years of ship hull optimization can not directly be applied to GBF design. The lack of previous knowledge in the field requires a fundamental treatment of the design problem and a conceptually adapted optimization approach under consideration of the unique conditions. Generally, the VFS model could be utilized in combination with any of the aforementioned optimization methods. However, the characteristics of the specific optimization problem renders some approaches more suitable than others. As analyzed by [Tahara et al. \(2011\)](#), industrial marine optimization problems are typically nonlinear, multimodal,

and nonconvex. In the case of GBFs, this is a result of the complex flow environment and jumps in flow separation points in combination with altering reattachment zones. This characteristic is particularly problematic with regards to local optimization schemes such as gradient based methods, because the predicted optimum may in fact be a local minimum. This is particularly problematic because the problem at hand is in the early stages of optimization, for which the knowledge of favorable GBF shapes in the vicinity of the global optimum does not exist. A possible solution is the utilization of multistart local optimization methods, at the cost of a decreased efficiency. This is particularly restrictive when using CFD, which is computationally expensive even if reduced modeling techniques are applied.

These difficulties motivate using one of the aforementioned zero order approaches, which are global optimization techniques. The specific choice is dictated by the problem at hand. Because the GBF optimization problem is largely uninvestigated, the goal is to attain an unbiased representation of the design space, in addition to the global optimum. This allows for an analysis of the physical intricacies of the problem and a general characterization of shape variations with respect to the objective. Particularly suitable for this task is the utilization of meta models in the form of Kriging surfaces that approximate the design space based on discrete simulation results. These surfaces allow for a thorough investigation of the design space and provide valuable information that can directly be used to choose hydrodynamically efficient foundation shapes under consideration of the expected offshore environment. The results also give a sound basis to apply higher order methods to the optimization problem in the future.

The optimization framework is introduced in the following section. In addition, the method is applied to a shape investigation of bottom mounted structures subjected to waves, currents, and combined wave-current scenarios. Both horizontal and vertical forces are taken into consideration.

Part of the work presented in this chapter has been published in the International Journal of Offshore and Polar Engineering (Markus et al., 2015c), in the Proceedings of the tenth European Wave and Tidal Energy conference (Markus and Bletzinger, 2013), and in the Proceedings of the twenty-fourth International Conference of Offshore and Polar Engineering (Markus et al., 2014b). It is presented here with explicit written consent from the publishers.

## 5.2 Optimization Framework

The framework used to investigate the GBF optimization problem is introduced in Fig. 5.1. In a first step, the shape to be analyzed is parameterized in terms of the selected number of design variables  $n_d$ . In this thesis, the parametrization generally contains a geometric variable that is defined as a function of the area/volume of the structure (for example, in the design study of Section 4.5 this variable is the inclination length  $r$  defined in Tab. 4.1). This variable ensures that the area/volume equality constrained specified in all presented optimization problems is preserved.

Following, the point set  $q_{i,j}$  is generated, which consists of  $n$  initial points of dimension  $n_d$ , element of the  $n_d$ -dimensional experimental design  $Q$ :

$$q_{i,j} = [q_{i,1}, q_{i,2}, \dots, q_{i,n_d}] \in Q \quad \text{with} \quad i = 1, \dots, n \quad (5.1)$$

Here,  $Q$  is limited to the lower and upper side constraints  $q_j^l$  and  $q_j^u$ , which are applied to  $q_{i,j}$ :

$$q_j^l = (q_1^l, q_2^l, \dots, q_{n_d}^l) \quad (5.2a)$$

$$q_j^u = (q_1^u, q_2^u, \dots, q_{n_d}^u) \quad (5.2b)$$

$$q_j^l \leq q_{i,j} \leq q_j^u \quad (5.2c)$$

The selection of the point set  $q_{i,j}$  is carried out with a space-filling experimental design using the Monte Carlo method (Crombecq and Dhaene, 2010). Initially,  $Q$  consists of the two corner points  $q_j^u$  and  $q_j^l$ . Following, the Monte-Carlo method is used to generate a random set of  $n_d$ -dimensional candidates, following a uniform probability distribution. Each candidate  $q_j^c$  is ranked according to the minimum distance between the point and all other points in  $Q$  (intersite distance) and their minimum projected distance on all axes of the design space (projected distance) using the following distance function:

$$\begin{aligned} \text{dist}(q_j^c, q_{i,j}) &= \frac{(n+1)^{\frac{1}{n_d}-1}}{2} \min_{q_{i,j} \in Q} \sqrt{\sum_{j=1}^{n_d} |q_{i,j} - q_j^c|^2} \\ &\quad + \frac{n+1}{2} \min_{q_{i,j} \in Q} \min_{1 \leq j \leq n_d} |q_{i,j} - q_j^c| \end{aligned} \quad (5.3)$$

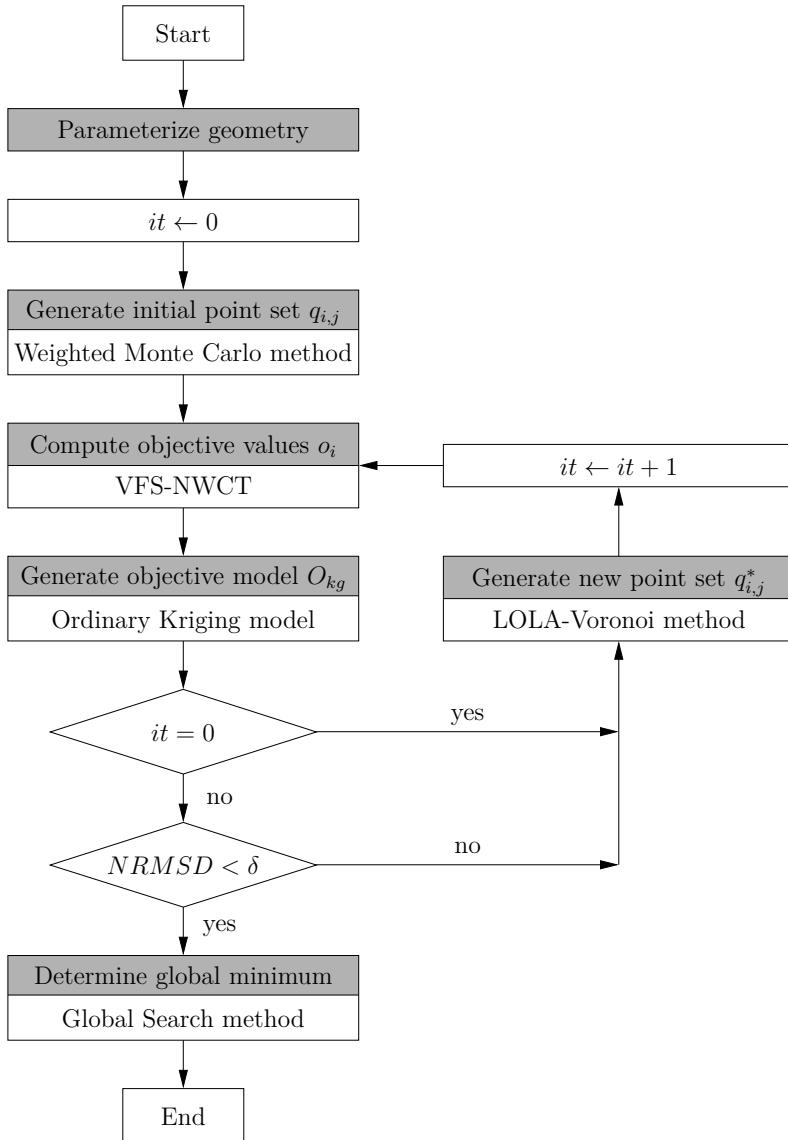


Figure 5.1: Optimization framework

Here, the first term of the equation consists of the minimum intersite distance, while the second term is written in terms of the minimum projected distance. The fractional multipliers ensure that each term is given equal weights based on their scales. According to the distance ranking, the best candidate is selected to be added to  $Q$ , which will have the most favorable space-filling characteristics in terms of the intersite and projected distance to all previously selected points. The procedure is repeated until the  $n$  initial points of the point set  $q_{i,j}$  are generated.

After the initial experimental design  $Q$  is determined, the VFS-NWCT is applied to compute the discrete objective function values  $o_i$  corresponding to the point set  $q_{i,j}$ :

$$o_i = (o_1, o_2, \dots, o_n)^T \quad (5.4)$$

In this thesis, the objective  $O$  is defined as either the horizontal or vertical peak force on the structure.

Based on the computed objective function values, an objective Kriging approximation model  $O_{kg}$  is build. The basic concept is to use interpolation in order to derive an estimation of the objective function using a regression of the computed samples. In order to determine this regression, the experimental semivariogram  $\gamma_e$  according to [Cressie \(1992\)](#) is computed, which gives the relationship between the variance and the distance  $h_e$  between the sample points  $q_{i,j}$ :

$$\gamma_e(h_e) = \frac{1}{2|N(h_e)|} \sum_{(i,j) \in N(h_e)} |o_i - o_j|^2 \quad (5.5)$$

Here,  $h_e$  is an approximation distance defined with a certain tolerance. All point combinations in  $Q$  separated by a distance  $h_e$  are combined into the subset  $N(h_e)$ . The total number of points in the subset is equal to  $|N(h_e)|$ . In order to allow for a spatial prediction formulation that is a continuous function of all feasible distances  $h_m$ , a model semivariogram  $\gamma_m$  in the form of an analytical function is fitted to  $\gamma_e$ . For the optimization studies carried out in this thesis both exponential ( $e = 1$ ) and gaussian ( $e = 2$ ) models are utilized to define  $\gamma_m$ :

$$\gamma_m(h_m) = c_0 + c_1 \left( 1 - \exp \left( - \frac{h_m^2}{c_2^e} \right) \right) \quad (5.6)$$

The model constants  $c_0$ ,  $c_1$ , and  $c_2$  represent the semivariogram intercept (nugget), the semivariance as  $h_m$  goes to infinity, and the

data point correlation scalar, respectively. Appropriate values for these constants can be computed by applying the weighted least squares technique presented by [Cressie \(1985\)](#).

The continuous ordinary Kriging model  $O_{kg}$  as a function of an arbitrary point coordinate  $q_j^p \in Q$  is computed as a weighted sum over all simulated point set results  $o_i$ :

$$O_{kg}(q_j^p) = \sum_{i=1}^n W_i(q_j^p) o_i \quad (5.7)$$

The weights  $W_i$  are determined based on the analytical function  $\gamma_m$  by solving the following system of linear equations:

$$\begin{aligned} \begin{bmatrix} W_1 \\ \vdots \\ W_n \end{bmatrix} \begin{bmatrix} \gamma_m(|q_{1,j} - q_{1,j}|) & \cdots & \gamma_m(|q_{1,j} - q_{n,j}|) \\ \vdots & \ddots & \vdots \\ \gamma_m(|q_{n,j} - q_{1,j}|) & \cdots & \gamma_m(|q_{n,j} - q_{n,j}|) \\ 1 & \cdots & 1 \end{bmatrix} + \begin{bmatrix} \lambda_s \\ \vdots \\ 0 \end{bmatrix} \\ (5.8) \\ = \begin{bmatrix} \gamma_m(|q_{1,j} - q_j^p|) \\ \vdots \\ \gamma_m(|q_{n,j} - q_j^p|) \\ 1 \end{bmatrix} \end{aligned}$$

This system of equations incorporates the condition that the sum of the weights is equal to one. The slack variable  $\lambda_s$  ensures that the introduction of this condition does not lead to an overconstrained system. Good references with further information on Kriging include [Lam \(1983\)](#), [Clayton and Andre \(1997\)](#), [Stein \(1999\)](#), and [Davis and Sampson \(2002\)](#).

The initial Kriging model can be further refined by computing additional discrete objective values for successively selected new point sets. The selection of new points is carried out using the adaptive LOLA-Voronoi sampling algorithm, as proposed by [Crombecq et al. \(2009b\)](#). The method is a hybrid sampling strategy that combines an exploration-based Monte Carlo Voronoi approximation with an exploitation-based Local Linear Approximation (LOLA) sampling algorithm.

The Voronoi approximation gives a measure of the sampling density of the previously analyzed point set  $q_{i,j}$ . Each point in the set is



assigned a so called Voronoi cell. This cell defines the region of the design space that is closer to the individual point than to all other points in  $q_{i,j}$ . It can efficiently be computed using a Monte Carlo approach. A large set of  $n_s$  randomly distributed sample points  $p_s$  is generated and each sample is assigned to the point in  $q_{i,j}$  that is the closest. The Voronoi weighting vector  $V_i$  is then defined as:

$$V_i = \begin{bmatrix} V_1 \\ \vdots \\ V_n \end{bmatrix} = \frac{1}{n_s} \begin{bmatrix} |N(p_s \rightarrow q_{1,j})| \\ \vdots \\ |N(p_s \rightarrow q_{n,j})| \end{bmatrix} \quad (5.9)$$

where  $|N(p_s \rightarrow q_{i,j})|$  is the number of points in the subset containing the sample points  $p_s$  assigned to a specific point  $q_{i,j}$ . The vector  $V_i$  weights each previously selected point in  $Q$  according to the density of sample points in that region.

The LOLA component of the hybrid sampling technique ranks the computed samples based on the local linearity of the objective function, emphasizing points that are in regions of high non-linearity. This approach stems from the fact that function values for points in regions with a nearly linear behavior can more easily be predicted based on neighboring points than those in non-linear regions. Simultaneously, this ranking favors points in regions of local extrema, thereby enforcing a refinement of the point grid in high-interest regions. The degree of non-linearity at a point  $q_{i,j}$  is quantified based on local gradient approximations  $g_i^{nb}$  at a set of neighborhood points  $q_{i,j}^{nb} \in Q$ . The gradients are computed by applying a least squares regression in the neighborhood of  $q_{i,j}$ . The computation of the gradients and the selection of an ideal set of neighborhood points is analyzed in detail by [Crombecq et al. \(2011\)](#). Finally, the LOLA weighting vector  $L_i$  for each point in  $Q$  is defined as a measure of the difference of the true objective value and a local linear approximation based on the estimated neighborhood points gradients:

$$L_i = \begin{bmatrix} L_1 \\ \vdots \\ L_n \end{bmatrix} = \begin{bmatrix} \left| \sum_{i=1}^{n_{nb}} o_i^{nb} - (o_1 + g_i^{nb}(q_{i,j}^{nb} - q_{1,j})) \right| \\ \vdots \\ \left| \sum_{i=1}^{n_{nb}} o_i^{nb} - (o_n + g_i^{nb}(q_{i,j}^{nb} - q_{n,j})) \right| \end{bmatrix} \quad (5.10)$$

where  $n_{nb}$  is the number of points in each neighborhood and  $o_i^{nb}$  are the neighboring point objective values. The final LOLA-Voronoi weighting vector  $LV_i$  is defined as a combination of  $L_i$  and  $V_i$ :

$$LV_i = \frac{1}{2}V_i + \frac{1}{2\sum_{i=1}^n L_i}L_i \quad (5.11)$$

The normalization of  $L_i$  is carried out in order to scale the weights to the range  $[0, 1]$ , while the entries of  $V_i$  are already scaled to this range. Following, a new candidate point set  $q_{i,j}^*$  is defined by selecting the desired number of new points  $n^*$  in the vicinity of the highest ranked points  $q_{i,j}$ , based on the LOLA-Voronoi weights. The exact new locations are determined by generating a large random sample point set in the Voronoi cells of each selected point  $q_{i,j}$ , and by adding the sample point farthest away from  $q_{i,j}$  and its neighbors to  $q_{i,j}^*$ . Further information regarding the intricacies of the LOLA-Voronoi sampling strategy has been documented by Aurenhammer (1991), Crombecq et al. (2009a, 2011), and Singh et al. (2013).

After each refinement iteration, the objective values  $o_i^*$  for the newly specified point set  $q_{i,j}^*$  are determined using the VFS-NWCT. The results are combined with all previously analyzed points to generate a new Kriging model. The procedure is repeated iteratively until a convergence criterion is fulfilled. This criterion is defined in this thesis as the Normalized Root-Mean-Square Deviation (NRMSD) between the Kriging model  $O_{kg}^{it-1}$  of the previous iteration, and the new Kriging model  $O_{kg}^{it}$  of the current iteration:

$$RMSD = \sqrt{\frac{\int_{v_1^l}^{v_1^u} \int_{v_2^l}^{v_2^u} \dots \int_{v_{n_d}^l}^{v_{n_d}^u} (O_{kg}^{it} - O_{kg}^{it-1})^2 dv_1 dv_2 \dots dv_{n_d}}{\prod_{i=1}^{n_d} (v_i^u - v_i^l)}} \quad (5.12a)$$

$$NRMSD = \frac{RMSD}{\max(O_{kg}^{it}) - \min(O_{kg}^{it})} \quad (5.12b)$$

where  $v_i$  is the vector of design variables with lower and upper bounds  $v_i^l$  and  $v_i^u$ , respectively. If each new point set  $q_{i,j}^*$  is sufficiently large, the NRMSD gives a good indication of the Kriging model convergence in the regions of interest. In this thesis, the overall Kriging model is deemed sufficiently refined when NRMSD drops below 2%. At this point, the Kriging model refinement loop is terminated and the final Kriging model is returned for further analysis.

As a final step of the optimization framework, the global minimum of the function is determined. Because the Kriging model can be expressed in the form of an analytical function in terms of the design variables, the

optimum can be computed efficiently using a number of optimization algorithms. In this thesis, the Global Search method described by [Ugray et al. \(2007\)](#) is utilized. The method consists of a global phase and a local phase. In the global phase, a population based meta-heuristic scatter search algorithm ([Glover, 1999](#)) is utilized to generate a set of starting points in the objective function domain. Following, these starting points are used in the local phase to determine local minima of the constrained non-linear objective function by applying Successive Quadratic Programming (SQP). A thorough description of SQP has, for instance, been documented by [Edgar et al. \(2001\)](#), [Bonnans et al. \(2003\)](#), and [Sun and Yuan \(2006\)](#). Finally, the full set of local minima provides the global minimum of the optimization problem.

In this thesis, the optimization framework was executed in a software environment consisting of the VFS-NWCT implemented into the in-house code LATOS, in combination with the Sequential Experimental Design (SED) and Surrogate Modeling (SUMO) Matlab toolboxes developed in the Department of Information Technology of Ghent University. Further information regarding these toolboxes can be found in [Crombecq et al. \(2009a,b\)](#), [Crombecq and Dhaene \(2010\)](#), and [Gorissen et al. \(2010\)](#).

### 5.3 Horizontal Force Analysis

The optimization framework is applied to an in-depth analysis of optimal shapes for GBFs. A fundamental insight into the problem is gained in this chapter by carrying out a series of two-dimensional design studies incorporating basic shape configurations. This allows for an efficient analysis of the physical properties underlying the problem, before the framework is applied to the design of a three-dimensional tidal-turbine foundation in [Chapter 8](#).

The two-dimensional design studies of this chapter are carried out in two stages. First, the optimization problem is defined in terms of one Design Variable (DV) only. Using this simple configuration, a variety of different load cases are analyzed in order to investigate potential dependencies of the optimal shape on the magnitude of loading. Following, the problem is extended to a multiple DVs optimization problem analyzed under a few selected conditions. Here, the focus is put on investigating a broader design space to gain a deeper understanding of optimal shape characteristics. In this section, this two-stage approach

is followed with the objective to minimize the horizontal loads on the structure, before it is again applied in the analysis of vertical forces in [Section 5.4](#).

### 5.3.1 Single-Variable Optimization

The geometry parametrization carried out as part of the single DV optimization problem is an extension of the parametrization used in the verification study of [Section 4.5](#). The configuration of the body is adjusted towards a more realistic foundation shape by introducing a central base of width  $b$  at the top of the geometry, representing the mounting point for connection to an offshore energy device ([Fig. 5.2a](#)). The inclination angle  $\phi$  is selected as the only DV of the problem. As before, the area of the structure is enforced to remain constant, by defining the geometric variable  $r$  as a function of  $A$ . The structure point coordinates  $p_{i,j}$  as a function of  $\phi$  and  $r$  are defined in [Tab. 5.1](#) and shown in [Fig. 5.2a](#). The geometric constants of the structure are defined as  $h = 3$  m,  $b = 2$  m, and  $A = 24$  m<sup>2</sup>. The resulting shape evolution for selected angles  $\phi$  is given in [Fig. 5.2b](#). In this study,  $\phi$  is subject to lower and upper side constraints of  $1^\circ$  and  $26^\circ$ , respectively. The consideration of a one-dimensional design space allows for a fine spatial resolution for  $q_{i,j}$  using relatively few sample points. In this particular study, the selection of 26 sample points is already sufficient to reduce the maximum neighbor distance to  $1^\circ$ . As a result, the optimization framework of [Fig. 5.1](#) can be applied without initiating the LOLA-Voronoi refinement loop.

The spatial discretization of the CFD problem is carried out using an unstructured, hex-dominant mesh with local refinement in the vicinity of the structure. Three prism layers are defined in the near wall region of the structures, with a first row wall distance of 1.5 mm. In the simulations, this results in a dimensionless wall distance  $y^+$  of approximately 100, which is within the range of application of wall functions. A refinement and integration down to the linear sublayer was avoided because the structure is composed of sharp edges resulting in distinct separation points. The domain length is equal to 1300 m and the domain height varies from 39 m to 42 m, corresponding to the wave height dependent VFS height. Overall, each mesh consists of approximately 85,000 cells with 98.5% hexahedra. The remaining 1.5% comprise of polyhedral and prism cells. In the optimization study, the set of current and wave conditions defined in [Tab. 4.2](#) on [page 85](#)

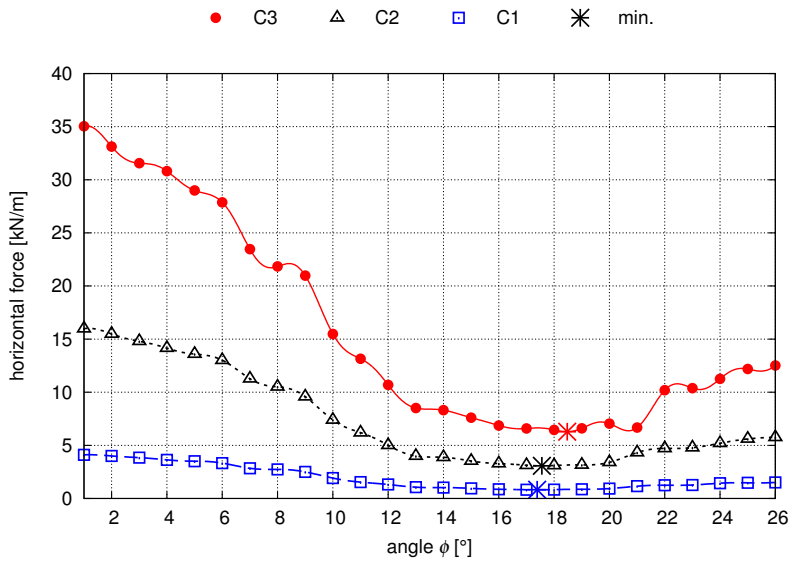


are used as boundary conditions for the CFD simulations. The water depth is set to  $d = 45$  m.

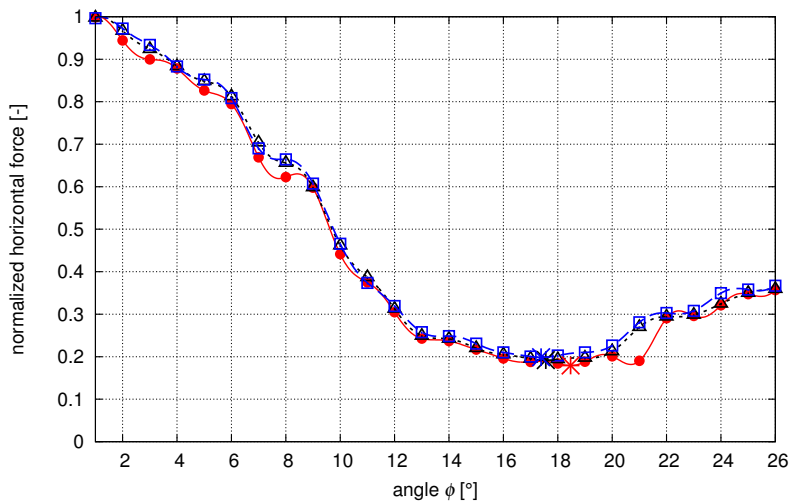
In a first step, the results from the three current load cases are analyzed. Fig. 5.3a shows the discrete objective values and the corresponding Kriging curves for each load case. All three curves initially decrease as  $\phi$  is gradually increased starting from  $0^\circ$  until a minimum of the horizontal forces is reached at around  $18^\circ$ . Higher values of  $\phi$  result in an increase of the objective. This behavior can be explained by analyzing the velocity contour plots shown in Fig. 5.4. For angles between  $1^\circ$  and  $18^\circ$ , the flow separates at the leading edge, triggering a large dead water zone above and beyond the structure that is particularly large for small inclination angles (Fig. 5.4a and Fig. 5.4b). For  $\phi = 18^\circ$  and higher, flow re-attachment occurs on the leading edge before the flow separates again at the peak of the structure. The flow remains attached to the entire leading edge for  $\phi = 26^\circ$  (Fig. 5.4d). The optimum with regards to horizontal forces is reached when a near symmetric flow pattern on the leading and trailing edge of the structure develops (Fig. 5.4c). At this point, the pressures on the leading and trailing edge of the structure are approximately equal in magnitude, while producing force resultants of opposing  $x'$ -directions. The observed behavior and the location of the objective minimum are largely independent of the current magnitude for the analyzed range of flow conditions, as shown in Fig. 5.3b. When normalized with respect to the maximum forces of each load curve, the profiles collapse onto nearly the same line. This finding is particularly valuable for design practice, because the optimal configuration with regards to horizontal current forces is not limited to an individual flow scenario.

The results of the wave load case optimization runs are shown in Fig. 5.5a. Here, the peak forces during wave loading are defined as the problem objective. In accordance with the predictions of the Section 3.3.2 shape investigations, the optimization study confirms that a redistribution of structure area towards the sea floor has a favorable effect on the horizontal forces. As a result, the optimum is attained for the largest feasible value of  $\phi$ . As with the current load case, the normalized shape of the wave force objective function and the resulting optimal configuration are largely independent of the analyzed range of conditions (Fig. 5.5b).

In addition to the analyzed individual wave and current scenarios, two sets of WCI load cases are considered by combining the individual



(a) Objective



(b) Normalized objective

Figure 5.3: Current horizontal force optimization results. Markers indicate CFD results. Kriging approximations are shown with lines.

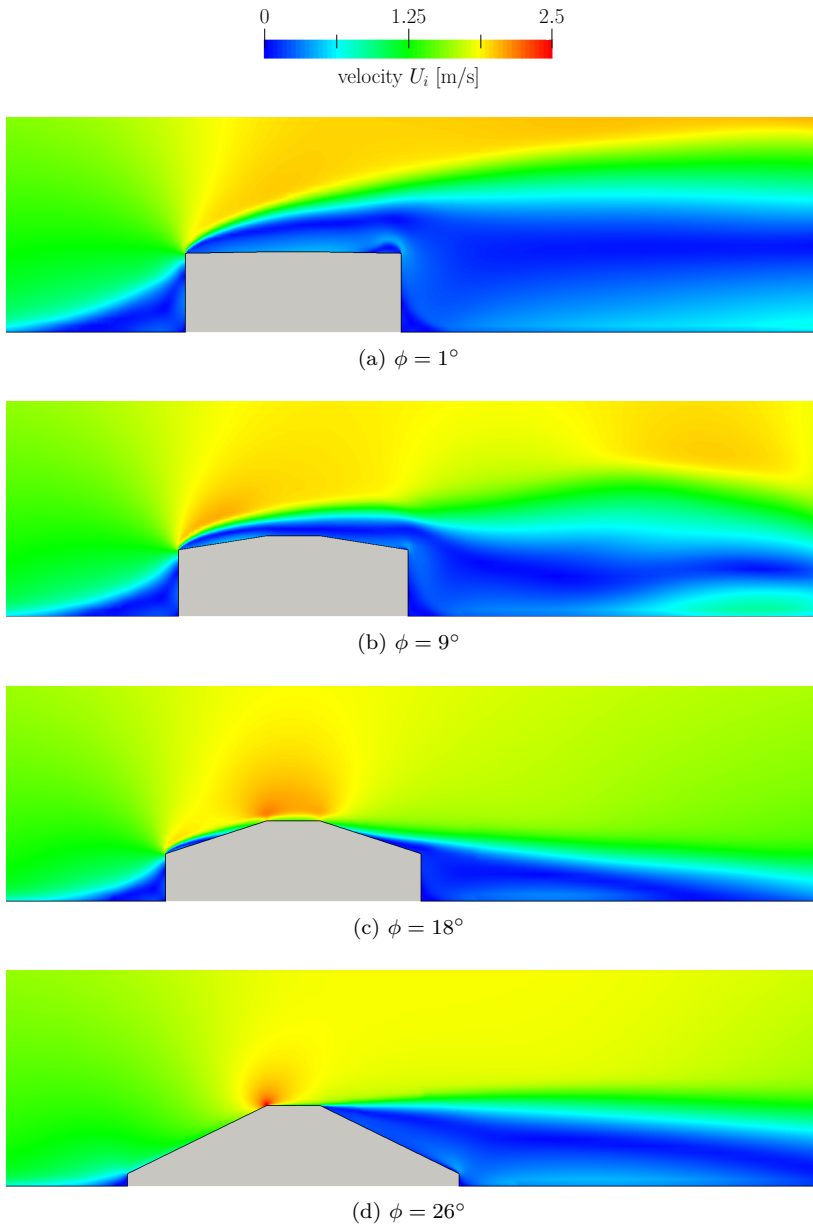
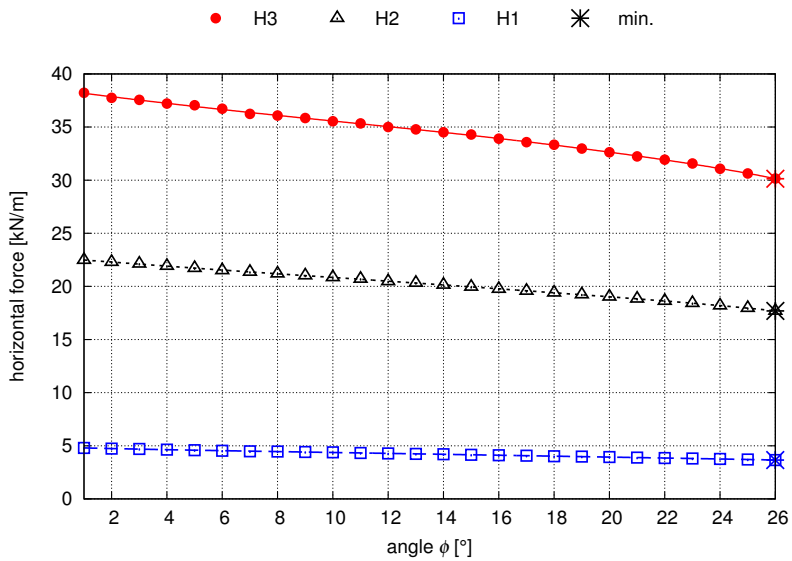
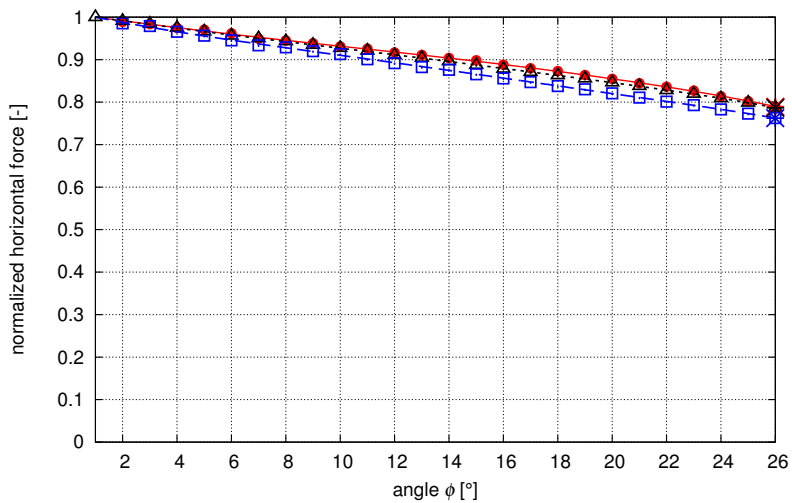


Figure 5.4: Velocity contour plots of the C1 current simulations.





(a) Objective

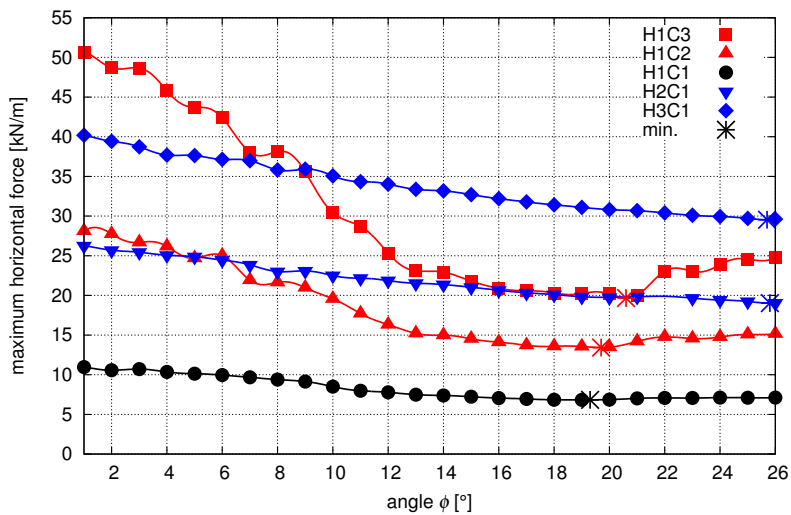


(b) Normalized objective

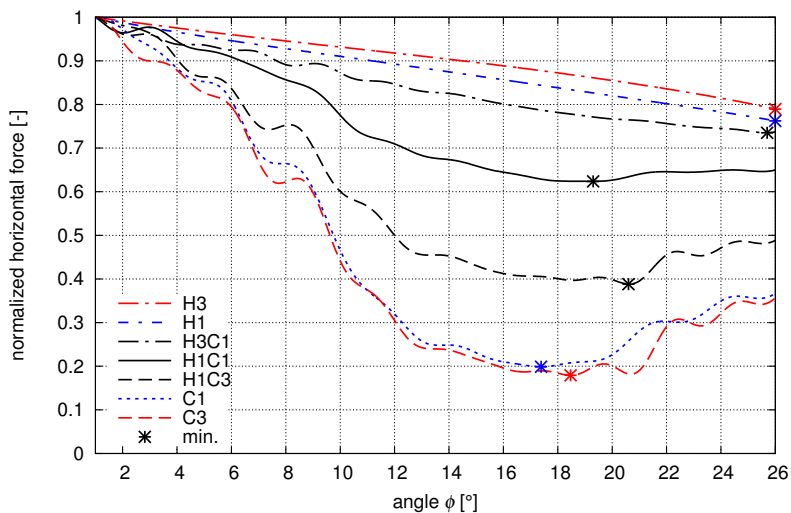
Figure 5.5: Wave horizontal force optimization results. Markers indicate CFD results. Kriging approximations are shown with lines.

load cases given in Tab. 4.2 on page 85. The first set comprises of the H1 wave load case in combination with the three current load cases. Additionally, the load cases in a second set are defined using the current load case C1 in combination with the three wave load cases. All simulations are carried out under consideration of the interaction between the wave and the current. The results for the analyzed load cases are given in Fig. 5.6a. As can be seen, the general development of the forces as a function of  $\phi$  as well as the optimum highly depend on the contribution of the wave and current scenarios. This can be seen more clearly when normalizing the wave-current forces with respect to the maximum load computed for each case, as shown in Fig. 5.6b together with pure wave and pure current curves. For load cases in which the wave or current is dominant, the resulting WCI force curve resembles the individual force curve of the dominating field. For load case H3C1 this results in a normalized objective function approximation close to the pure wave solution while the force curve of load case H1C3 is closer to the pure current solution. When the contribution of the wave and the current is of similar magnitude (load case H1C1), an intermediate solution is attained. The shape optimum of the combined scenarios varies within a range between the optima computed for the individual load cases.

These observations are particularly important for design practice of offshore structures in waves and currents. The physical characteristic of forces resulting from drag dominated current loads and inertia dominated wave loads are fundamentally different. As shown, this may result in dissimilar individual optima for the current and wave load cases, while yet another optimum is attained for a combined scenario. Consequently, an optimal design for extreme wave-current loads cannot be derived from the individual scenarios, but requires the consideration of the WCI scenario.



(a) Objective



(b) Normalized objective

Figure 5.6: Wave-current horizontal force optimization results. Markers indicate CFD results. Kriging approximations are shown with lines.

### 5.3.2 Multiple Variables Optimization

The GBF optimization task is extended to a multidimensional DV problem in order to unveil further shape optimization potential of the structure. This is achieved by introducing  $n_d$  point coordinates along the leading and trailing edge of the geometry defined in Fig. 5.7a and Tab. 5.2. These point coordinates are equidistantly spaced in  $x'$  and are varied in  $y'$  through  $v_i$ . A general description of the geometry for an arbitrary DV number  $n_d$  is given in Tab. 5.2. In order to visualize the objective functions in a three-dimensional frame work, the investigation carried out in this section is limited to  $n_d = 2$ . Nevertheless, this allows for a wide spectrum of geometry variations, as for example shown in Fig. 5.7b. The step towards a multidimensional design problem significantly increases the number of CFD simulations required to attain a good approximation of the objective function. Consequently, the full optimization framework of Fig. 5.1 is utilized including the LOLA-Voronoi model refinement loop. The side constraints for the selection of the point set  $q_{i,j}$  during the initial Monte Carlo simulation and the subsequent LOLA-Voronoi point selection steps are set to  $q_j^u = h$  and  $q_j^l = h_p$ . Here,  $h_p$  is the height of the base plate on the lower section of the structure, which is set equal to 0.5 m in this example. For the sake of comparison, all other geometry constants are defined analogue to the specifications of Section 5.3.1 ( $A = 24 \text{ m}^2$ ,  $h = 3 \text{ m}$ ,  $b = 2 \text{ m}$ ).

After demonstrating in Section 5.3.1 that the shape optimum for the pure wave and pure current scenario is independent of the load case magnitude for the range of interest, the investigation in the two DVs study is limited to load cases C1 and H1. The optimization procedure leads to the objective function approximations shown in Figs. 5.8a and 5.9a. While the current Kriging model consists of various regions with high non-linearities and local minima, the response surface for the wave scenario is near-linear with a distinct optimum. These characteristics are also reflected in the optimization run point selection history shown in Figs. 5.8b and 5.9b. After an initial 40 sample point set is generated using the weighted Monte Carlo method, subsequent LOLA-Voronio refinement steps result in 15 new samples generated at each iteration. In the current load case investigation, there is a clear tendency towards favoring certain regions of the design space, as a result of varying weights resulting from the ranking of the LOLA component of the sampling technique. Conversely, the degree

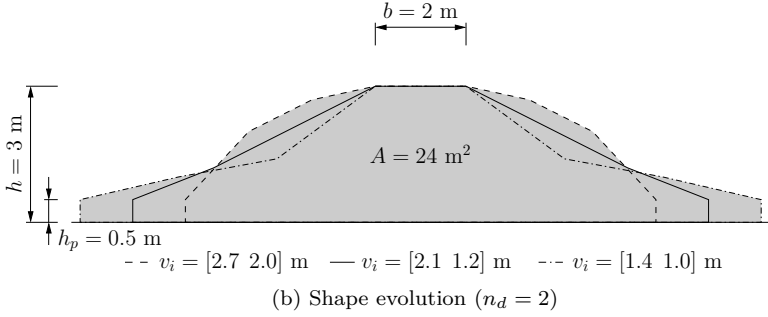
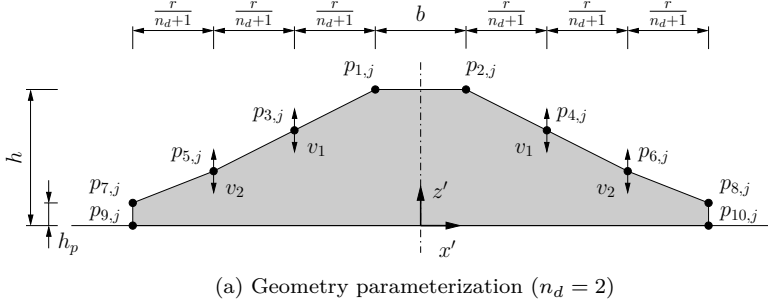
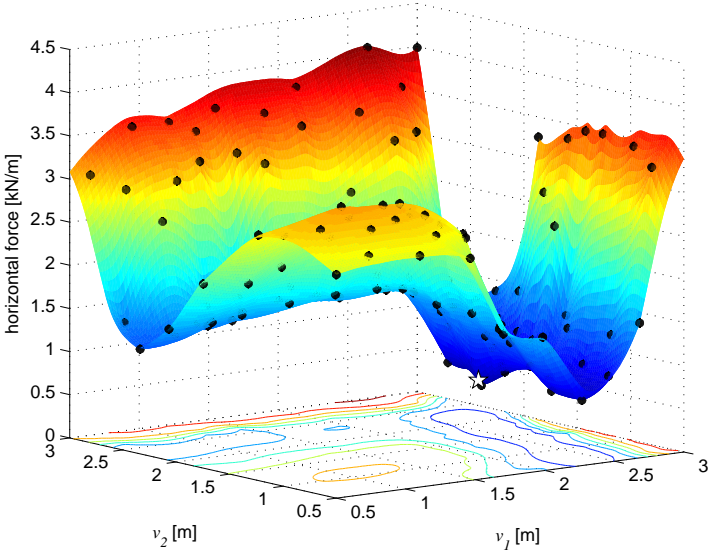


Figure 5.7: Geometry specification for the 2 DVs horizontal force study.

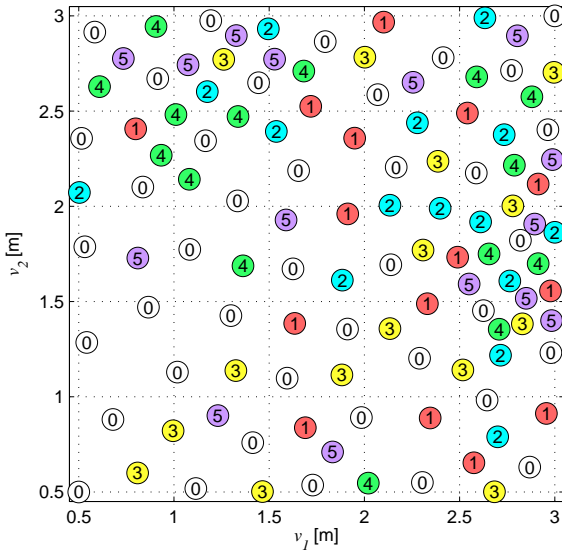
Table 5.2: Point coordinates

point	$x'$	point	$z'$
$p_{1,1} = -p_{2,1}$	$-\frac{b}{2}$	$p_{1,3} = p_{2,3}$	$h$
$p_{3,1} = -p_{4,1}$	$-\frac{b}{2} - \frac{1r}{n_d+1}$	$p_{3,3} = p_{4,3}$	$v_1$
$p_{5,1} = -p_{6,1}$	$-\frac{b}{2} - \frac{2r}{n_d+1}$	$p_{5,3} = p_{6,3}$	$v_2$
$\vdots$	$\vdots$	$\vdots$	$\vdots$
$p_{2n_d+1,1} = -p_{2n_d+2,1}$	$-\frac{b}{2} - \frac{n_d r}{n_d+1}$	$p_{2n_d+1,3} = -p_{2n_d+2,3}$	$v_{n_d}$
$p_{2n_d+3,1} = -p_{2n_d+4,1}$	$-\frac{b}{2} - r$	$p_{2n_d+3,3} = -p_{2n_d+4,3}$	$h_p$
$p_{2n_d+5,1} = -p_{2n_d+6,1}$	$-\frac{b}{2} - r$	$p_{2n_d+5,3} = -p_{2n_d+6,3}$	$0$

$$r = (n_d + 1)(A - bh)(h + h_p + 2 \sum_{i=1}^{n_d} v_i)^{-1}$$

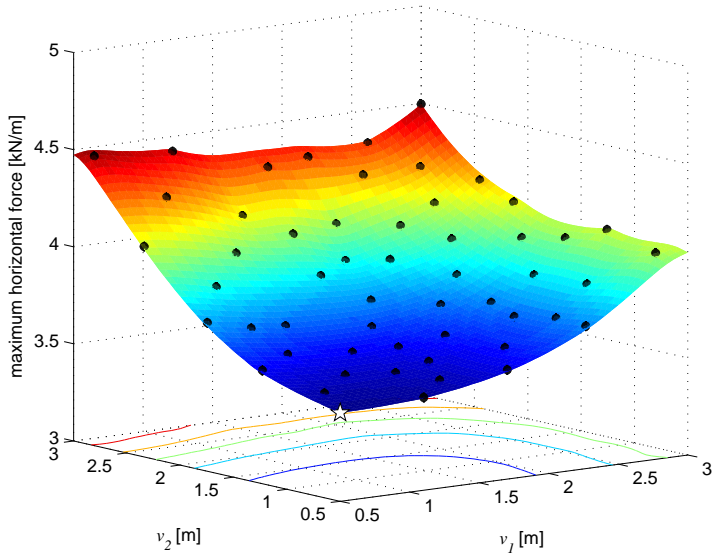


(a) Objective: Dots indicate CFD results, star marks global optimum.

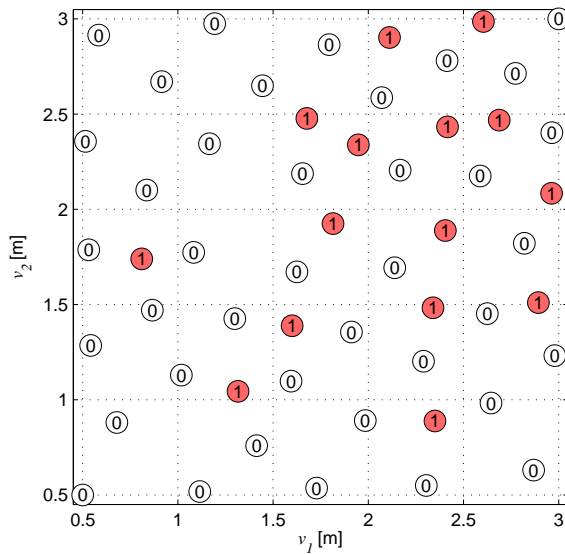


(b) Point selection history: Circled numbers indicate model iterations.

Figure 5.8: Current load case horizontal force optimization with 2 DVs.



(a) Objective: Dots indicate CFD results, star marks global optimum.



(b) Point selection history: Circled numbers indicate model iterations.

Figure 5.9: Wave load case horizontal force optimization with 2 DVs.

of non-linearity varies significantly less for the wave load case. As a result, the space filling characteristic of the Voronoi component is predominant, with a more evenly distributed point selection at each iteration. In addition, the shape of the wave objective function can be approximated using significantly fewer refinement steps. A single iteration was sufficient to reduce the NRMSD of the wave load case model to below 2%, while in the case of the current load case, the convergence criterion was not met until the fifth iteration.

The optimal shapes for current and wave loading are shown in Fig. 5.10, with the corresponding maximum pressure distributions. Again, significantly different characteristic shapes are attained. While the current optimum tends towards an ellipsoid shape, the structure most suitable for reduced wave loading once again consists of the largest near sea floor area distribution permitted by the constraints. One final conclusion is drawn from the DV investigation with regards to design practice of the structure. The chosen constraints permit shape variations for which  $v_2 > v_1$ , resulting in a peak at the outer top sections of the structure. Somewhat surprisingly, relatively low objective values are attained in parts of this particular design space region for the current load case, particularly around  $v_2 = 2.3$  m. However, the global optimum for both the wave and current load case are within the reduced design space for which  $v_i \geq v_{i+1}$ . This characteristic is taken advantage of in the elaborate three-dimensional foundation design of Chapter 8.

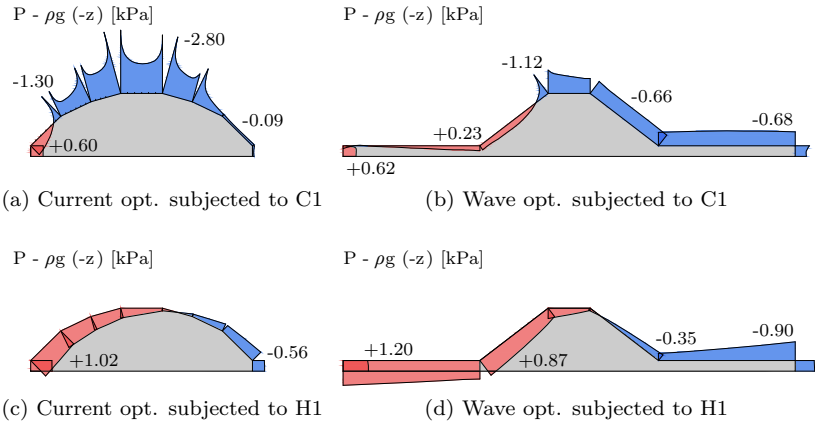


Figure 5.10: Pressure distributions for the 2 DVs horiz. force optima.



## 5.4 Vertical Force Analysis

In the development of offshore support structures, the horizontal force analyzed in the previous section is often a design determining factor. This is particularly true for piled structures, which are commonly used in the offshore wind sector. For current loads acting on these structures, fluid induced vertical forces can typically be neglected. However, when a bottom mounted bluff body is subjected to a flow field, considerable vertical forces develop. This phenomena is of particular relevance in the design of GBFs, which solely rely on the gravitational force to counteract the lift force.

For offshore foundation design, research on optimization with regards to lift has not been as extensive compared to other fields, such as aeronautics and the automotive industry. Here, the consideration of lift forces in optimal design is an ongoing subject of high interest. Recent publications focusing on this subject include works by [Moens and Wervaecke \(2013\)](#) as well as [Marklund \(2013\)](#). Two distinct concepts are followed in these publications: While the design of an airplane relies on secondary components (wings) to induce lift forces, the automotive sector targets the primary structure by taking advantage of the under-body flow of the car body to influence lift forces. The former approach was adapted to the design process of gravity base offshore structures by [Owen and Bryden \(2005\)](#) and more recently by [Harding and Bryden \(2012\)](#). These works propose the attachment of hydrofoils to tidal turbine support structures, to induce a downward force during current loading. When the direction of the tidal flow reverses, the hydrofoils rotate in order to function properly for both current directions. Alternatively, a stationary system is proposed in this section, which reduces lift forces by adopting the under-body flow concept to the design process of gravity base foundations.

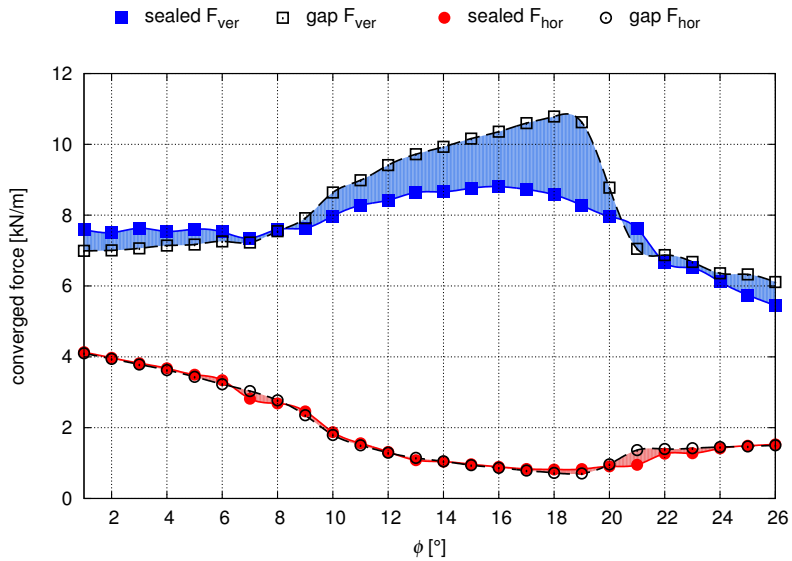
In a first step, a modeling strategy is introduced that considers the pressure field development on the bottom of the structure during loading. Following, the lift forces on the geometry of [Section 5.3.1](#) are analyzed. Based on the resulting findings, the structure is optimized with regards to lift by introducing a diffuser at the base of the structure. The diffuser is configured using both single variable and two variables optimization. In addition to the steady current considerations typically presented in the literature, this section also investigates the lift force performance of the structure with respect to wave and wave-current loading.

### 5.4.1 Foundation Base Modeling

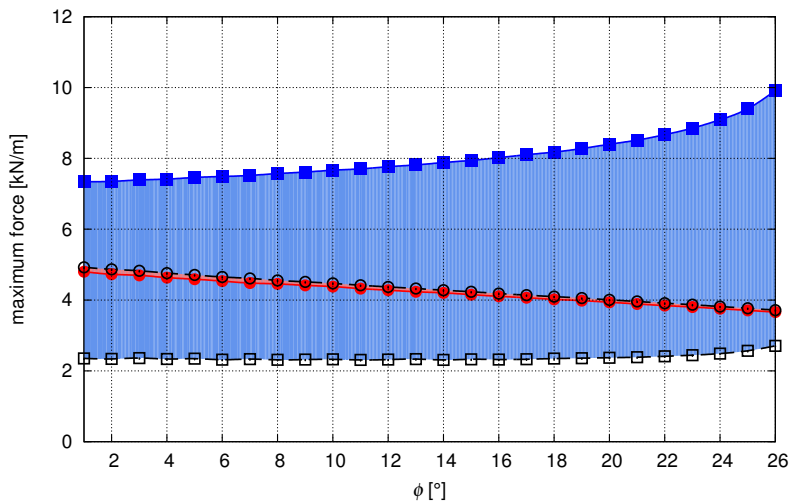
Typically, GBFs are freely placed on the sea floor or on a previously constructed base layer. In either case, a pressure field will arise between the bottom of the structure and the contact surface, a phenomena which is time dependent in the case of wave loading. The distribution and magnitude of this pressure field is highly dependent on the properties of the two contact surfaces. If both surfaces are idealized as perfectly smooth and impermeable (0% porosity), no water and hence no pressure will occur between the surfaces. The other extreme presents itself when gaps occur between the surfaces or the ground is extremely permeable, in which case the porosity is close to 100%. In offshore construction, an intermediate scenario between these two extreme cases will occur, although it is often not possible to accurately define the state of the contact surfaces or to foresee property changes during the lifespan of the structure. Consequently, both extremes are considered in this thesis.

The numerical modeling for the sealed condition is straight forward and simply attained by connecting the structure boundaries directly to the bottom boundary. However, the other extreme representing 100% permeability is less intuitive and requires some model assumptions. [Bishop \(1981\)](#) determined that a small continuous gap between the bottom mounted structure and the floor has a similar effect as a highly porous bottom. This approach was also employed by [Schmitz \(1987\)](#) in order to investigate the hydrodynamics of foundations both analytically and experimentally. This modeling techniques is incorporated into the CFD environment, through the introduction of FV cells on the bottom of the structure, which are connected to the outer flow domain. Various gap sizes were analyzed ranging from 10 mm to 50 mm, in accordance to the investigations carried out by [Schmitz \(1987\)](#). Analogue to that study, it was found that the ensuing forces for a number of different load cases are not particularly sensitive to the gap size, within the given range. Finally, a gap size of 10 mm was chosen for the numerical study, incorporating 4 cell layers between the foundation and the bottom boundary.

The foundation base modeling approach is applied to the structure defined in [Fig. 5.2](#), which was investigated in terms of the horizontal forces in [Section 5.3.1](#). For the sealed bottom condition, the forces are attained directly from the previous simulations. In addition, computations are carried out for the gap scenario, where  $\phi$  is once



(a) Current loading



(b) Wave loading

Figure 5.11: Force comparison of a sealed foundation base vs. a continuous gap on the foundation bottom.

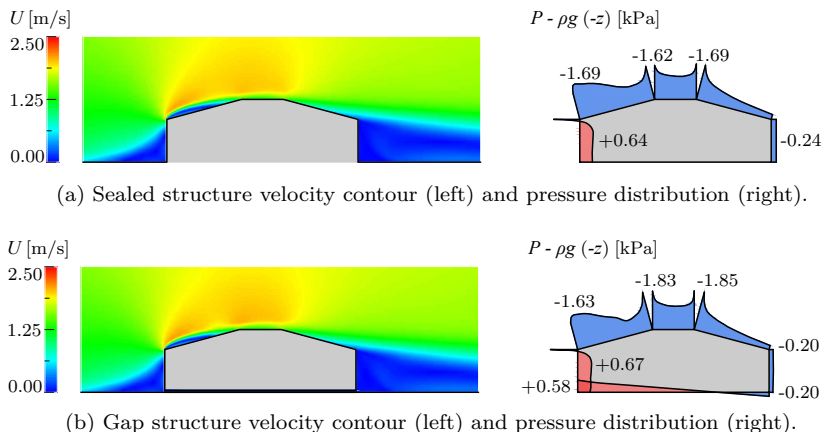


Figure 5.12: Current load case comparison of a sealed foundation base vs. a continuous gap on the foundation bottom for  $\phi = 15^\circ$ .

again varied from  $1^\circ$  to  $26^\circ$  in  $1^\circ$  increments. The resulting forces for current scenario C1 with a shape exponent of 0.11 at 45 m water depth are shown in Fig. 5.11a. It follows that the horizontal forces are largely unaffected by the gap on the bottom of the structure. On the contrary, certain geometric configuration induce significant deviations for the vertical loads acting on the structures. The source of this behavior is demonstrated by comparing Fig. 5.12a with Fig. 5.12b, which give the velocity contours and pressure distributions for  $\phi = 15^\circ$  of the current load case. The velocity field surrounding the sealed and gap structure and the ensuing dead water region are largely identical. Consequently, a similar pressure distribution on the top and sides of the structure can be observed. However, the gap induces a pressure balancing across the bottom of the structure, which is observed to be linear. Depending on the pressure boundary values of the leading and trailing opening of the gap, the net force acting on the body is directed upward or downward. In the special case, where the gap boundary values are equal in magnitude and opposite in sign, the net bottom force becomes zero. In this design study, this occurs for geometries with angles  $\phi = 8^\circ$  and  $\phi = 20.5^\circ$ .

Regardless of the structure shape or bottom configuration, the vertical forces are dominant compared to the horizontal force

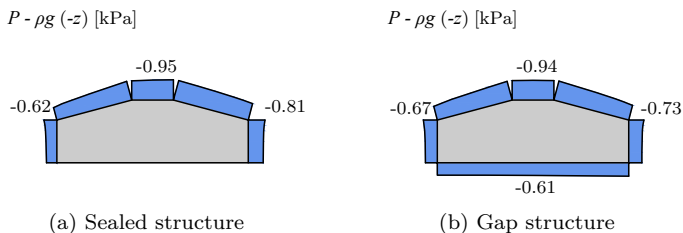
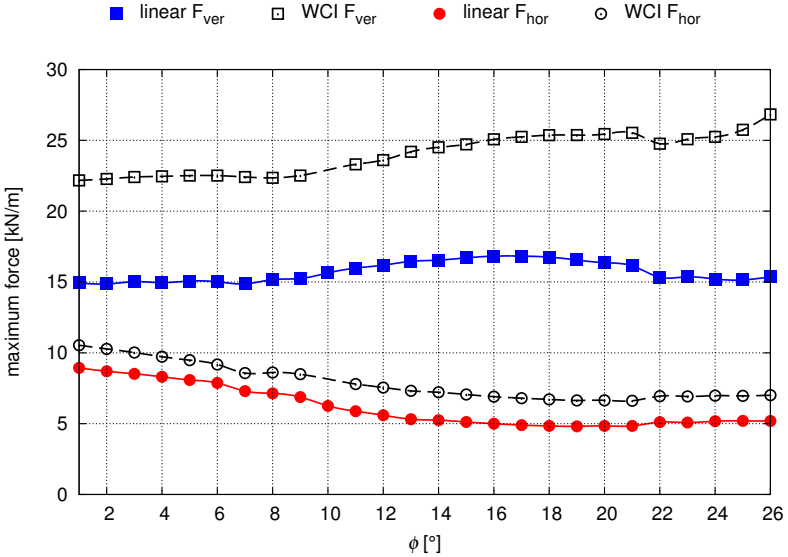


Figure 5.13: Maximum wave load pressure comparison of a sealed foundation base vs. a continuous gap on the bottom for  $\phi = 15^\circ$ .

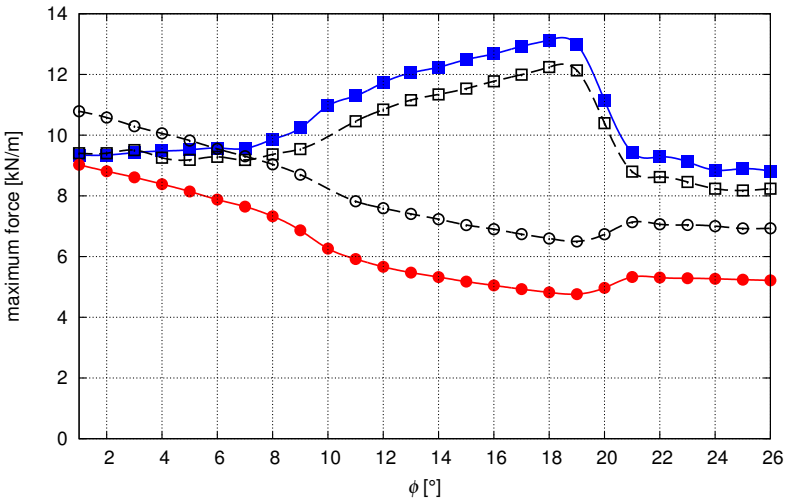
contribution, in the current load case. Furthermore, a striking observation can be made regarding the development of the load curves. The lowest horizontal loads occur for shape configurations that show the largest vertical forces on the structure. Such an opposing trend in the force distribution is particularly critical in optimal shape design, when aiming to reduce the total forces.

The force computations for the gap structures were repeated for wave load case H1 at  $d = 45$  m and compared to the sealed results. The maximum horizontal and vertical forces that occurred during the wave cycle are given in Fig. 5.11b. Once again, the horizontal forces are largely unaffected by the introduction of a gap beneath the structure. However, the difference in the maximum vertical forces is even more pronounced compared to the previously analyzed current load case. The significant load reduction for an open bottom structure computed in the CFD model is in agreement with experimental studies carried out by Chakrabarti and Naftzger (1976). The difference in vertical loading is again a result of pressure forces acting on the base of the structure when a gap is present, as demonstrated in the comparison of the pressure fields for  $\phi = 15^\circ$  given in Fig. 5.13a and Fig. 5.13b.

Finally, the effect of WCI is analyzed using the combined H1C1 load case applied to both the sealed bottom structure and the configuration with the small gap. The results for both configurations are plotted in Fig. 5.14. Once again, the vertical loads are significantly higher for the sealed scenario (Fig. 5.14a) than for the gap configuration (Fig. 5.14b). In addition, an entirely different load behavior is attained for the two structure configurations, when comparing the combined H1C1 WCI results to a linear superposition of the individually simulated wave and



(a) Sealed structure bottom



(b) Gap structure bottom

Figure 5.14: Force comparison of combined WCI load scenario H1C1 to a linear superposition of the results from load cases H1 and C1.

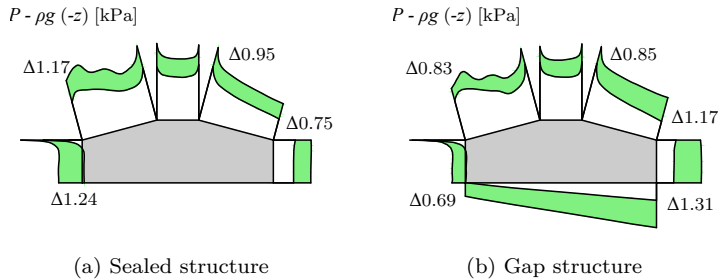


Figure 5.15: H1C1 WCI pressure distributions. Shaded green regions indicate difference  $\Delta$  to a linear superposition of H1 and C1 pressures.

current load cases. For the sealed configuration, the combined WCI simulation results in larger horizontal and vertical forces compared to a linear superposition, as a result of the change in fluid particle kinematics assessed in [Section 3.2](#). However, in the case of the gap structure bottom, the vertical forces are actually lower when considering WCI, compared to a linear superposition. This somewhat surprising behavior is a result of the previously analyzed depth varying change in fluid particle kinematics due to WCI ([Fig. 3.1](#) on [page 40](#)). Because the change is more pronounced in the lower regions of the water column, the change of the WCI pressure distribution is also larger on the bottom of the structure than on the top. This effect is visualized in [Fig. 5.15](#). The figure gives the combined wave-current pressure solution, with green regions indicating the difference  $\Delta$  to the linearly superimposed results. For the analyzed load case, the larger pressure change on the bottom of the structure has a favorable effect on the lift forces, compared to a linear wave and current force superposition.

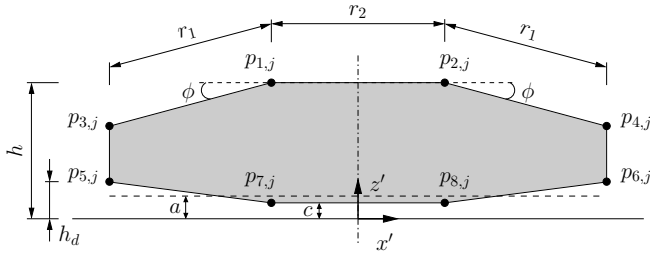
All analyzed offshore conditions showed large deviations in the vertical force solutions between the sealed and gap configuration. These deviations are particularly alarming for offshore engineering applications, if changes of conditions at the foundation base are expected to occur over the life span of the structures. Particularly when an initially porous contact surface between the structure and the sea floor is eventually sealed off due to sedimentary deposition or marine growth, a large vertical force increase occurs in all offshore environments.

### 5.4.2 Single Variable Optimization

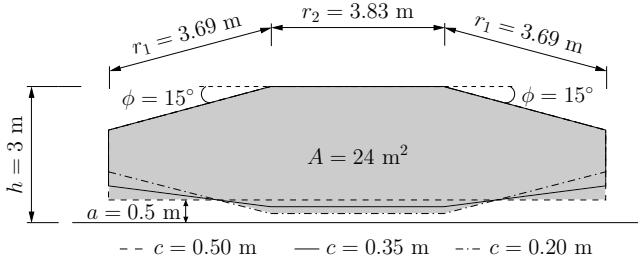
The presented vertical force shape evaluation study demonstrated a design situation for which opposing trends for horizontal and vertical forces during current loading occur. A number of options are available to handle such a behavior of the force functions when aiming to optimize the structure. One possibility is to define the total force as the objective function to be minimized, rather than an individual force component, thereby reducing the overall loading on the structure. Alternatively, a weighted approach is conceivable, for which individual weights are assigned to the force components, thereby allowing for a prioritization. However, the presented study also revealed a highly unbalanced ratio of relatively small horizontal forces to large vertical forces. This characteristic is unaffected by both the minimization of the overall loads as well as the weighted approach. Therefore, a different concept is pursued in this thesis. The idea is to configure the top shape of the structure such that it is particularly suitable in terms of the horizontal forces, and to control the vertical loading by introducing a flow diffuser at the bottom of the structure. The principle of operation for a diffuser is to accelerate the flow on the bottom of the structure, thereby creating a low pressure area and a down-force that counteracts the up-forces induced by the flow on the top of the structure. This flow acceleration is typically achieved by gradually altering the cross-section in the diffuser section.

The introduction of a diffuser to a gravity base foundation gives rise to a number of additional geometric parameters. The adjusted diffuser parametrization is given in [Fig. 5.16a](#) and [Tab. 5.3](#). The diffuser flow rate is adjusted using the average flow height  $a$  and central diffuser height  $c$ . The geometric variable used to enforce the area constraint for the selected angle  $\phi$  is referred to as  $r_1$  in this section. In addition, a second variable  $r_2$  is introduced. This variable defines an adjustable central base width, which increases the central section area by the amount that is lost in the diffuser region. The idea of introducing this second variable is to ensure that the selected inclination angle  $\phi$  remains unaltered as different diffuser configurations are analyzed. The parameter  $h_d$  represents the diffuser inlet and outlet height and is defined as a function of the other parameters, while  $b$  is the minimum central base width when  $a = 0$  m. For the diffuser optimization study, the inclination angle  $\phi$  is kept constant at  $15^\circ$ . Once again the total height, minimum central base width, and area of the structure are





(a) Geometry parameterization



(b) Shape evolution ( $a = 0.5$ )

Figure 5.16: Geometry specifications for the vertical force study.

Table 5.3: Point coordinates

point	$x'$	point	$z'$
$p_{1,1} = -p_{2,1}$	$-\frac{1}{2}r_2$	$p_{1,3} = p_{2,3}$	$h$
$p_{3,1} = -p_{4,1}$	$-\frac{1}{2}r_2 - r_1 \cos \phi$	$p_{3,3} = p_{4,3}$	$h - r_1 \sin \phi$
$p_{5,1} = -p_{6,1}$	$-\frac{1}{2}r_2 - r_1 \cos \phi$	$p_{5,3} = p_{6,3}$	$h_d$
$p_{7,1} = -p_{8,1}$	$-\frac{1}{2}r_2$	$p_{7,3} = p_{8,3}$	$c$

$$r_1 = \frac{h \cos \phi - \sqrt{(h \cos \phi)^2 - (A - bh) \cos \phi \sin \phi}}{\cos \phi \sin \phi}$$

$$r_2 = b + \frac{2a}{h-a} \left( \frac{1}{2}b + r_1 \cos \phi \right)$$

$$h_d = \frac{a-c}{r_1 \cos \phi} \left( \frac{1}{2}r_2 + \sqrt{\frac{1}{4}r_2^2 + (r_1 \cos \phi)^2 + r_1 r_2 \cos \phi} \right) + a$$

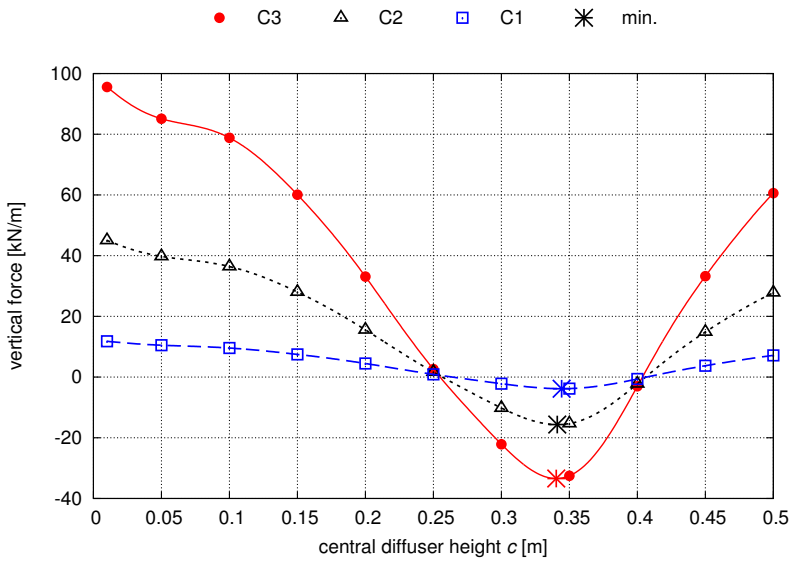
defined as 3 m, 2 m, and 24 m<sup>2</sup>, respectively. The resulting shape evolution for varying central diffuser heights  $c$  and constant central flow height  $a = 0.5$  m is given in Fig. 5.16b.

In a first step, the effect of the diffuser on the vertical loads is analyzed in a single DV optimization approach. The focus of this study is set on investigating various offshore conditions, including combined wave-current loading. The aim is to determine possible load case dependencies in the optimal design, before introducing further design variables. For this purpose,  $c$  is defined as the design variable of the optimization problem, while  $a$  is kept constant at 0.5 m. With  $\phi = 15^\circ$ , this results in a constant central base width  $r_2 = 3.83$  m and inclination length  $r_1 = 3.69$  m for all single DV configurations. The side constraints for  $c$  are set to  $q^u = a = 0.5$  m and  $q^l = 0.01$  m.

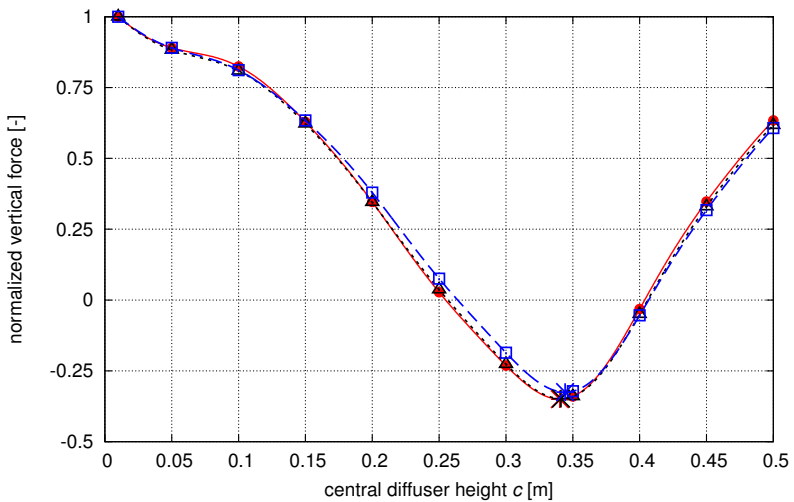
The consideration of a relatively small, one-dimensional design space allows for an initial point set resolution that is refined to the point that no additional refinement iterations in the optimization framework are necessary. Here,  $c$  is varied in 5 cm increments from the lower to the upper bound. The diffuser structure is subjected to the three current load cases defined in Tab. 4.2b on page 85. The water depth and velocity exponent are kept constant at 45 m and 0.11, respectively.

The CFD results for the analyzed point set and the resulting Kriging models for the lift force minimization objective are summarized in Fig. 5.17. The vertical loads on the structure decrease significantly as  $c$  is increased from 0.01 m to approximately 0.35 m. The force decrease is a result of the fluid velocity increase beneath the structure, as visualized for the computed optimum one DV diffuser subjected to current C1 in Fig. 5.18. Only a small dead water eddy forms in front of the diffuser inlet, allowing for a large discharge through the diffuser. Past the optimum, the entrance eddy increases and a larger portion of the flow is redirected over the structure, thus decreasing the efficiency of the diffuser. Overall, the diffuser has the potential of decreasing the lift forces on the structure during current loading to the extent that a vertical downward force is attained. This results in a significantly improved design compared to the previously analyzed structure without a diffuser, as shown in Fig. 5.20 for the  $\phi = 15^\circ$  structure.

For a better comparison of the diffuser performance for variations in the current velocity, the results of the three current load cases are transformed into a dimensionless form, by normalizing each load curve with respect to its maximum force (Fig. 5.17b). The figure reveals



(a) Objective



(b) Normalized objective

Figure 5.17: Current vertical force optimization results. Markers indicate CFD results. Kriging approximations are shown with lines.

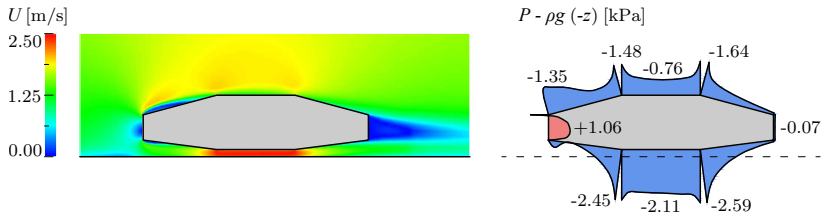


Figure 5.18: Current load case velocity contour (left) and pressure distribution (right) of the one DV optimal diffuser ( $c = 0.34$  m).

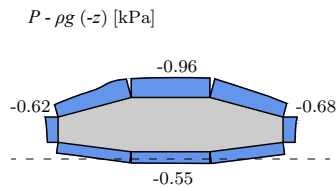


Figure 5.19: Wave pressure of the one DV optimal diffuser ( $c = 0.34$  m).

that the normalized objective function models collapse onto nearly the same curve. This implies that the performance of the diffuser and its optimal configuration are largely independent of the current velocity for the analyzed range.

In addition, the diffuser is investigated with respect to its performance during wave loading. Again, all three wave load cases defined in Tab. 4.2a on page 85 are considered. The results are summarized in Fig. 5.21. The vertical load curves attained for the various load cases are nearly horizontal, indicating that the wave loads are largely unaffected by variation in  $c$  when  $a$  is kept constant. For the analyzed wave load cases, the pressure profile distribution at the bottom of the structure is nearly constant, as shown in Fig. 5.19. In terms of the vertical wave force magnitudes, the diffuser structure ranks between the sealed and gap-base structures analyzed in the previous section (Fig. 5.20).

Finally, the diffuser structure is assessed when subjected to the WCI load condition H1C1. The results from the combined wave-current simulations are summarized in Fig. 5.22, together with a linear superposition of the individual H1 wave and C1 current solutions.

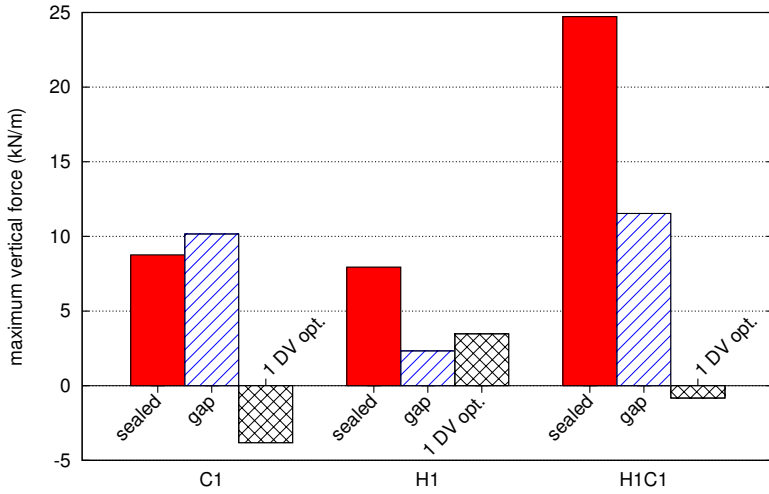


Figure 5.20: Vertical force comparison for the  $\phi = 15^\circ$  structure without diffuser and with the optimal one DV diffuser configuration.

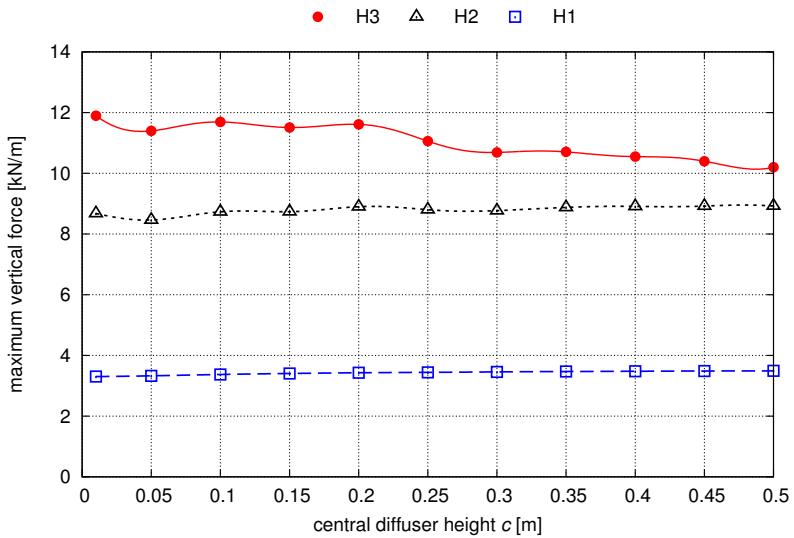


Figure 5.21: Wave vertical force objective function models. Markers indicate CFD results. Kriging approximations are shown with lines.

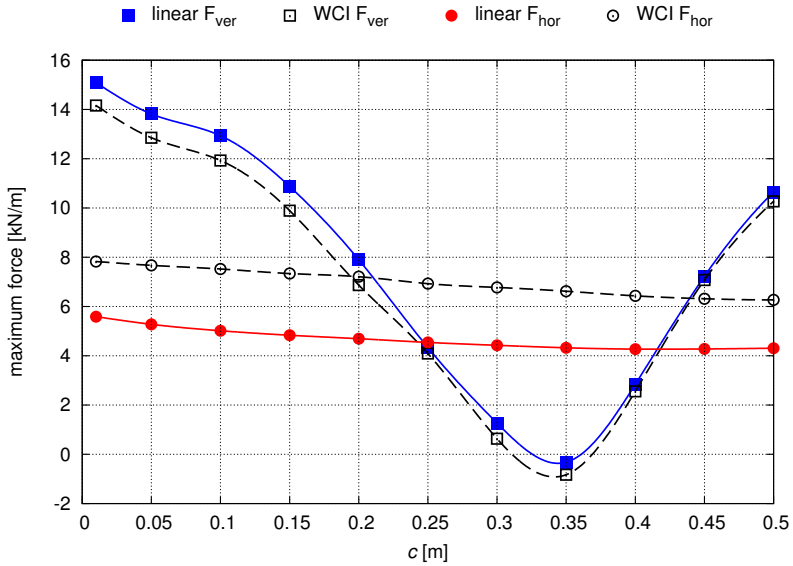


Figure 5.22: Diffuser force comparison of combined WCI scenario H1C1 to a linear superposition of results from load cases H1 and C1.

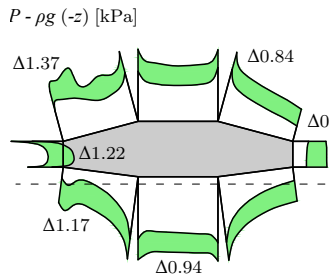


Figure 5.23: WCI pressure of the one DV optimal diffuser. Green regions indicate difference  $\Delta$  to a linear superposition of H1 and C1.

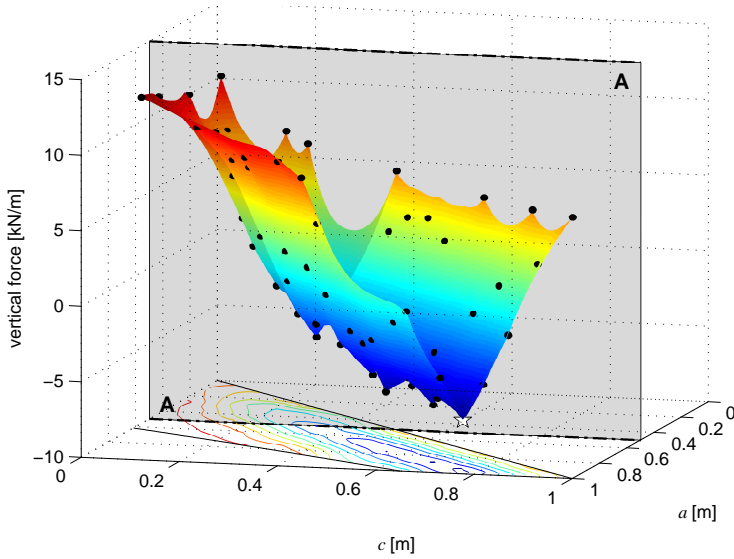
Much like the results attained for the gap structure in [Section 5.4.1](#), the diffuser lift force performance is better in combined wave-current conditions than a linear superposition of the individual scenarios would suggest. Again, this behavior is a result of a more pronounced near sea floor change in wave kinematics due to the current. As a result, a larger pressure change  $\Delta$  between the WCI solution and linearly superimposed results is attained on the bottom of the structure, compared to the top ([Fig. 5.23](#)). In the combined load case, the diffuser initiated downwards current force counteracts the wave lift forces. As a result, the overall WCI vertical loads are much reduced at the optimal one DV diffuser configuration, particularly in comparison to the sealed condition, as shown in [Fig. 5.20](#). For the analyzed load scenarios, the pure wave load case becomes the critical load condition in terms of the lift forces. This change comes along with an enormous reduction of the vertical forces compared to the structure without a diffuser, for which the wave-current scenario marks the critical lift force condition.

### 5.4.3 Multiple Variables Optimization

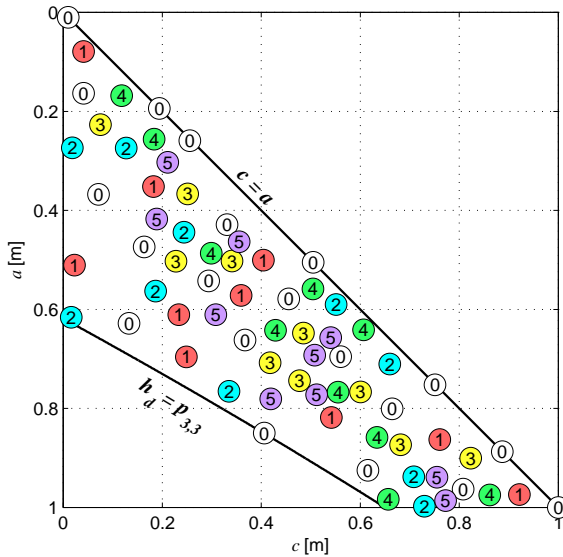
The diffuser optimization study is extended to a two DVs problem by additionally defining the mean flow height  $a$  as a design variable rather than a constant. This provides the possibility of increasing the efficiency of the diffuser beyond the optimum attained in the single DV study. The mean flow height side constraints are defined as  $0.01 \text{ m} \leq a \leq 1 \text{ m}$ . In addition, the design space is limited to regions where  $c \leq a$ , ensuring a smooth flow redirection beneath the structure, and to  $h_d \leq p_{3,3}$ , safeguarding the integrity of the structure. The resulting design space border lines are plotted in [Figs. 5.24](#) and [5.25](#).

The two DVs diffuser is analyzed for the H1 and C1 load cases defined in [Tab. 4.2](#) on [page 85](#). Because a relatively small design space is considered, the optimization framework is initiated using a point set  $q_{i,j}$  consisting of only 20 samples. Each LOLA-Voronoi refinement iteration adds an additional 10 points to the set. Overall, five refinement iterations were required to reduce the NRMSD of the highly non-linear current load case Kriging model to below 2%, while one iteration was sufficient in the case of the wave load case. The resulting models are plotted together with the according point selection history in [Figs. 5.24](#) and [5.25](#).

The quality of the two DVs Kriging models is assessed in [Fig. 5.26](#) by comparing the results with the previously computed high resolution



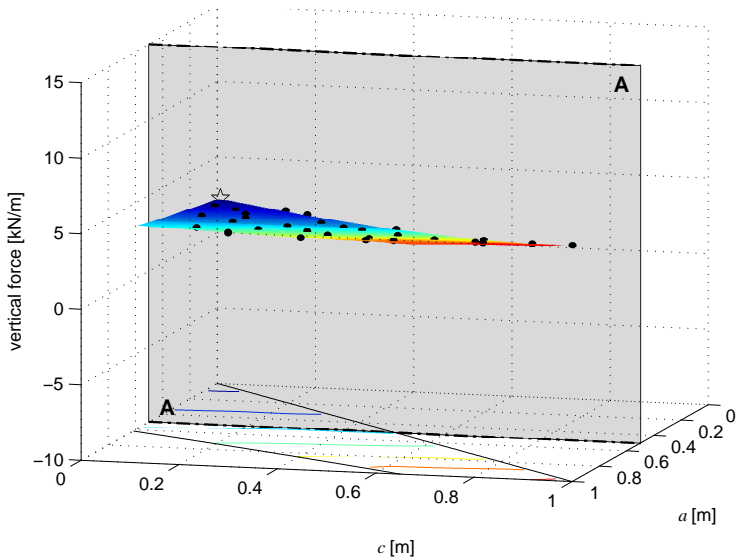
(a) Objective: Dots indicate CFD results, star marks global optimum.



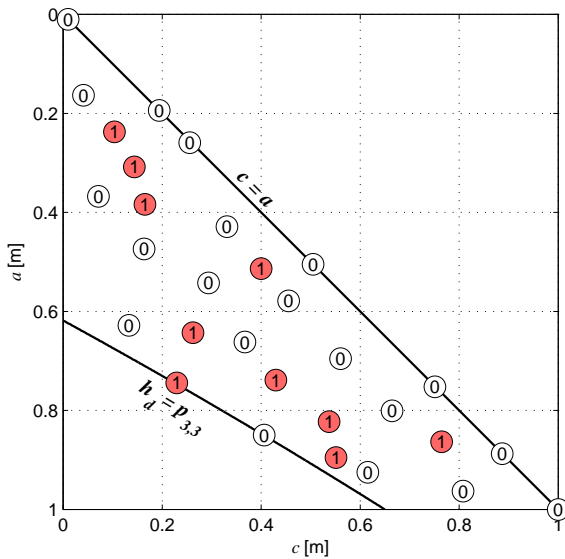
(b) Point selection history: Circled numbers indicate model iterations.

Figure 5.24: Current load case vertical force optimization with 2 DVs.





(a) Objective: Dots indicate CFD results, star marks global optimum.



(b) Point selection history: Circled numbers indicate model iterations.

Figure 5.25: Wave load case vertical force optimization with 2 DVs.

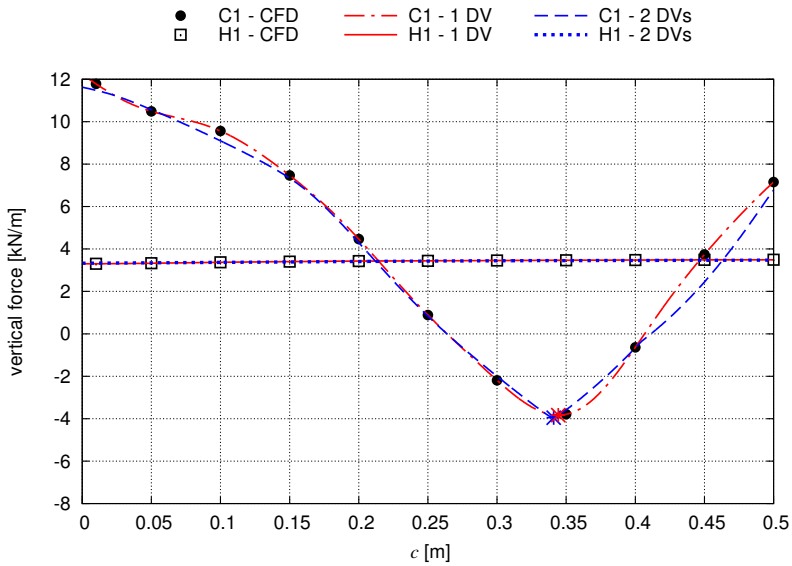


Figure 5.26: Cut A-A through the two DVs Kriging model at  $a = 0.5$  m.

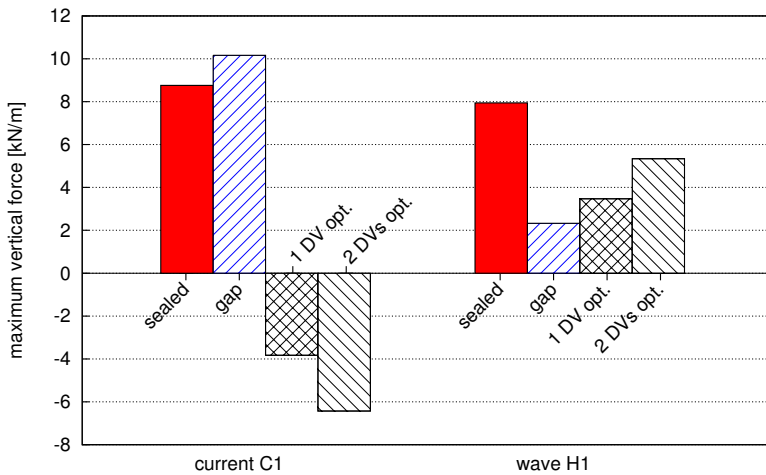


Figure 5.27: Vertical force comparison for the  $\phi = 15^\circ$  structure without diffuser and with the optimal one and two DVs diffuser configurations.

one DV Kriging models and the corresponding CFD objective values. For this purpose, the two DV models are cut along the plane A-A for which  $a = 0.5$  m, as shown in Figs. 5.24a and 5.25a. A very good agreement is achieved for the wave load case, due to the nearly planar objective function that can be modeled accurately with relatively few sample points. For the current load case, the models agree well in the region of the local minimum, as a result of the additional sample point selection in that region. Further away from the minimum, where less sample points are used in the two DVs model, a slight divergence from the more refined one DV model is noticeable. The global minimum for the current load case is reached when the mean flow height is close to its maximum value ( $a = 0.98$  m). At this point, the fluid discharge through the diffuser is maximum.

Due to the defined geometric dependencies, an increase in  $a$  results in a simultaneous increase in  $r_2$ , and therefore a broadening of the structure. This elongation of the central diffuser section is disadvantageous with respect to the inertia wave loading, because it results in a larger area distribution in the top region of the structure. Overall, the two DV study thus results in a structure that is further optimized with regards to the current loading, at the cost of larger wave loads compared to the optimal one DV diffuser (Fig. 5.27). Therefore, the choice of an efficient diffuser in the design process of a GBF depends on the contribution of the wave and current loads at the specific site. The presented procedure is an example of how CFD modeling, as part of the introduced optimization framework, can aid the designer in making this choice.

## 5.5 Conclusions and Summary

In this chapter, the VFS modeling technique was successfully applied as part of an extensive investigation of forces acting on offshore GBFs. The CFD based reduced modeling approach allowed for an analysis of a great variety of structures and boundary conditions. Overall, the presented data is the result of more than 900 simulations, efficiently carried out in an automated fashion using the LATOS software environment, taking into account 11 load cases and over 250 geometry variations.

By applying the introduced Kriging based optimization framework to the design of GBFs, it was possible to gain insight into previously unknown shape sensitivities to complex offshore conditions as well as

the physical aspects dictating the overall characteristics of the design space. A number of key conclusions regarding optimal shape design of GBFs are drawn from the systematic analysis carried out as part of this chapter. With regards to horizontal loading, these are summarized as follows:

- In current conditions, optimal shape design is dictated by the ensuing dead water zones engulfing the body. Reduced horizontal loads are attained for shapes with small separation zones. Alternatively, matching separation patterns on the leading and trailing edge of symmetric bodies also result in strongly reduced horizontal loads.
- In inertia dominated wave conditions, the loading on the structure is dictated by the cross-sectional area distribution throughout the water column. Favorable are structures with a maximum distribution in the near sea floor regions.
- As a result of the different physical characteristics of current and wave loads, the optimal design for each scenario may differ. Yet another solution is plausible for combined wave-current loading. Therefore, the optimal shape for an offshore GBF is strongly dependent on the marine environment expected at the site.
- Combined wave-current conditions should be analyzed as part of a single simulation incorporating the interaction between both flow fields. A linear superposition of separately computed wave and current loads may result in large deviations from the combined wave-current solution.
- The optimal shapes in waves and currents are independent of the magnitude of each load case, within the analyzed range of conditions. However, an optimal design for combined wave-current conditions strongly depends on the contribution and magnitude of each condition.

In addition to the horizontal load analysis, vertical forces on GBFs were analyzed. The following key conclusions are drawn from the investigation:

- Significant vertical loads on bottom mounted bluff bodies develop when subjected to a current. In extreme cases, these loads are up

to one order in magnitude higher than the computed horizontal loads.

- In terms of wave loading, the magnitude of the vertical loads highly depends on the characteristics of the body-ground contact surface and the possibility of the wave pressure field to propagate beneath the structure. A severe vertical load increase during wave loading should be expected if at any time during the device lifespan the bottom of the structure becomes sealed.

A targeted reduction of the lift forces was proposed and analyzed, by introducing an under-body flow through a diffuser on the bottom of GBFs. This concept is a robust alternative to reducing lift forces by mounting movable hydrofoils on the foundation top. The diffuser study findings can be summarized as follows:

- The diffuser can be configured such that the vertical loads are reduced to the extent that a net downward force on the structure is generated.
- This downwards current force also acts favorable in combined wave-current conditions. As a consequence, the pure wave load case may become the critical lift force scenario. It should be noted that this is not a general rule, but is dependent on the contributions of the wave and current loads. Therefore, a combined wave-current simulation should not be omitted.
- For wave loading the structure should ideally be configured with a maximum amount of the volume located near the ground, while allowing the wave pressure to develop freely beneath the structure.
- For the analyzed load combination it was found that WCI has a favorable influence on the vertical loading of the diffuser structure, compared to a linear superposition of wave and current loads.

It was demonstrated how the proposed global optimization framework can be utilized in order to explore the design space and determine an optimal structure configuration for the desired objective. The possibility of unveiling further optimization potentials by considering multiple design variables was exploited. For current load cases, the complexity of the design space requires significantly more CFD simulations in order to attain a good Kriging approximation than

is necessary to attain an equally good wave load case Kriging model. The latter model is typically quite smooth and lacking large gradient changes or inflection points, allowing for a good approximation of the design space using relatively few sample points.

Overall, the optimization procedure led to a systematic improvement of the structure. The findings and knowledge gained in this chapter are directly used as a basis for the elaborate, three-dimensional optimal shape design of a new generation of tidal turbine GBFs in [Chapter 8](#). In order to confirm the validity of the methods used to attain the design proposal, and the legitimacy of the general conclusions drawn from this chapter, an extensive experimental validation study is presented in the following chapters.

---

## Chapter 6

# Experimental Wave-Current Modeling

---

### 6.1 Introduction and Overview

The numerical simulations carried out as part of this thesis are validated and complimented through experimental modeling of bottom mounted structures in waves and currents. In order to carry out these experimental studies, a new experimental wave-current modeling approach was developed, which is described in this chapter. The experimental studies as well as the evaluation and documentation of the results were carried out in cooperation with Morten Møller Jakobsen from Aalborg University (Denmark).

A number of experimental setups have been developed in order to model waves in combination with a current. In the design of a structure or device subjected to wave-current conditions, one approach is to utilize a wave towing tank. Previous experimental studies following this concept have for example been carried out by [Barltrop et al. \(2007\)](#), [Galloway et al. \(2010\)](#), as well as [Faudot and Dahlhaug \(2012\)](#). These experiments aimed at modeling tidal turbine behavior in wave-current conditions. Towing tank experiments do not require the generation of a current as part of the experimental setup. However, as discussed by

Myers and Galloway (2011), the free stream turbulence levels from the current are zero when carrying out a towing tank experiment, because the water in the free stream is only subjected to the wave motion. Furthermore, the boundary layer of the current is not represented in this approach, which is particularly problematic in the case of bottom mounted structures. Therefore, the physical characteristics of the flow are only partially considered in towing tank experiments.

The alternative is to utilize a recirculating water channel in combination with a wave maker. This approach was followed by de Jesus Henriques et al. (2013). In the suggested setup, the water is directed through a flow straightener at the inlet of the channel. Prior to entering the working section, the water flow passes under a hinged wave paddle located on the water surface. Using an electrical motor, the paddle generates waves by oscillating vertically. The resulting wave-current field generated with this setup agrees well with theoretical reference solutions, motivating a number of tidal turbines studies that were carried out on its basis. One significant trade-off with this type of wave-current flume is the reduced capability of wave generation, which limits the usability within coastal engineering.

This is likely part of the reason why a majority of flumes still consist of a vertical wave paddle with the current typically entering the channel in front of the paddle, or below the paddle. Under such conditions, the current will have a strong circulatory motion in the inlet region, particularly when the inlet pipe is oriented vertically. As assessed by Nowell and Jumars (1987), these circulations propagate through the flume for about 20 times the inlet diameter. This distance is usually beyond the test section and thus the flow field will not consist of a simple boundary layer in the vicinity of testing.

Several approaches have been developed to unify and straighten flows in pure current flumes. At present, this is usually achieved by passing the flow through a wire mesh screen and a honeycomb (Kulkarni et al., 2011). Flow distribution control using screens is well established and was analyzed in detail by Laws and Livesey (1978), including calculations that can be used to predict the effects of the screen on the flow field. Although screens can be used effectively to either suppress or generate turbulence in the flow, their functionality in essence is limited to flows that are already well developed, as pointed out by Nowell and Jumars (1987). The dissipation of large-scale motion in a flume is achieved more effectively using honeycombs. Here, the flow is passed through an assembly of horizontal ducts in order to



break down large-scale motion. The characteristics of honeycombs and the optimal geometric dimensions to reduce turbulence in a flow were analyzed and documented by [Mikhailova et al. \(1994\)](#). [Scheiman and Brooks \(1981\)](#) analyzed both screens and honeycombs and concluded that a combination of the two setups is the most effective approach to reduce turbulence in a flow. This setup is specifically designed and optimized for pure current scenarios, while it is not intended to function in combination with waves. The closed chamber walls of a honeycomb serve to break down the vertical motion, which would also affect wave induced vertical velocities. This motivates the introduction of alternative experimental methods that are specifically geared towards wave-current scenarios.

In this chapter, a physical flow filter is introduced that serves the purpose of diffusing undesirable velocity fluctuations in the current flow, while simultaneously allowing for the passage of waves. The filter consists of net tubes that permit fluid motion in both horizontal and vertical direction. The setup consists of vertically placed tubes to diffuse large-scale turbulence from the current, as well as horizontally oriented sections that act as a flow straightener. A detailed description of the filter layout and experimental setup used to test the filter is given in the succeeding sections. Following, the results of an elaborate test series are documented, which describe the characteristics of different filter configurations in waves and currents. It is shown that the setup allows for the generation of stable and well formed wave-current conditions. The filtering technique is a low cost approach to enhancing recirculating wave-current flumes consisting of vertical wave paddles, allowing for laboratory testing of devices and sea floor conditions in wave-current environments.

Part of the work presented in this chapter has been published in Coastal Engineering ([Markus et al., 2015b](#)). It is presented here with explicit written consent from the publisher.

## 6.2 Wave-Current Filter

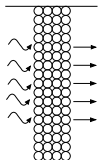
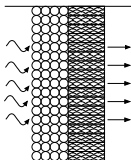
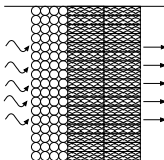
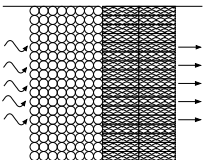
The basic concept of the filter setup is to diffuse turbulence in the flow field, while permitting a vertical flow through the setup. This is achieved by utilizing perforated net tubes. The flow is directed through an arrangement of vertical tubes that function similar to a flow screen. In this filter section, the water can move freely in the vertical direction.

In addition, horizontally oriented tubes can be added to the setup to act as a flow straightener. These function similar to a honeycomb, with the distinct difference that a flow through the tube walls in the vertical direction is possible.

Prefabricated tube blocks, typically used in drainage systems and waste-water treatment plants, allow for a simple and quick assembly of the filter setup. In this study, the BIO-BLOK<sup>®</sup> 80 HD G produced by EXPO-NET Danmark A/S was used. The tubes are made of polyethylene and are welded together to form square blocks of dimensions 0.54 m x 0.54 m x 0.55 m. The individual tubes have an inner diameter of 5.5 cm and the tube walls consist of a 0.2 cm thick mesh with a mesh size equal to 0.8 cm x 0.8 cm. This leads to a horizontal free flow area through the tubes equal to approximately 70 %, a vertical free flow area through the tube walls of approximately 40 %, and an overall void percentage of 95 %. The individual blocks are lightweight (approximately 60 kg/m<sup>3</sup>) and can be combined and cut easily to fit into the designated flume section.

For the experimental study, the filter blocks were cut in half and combined to span across the width of the flume. In the vertical direction, the blocks were stacked to a height of approximately 1 m. A total of four such segments were built: two segments, referred to as ‘h’, consisting of tubes pointing in flow direction (Fig. 6.1a), and two segments, referred to as ‘v’, with a vertical tube orientation (Fig. 6.1b). The four segments were combined to form different filter configurations (1v0h, 1v1h, 1v2h, and 2v2h), which were tested individually in order to determine an optimal setup configuration. The different arrangements are given in Tab. 6.1. An example of the installed filter for configuration 2v2h is shown in Fig. 6.2.

Table 6.1: Tested filter arrangements and corresponding filter widths.

1v0h	1v1h	1v2h	2v2h
			
27.5 cm	54.5 cm	81.5 cm	109.0 cm

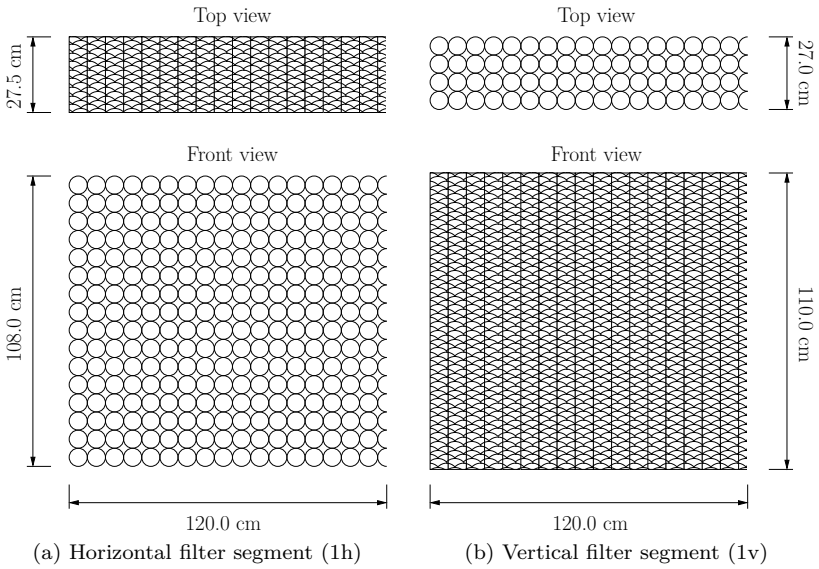


Figure 6.1: Dimensions of each horizontal and vertical filter segment.

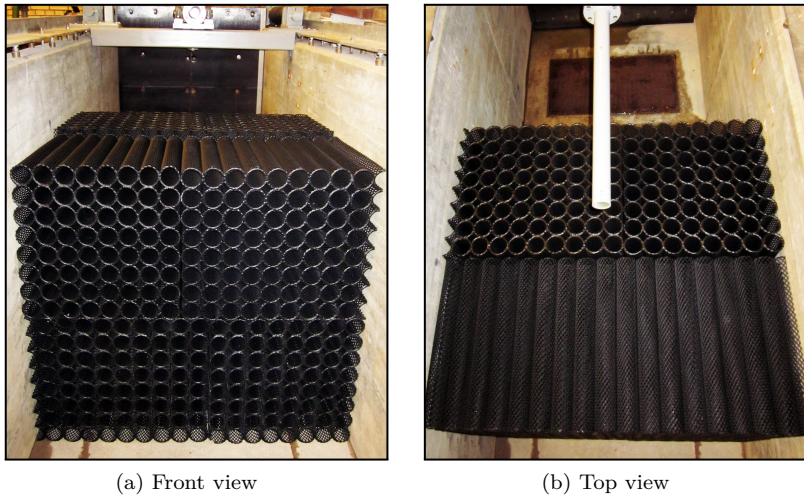


Figure 6.2: Flow filter setup 2v2h installed in the flume inlet region.

### 6.3 Experimental Filter Setup

A detailed analysis of the introduced filtering concept was carried out in the Aalborg University (Denmark) wave-current flume. The flume consists of a piston wave maker as well as a recirculating water pump that drives a current from the outlet to the inlet through pipes located below the flume floor. A layout of the flume is given in Fig. 6.3. The flume bottom is horizontal in the test section and slopes towards the wave paddle at an inclination angle of approximately  $3^\circ$ . In order to absorb the main part of the incident energy from waves at the outlet, an adjustable absorption beach was used, covered by porous absorption material. The water depth for all conducted tests was 0.35 m in the test section, corresponding to 0.70 m at the location of the wave paddle.

The overall aim of the study was to characterize the effects of the filter on the ensuing flow field. For this purpose, eight resistance type wave gauges were installed in the flume, in order to measure the surface elevation and carry out a reflection analysis. Four of these wave gauges were situated between the wave paddle and the flow filter, while the remaining four wave gauges were installed in the test section between the flow filter and the absorption beach. In addition, a Nortek Acoustic Doppler Velocimeter (ADV) was installed in the test section. The sampling volume is a cylinder of 6 mm diameter and 5 mm height, measured 5 cm below the sensor head. The device was pre-calibrated by the manufacturer and its overall functionality was confirmed by carrying out comparative velocity measurements with a propeller current meter. Because the ADV measures acoustic signals reflected by particles in the flow, a seeding material (Potters hollow microspheres) is added to the water. By adding this compound, a signal to noise ratio higher than 20 dB was ensured throughout the duration of the experiments. This ratio adheres to the manufacturer's suggested 15 dB minimum. Using the ADV, three-dimensional flow velocities were measured 0.15 m below the water surface at a sampling rate of 25 Hz. The ADV recordings were also used to compute the turbulence intensity in the test section, an approach analyzed thoroughly by García *et al.* (2005) and previously applied successfully in various experiments, such as those carried out by Hendriks *et al.* (2006) and Chamorro *et al.* (2013). Studies by Chanson *et al.* (2007) and Khorsandi *et al.* (2012) have shown that the data should be post-processed to remove unphysical noise, as discussed in the subsequent section. The precise wave gauge and ADV locations as well as the filter positioning in the flume are given in Figs. 6.3 and 6.4.

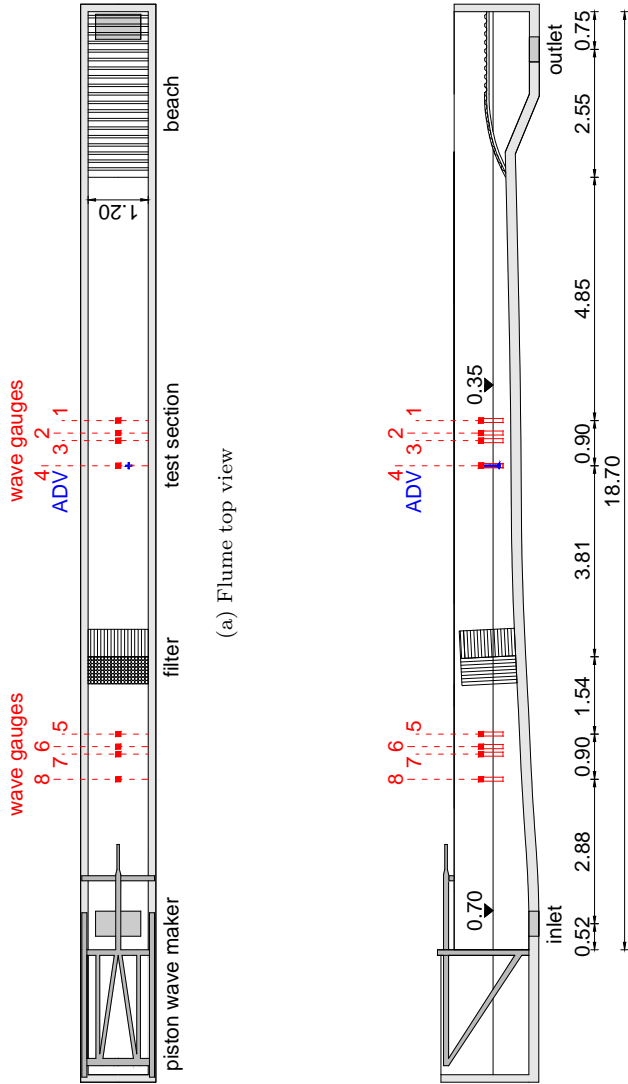


Figure 6.3: Test setup in the Aalborg University recirculating wave flume. Measurements are in meters.

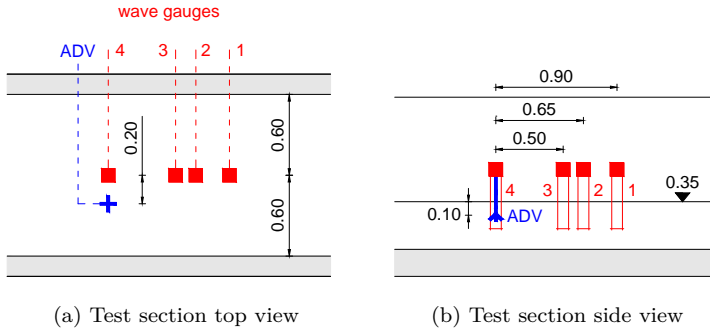


Figure 6.4: Test section detail of the recirculating wave flume. All measurements are in meters.

## 6.4 Filter Analysis

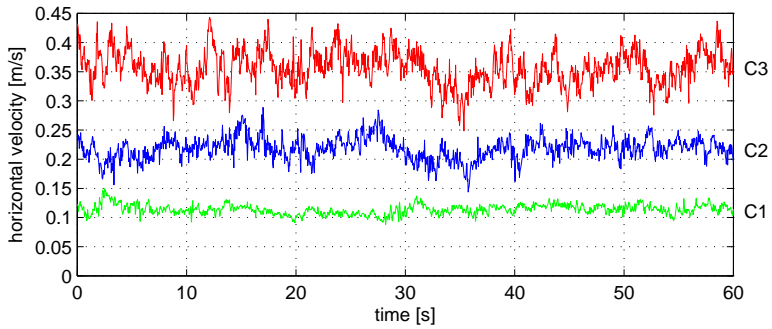
### 6.4.1 Current Scenario

In a first step, the effect of the flow filter on velocity fluctuations and turbulence intensity in a pure current scenario is demonstrated. Three current velocities are analyzed in a water depth of 0.35 m, as given in Tab. 6.2. The flow velocities for each current are measured over a period of 3 minutes using the ADV positioned in the test section. Examples of recorded test data for selected filter configurations are shown in Fig. 6.5.

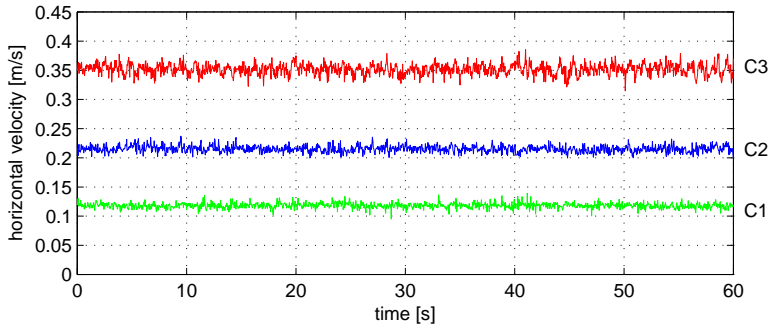
In order to evaluate the characteristics of each flow field, the mean velocities  $\bar{U}$  are compared to the velocity fluctuations  $U'$ . The latter is defined as the Root Mean Square (RMS) of the recorded velocity data. From these values, the turbulence intensity  $I$  can be computed based on the following definition:

$$I = \frac{U'}{\bar{U}} \quad (6.1)$$

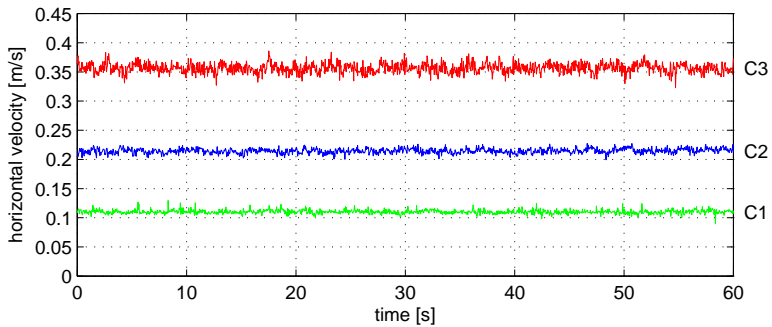
Although ADV velocity recordings are a popular approach to determine experimental flow conditions, the recorded data may contain spurious peaks due to Doppler signal aliasing or air bubbles, as assessed by Voulgaris and Trowbridge (1998). These unphysical spikes in the data set are recorded together with the physical turbulence components



(a) Unfiltered



(b) Filter 1v0h



(c) Filter 2v2h

Figure 6.5: Comparison of horizontal velocity time series before and after flow filter installation.

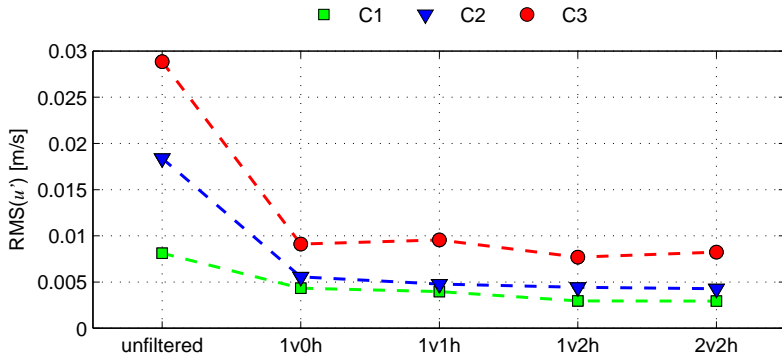
Table 6.2: Turbulence intensity for each configuration.

case	velocity [m/s]	unfilt. [%]	1v0h [%]	1v1h [%]	1v2h [%]	2v2h [%]
C1	0.11	7.1	3.7	3.4	2.8	2.7
C2	0.22	8.5	2.6	2.2	2.1	2.0
C3	0.36	8.1	2.6	2.7	2.1	2.3

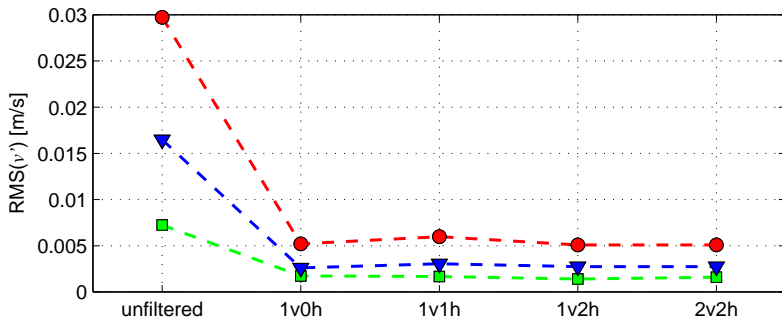
of the flow, thereby distorting the true flow characteristics. In order to avoid incorporating these unphysical components in the computation of the turbulence intensity, a despiking algorithm is applied to the data set to remove the ADV spike noise. Phase-space threshold despiking is applied, as introduced by [Goring and Nikora \(2002\)](#) and modified by [Wahl \(2003\)](#). The basic concept of the method is to take advantage of the characteristic of good ADV data to be tightly clustered within an ellipsoid in three-dimensional phase space, defined by the velocity recordings as well as approximations of their first and second derivatives. In an iterative procedure, those points outside of the ellipsoid are eliminated, thereby despiking the data set. As discussed by [Mori et al. \(2007\)](#), the approach is very efficient and has the advantage of not relying on empirical coefficients.

The horizontal and vertical RMS velocity fluctuations  $u'$  and  $v'$  from the despiked ADV data recorded in the test section are plotted in [Figs. 6.6a](#) and [6.6b](#), respectively. The Reynolds stresses, turbulence kinetic energy, and turbulence intensity are all defined as a function of these velocity fluctuations, giving a measure of the flow turbulence. Overall, the filter setups have a similar effect on both the horizontal and vertical fluctuations, resulting in a significant reduction compared to the unfiltered configuration. This reduction is further assessed based on the turbulence intensities plotted in [Fig. 6.6c](#) and documented in [Tab. 6.2](#). The relatively high intensities ranging from 7% to 9% in the case of the unfiltered flow, decrease dramatically even when only one filter section is positioned in the flume. Introducing additional filter sections further reduces the turbulence intensity, although the reduction is relatively small in comparison. In the case of higher flow velocities, all combinations of tested filters result in a turbulence intensity of 2% to 4%, which amounts to a reduction of approximately 70% when compared to the unfiltered result.

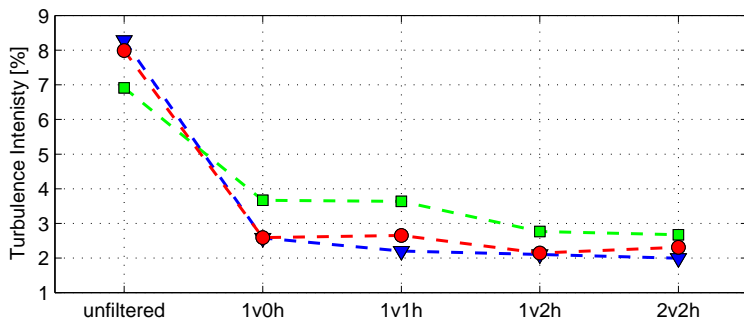




(a) Horizontal velocity fluctuations



(b) Vertical velocity fluctuations



(c) Turbulence Intensity

Figure 6.6: Current velocity field filtering effect for each configuration.

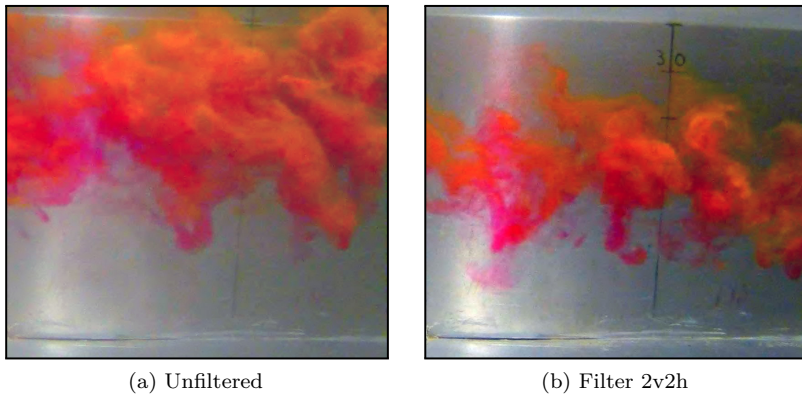


Figure 6.7: Visualization of the C1 flow fields using dye injection.

The findings are further supported by injecting red dye into the flume through a narrow tube and recording the flow with an underwater camera. Care was taken, that equal amounts of dye were injected into the test section for each recording. The resulting images for the unfiltered and filtered 2v2h setup are compared in Fig. 6.7 for the C1 current case at a distance of approximately 25 cm from the dye-inlet. The noticeable spread of the dye filament in Fig. 6.7a is evidently a result of high turbulence in the flow. By introducing the flow filter, the flow becomes significantly more steady, allowing for a visualization of smaller eddies due to a more concentrated dye propagation in Fig. 6.7b. Overall, the tests show that an introduction of the flow filter into the setup results in a significant decrease in turbulence intensity and a unification of the flow field.

### 6.4.2 Wave Scenario

The porosity of the flow filter allows for fluid motion in both horizontal and vertical direction. This characteristic of the device permits the penetration of waves through the filter and into the test section of the flume. As the wave passes through the filter, the wave field is influenced by the filter in the form of wave deflections as well as wave dissipation, resulting in a loss of wave energy. The degree of dissipation as well as its sensitivity to varying wave heights and wave periods is assessed in this section.

Data from a comprehensive parameter study is presented, incorporating 9 wave heights (ranging from 0.044 m to 0.171 m) and 3 wave periods (ranging from 1.00 s to 1.75 s) at a water depth of 0.35 m. The results for the various filter setups are summarized in Fig. 6.9. The given reference wave heights  $H_{ref}$  corresponds to the unfiltered, averaged wave heights measured in the test section.

Each curve given in Fig. 6.9 shows the relation between the measured wave height and the reference for all tested filters. As shown, the introduction of the first filter section results in a significant drop of the measured wave heights. As additional filter sections are introduced, the wave heights decreases further. The amount of wave damping for configuration 1v0h ranges from 20% to 35% while for the largest filter setup (2v2h) the damping range amounts to 40% to 70%. The degree of damping is both dependent on the wave height and wave period. This is demonstrated in Fig. 6.8, which gives damping curves for the different setups as a function of the wave period for a 0.10 m wave. The amount of wave damping is particularly pronounced at small wave periods and reduces steadily as the wave period is increased. This suggests that for the analyzed range of waves, the setup acts as a low pass filter, with a near linear damping ratio with respect to the wave period.

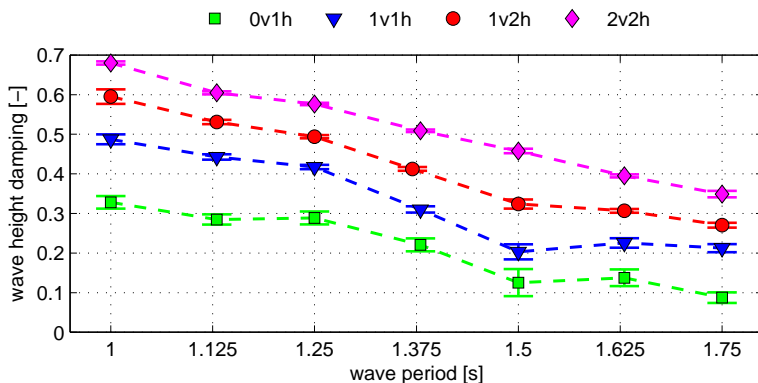


Figure 6.8: Amount of damping for  $H = 0.1$  m at various periods.

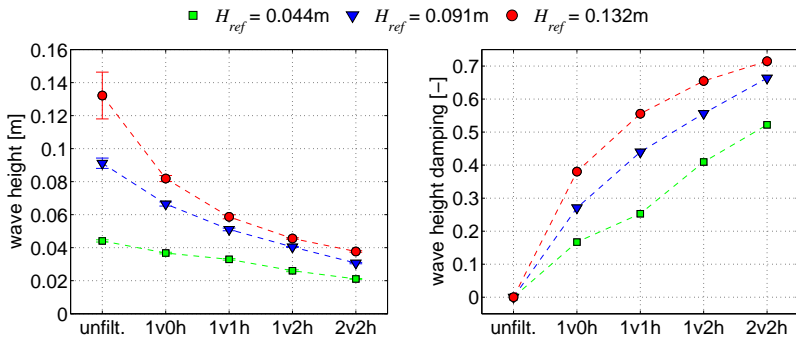
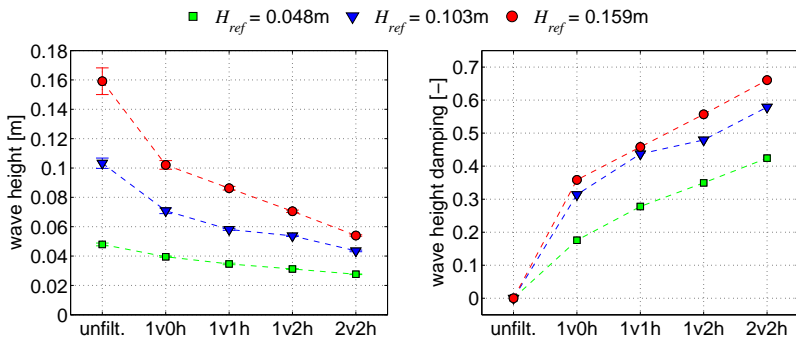
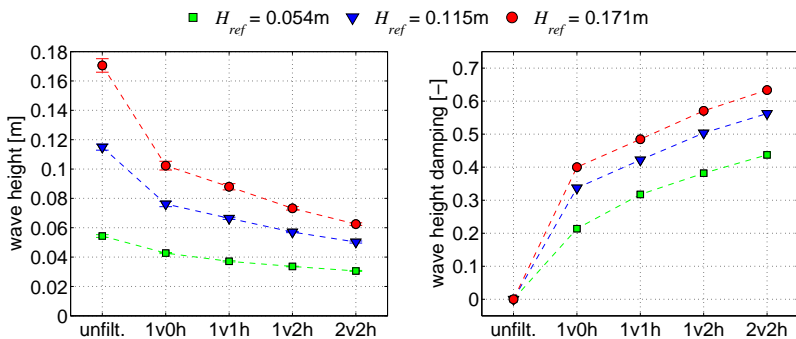
(a) Wave Period  $T = 1.00$  s(b) Wave Period  $T = 1.25$  s(c) Wave Period  $T = 1.50$  s

Figure 6.9: Wave height comparison at different wave periods.

Table 6.3: Coefficients for damping estimation.

filter	$a_D$ [-]	$b_D$ [-]	$c_D$ [-]	$d_D$ [-]
1v0h	7.33	-14.10	-3.23	4.88
1v1h	13.89	-49.24	-6.70	24.53
1v2h	18.67	-73.89	-9.20	37.99
2v2h	22.76	-102.40	-11.05	53.31

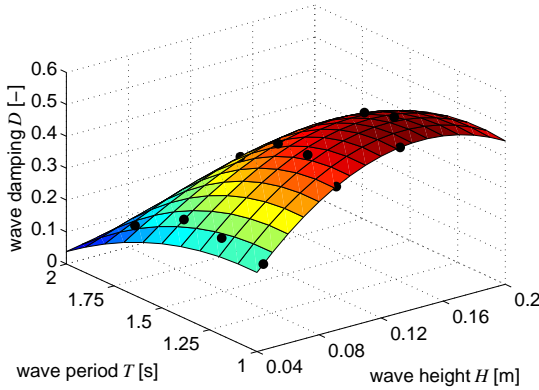


Figure 6.10: Polynomial fit for filter setup 1v1h.

Based on the collected data, a damping estimation equation in the form of a polynomial function was derived, as given in Eq. 6.2. The polynomial coefficients  $a_D \dots d_D$  for each filter setup are documented in Tab. 6.3. As an example, the fitted surface for filter set up 1v1h is shown in Fig. 6.10. Using the polynomial equation and the corresponding coefficients, the degree of damping  $D$  can be estimated.

$$D(H, T) = a_D HT + b_D H^2 T + c_D HT^2 + d_D H^2 T^2 \quad \forall \begin{cases} H \in [0.04, 0.2] \text{ m} \\ T \in [1.0, 2.0] \text{ s} \end{cases} \quad (6.2)$$

The source of damping of the wave field was further analyzed by Jakobsen in Markus et al. (2015b). For each modeled wave scenario, the reflection, absorption, and transmission coefficients were determined using wave gauges positioned both in front and behind the filter

(Fig. 6.3). It was found, that the wave energy loss is highly dominated by absorption within the filter, while the measured reflections are small in comparison, with a maximum reflection coefficient of approximately 0.2. The low reflective properties of the filter ensure that the incoming waves from the wave maker remain largely undisturbed. Therefore, the generation of a stable wave field is warranted even when carrying out long term testing.

In addition to analyzing the damping effect on the wave heights for each filter configuration, the wave profiles are verified after passage through the filters. In general, it was found that independent of the filter setup, the specified wave periods were preserved throughout all tests. Fig. 6.11 shows a comparison of waves with a large bandwidth of varying wave heights and wave periods for the largest filter setup. Each wave profile was derived by averaging the shape over three wave periods of the recorded wave-gauge data. The average shape of the wave is then compared to Dean's Stream Function theory (Dean, 1965) to determine if there are any significant bound components created by the filter. It becomes apparent that the shape of the waves very much resembles the expected distributions. Overall it can thus be concluded that when taking into account the damping effects of the filter, realistic wave conditions are retained using the filter.

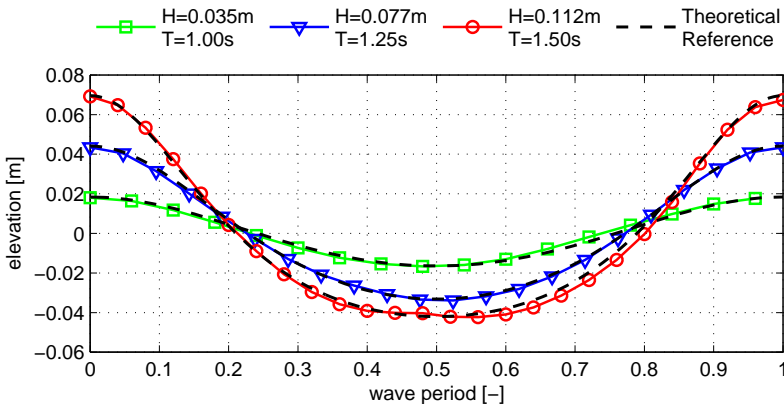


Figure 6.11: Measured and computed wave elevation over one period for various wave conditions passed through the 2v2h filter.

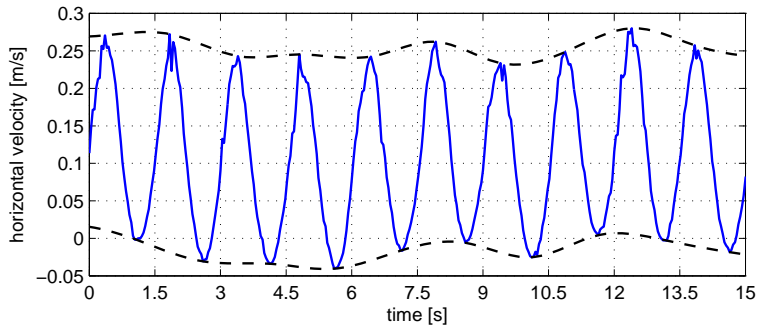
### 6.4.3 Wave-Current Scenario

After verifying the characteristics of the flow filter for pure wave and pure current flows in the previous sections, the two scenarios can be combined at will to generate stable wave-current flow conditions. To assess the quality of the ensuing flow field, ADV velocity recordings are analyzed in this section for the smallest (1v0h) and largest (2v2h) filter setup, and compared to the unfiltered results.

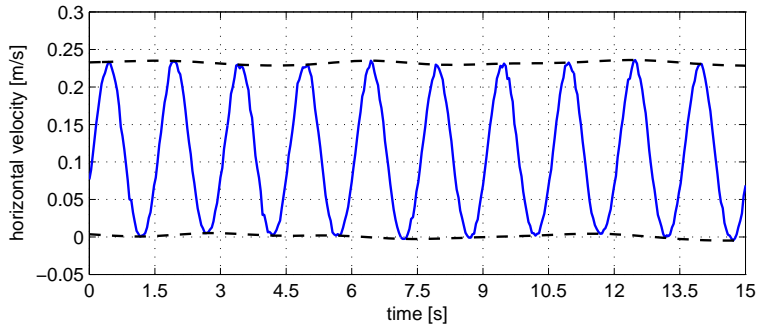
The scenario chosen for the comparison consists of a 0.055 m high wave of period 1.5 s in combination with a 0.11 m/s current. Fig. 6.12a shows the horizontal velocity field over a time span of 15 s for the unfiltered flow. As can be seen, the variation of wave peaks and troughs is relatively high, as a result of the fluctuations in the underlying current. For the given scenario, this results in a Relative Standard Deviation (RSD) of the wave heights equal to 12.6 %.

After installing one vertical filter section, the fluctuation of the current and the resulting variations in wave peaks and troughs are reduced significantly, as seen in Fig. 6.12b. For this setup, the wave height RSD reduces to 2.1 %. This value can be reduced further by installing further filter sections, as demonstrated in Fig. 6.12c. As expected, the difference in results for the two filter setups is relatively small, as a result of the similar current turbulence intensities documented in Fig. 6.6c.

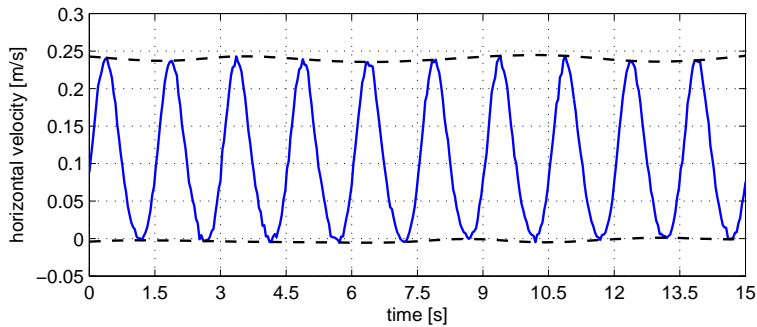
Overall, the recorded wave-current data shows the capability of the filter setup to reduce current-induced fluctuations and to render stable wave-current flow fields, thus allowing for a reliable experimental analysis of offshore structures subjected to such combined conditions.



(a) Unfiltered (wave height RSD = 12.6%)



(b) Filter 1v0h (wave height RSD = 2.1%)



(c) Filter 2v2h (wave height RSD = 1.9%)

Figure 6.12: ADV velocity recordings for a 0.055 m wave of period 1.5 s with a 0.11 m/s current measured 0.15 m below the mean water level.



## 6.5 Conclusions and Summary

This chapter addressed challenges frequently encountered when performing combined wave-current laboratory testing, in preparation for the experimental validation study documented in [Chapter 7](#). In particular, these challenges concern undesirable velocity fluctuations in current flows generated by a recirculating water pump, in combination with waves generated by a vertical paddle wave maker. The novel physical flow filtering approach introduced in this study handles this problem by dissipating turbulence in the flow field, while permitting the generated wave motion to pass through the filter setup. The key to this approach is the utilization of perforated tubes that allow for water passage in both the horizontal and vertical flow direction.

Various filter configurations were analyzed, with different arrangements of vertical and horizontal tube sections. The analysis involved elaborate testing in pure current, pure wave, and combined wave-current conditions. It was shown that even the smallest tested filter width (27.5 cm) results in a significant decrease of turbulence in the current flow, reducing fluctuations by approximately 70%. The incorporation of additional filter segments up to a total filter width of 109 cm allowed for a further reduction of the turbulence intensity. Overall, it was possible to reduce the turbulence in a pure current flow from approximately 8% in the unfiltered scenario down to 2% for the maximum filter width.

The properties of the filter with regards to its effect on wave flows were quantified in a series of dissipation tests. It was found that the largest tested filter setup results in a wave height damping ranging from 40% to 70% depending on wave height and period, when compared to the unfiltered scenario. The amount of dissipation is significantly lower for smaller filter configuration, amounting to approximately 15% to 20%. A reflection analysis of the wave field showed that the source of damping is mainly due to dissipation within the filter, while the wave reflections from the filter are relatively small in comparison. Consequently, only small alterations of the wave field between the wave paddle and the filter setup ensue. This characteristic of the filter accounts for the high quality of the measured wave profiles in the test section. Taking into account the damping effects of the filter, these profiles closely match computed theoretical reference solutions. Furthermore, the wave periods remain entirely unaltered by the filter setup. The overall amount of wave energy dissipation can be estimated

using a polynomial expression derived as a function of the wave height and period.

Finally, the effectiveness of the filter setup in combined wave-current flows was demonstrated. Current induced fluctuations are largely dissipated by the filter, allowing for the generation of stable wave-current flow conditions. Whereas disturbances in the unfiltered current field result in a relative wave height standard deviation of over 12%, the deviation in the filtered scenario reduce to below 2%.

The filter system can easily be adjusted to and installed in an existing flume setup using lightweight prefabricated net tube blocks. Therefore, the introduced flow filter is a highly efficient approach to enhancing recirculating wave-current flumes. Overall, the physical filter setup can be effectively applied to laboratory studies of offshore engineering applications involving combined wave-current flow conditions, as presented in the following chapter.

---

## Chapter 7

# Experimental Validation

---

### 7.1 Introduction and Overview

In this chapter, the experimental wave-current modeling approach of [Chapter 6](#) is applied as part of an elaborate experimental shape-optimization study. The study serves two purposes: First of all, the aim is to validate the numerical methods introduced in this thesis and to substantiate the predictions regarding the physical implications of wave and current flows subjected to offshore structures. Secondly, the presented research of this chapter serves as a new benchmark for related numerical and experimental studies.

For the purpose of testing new and established methods, a great variety of benchmark studies have previously been proposed and analyzed. Numerical and experimental results for a number of fundamental flow problems were documented by [Freitas \(1995\)](#). These include the two-dimensional flow over a backward-facing step and the three-dimensional flow in a shear-driven cubical cavity. Concerning flows around a structure, the cylinder is arguably the best documented reference problem, including studies at various flow conditions, orientations, and aspect ratios (e.g. [Roshko, 1961](#); [Dennis and Chang, 1970](#); [Nakamura and Ohya, 1984](#); [Graham, 1993](#); [Norberg, 1993](#); [Vengatesan et al., 2000](#); [Venugopal et al., 2009](#); [Bayraktar et al., 2012](#)).

For computational wind engineering applications, the Silsoe cube, a 6 m cube exposed to a physical wind field, has been studied vigorously both experimentally and numerically (e.g. Hölscher and Niemann, 1998; Richards et al., 2001; Haupt et al., 2011). For the purpose of code refinements and validation of aeroelastic problems, NASA carried out a program that established the NACA 0012 airfoil benchmark, which has been the subject of various experimental investigations (e.g. McCroskey, 1987; Seidell and Bennett, 1991) and numerical studies (e.g. Paparone and Tognaccini, 2003; Eleni et al., 2012). Fluid Structure Interaction codes are frequently verified based on the so-called “Turek benchmark”, consisting of an elastic object in an incompressible flow (Turek and Hron, 2006; Turek et al., 2010). For free surface methods, a dam-break flow (Ozmen-Cagatay and Kocaman, 2011), breaking wave impact (Guilcher et al., 2012) and sloshing in tanks (Liu and Lin, 2008) serve as popular validation problems.

The aforementioned studies serve as an example of the multitude of different benchmark tests that provide excellent information for validation and verification of different fluid related solution methods and modeling aspects. However, only few studies have been carried out that specifically target optimization problems, where the primary concern is to capture the differences between the individual optimization runs and to attain a precise optimal solution. Even fewer studies focus specifically on shape optimization in ocean engineering related topics, which typically involve not only steady current flows but also dynamic wave loading. Those studies concerned with ocean engineering related applications have mainly targeted the shape optimization of ship hulls (e.g. Percival et al., 2001; Campana et al., 2006; Tahara et al., 2011). As part of these studies, the results of the numerical optimization runs were validated by carrying out a few selected experimental reference tests. Although the approach was very successful, the complexity of the analyzed problems renders these studies not ideally suited as general benchmark problems for the validation of codes and methods. This pertains particularly to the complex three-dimensional hull geometries that require a significant discretization effort when utilizing mesh based numerical methods. Furthermore, the solution of the ensuing three-dimensional flow problem involves substantial computational costs. Complex optimization problems often also suffer from being highly non-convex, which may be problematic when testing certain optimization approaches.

This chapter addresses the need for a simple optimization benchmark

problem that can efficiently be applied as part of fluid related validation and verification studies. Specifically, it targets the analysis of force sensitivities of an object subjected to a steady current flow field, a dynamic wave flow field, as well as a combination of both load scenarios. The key to the study is to reduce the complexities of the geometries and flow fields to a bare minimum and to focus in detail on the optimization aspect of the problem. This is achieved by introducing a simple, bottom mounted, polygonal structure that is varied in one design variable only. Furthermore, the experimental validation tests are specifically designed to render a two-dimensional flow field around a total of 5 test geometries. This allows for highly efficient two-dimensional simulations and an analysis of multiple shape variations in a reasonable amount of time. The chapter provides not only an experimental reference solution, but also analyzes the validity of the NWCT as a powerful tool for shape optimization studies of structures. Both the experimental and numerical setup are described in detail in order to allow for and encourage future comparative validation and verification studies. A detailed description of the measured and simulated boundary conditions is given, including turbulence data for the considered flow conditions. Following, results for peak horizontal loads on the geometries as well as selected load time series are presented and analyzed. Objective function approximations are compared, showing the capabilities of numerical methods to predict changes in loading as a result of shape variations. Furthermore, data is provided to validate wave-current interaction studies. Finally, the study is extended to a consideration of three-dimensional flow scenarios, as a reference for computationally demanding three-dimensional validation studies. Overall, the presented work gives a comprehensive description of a reproducible benchmark problem for shape optimization, embracing a brought spectrum of different flow conditions, motivated by structural design requirements in ocean engineering.

The laboratory tests documented in this thesis were carried out in cooperation with Francesco Ferri from Aalborg University (Denmark). Part of the work presented in this chapter has been published in *Computers & Fluids* (Markus et al., 2015a). It is presented here with explicit written consent from the publisher.

## 7.2 Benchmark geometry specification

The body to be analyzed in the benchmark study is a bottom mounted, fully submerged structure that is varied in one design variable only. Much like the geometries analyzed in [Section 5.3.1](#), the benchmark geometry consists of a simple polygonal shape, parameterized as a function of the inclination angle  $\phi$  as the only DV ([Fig. 7.1a](#)). The geometry point coordinates are given in [Tab. 7.1](#). Once again, the parameter  $r$  serves as a geometric variable enforcing a constant structure area for all geometry variations. The analyzed geometry is subject to the following geometry specifications:

- cross sectional area  $A = 250 \text{ cm}^2$
- base width  $b = 5 \text{ cm}$
- structure height  $h = 10 \text{ cm}$
- gap size  $s = 0.5 \text{ cm}$
- inclination angle  $0^\circ \leq \phi \leq 26.57^\circ$

Based on these specifications, the shape evolution given in [Fig. 7.1b](#) ensues. The gap size  $s$  has practical implications, as part of the experimental setup described in [Section 7.3](#). The base section of height  $s$  below the body does not hold any significance concerning the loads exerted on the structure. Forces recorded in this study pertain solely to the geometry enclosed by points  $p_{1,j}$  through  $p_{6,j}$ .

The benchmark is specifically designed to allow for a validation based on two-dimensional simulations. This is made possible by restraining the flow to only pass above the geometries in the experimental study, as described in detail in [Section 7.3](#). For comparison, three-dimensional results are also included in this chapter ([Section 7.5.5](#)). For the three-dimensional cases, the width of the structures perpendicular to the  $x'-z'$  plane is equal to 20 cm.

As part of the numerical benchmark studies, the angle  $\phi$  of the parameterized geometries is varied from  $\phi = 0^\circ$  to  $\phi = 25.67^\circ$  in  $2^\circ$  increments. In addition, results for experimental reference studies are given for a total of five shape variations, as documented in [Tab. 7.2](#). Overall, the introduced geometric parameterization establishes a single DV optimization problem. The horizontal force acting on the structure is defined as the optimization problem objective to be minimized.

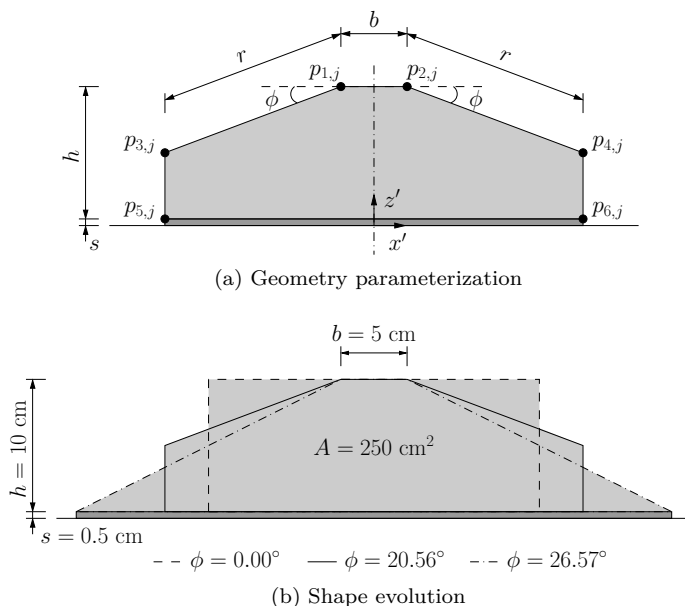


Figure 7.1: Benchmark geometry specifications.

Table 7.1: Benchmark point coordinates

point	$x'$ -coordinate	point	$z'$ -coordinate
$p_{1,1} = -p_{2,1}$	$-\frac{1}{2}b$	$p_{1,3} = p_{2,3}$	$s + h$
$p_{3,1} = -p_{4,1}$	$-\frac{1}{2}b - r \cos \phi$	$p_{3,3} = p_{4,3}$	$s + h - r \sin \phi$
$p_{5,1} = -p_{6,1}$	$-\frac{1}{2}b - r \cos \phi$	$p_{5,3} = p_{6,3}$	$s$

$$r(\phi = 0) = \frac{1}{2} \left( \frac{A}{h} - b \right)$$

$$r(\phi > 0) = \frac{h \cos \phi - \sqrt{(h \cos \phi)^2 - (A - bh) \cos \phi \sin \phi}}{\cos \phi \sin \phi}$$

Table 7.2: Discrete benchmark point coordinates

geometry	angle	$p_{1,1}$	$p_{1,3}$	$p_{3,1}$	$p_{3,3}$	$p_{5,1}$	$p_{5,3}$
ID	$\phi$ [°]	$-p_{2,1}$ [cm]	$p_{2,3}$ [cm]	$-p_{4,1}$ [cm]	$p_{4,3}$ [cm]	$-p_{6,1}$ [cm]	$p_{6,3}$ [cm]
1	0	-2.5	10.5	-12.5	10.5	-12.5	0.5
2	12.34	-2.5	10.5	-13.9	8.0	-13.9	0.5
3	20.56	-2.5	10.5	-15.8	5.5	-15.8	0.5
4	25.11	-2.5	10.5	-18.5	3.0	-18.5	0.5
5	26.57	-2.5	10.5	-22.5	0.5	-22.5	0.5

For the purpose of validating the methods, all simulations are carried out at model scale. However, the results also have some practical implications for full scale devices. Scaling of the results is however restricted to certain limitations. First of all, it should be noted that Froude number scaling is per se not particularly sensible for the scenarios involving a current, as these flows are not gravity driven. At the same time, Reynolds scaling of realistic full scale conditions is typically unattainable in a laboratory environment. However, some general guidelines were established by [McCombes et al. \(2010\)](#) for tank testing practice of marine energy devices, including recommendations for scaling. According to these guidelines, length scale factors of up to 1:100 are reasonable for tidal energy converters in extreme loading. For the presented study this implies a maximum up-scaling of the models to a structure height of 10 m, in a maximum water depth of 35 m. Many tidal turbine structures, including the prototype analyzed in [Section 3.4](#), satisfy these limitations.

## 7.3 Experimental Benchmark Setup

### 7.3.1 Flume

The experimental investigations for the introduced benchmark study were carried out in the Aalborg University (Denmark) wave-current flume. Both the sides and bottom of the flume test section were covered with aluminum plates, thereby establishing a smooth wall boundary. In order to reduce the energy reflected from the downstream wall of the flume, an energy absorbing beach is used. The beach is upwards sloping and made of porous material of various characteristic lengths.



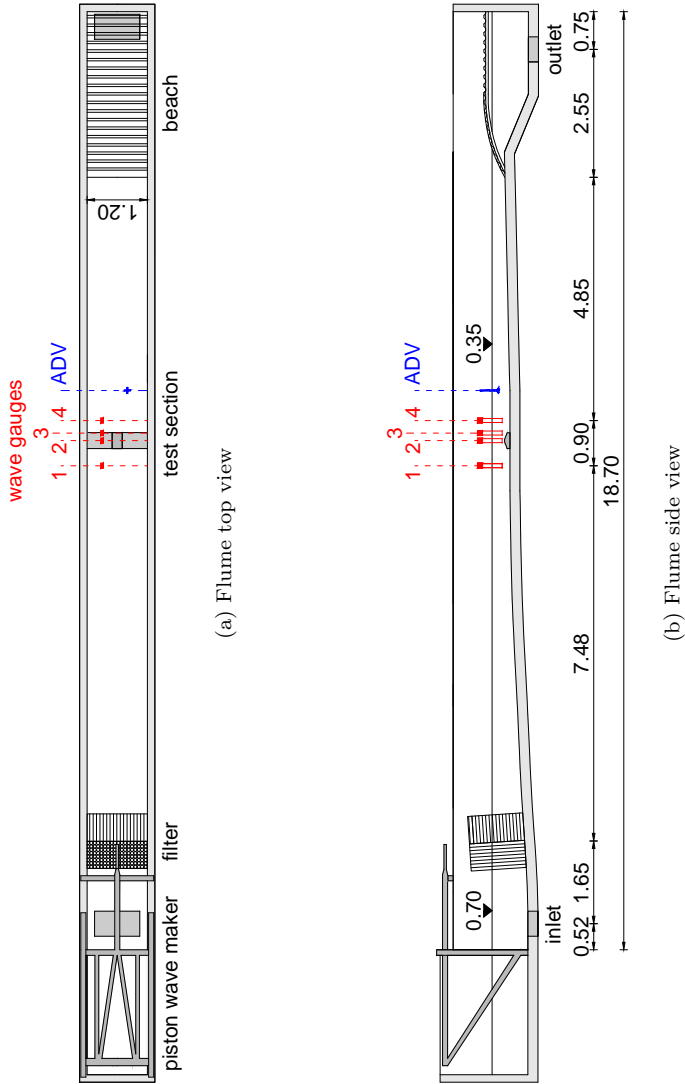


Figure 7.2: Benchmark setup in the Aalborg University recirculating wave flume. Measurements are in meters.

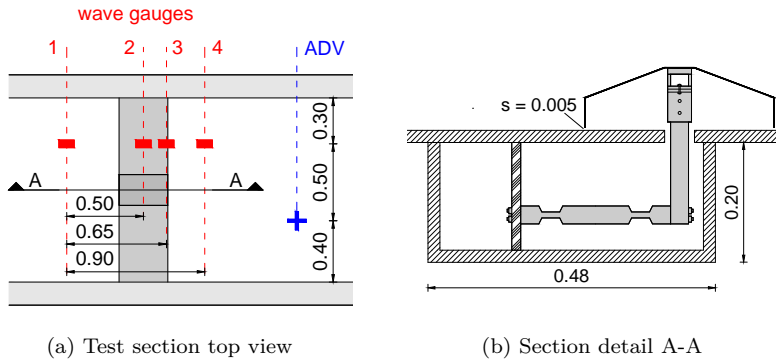


Figure 7.3: Test section detail of the experimental benchmark setup. All measurements are in meters.

The water depth for all conducted tests was 0.35 m in the test section, corresponding to 0.70 m at the location of the wave paddle.

The complete benchmark study was carried out using the 2v2h flow filter setup of Chapter 6, thus significantly reducing unwanted turbulence induced by the recirculating water pump. The filter positioning in the flume during the benchmark testing and the location of the test section is given in Fig. 7.2. The filter remained in the flume for all conducted tests, including the pure wave experiments.

### 7.3.2 Load Measurement

The benchmark study required a robust load measuring device sensitive enough to accurately measure the forces acting on the test structures. A broad bandwidth of forces was to be covered ranging from 0.1 N to 16 N, as well as relatively small force deviations between the different test configurations. The range was predetermined based on numerical simulations. The requirements were satisfied by designing a measuring unit specifically configured for the needs of this study. The resulting device is shown in Fig. 7.4. The bottom of the device is mounted in a pit located in the floor of the test section, while the models are fixed atop the device, as shown in Fig. 7.3b. The measuring device consists of two strain gauges located at the bottom and two load cells positioned at the top. The configuration of the sensors allows for the recording of

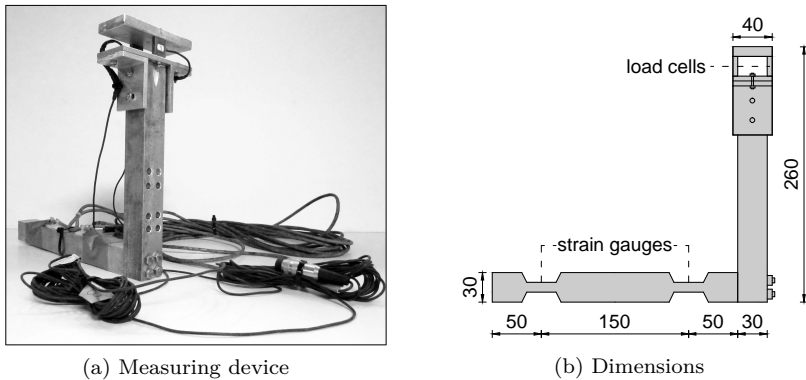


Figure 7.4: Designed measuring device. Dimensions are given in mm.

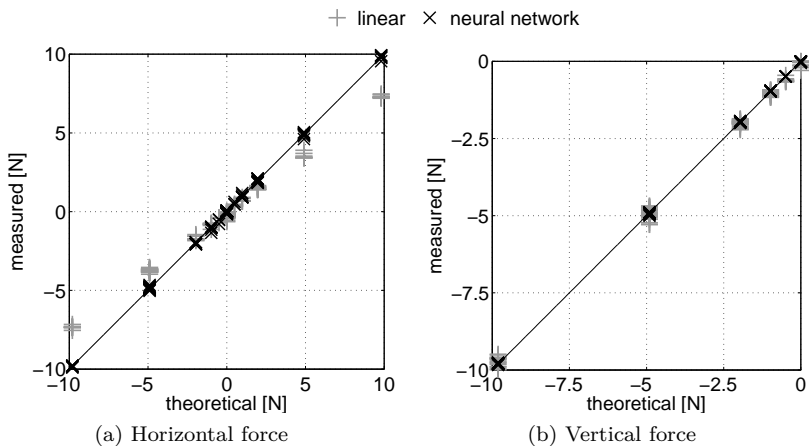


Figure 7.5: Measuring device calibration curves of measured vs. theoretical forces using linear and neural network calibration functions.

moments at the strain gauge locations as well as forces at the locations of the load cells. In addition, the positioning of the load cells allows for the computation of the moment at the top of the device.

Based on these measurements, the forces and moment acting on the models are determined. This can be achieved using simple mechanics in combination with linear calibration functions applied to the individual strain gauge and load cell measurements. However, initial calibration

tests showed significant deviations between theoretical and computed loads, particularly when applying large forces. These deviations are a result of deformations in the measuring unit that are not accounted for in the linear calibration model. As a consequence, an alternative calibration approach is chosen, in the form of an artificial Neural Network (NN). A feedforward-type network is used in this study (Rumelhart et al., 1995; Vogl et al., 1988), for which the four device measurements are defined as input layers. Tangent-sigmoid transfer functions are applied in the hidden layer, with a total of ten assigned neurons. In the output layer, linear transfer functions are utilized. Three target values are assigned in the output layer for each four-dimensional input vector. The target values correspond to the horizontal force, vertical force, and moment at the interface between the measuring device and the structures. Training of the network is carried out using the Levenberg-Marquardt algorithm, an efficient approach with good performance, as demonstrated by Tan and Van Cauwenberghe (1999). Further information on NN architecture is documented in previous works published by Flood and Kartam (1994), Hassoun (1995), and Rojas (1996), to name a few. The results of the NN device calibration are shown in Fig. 7.5, in comparison to the initial approach using linear calibration functions. A root-mean-square error improvement from 0.935 for the linear approach to 0.999 in the case of the NN calibration is achieved.

### 7.3.3 Models

Five geometries are analyzed in the experimental study, according to the coordinate definitions given in Tab. 7.2. The model designs for geometry 2 and geometry 4 are shown in Figs. 7.6a and 7.6b, respectively. All models consist of an aluminum plate that spans over the front, top, and back of each geometry, supported by coated wooden side walls. All wetted surfaces are smooth. The inner section of each model is hollow, allowing for a connection to the measuring unit in the flume as shown in Fig. 7.3b. A 5 mm gap between the models and the flume floor ensures that all forces acting on the body are fully transferred into the measuring unit, without frictional losses.

In addition, side panels were constructed for each model, as shown in Figs. 7.6c and 7.6d. These panels are of the same materials and cross sectional area (in flow direction) as the models. Installed in the flume, the panels span from the 0.2 m wide models to the flume walls on both

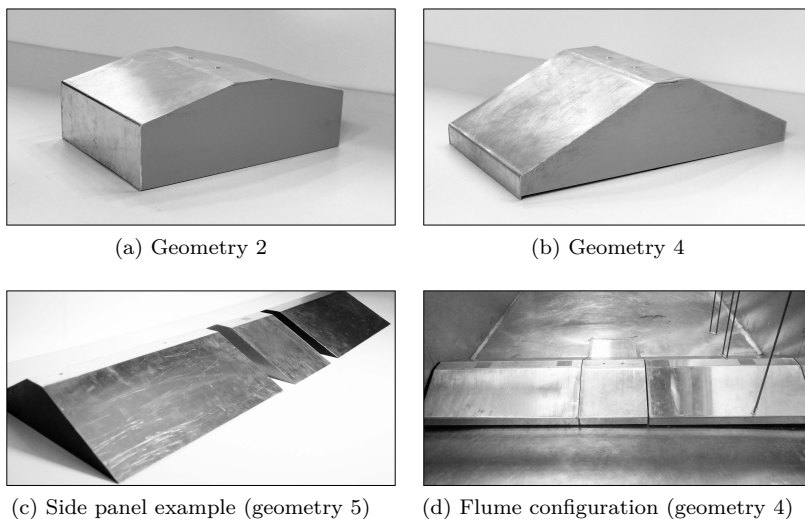


Figure 7.6: Examples of selected benchmark models and side panels.

sides (Fig. 7.6d), with a 2 mm gap between the model walls and side panel walls. The side panels serve the purpose of enforcing a flow field that is assumed to be constant along the width of the model in the center of the flume, thereby allowing for two-dimensional validation studies. For the sake of comparison, all tests were repeated without the side panels, allowing for the development of a three-dimensional flow field around the structures.

### 7.3.4 Flow Measurement

In addition to the installed load sensors, the flume was equipped with measuring devices to record the kinematics of the flow field. Four resistance type wave gauges were installed in the test section, to measure the surface elevation in the vicinity of the models. The wave gauges were calibrated assuming a linear relationship between voltage and displacement, an assumption that was verified for the full range of wave heights analyzed in this study. In addition, the Nortek ADV previously described in Section 6.3 was installed in the test section. Using the ADV, three-dimensional flow velocities and turbulence intensities were measured again at a sampling rate of 25 Hz. The precise wave gauge

and ADV locations during model testing are given in Fig. 7.3a. Prior to carrying out the model tests, flow field recordings in the test section were carried out. During these tests, the ADV was located adjacent to wave gauge 2.

## 7.4 Numerical setup

Numerical validation simulations are carried out at model scale using the NWCT introduced in Chapter 2. The computational mesh required in the solution process is generated using a hex-dominated mesh (approximately 99% hexahedra cells and 1% polyhedra cells) with local refinement in the vicinity of the structures and two prism layers at the geometry walls. The maximum mesh size in the  $x$ - $z$  plane of the domain is equal to 1 cm. In order to accurately capture the boundary layer at the geometry walls, the meshes are generated with a first cell node wall distance of 0.2 mm. For the analyzed flow conditions, this yields an average dimensionless wall distance  $y^+$  of approximately 0.5. The domain dimensions and number of cells for the two-dimensional and three-dimensional meshes generated as part of the benchmark study are given in Tab. 7.3.

As described in section Section 7.3.3, the models in the experimental study are mounted 5 mm from the flume bottom, therefore allowing for a water flow within the shell-like geometries. Nevertheless, the inside of the models in the numerical benchmark are not discretized for the sake of simplicity and to reduce computational costs. This simplification is done based on analytical and experimental studies of submerged open-bottom structures carried out by Chakrabarti and Naftzger (1976) and Garrison and Snider (1970). These studies concluded that the pressure during wave loading inside the structure is uniform if the opening between the bottom and the edge of the shell is small. Therefore, the horizontal loads acting on an open and sealed axially

Table 7.3: Computational domain specifications.

case	domain length [m]	domain height [m]	domain width [m]	model-inlet distance [m]	number of cells
2D	13.50	0.55	-	3.50	100,000
3D	13.50	0.55	1.20	3.50	10,000,000

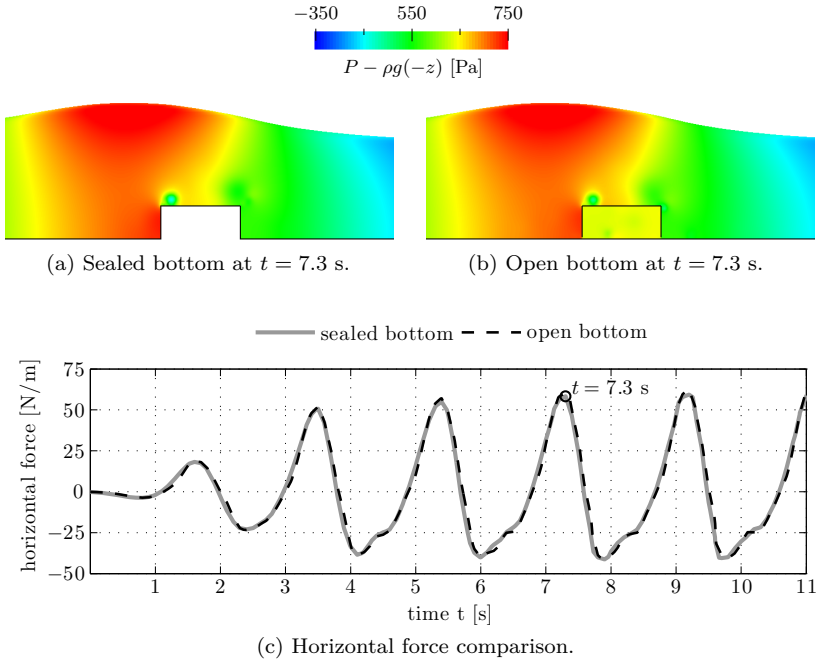


Figure 7.7: 2D Comparison of sealed and open bottom geometry 1 subjected to a 12 cm wave of 1.9 s period at 35 cm water depth.

symmetric structure will be approximately the same. This phenomenon is verified for the benchmark study by comparing a two-dimensional wave simulation of geometry 1 with a test simulation carried out for the corresponding open bottom structure. Figs. 7.7a and 7.7b show the resulting pressure fields for both scenarios at peak loading. Although a large pressure difference occurs between the leading and trailing edge in both scenarios, the pressure distribution inside the open structure is approximately uniform, confirming the observations of previous studies. Furthermore, the pressure field outside the sealed and open body agree completely. As a consequence, largely equivalent horizontal forces develop on the structures during wave loading (Fig. 7.7c). Therefore, it is reasonable to carry out the numerical benchmark simulations using the simplified sealed model.

## 7.5 Benchmark Results

### 7.5.1 Flow kinematics

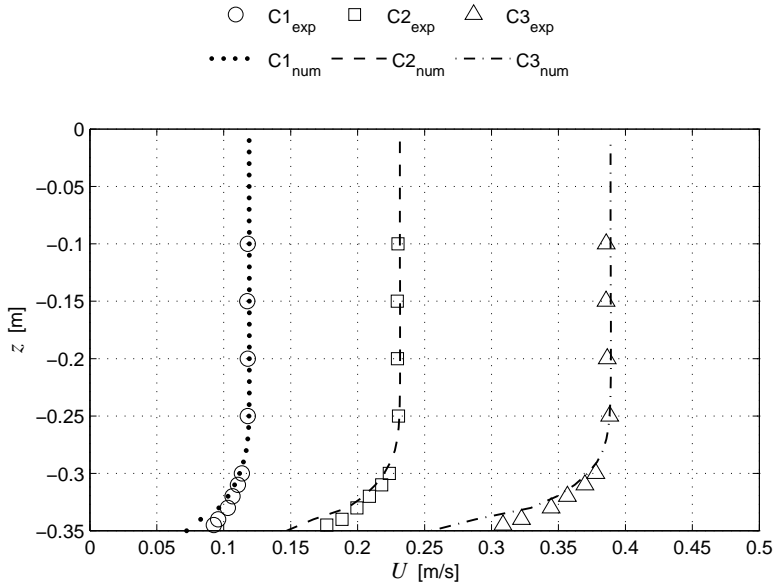
The flow conditions considered in the optimization benchmark include both current and wave flows, as well as the combination of both scenarios. Overall, three current velocities and three wave heights are modeled both physically and experimentally, as defined in [Tab. 7.4](#). Here, the velocity  $U_s$  corresponds to the current surface velocity and  $U_a$  denotes the depth averaged current velocity. The water depth  $d$  for all cases is equal to 0.35 m. In addition to the individual conditions, the H1 wave load case is combined with every current load case, rendering 3 combined wave-current scenarios. The scenarios are chosen specifically to cover a broad bandwidth of conditions. The maximum flow velocity C3 was limited by the pump capacity in the flume, while the highest wave H3 was selected such that no wave breaking occurs as the wave passes the structure. In addition, the minimum conditions (C1 and H1) and intermediate conditions (C2 and H2) were selected to confirm the observed trends from the numerical simulations of [Section 5.3.1](#), which suggested that for each scenario (current or wave), the normalized horizontal load curves collapse onto a single line, independent of the flow velocity or wave height.

The current properties in the laboratory wave-current flume are assessed based on 60 s measurements taken with the ADV at various heights throughout the water column in the test section prior to installing the models. The recorded horizontal velocities are shown in [Fig. 7.8a](#). The turbulence properties of the flow were also determined in order to provide the necessary information for boundary conditions of numerical turbulence models.

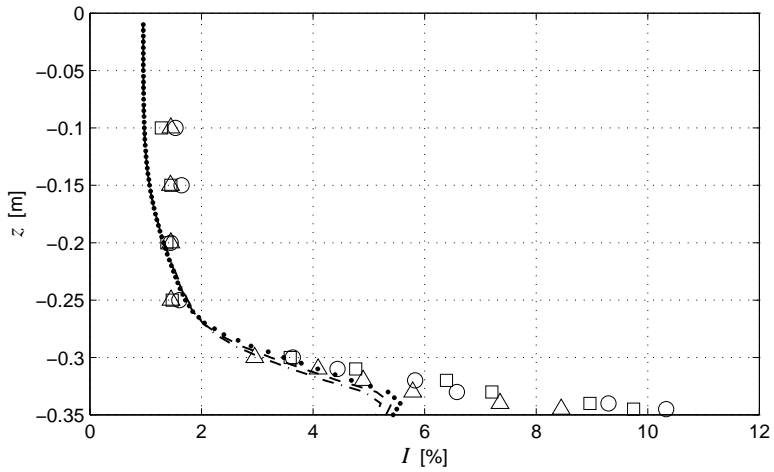
Table 7.4: Benchmark load case data.

(a) Current			(b) Wave		
ID	$U_s$ [m/s]	$U_a$ [m/s]	ID	$H$ [m]	$T$ [s]
C1	0.119	0.116	H1	0.040	1.90
C2	0.232	0.225	H2	0.082	1.90
C3	0.386	0.380	H3	0.120	1.90





(a) Horizontal velocity



(b) Turbulence intensity

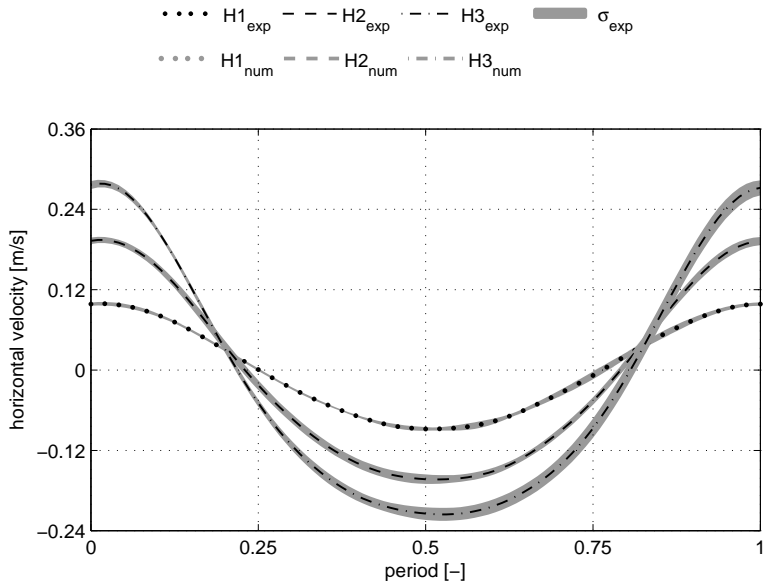
Figure 7.8: Experimental (subscript  $\text{exp}$ ) and numerical (subscript  $\text{num}$ ) current velocities and turbulence intensities over the water column.

In the numerical model, a constant velocity profile of magnitude  $U_a$  according to [Tab. 7.4a](#) is specified at the inlet boundary. The boundary conditions for the turbulence model are specified using the continuous exponential function given in [Eq. 7.1](#), which was fitted to the discrete ADV recordings. Because the distribution of the measured turbulence intensities is largely velocity independent for the considered current load cases, the same intensity function was utilized for all current conditions. A turbulence length scale  $l = 0.05$  m is used in the numerical model. This distance corresponds to the tube diameter of the physical flow filter through which the water passes in the experimental wave-current flume.

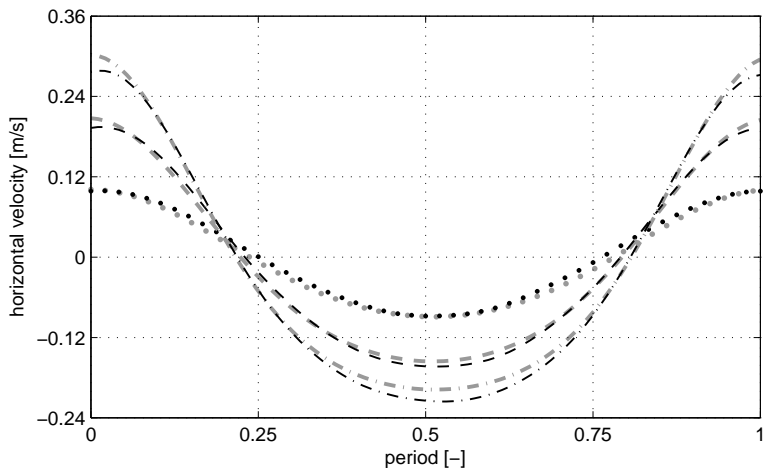
$$I(z) = 0.096e^{-28.38(z+0.35)} + 0.0126e^{0.0208(z+0.35)} \quad \forall z \in [-0.35, 0] \text{ m} \quad (7.1)$$

Empty channel simulations of the numerical setup for the three current conditions resulted in the horizontal velocity and turbulence intensity profiles shown in [Figs. 7.8a](#) and [7.8b](#). The profiles were computed 3.5 m from the domain inlet, the central position of the geometries analyzed in subsequent sections. Overall, the numerical results agree well with the experimental measurements. Distinct deviations occur only in the immediate vicinity of the bottom boundary. Here, the numerical model underestimates the magnitude of the velocity gradients, which also results in lower turbulence intensities in the near wall region. This behavior was also observed in previous studies, in which wind tunnel tests were compared to numerical simulations (e.g. [Meroney et al., 2002](#); [Andre et al., 2014](#)). The deviations are a result of the near wall turbulence modeling. However, in this study the effect is limited to the first 1.5 cm near the bottom boundary, while a good agreement is reached throughout the remainder of the water column.

In addition, ADV measurements were also taken for the three wave conditions at  $z = -0.30$  m, corresponding to the location of the geometry height midpoint. The resulting horizontal velocities over one period are given in [Fig. 7.9a](#). Each profile is computed by averaging the velocities over nine wave periods of recorded ADV data. In addition, the figure shows the standard deviation  $\sigma_{exp}$  of the averaged velocities, marked by the gray surfaces. The numerical wave simulations are carried out using the NWCT described in [Chapter 2](#). The inlet turbulence boundary conditions are specified such that a low inlet turbulence intensity ensues, with  $k = 10^{-5} \text{ m}^2/\text{s}^2$  and  $\omega = 0.1 \text{ 1/s}$ .



(a) Experimental



(b) Experimental vs. numerical

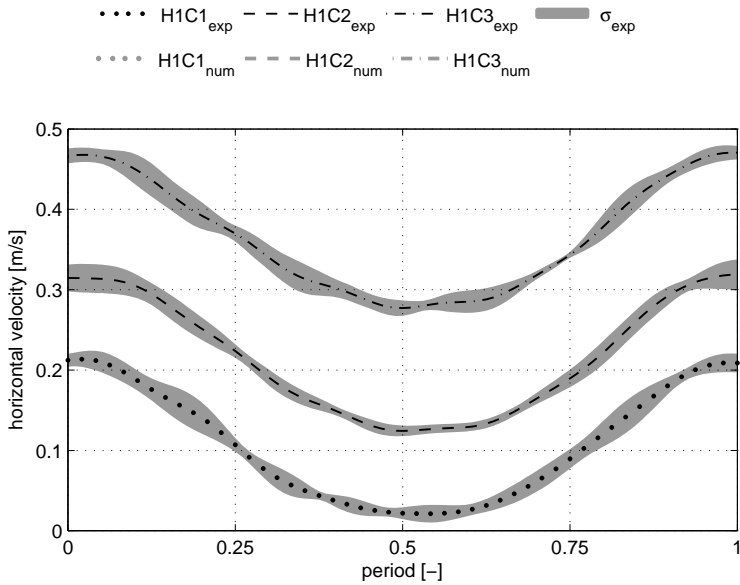
Figure 7.9: Experimental (subscript  $_{exp}$ ) wave velocities averaged over 9 periods with standard deviation  $\sigma_{exp}$  and comparison to numerical results (subscript  $_{num}$ ) at  $z = -0.30$  m.

This is done because the oscillatory wave motion is largely free of wave-induced vorticity in the far field of the flow (Lighthill, 1986). In Fig. 7.9b, the CFD results are compared to the experimental profiles, showing a good agreement of the profiles.

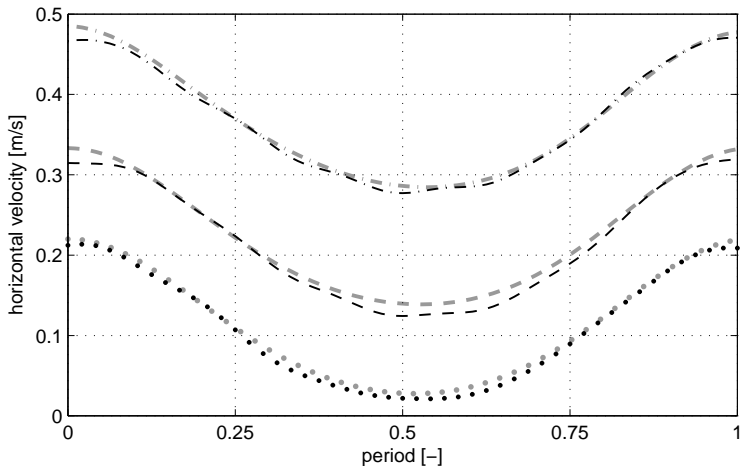
Finally, combined wave-current kinematics is assessed. ADV recordings of the laboratory conditions averaged over nine wave periods with the corresponding standard deviations are shown in Fig. 7.10a for the H1 wave scenario in combination with the three current scenarios. In the wave-current scenario, the turbulence in the flow is mainly a result of the underlying current, while the far field turbulence from the wave motion is negligible in comparison. Therefore, the turbulence parameters for the numerical simulations are defined analogue to the pure current conditions using Eq. 7.1. The corresponding numerical results are shown in Fig. 7.10b. The wave-current flow velocities agree well with the experimental data.

## 7.5.2 Two-Dimensional Current Forces

After establishing that the simulated numerical flow fields and the experimental flow conditions are in close agreement, the shape optimization benchmark is presented. In a first step, the horizontal loading on the structures for the three current load cases is analyzed for the two-dimensional flow scenario. As part of the experimental test series, each current load case is repeated 12 times for every tested geometry. Based on this data, the mean force and standard deviation for each geometry and load case is computed. In order to compare the results with numerical two-dimensional simulations, the horizontal forces measured in the experiment are divided by the geometry width (0.2m), perpendicular to the flow direction. The resulting forces for the five geometries are shown in Fig. 7.11a, with error bars indicating the experimental standard deviations. For each experimental current load case, cubic spline curves are drawn through the five discrete force results. In the case of the numerical results shown in the figure, the benchmark geometry is varied in two degree increments of the design variable  $\phi$ , resulting in a total of 15 shape variations subjected to each two-dimensional load scenario. The magnitude of the computed numerical results is in close agreement with the experimental loads. For an increase in the current velocity, both the numerical and experimental models show an approximately quadratic relationship between the force magnitude and the horizontal forces, as predicted by



(a) Experimental



(b) Experimental vs. numerical

Figure 7.10: Experimental (subscript <sub>exp</sub>) wave-current velocities averaged over 9 periods with standard deviation  $\sigma_{exp}$  and comparison to numerical results (subscript <sub>num</sub>) at  $z = -0.30$  m.

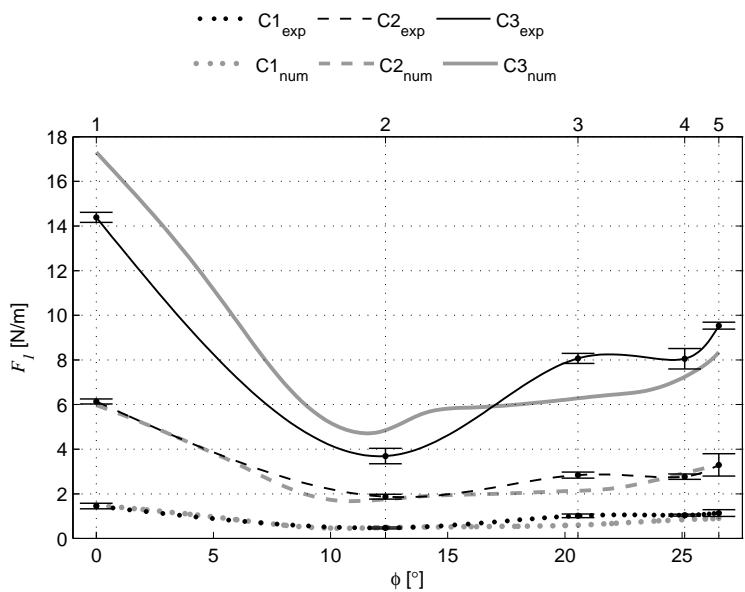
Table 7.5: 2D forces  $F_1$  for the 3 current scenarios.

geometry ID	experimental [N/m]			numerical [N/m]		
	C1	C2	C3	C1	C2	C3
1	1.45	6.14	14.39	1.50	5.97	17.30
2	0.47	1.87	3.69	0.49	1.78	5.04
3	1.02	2.84	8.07	0.60	2.16	6.31
4	1.04	2.77	8.05	0.84	2.94	7.10
5	1.14	3.30	9.53	0.90	3.26	8.35

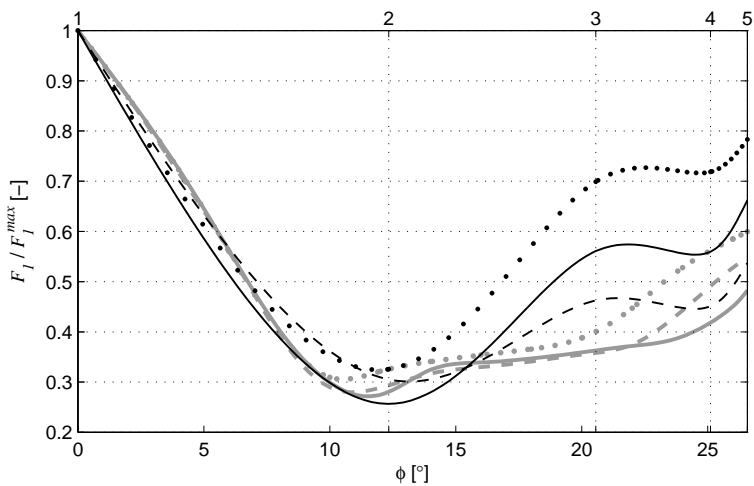
the drag equation (Batchelor, 1968). A summary of the computed and measured benchmark forces is given in Tab. 7.5.

With regards to optimizing a structure, the shape of the objective function (in this case the horizontal force) and the optimization potential of the given problem are of particular interest. In order to analyze this aspect more thoroughly, the objective functions are normalized by dividing each load curve  $F_1$  by its maximum value  $F_1^{max}$ . The curves corresponding to the resulting normalized objective functions are shown in Fig. 7.11b. The numerical prediction of the objective improvement between geometry 1 and geometry 2 matches the experimental results remarkably well. The subsequent objective increase is also captured in both approaches. A steeper increase in the forces is measured in the experimental study between geometries 2 and 3, compared to the corresponding numerical results. This may be contributed to sudden changes of the flow separation point and reattachment zone on the leading edge of the body, which are influenced by both the near wall turbulence model performance in the numerical simulations, as well as geometry imperfections in the experimental tests. However, the overall shape of the objective functions match well and the same objective minimum is predicted.

The overall agreement of the results allows for an in depth hybrid analysis, taking advantage of the strengths of both the numerical and experimental modeling approaches. This is demonstrated in an investigation of the reasons behind the lower horizontal forces attained for geometry 2 when compared to geometry 4. The experimental geometry 2 flow field is visualized in Figs. 7.12a and 7.12b, which show recordings from an underwater camera of red dye injections through a narrow tube positioned at the flume bottom in front of the structure.



(a) Horizontal force



(b) Normalized horizontal force

Figure 7.11: Comparison of experimental (subscript  $\text{exp}$ ) and numerical (subscript  $\text{num}$ ) 2D horizontal current forces.

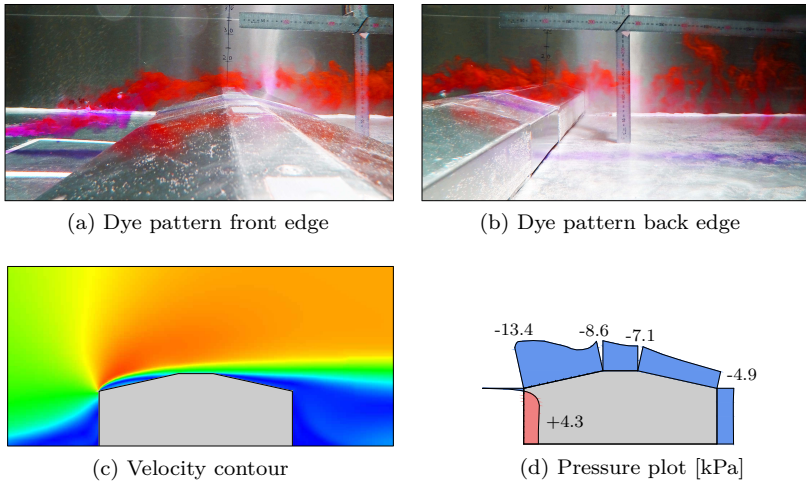


Figure 7.12: Geometry 2 experimental flow field visualization and numerical velocity and pressure fields for the 2D flow scenario C1.

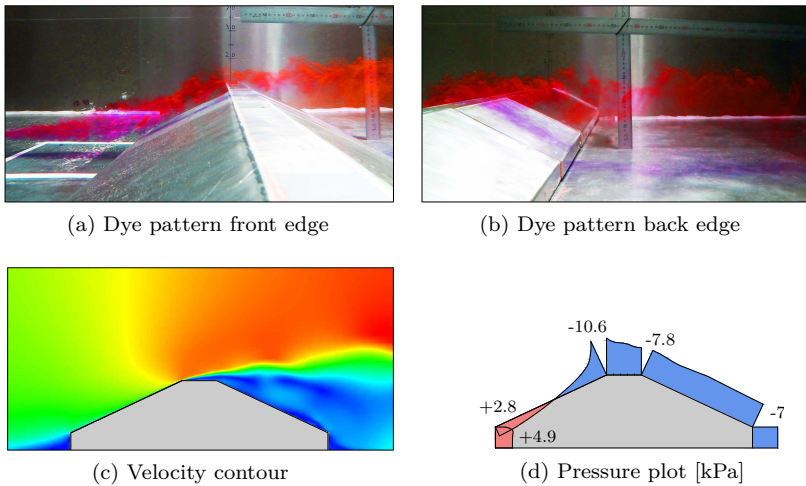


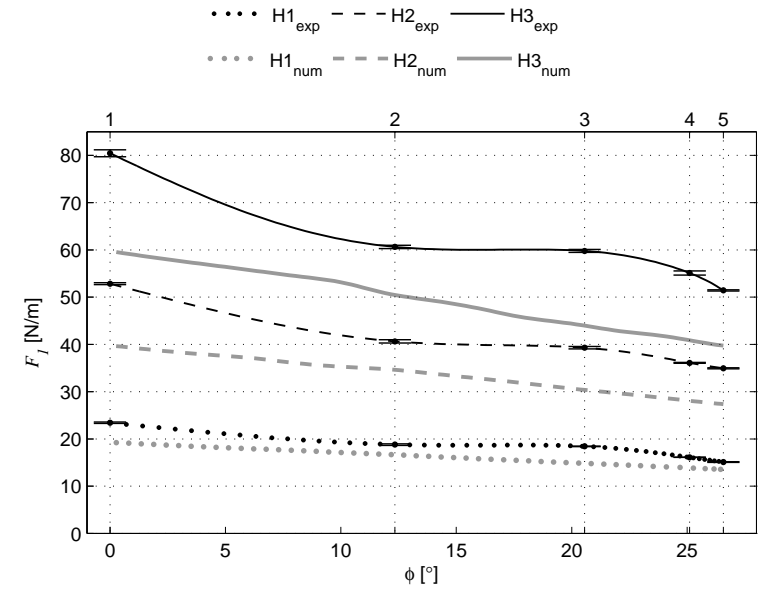
Figure 7.13: Geometry 4 experimental flow field visualization and numerical velocity and pressure fields for the 2D flow scenario C1.



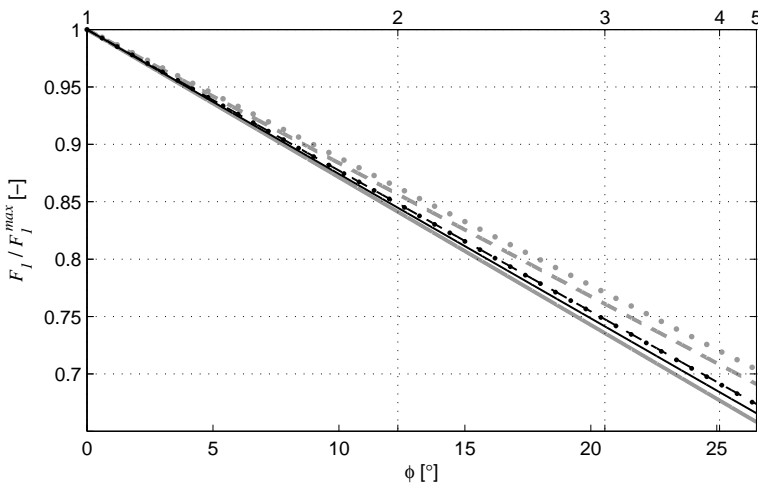
Particularly the back edge view shows a separated flow that does not reattach on the trailing inclination of the body. In addition, the corresponding numerical velocity contour plot given in Fig. 7.12c, shows that the initial separation actually occurs on the leading edge and that the body is enclosed in a large dead water zone. As a result, the pressure field on the front and back side of the body is of opposite sign but similar magnitude, as shown in Fig. 7.12d. Overall, this leads to relatively small horizontal forces on the body. Although, a separated flow is also encountered on the trailing inclination of geometry 4 (Fig. 7.13b), the flow remains attached on the leading inclination of the structure (Figs. 7.13a and 7.13c). This results in a larger difference between pressures on the front and back side of the body (Fig. 7.13d) and therefore larger horizontal forces on geometry 4 compared to geometry 2. Overall, the availability of both numerical and experimental results allows for a thorough understanding of the physical flow field based on substantial, validated data.

### 7.5.3 Two-Dimensional Wave Forces

Horizontal peak forces during wave loading are analyzed for the previously defined wave load cases. The experimental peak loads for each geometry and wave case are based on 6 successive test runs. From each run, 3 wave periods are isolated after stable conditions are reached. The average horizontal force computed from the resulting 18 peak values is given in Tab. 7.6 and is plotted in Fig. 7.14a, together with the standard deviations indicated by error bars (due to relatively small standard deviations, the bars diminish onto a single line for most measurements). The results of each load case are connected by cubic spline curves. The numerical results shown in the figure are once again computed for a variation of the design variable  $\phi$  in two degree increments. The numerical results suggest that the angle  $\phi$  and the horizontal peak wave loads are linearly related in the case of the tested benchmark. This behavior was also observed in the numerical optimization simulations of Section 5.3.1. Furthermore, it was found that a linear fit of the experimental wave data results in normalized objective function approximations that match the numerical results remarkably well (Fig. 7.14b). Both the numerical and experimental tests predict an objective improvement of approximately 70% going from geometry 1 to geometry 5. In addition, both studies indicate that the optimization potential is largely independent of the wave height



(a) Horizontal force



(b) Normalized horizontal force

Figure 7.14: Comparison of experimental (subscript  $_{exp}$ ) and numerical (subscript  $_{num}$ ) 2D horizontal wave forces.

Table 7.6: 2D peak forces  $F_1$  for the 3 wave scenarios.

geometry ID	experimental [N/m]			numerical [N/m]		
	H1	H2	H3	H1	H2	H3
1	23.43	52.86	80.45	19.28	39.79	59.73
2	18.81	40.65	60.64	16.66	34.57	50.39
3	18.44	39.30	59.79	14.84	30.38	44.02
4	16.11	36.10	55.11	13.89	28.09	40.77
5	15.12	34.95	51.44	13.55	27.37	39.76

for the tested range of conditions. Despite relatively small standard deviations computed for the experimental wave load case, many factors may introduce small errors as part of the physical modeling, including limits in the manufacturing precision of the models, misalignment during installation of the models, and small deviations in the flume water depth. These factors may contribute to the small deviations of the experimental force curves from a precise linear fit.

In addition to the maximum wave loads, the force development as a function of the wave period is analyzed. As previously shown, the magnitude of the total wave amplitudes differs between the experimental and numerical results. However, when normalizing the results, it becomes apparent that the general characteristics of the load time series are in agreement. This is demonstrated in Fig. 7.15, which gives a comparison of the simulated and measured wave forces over 2 periods for geometries 1 and 3, subjected to the linear wave H1 and nonlinear wave H3. The change from a symmetric peak to trough ratio in the case of linear wave loading to a non-symmetric profile for higher waves is captured by both the numerical and physical model. Also, both models suggest that the wave profile shape is geometry dependent when the structures are subjected to nonlinear waves. These results suggest that the utilized numerical models are quite accurate when aiming to capture the general characteristics of wave loads and the resulting objective functions. This is of particularly great value when generally searching for a design optimum, a task that does not require precise force magnitudes so long as the computed objective function shape is captured correctly.

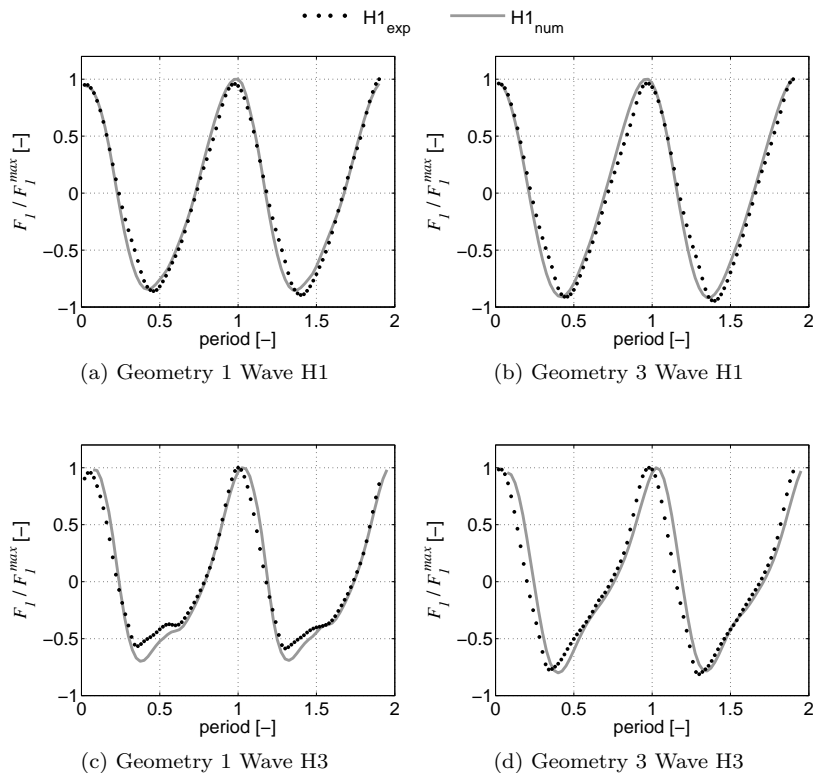


Figure 7.15: Time series comparison of experimental (subscript <sub>exp</sub>) and numerical (subscript <sub>num</sub>) 2D horizontal forces over two wave periods.

### 7.5.4 Two-Dimensional Wave-Current Forces

The two-dimensional investigations are concluded by analyzing forces resulting from combined wave-current conditions. For this purpose, the H1 wave load case is combined with the three current load cases. The smallest wave height was chosen deliberately, in order to attain a more balanced ratio of force contributions from the wave and the current. The aim of the study is to investigate the load characteristic in conditions where the wave field changes as a result of the underlying current. This change is significantly less pronounced when the waves are overly dominant in comparison with the current, as would be the case for the H2 and H3 wave heights in combination with the analyzed

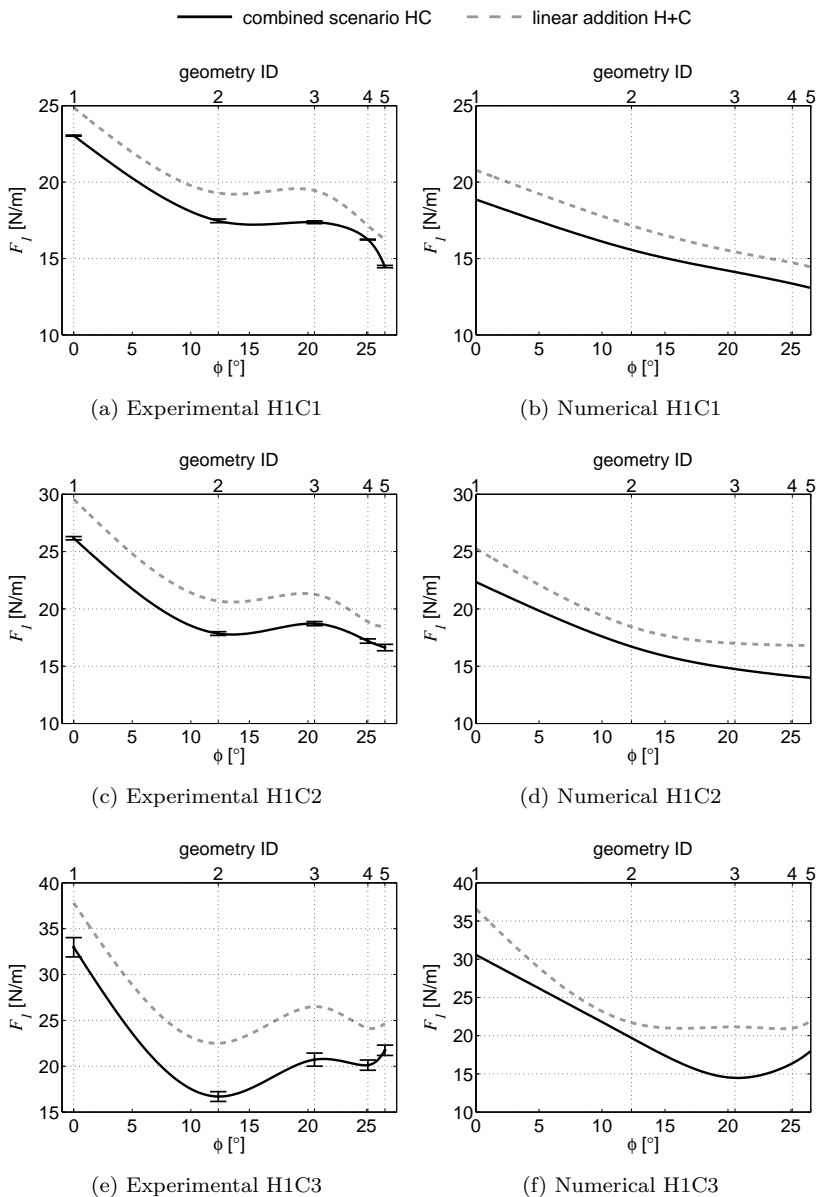


Figure 7.16: Comparison of combined wave-current conditions (HC) vs. a linear superposition of pure wave and pure current forces (H+C).

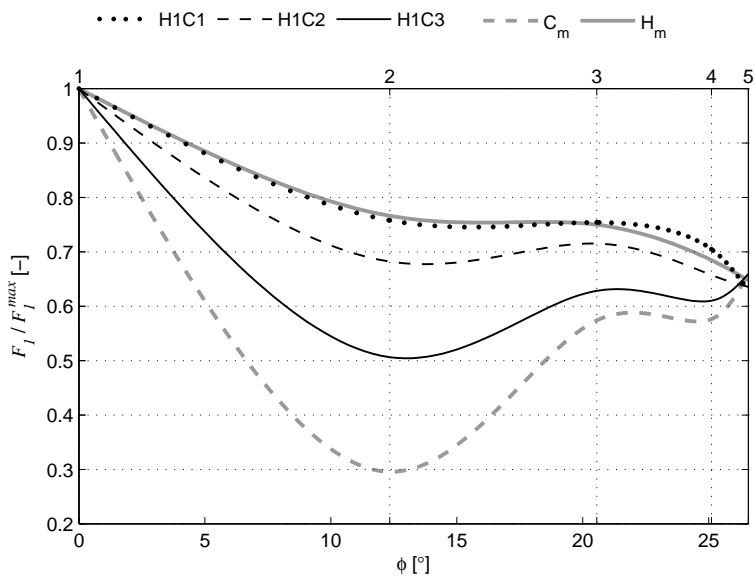
Table 7.7: 2D peak forces  $F_1$  for the 3 wave-current scenarios.

geometry ID	experimental [N/m]			numerical [N/m]		
	H1C1	H1C2	H1C3	H1C1	H1C2	H1C3
1	23.04	26.17	32.98	18.86	22.34	30.57
2	17.47	17.85	16.70	15.57	16.71	19.71
3	17.38	18.72	20.72	14.12	14.76	14.48
4	16.24	17.20	20.12	13.36	14.14	16.39
5	14.48	16.63	21.75	13.08	13.99	17.99

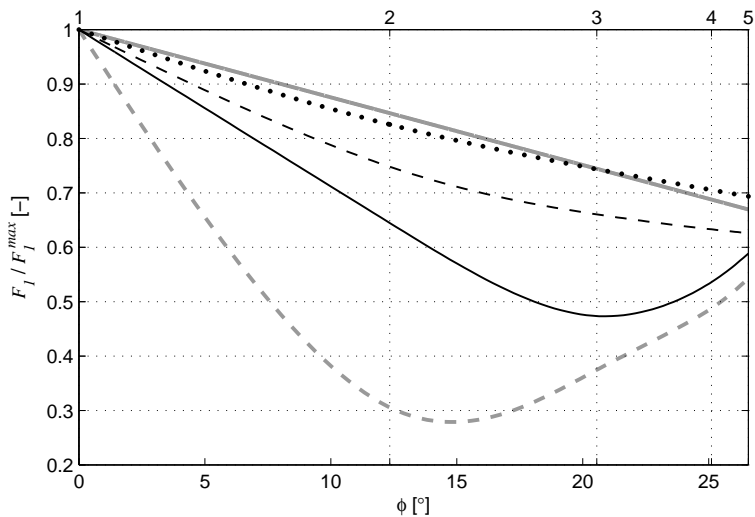
current conditions.

Analogue to the procedure outlined for the pure wave load case, the experimental results are derived by isolating and averaging the peak forces from the recorded load histories of multiple test runs. The resulting peak loads are given in [Tab. 7.7](#) and plotted in [Fig. 7.16](#), together with the corresponding numerical results. Also given in the figure are load curves attained by a linear superposition of the pure current and pure wave results. As demonstrated in [Section 3.3.2](#), the forces on a structure in wave-current conditions may deviate significantly from a linear superposition of pure wave and pure current forces. This trend is also observed in the benchmark study for both the numerical and experimental tests. It should be noted that the decrease of the combined wave-current forces compared to a linear superposition is not a general tendency. In certain critical conditions (such as those analyzed in [Section 3.3.2](#)), combined wave-current simulations rendered an increase of the forces by approximately 30%.

A normalized approximation of the objective functions for the combined wave-current scenarios is shown in [Fig. 7.17](#). In addition, the normalized mean pure wave ( $H_m$ ) and pure current ( $C_m$ ) results are given, which are computed by averaging the normalized results of the three wave and three current scenarios. Depending on the magnitude of the current in relation to the wave height, the shape of the combined scenario curves and the corresponding optimization potential take after the individual wave or current curves, as captured by the experimental tests and numerical simulations. This confirms earlier observations of combined wave-current loads analyzed in the optimization studies of [Section 5.3.1](#), where the same conclusion was reached.



(a) Experimental results



(b) Numerical results

Figure 7.17: Normalized horizontal wave-current forces in comparison with pure mean current results ( $C_m$ ) and pure mean wave results ( $H_m$ ).

### 7.5.5 Three-Dimensional Forces

Finally, forces resulting from three-dimensional flow fields for the pure current and pure wave scenarios are compared. In the experimental study, the side panels are removed resulting in a fluid flow above and on the sides of the models. These flow fields are simulated by remodeling the flume cross section in the numerical domain. The resulting mesh properties are given in [Tab. 7.3](#). Because the computational costs of the three-dimensional simulations are significantly higher than those of the two-dimensional cases, only the geometries tested in the experiment are evaluated numerically, while intermediate configurations are omitted.

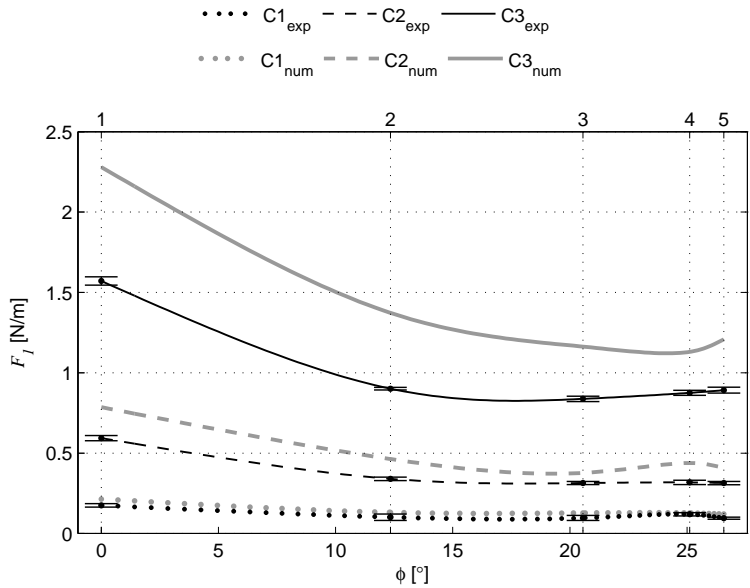
The resulting current forces are compared in [Fig. 7.18](#) and given in [Tab. 7.8](#). A good agreement of the normalized horizontal forces is attained for current velocities C2 and C3. For the C1 current case, some deviations occur. It should be noted that at this flow velocity in the three-dimensional scenario the mean forces on the structure are extremely low (approximately 0.1 N) with relative standard deviations of up to 20%. These small forces approach the limits of accurately measurable loads with the utilized measuring device. Nevertheless, the numerically and experimentally predicted overall trends once again match quite well. A central difference arises between the two-dimensional and three-dimensional cases in terms of the overall optimization potential. While for the two-dimensional current scenario a maximum force difference between the geometries of over 70% was predicted, this value reduces to approximately 50% for the three-dimensional scenarios. This behavior is captured by both the numerical and experimental model.

The three-dimensional wave load case results are given in [Fig. 7.19](#)

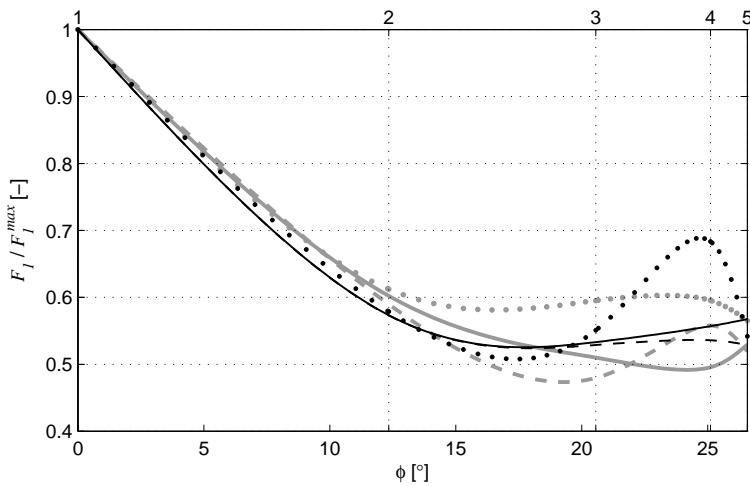
Table 7.8: 3D forces  $F_1$  for the 3 current scenarios.

geometry ID	experimental [N]			numerical [N]		
	C1	C2	C3	C1	C2	C3
1	0.175	0.593	1.571	0.214	0.786	2.280
2	0.101	0.340	0.901	0.131	0.463	1.373
3	0.096	0.314	0.838	0.128	0.377	1.163
4	0.120	0.318	0.875	0.128	0.439	1.130
5	0.095	0.314	0.892	0.121	0.408	1.208



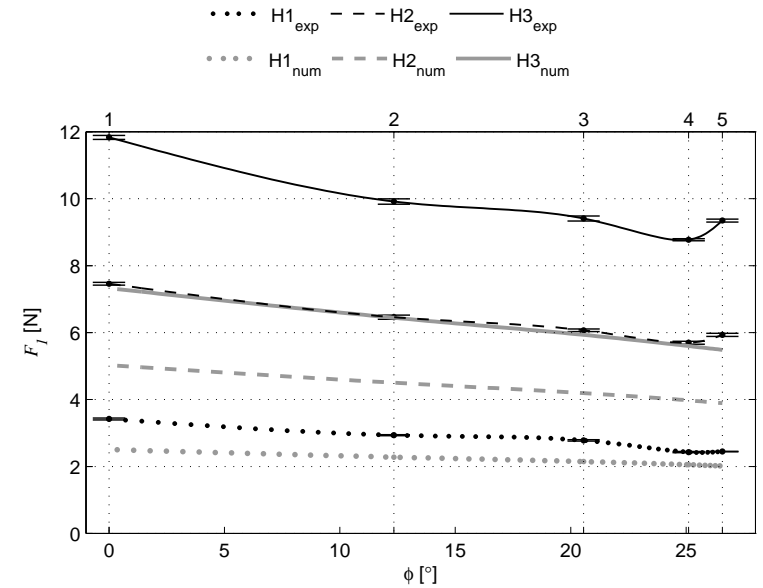


(a) Horizontal force

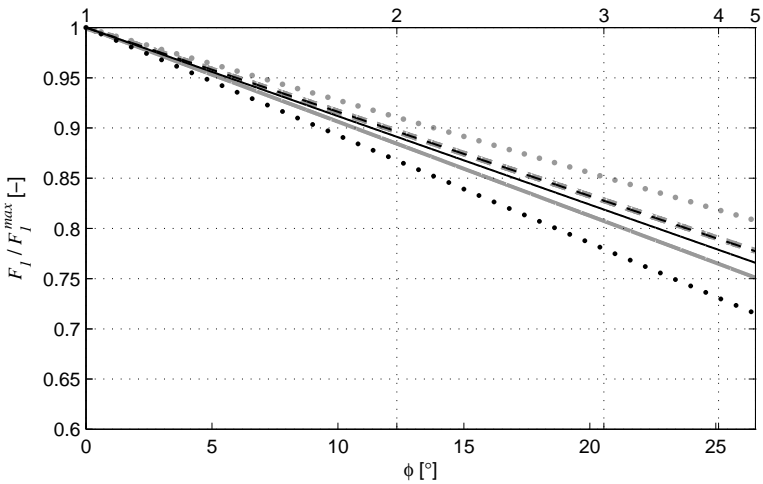


(b) Normalized horizontal force

Figure 7.18: Comparison of experimental (subscript  $_{exp}$ ) and numerical (subscript  $_{num}$ ) 3D horizontal current forces.



(a) Horizontal force



(b) Normalized horizontal force

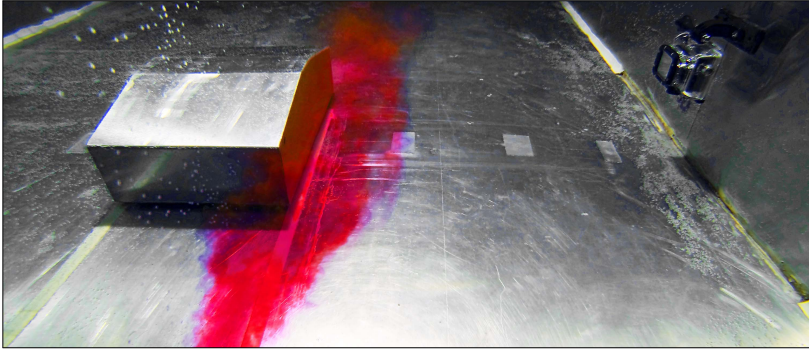
Figure 7.19: Comparison of experimental (subscript <sub>exp</sub>) and numerical (subscript <sub>num</sub>) 3D horizontal wave forces.

and Tab. 7.9. A linear fit through the experimental data once again results in normalized objective function approximations that closely resemble the predictions of the numerical models. Similar to the pure current load case the optimization potential for the three-dimensional wave scenario ( $\approx 35\%$  maximum force difference between tested structures) is smaller compared to the corresponding 2D scenario ( $\approx 45\%$  maximum force difference between tested structures), as predicted by both the numerical and experimental model.

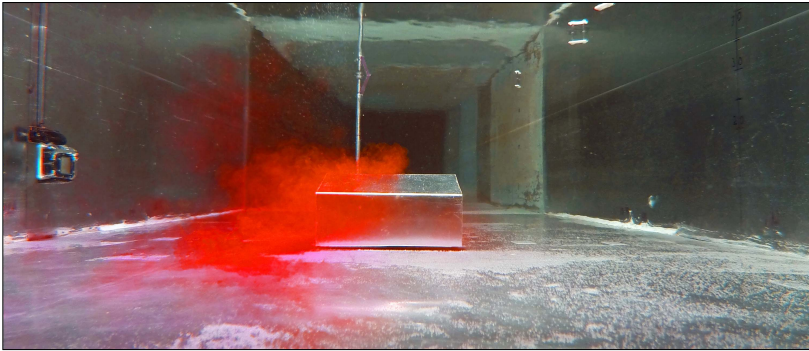
The possibilities of gaining in depth information from a hybrid numerical and experimental modeling approach are demonstrated by analyzing the current flow fields developing around geometries 2 and 4. Recordings of the experimental dye injections into the flume are shown in Figs. 7.20a, 7.20b, 7.21a, and 7.21b. While in the case of geometry 2 a large portion of the flow in front of the structure is redirected to the sides of the model, a larger vertical movement of the flow field is observed for geometry 4. More clearly, this behavior is indicated by the numerical velocity contours shown in Figs. 7.20c and 7.21c. Here, the blue regions indicate dead water zones with low velocity magnitudes. These regions are particularly pronounced on the sides of geometry 2, as a result of velocity circulations developing in these regions. In the case of geometry 4, the regions of circulating fluid motion are much more pronounced on the trailing inclination on the top of the geometry. These considerations may be of particular importance when analyzing an array of turbines mounted to GBFs. In such a case, turbulent eddies projected from the foundations into subsequent rotor axes may be undesirable, while a foundation design resulting in predominantly horizontal flow redirection may be preferable.

Table 7.9: 3D horizontal forces  $F_1$  for the 3 wave scenarios.

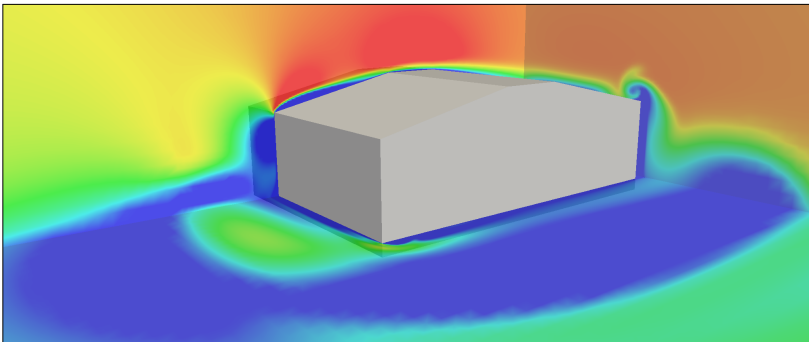
geometry ID	experimental [N]			numerical [N]		
	H1	H2	H3	H1	H2	H3
1	3.422	7.460	11.831	2.506	5.029	7.325
2	2.936	6.462	9.916	2.280	4.503	6.444
3	2.780	6.069	9.409	2.147	4.194	5.933
4	2.431	5.698	8.775	2.054	3.977	5.599
5	2.447	5.932	9.348	2.016	3.891	5.484



(a) Dye pattern front

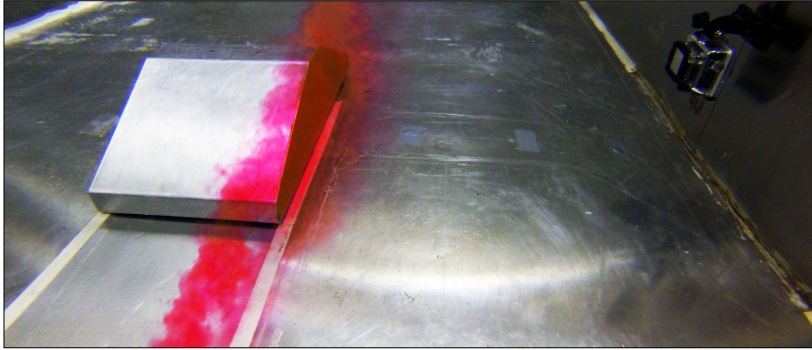


(b) Dye pattern back

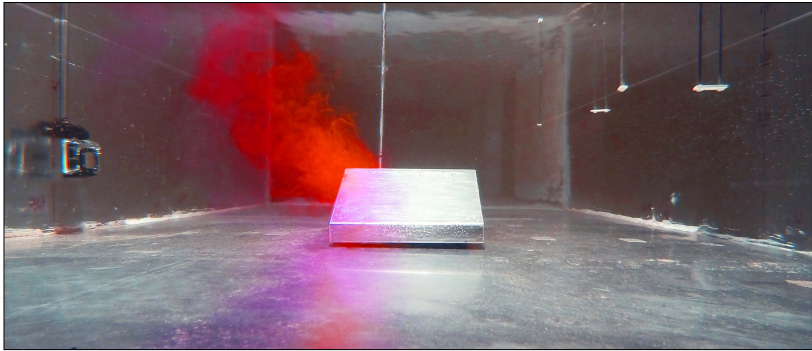


(c) Velocity contour

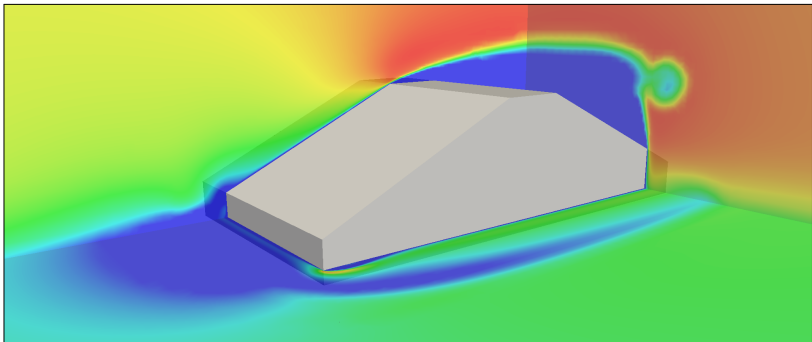
Figure 7.20: Geometry 2 experimental flow fields (top and middle) and numerical velocity contour (bottom) for the 3D current scenario C1.



(a) Dye pattern front



(b) Dye pattern back



(c) Velocity contour

Figure 7.21: Geometry 4 experimental flow fields (top and middle) and numerical velocity contour (bottom) for the 3D current scenario C1.

## 7.6 Conclusions and Summary

The presented optimization benchmark is a result of an elaborate experimental and numerical investigation, including data from over 450 experimental test runs and more than 200 numerical simulations. Based on this data set, a great variety of different test scenarios was presented that allowed for a widespread validation of the numerical methods presented in this thesis with respect to the following topics:

- Open channel flow kinematics of waves, currents, and combined wave-current conditions.
- Maximum horizontal forces on bottom mounted structures resulting from the specified conditions.
- Characteristics of the horizontal force time series during dynamic wave loading.
- Objective function characteristics of horizontal forces as a function of shape variation.
- Forces from interacting wave-current flows in comparison to pure wave and pure current conditions.
- Differences in loading of structures subjected to two-dimensional and three-dimensional flow fields

A number of valuable conclusion are drawn for the results. It was shown that the NWCT flow fields closely resemble the measured data from the experiment in terms of particle kinematics and turbulence properties in wave and current conditions. Furthermore, the magnitude of the horizontal forces on the benchmark geometries, subjected to the various flow conditions, are generally of the same order as the experimental results. In the case of the two-dimensional current scenarios the results match particularly well, with differences of as little as 4% between experimental and numerical results. However, the quantitative difference of the individual forces reached values of up to 40% in some scenarios, such as the three-dimensional wave conditions.

The root cause of these differences is versatile and can be contributed to the modeling choices made both experimentally and numerically. Moreover, the contribution of individual imperfections to the overall discrepancy may vary between models and load cases. For instance, the

edges of the experimental models have a slight round-off, while they are perfectly sharp in the numerical models. Depending on the inclination angle and the ensuing separation and reattachment points, the impact of this model discrepancy can vary significantly between the models and the flow conditions. From the numerical side, additional modeling errors contribute to the discrepancies of the results, although these errors are fundamentally different in nature. In the experimental model a physically correct environment is naturally given and sources of errors are a result of imperfections in manufacturing and measurement. For the numerical model the opposite holds true: the simple geometry can be generated precisely, while modeling errors ensue in the representation of the physical environment. These errors are a result of the space and time discretization as well as the modeling of turbulence. Overall, the different error contributions highly motivate the utilization of a hybrid numerical-experimental modeling approach.

Regarding optimization, the magnitude of the attained forces is of secondary significance, so long as the general shape of the objective functions and the predicted optima are modeled correctly. With regards to these criteria, it was shown that the quality of results computed with the NWCT is remarkably high, and that the predicted optimization potentials are captured well for all scenarios. Furthermore, a great many of the analyzed general trends observed in the numerical models were also captured as part of the experimental study. Particularly this applies to the shape of force time series during wave loading, the overall combined wave-current forces compared to the addition of pure wave and pure current forces, and the differences in the objective function shapes for two-dimensional and three-dimensional flow conditions.

These results strongly motivate a hybrid numerical and experimental modeling approach. It was shown that the NWCT is a powerful tool that can efficiently and accurately be utilized as part of shape optimization studies to explore the design space and to carry out a sound pre-selection of optimized structures. When combined with experimental modeling of a few chosen designs, a great wealth of information is attained, allowing for a detailed analysis of the optimization problem and offering the possibility to attain innovative and reliable solutions.

Overall, the experimental benchmark demonstrated the validity of the introduced numerical modeling strategies for shape optimization of offshore structures. The findings give a sound foundation for optimal design of innovative structures, as demonstrated in the following chapter.





---

## Chapter 8

# Advanced Foundation Design

---

### 8.1 Introduction and Overview

The GBF prototype analyzed in [Section 3.4](#) withstood all environmental forces encountered during the test period of the SeaTurtle project. Overall, the project was very successful and delivered valuable information for future development. In terms of the GBF, this particularly concerns the weight of the structure and the implications it holds for installation. The support structure and turbine combined to an overall weight of approximately 800 t, which approached the capacity limit of the crane vessel utilized for installation. Although vessels with higher capacities exist, their availability is typically significantly lower, while the costs are considerably higher. In order to avoid these additional expenses as well as possible vessel shortages, the aim was to design a GBF that would have the same weight as the prototype structure, but could withstand the loads of higher capacity next generation turbines. The compulsory increase in loading from these turbines can be counterbalanced by reducing the forces on the foundation through shape optimization.

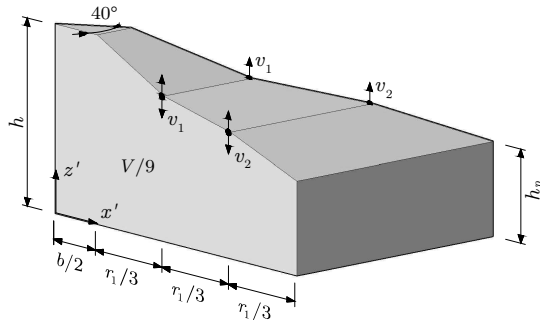
For this purpose, the validated numerical methods of this thesis are collectively applied to the design of an advanced GBF for tidal turbines. The previously analyzed SeaTurtle project forms the basis

for comparison of the new design. Drawing from the experiences of this prototype project, as well as the knowledge gained from the performed basic shape studies, a new geometry is proposed in the form of a Point Symmetric Diffuser (PSD) foundation. This structure is parameterized using a number of design variables that allow for a site specific shape optimization by means of the VFS-NWCT, with the objective of reducing the design relevant horizontal and vertical peak loads. The final optimized structure is analyzed using high fidelity VOF-CFD simulations, carried out analogue to those performed as part of the prototype analysis. The comparison of the results reveals a significantly improved hydrodynamic performance of the newly proposed PSD foundation.

## 8.2 Foundation Description

The prototype foundation of [Section 3.4](#) performs relatively well in  $0^\circ$  flow conditions, for which the direction of the flow field is aligned with the main foundation axis. However, the critical load case for the construction site of interest was defined as a combined wave-current scenario with a flow field deviation of  $55^\circ$ . For this scenario, the loads on the prototype structure are approximately 25% higher than those computed for the corresponding  $0^\circ$  scenario. The large effect of flow field deviations on the loading of the prototype structure led to the design choice of a new foundation shape with a point symmetric base area. For this configuration, the overall loading on the structure is largely independent of the flow field direction. A polygonal rather than a round base shape was chosen, in order to avoid the necessity of high-cost formwork with curved surfaces. The polygon was defined as a nonagon, which allows for an arrangement of three supports, evenly distributed along the nine foundation corner points. This tripod support configuration is a further critical design enhancement. It forebodes instability problems that may be encountered when a structure with more supports is installed at a site with an uneven sea floor. The tripod support configuration may also reduce the amount of cost intensive sea floor preparation prior to the installation of the structure.

As demonstrated in [Chapter 5](#), the derivation of load reducing foundation shapes is highly dependent on the contribution of the wave and current loads at a particular site. For this reason, the PSD foundation is defined in terms of four adjustable shape variables



(a) Geometry parameterization

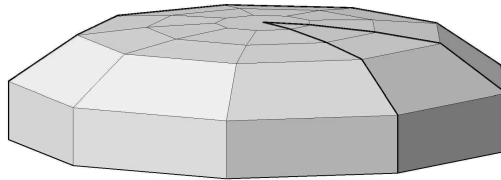
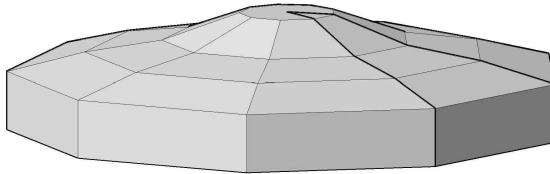
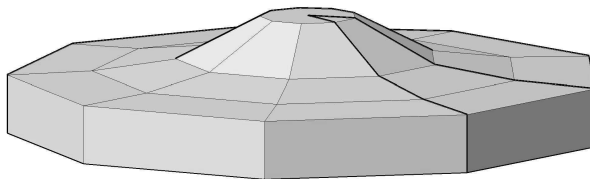
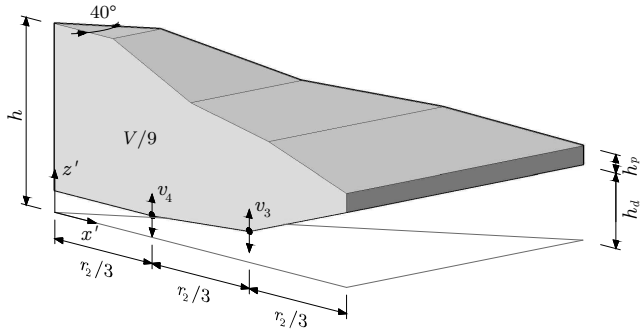
(b) Foundation shape for  $[v_1 \ v_2] = [2.9 \ 2.7] \text{ m}$ (c) Foundation shape for  $[v_1 \ v_2] = [2.3 \ 2.0] \text{ m}$ (d) Foundation shape for  $[v_1 \ v_2] = [1.9 \ 1.6] \text{ m}$ 

Figure 8.1: Foundation top geometry specifications and example shape variations used for offshore condition specific shape optimization.



(a) Geometry parameterization

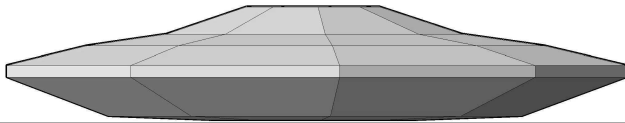
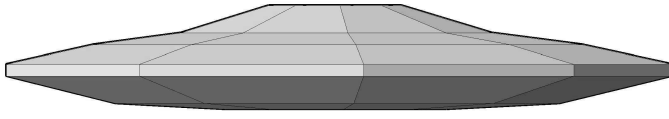
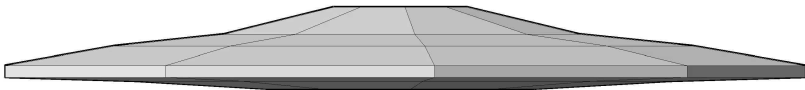
(b) Foundation shape for  $[v_3 \ v_4] = [0.2 \ 0.1] \text{ m}$ (c) Foundation shape for  $[v_3 \ v_4] = [0.5 \ 0.35] \text{ m}$ (d) Foundation shape for  $[v_3 \ v_4] = [1.1 \ 0.9] \text{ m}$ 

Figure 8.2: Foundation bottom geometry specifications and example shape variations used for offshore condition specific shape optimization.

$v_1, \dots, v_4$ , as defined in Figs. 8.1 and 8.2 with respect to the  $z'$  coordinate system axes. Using these variables, a site specific optimal solution can be found based on the design relevant load conditions. This pertains to both the foundation top shape, adjusted with variables  $v_1$  and  $v_2$ , and the foundation bottom shape, adjusted with variables  $v_3$  and  $v_4$ . As  $v_i$  is modified, the geometric variables  $r_1$  and  $r_2$  are adjusted such that the predefined volume of the structure is preserved, analogue to the approach followed in the two-dimensional studies of Secs. 5.3 and 5.4. The idea is to begin by determining a favorable shape for horizontal loading through an adjustment of variables  $v_1$  and  $v_2$ , while specifying a sufficiently large foundation base plate height  $h_p$  for later incorporation of the diffuser. For current dominated sites, the optimal structure for minimal horizontal loading will resemble the shape given in Fig. 8.1b, while in wave dominated conditions a shape similar to the one shown in Fig. 8.1d is favorable. Once a satisfactory top shape has been determined, the structure is further optimized with respect to the vertical loading on the structure by means of reducing  $h_p$  and introducing a diffuser on the foundation bottom with inlet and outlet height  $h_d$  (Fig. 8.2a). Through the adjustment of the variables  $v_3$  and  $v_4$ , the shape of the diffuser can once again be individualized under consideration of the site specific conditions. Following, the tripod supports and the cylinder transition piece for connection to the turbine are added to the structure. When adding the supports, parameter  $r_2$  is once again adjusted in order to preserve the volume constraint under consideration of the supports, which are in the form of circular cylinders. Finally, the loading on the end configuration is determined numerically, experimentally, or ideally using a hybrid numerical-experimental approach. Overall, the introduced PSD foundation concept allows for a straightforward, targeted, and efficient design process that leads to an optimal configuration for any given tidal turbine site. This design process is demonstrated in the following section by determining the optimal PSD configuration for the prototype site of the SeaTurtle project.

### 8.3 Optimization

In order to quantify the performance of the PSD foundation, the structure is configured under consideration of the critical offshore conditions measured as part of the SeaTurtle project (Tab. 3.3 on

page 52) and assessed in comparison to the prototype structure. For this purpose,  $V$  and  $h$  of the PSD foundation are set equal to  $311.125 \text{ m}^3$  and  $3 \text{ m}$ , respectively. These specifications are consistent with the dimensions of the prototype foundation. In addition,  $b$  is defined as  $3.5 \text{ m}$ .

Building on the findings of Chapter 5, the top shape of the foundation is configured such that the horizontal loads are minimized, while the bottom shape is optimized separately with respect to the vertical loading on the structure. The partitioned approach of separately optimizing the structure with respect to horizontal and vertical forces is plausible because of the perceptions of the 2D optimization studies. These studies showed that the introduction of the diffuser for vertical load control does not significantly alter the horizontal loads on the structure, and vice versa.

First, the foundation is defined according to Fig. 8.1a, with  $h_p = 1.5 \text{ m}$  and the constraint  $h_p \leq v_i \leq h$ . In addition, the design space is limited to  $v_2 \leq v_1$ , based on the findings of Section 5.3.2, which showed that the global optimum is within this subdomain for a comparable geometry specification. Using the optimization framework of Fig. 5.1 on page 100, an initial Monte Carlo point set of 20 shape variations is generated. Subsequently, the reduced modeling VFS-NWCT of Chapter 4 is used for CFD analysis of each shape subjected to the combined wave-current scenario, the critical load case for the given site. Based on the results, a Kriging objective function approximation is generated and refined in 9 LOLA-Voronoi iterations, after which the convergence criterion  $\text{NRMSD} < 2 \%$  was met. The global minimum of the final Kriging model occurs at  $[v_1 \ v_2] = [2.3 \ 2.0] \text{ m}$ , resulting in the foundation top shape given in Fig. 8.1c.

After specifying the top shape parameters, the optimization procedure is repeated for the bottom shape using the parameterization of Fig. 8.2a, with  $h_d = 1.2 \text{ m}$  and  $h_p = 0.3 \text{ m}$ . The constraints for  $v_3$  and  $v_4$  are set to  $0.1 \text{ m} \leq v_i \leq h_d$  and  $v_4 \leq v_3$ . The simulations of Section 5.4 showed that the vertical wave loads are very similar for all diffuser shapes, so long as at least a small gap beneath the structure remains. This gap is guaranteed by the specified lower constraint. Therefore, the optimization of the diffuser shape with the objective of minimizing lift is carried out based on the pure current load case, which is highly dependent on the design variables. Once again, the initial point set consists of 20 shapes. The Kriging model converged after 7 LOLA-Voronoi refinement iterations, resulting in the

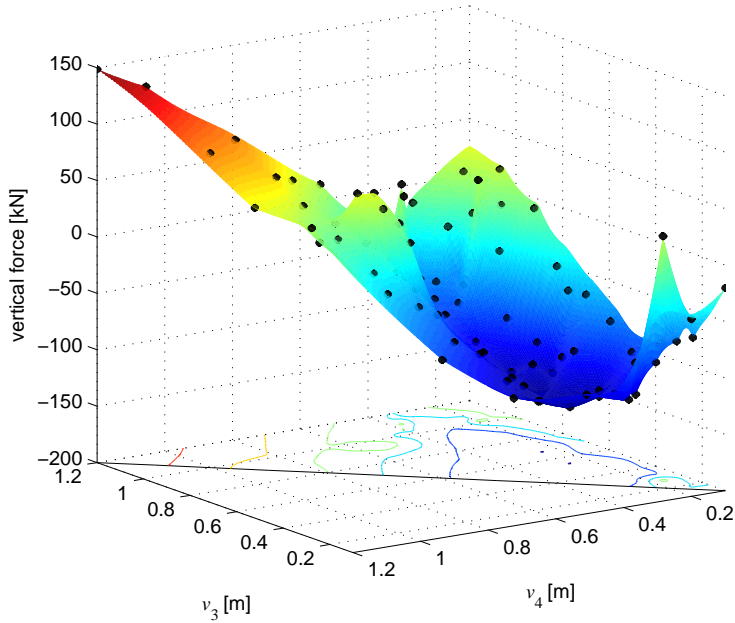


Figure 8.3: Diffuser vertical force Kriging objective function approximation. Dots indicate CFD results.

objective function approximation given in Fig. 8.3. In this case, the function shape does not consist of a pronounced optimum, but rather a region for which significant downwards forces of similar magnitude are attained. This region approximately spans across  $0.25 \text{ m} \leq v_3 \leq 0.8 \text{ m}$  and  $0.2 \text{ m} \leq v_4 \leq 0.4 \text{ m}$ . Within this range, the diffuser configuration is chosen based on practical implications. In order to avoid an overly reduced foundation to sea floor distance that may with time be blocked by debris, the bottom shape is defined with  $[v_3 \ v_4] = [0.5 \ 0.35] \text{ m}$ . The resulting structure is shown in Fig. 8.2c.

## 8.4 Assessment

The final optimized PSD foundation is assessed in detail using the high fidelity VOF based NWCT introduced in Chapter 2. The aim is to

compare the performance of the new design with the initial prototype foundation shape shown in Fig. 8.4a. As part of this analysis, three evenly spaced cylindrical supports with a diameter of 2 m are added to the PSD foundation geometry. In addition, a 5 m high cylindrical connection piece with a radius of 2.5 m is included on top of the foundation, analogue to the design of the prototype structure. The resulting structure is shown in Fig. 8.4b. The PSD foundation is analyzed numerically for the pure wave, pure current, and combined wave-current conditions defined as part of the SeaTurtle project. For these simulations, the boundary conditions and domain dimensions are defined in accordance with the specifications of Section 3.4.

The computed peak loads are summarized in Fig. 8.5, together with the previously determined prototype results. With respect to the horizontal loads, the new design out-performs the prototype structure for all three load cases. This holds true even in comparison to the prototype subjected to the  $0^\circ$  flow field direction. The critical load case for the prototype design comprised of the wave-current scenario at a  $55^\circ$  flow misalignment, for which loads of approximately 350 kN were determined. For the same load case, the direction invariant horizontal loads on the PSD foundation are reduced by over 30 %.

In addition, the new foundation is assessed with respect to the vertical loads on the structure, which are also summarized in Fig. 8.5. For the sake of better comparison, the results are given without the mean hydrostatic force  $F_{mhs}$ , which is constant and shape invariant. The added supports block part of the underflow and increase the resistance beneath the structure, thereby reducing the efficiency of the diffuser. In the simulation, the worst case scenario is considered, where

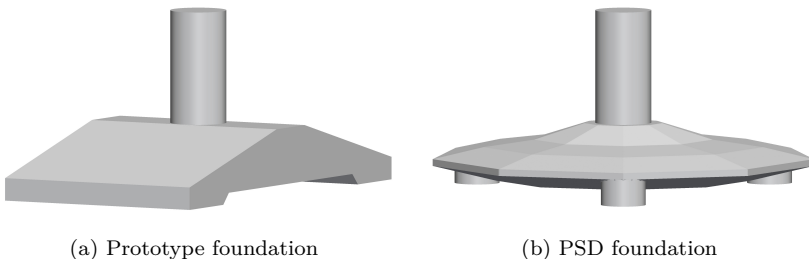


Figure 8.4: GBF shape comparison with equal volumes and heights.



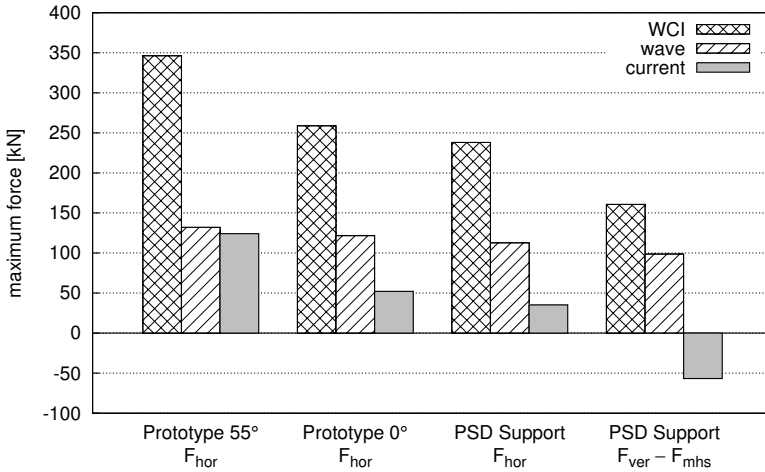
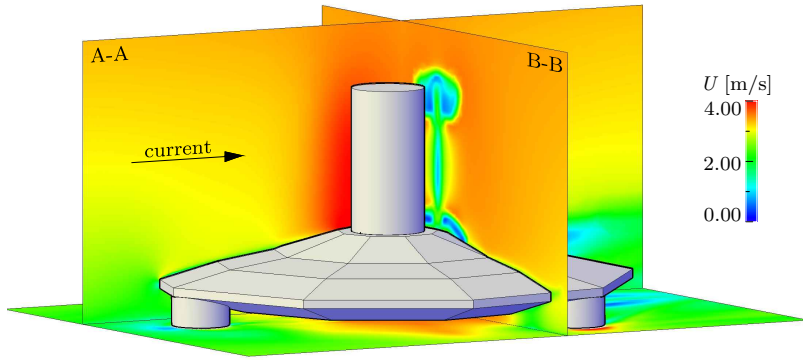


Figure 8.5: PSD foundation loads compared to the prototype design.

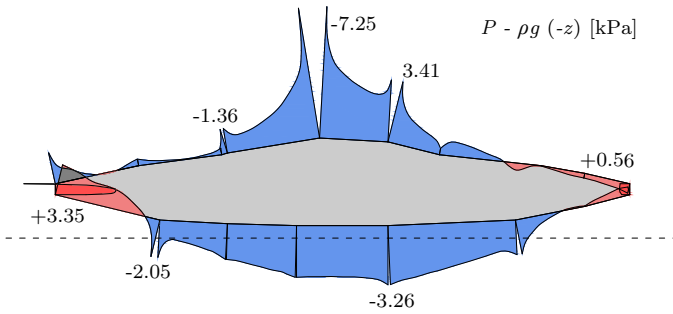
a support is blocking the diffuser central section. This effect is shown in the pressure plots of Fig. 8.6, which exhibit counteracting pressure distributions in the immediate vicinity of the supports. Nevertheless, for the pure current scenario a net downwards force is attained, amounting to approximately  $-55$  kN. The highest lift force ensues for the combined wave-current scenario. Remarkably, the magnitude of this forces is 33 % lower than the maximum horizontal force computed for the PSD foundation. A comparative study of various offshore wind foundation types carried out by Zaaiker (2003) identified the lift force as the dominant load contribution for GBFs. Evidently, the diffuser reduces lift to the extend that it is no longer the critical load contribution.

Finally, the overturning moment  $M_{ot}$  on the structure is analyzed. This moment is highly influenced by the turbine loads, which vary depending on the size of the device. Therefore, the focus of this analysis is not on the magnitude of  $M_{ot}$ , but rather on the time of occurrence of peak loads within the wave cycle during wave and wave-current loading. The moment is computed about the outer edge of the back supports, which is located 4.75 m from the foundation center when the front support is facing the flow field. Once again, the results are presented without the mean hydrostatic component  $M_{mhs}$ .

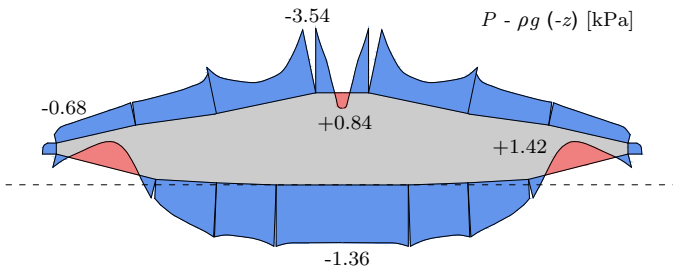
The load curves over one wave period are given in Figs. 8.7a and



(a) Velocity contour

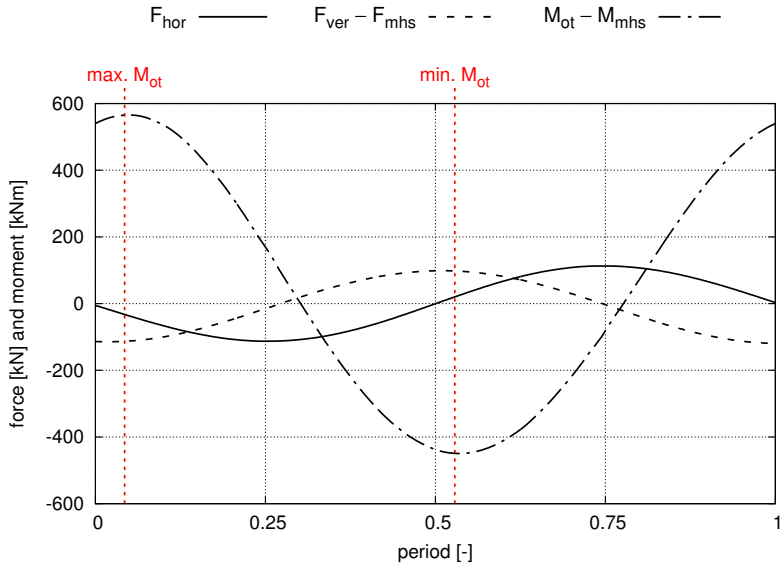


(b) Pressure distribution A-A

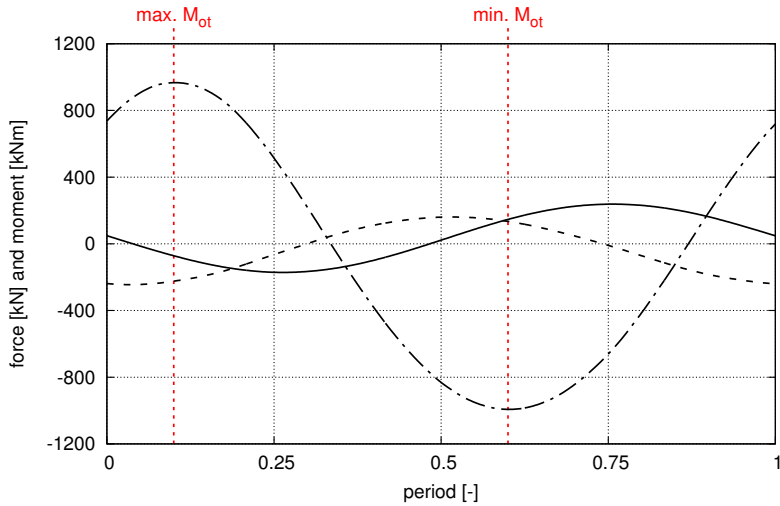


(c) Pressure distribution B-B

Figure 8.6: Current load case velocity and pressure solutions.



(a) Pure wave



(b) Combined wave-current

Figure 8.7: Simulated PSD foundation forces and overturning moment over one wave period computed with the NWCT.

8.7b for the pure wave scenario and combined wave-current scenario, respectively. The peak moments occur shortly after the peak vertical loads in the pure wave scenario, for the analyzed foundation dimensions. When the current is incorporated into the wave simulation, the time of the peak moments is shifted towards the peak horizontal loads. This shift is a consequence of differences in the degree by which the horizontal and vertical forces increase when the wave is combined with the current. While in the case of the horizontal forces the increase is greater than 100 %, a comparatively smaller increase is observed for the vertical forces, amounting to approximately 60 %. The smaller increase of the vertical forces can directly be contributed to the effect of the diffuser.

## 8.5 Conclusions and Summary

This chapter provided two major contributions to the overall framework of this thesis. First of all, the newly developed PSD foundation establishes an innovative GBF concept, consisting of the following key features:

- A clear framework for a targeted design process.
- An adaptive procedure adjustable to site specific conditions.
- Optimized solutions for horizontal and vertical load minimization.
- A hydrodynamic performance invariant of flow field directions.
- A stable and robust tripod support configuration.
- A lack of curved surfaces for simple formwork designs.

Secondly, the chapter demonstrated the capabilities of the numerical methods of this thesis as a powerful tool for the design of offshore structures. By applying the validated CFD optimization procedure, the critical horizontal loads on the initial prototype design were reduced by over 30 %, while the vertical loads were reduced to a sub-critical range. In addition, the methods allowed for a detailed analysis of flow field characteristics and load time series. Overall, this has resulted in a sound development of a new generation tidal turbine GBF shape.

---

## Chapter 9

# Conclusions and Outlook

---

The overall aim of this thesis was to approach and solve new challenges that have arisen as part of recent developments in the ocean energy sector. In particular, this concerns the modeling of complex wave-current flows and the analysis of the implications these flows hold for the design of offshore structures. This challenge was addressed through contributions that cover three main aspects:

- Development of numerical and experimental methods for analysis and optimization of offshore structures in waves and currents (Chapters 2, 4, and 6).
- Research on the physical intricacies of wave and current loads on offshore structures based on numerical and experimental modeling (Chapters 3, 5, and 7).
- Application of the methods and findings to the development of an advanced design process for tidal turbine gravity base foundations (Chapter 8).

The first aspect included the extension of CFD based wave modeling to incorporate a current flow. A VOF based NWCT was introduced that allows for the simulation of combined wave-current conditions, taking into account the interaction between the wave and the current field.

Particularly noteworthy is the possibility to combine the wave with a depth varying current using the NWCT, a task that is complicated by the rotational characteristic of the ensuing boundary layer flow. The overall methodology is particularly suitable for the assessment of distinct load cases and individual structure configurations, while it is limited by the relatively high computational costs of free surface CFD simulations.

In order to allow for efficient CFD wave-current modeling as part of optimization problems and extensive parameter studies, a reduced modeling methodology was developed. This method reduces the NWCT to a single phase model by replacing the physical free surface of the flow with what is referred to as a virtual free surface boundary condition. The VFS model has been developed in such a way that the general capabilities of the free surface approach are retained, including viscous wave-current modeling involving depth varying currents. Using the single phase VFS-NWCT, such simulations can be carried out at significantly lower computational costs, compared to the VOF based approach. The comparative efficiency gain was documented to be between one and two orders of magnitude.

In addition to the development of numerical methods, an experimental modeling approach for stable generation of laboratory wave-current conditions was introduced. This method uses a physical flow filter that dissipates unsteady fluctuations from pump driven current flows, while allowing for wave motion to pass through the setup. The dissipative and reflective properties of the filter were analyzed and documented to help determine the ideal configuration needed to generate desired flow conditions. Furthermore, the light-weight and cost effective filter design allows for efficient installation in any wave-current flume that operates with a current pump and a horizontal piston wave maker.

The research carried out as part of the second main aspect of this thesis applied the methods developed during the exploration of the first aspect to an analysis of wave-current flows and the ensuing forces on offshore structures. One of the major conclusions drawn from this research is that the results of a combined wave-current analysis may differ significantly from a linear superposition of the individual load cases. The latter approach is still frequently chosen in design practice because it allows for the utilization of simpler and computationally cheaper methods. However, this thesis demonstrated that depending on the contribution of the wave and current field, this simplified approach

---

can underestimate the peak loading on the structure by over 30%. This large discrepancy strongly motivates the utilization of the introduced combined wave-current simulation methods in the design process of offshore structures.

Furthermore, the new methods were applied as part of shape optimization studies of bottom mounted structures with the objective to reduce horizontal and vertical forces. For this purpose, an optimization framework was introduced, which incorporates the reduced modeling VFS-NWCT in combination with response surface modeling based on Kriging. Several key findings were drawn from the application of the framework to investigations of optimal shape characteristics. It was found that the smallest peak wave loads are attained for shapes with a maximum near sea floor volume distribution, while the current loads are dictated by the distribution of dead water zones and separation points. As a result, optimal shapes for current and wave loads are typically different, while yet another solution is plausible for the combined scenario. Consequently, optimal shape design of offshore structures in waves-current flows is site dependent and requires the utilization of methods that accurately capture the combined flow field. Additionally, the importance of taking into account the vertical forces on the structure was demonstrated, which usually exceed the horizontal loads if no counteractive measures are taken. It was shown that the introduction of a diffuser beneath the body is an effective approach to reduce the vertical loads as far as initiating a downwards force on the structure.

In addition to the numerical tests, experimental shape optimization studies were carried out using the new wave-current filter setup. These experiments confirmed and substantiated the numerical optimization approach and established a benchmark for validation and verification of related models and methods. In terms of optimization, it was found that the numerically and experimentally determined objective function predictions are in close agreement. This holds true for wave, current, and wave-current loading. In addition, both modeling approaches rendered matching tendencies concerning wave-current load predictions, and changes in objective function values for two-dimensional vs. three-dimensional flows. While an excellent agreement of the load sensitivities was observed, the quantitative differences in the individual load results were substantial in some cases. This behavior motivates a hybrid modeling approach in which a pre-selection of favorable shapes is carried out based on the introduced numerical methods, followed by an application of the developed experimental methods for detailed

analysis and load quantification of a few selected shapes.

Finally, the third main aspect covered in this thesis was the development of a novel approach to GBF design through a collective application of the developed methods and accumulated findings. The developed PSD foundation concept consists of a point symmetric structure that can be configured to render an optimal hydrodynamic performance under consideration of the design relevant wave-current conditions at a given site. As part of the procedure, the horizontal loading on the structure is minimized using two design variables that control the top shape of the structure, followed by an adjustment of two diffuser shape variables to reduce the vertical loading. This procedure was followed to configure the PSD foundation for the critical loads at an offshore site for tidal turbines. A numerical analysis of the newly developed foundation revealed a reduction of the horizontal loads by over 30%, compared to the previous prototype design. In addition, the vertical loads were reduced even further, below the magnitude of the horizontal component. Special features of the design are a stable tripod support configuration and the absence of curved surfaces for the main body, which reduces costs for fabrication and installation. The newly developed design process for advanced GBFs concludes the scope of this thesis.

Based on the presented research, further development of the introduced methods and modeling aspects is conceivable as part of future research. One possibility is an extension of the introduced optimization framework. The presented optimization studies provide a good understanding of the offshore condition dependent design space characteristics. This knowledge allows for a specification of high quality initial designs, which may be improved further using additional optimization steps. This could for example be achieved by incorporating the vertex morphing method (Hojjat et al., 2014) into the optimization framework.

Another offshore foundation design related topic that may be of interest in the future is the investigation of scour. The research of this thesis was largely based on experiences from previous prototype projects, in particular the SeaTurtle project carried out in South Korea. At the project site near Jindo Island, the foundation was installed on solid rock, where scour held no significance. In fact, most sites suitable for harvesting tidal energy share this characteristic of being relatively sediment free, as a result of the high tidal flow velocities (Owen, 2007). However, should the PSD foundation be considered for an application



involving a sandy substrate, scour protection studies should be carried out with a particular focus on the influence of the diffuser.

The effect of marine growth on tidal turbine foundations is another topic of interest for future research. Some work on the subject has been carried out with regards to offshore foundations in general (e.g. [Wolfram et al., 1985](#); [Schoefs, 2002](#); [Schoefs et al., 2004](#)) or specifically geared towards offshore wind turbine supports (e.g. [Shi et al., 2012](#)). However, the findings are not generally transferable to tidal turbine GBFs, because marine growth is dependent on site conditions such as the current velocities. These velocities are much higher at tidal turbine sites than those encountered at sites of most other offshore structures. Therefore, valuable information could be drawn from an analysis of how roughness and thickness of marine growth affects the hydrodynamic performance of tidal turbine foundations, once long term marine growth data from tidal turbine sites becomes available.

As mentioned in the introduction of this thesis, numerous studies have already been carried out in order to analyze and optimize tidal turbines. In addition, this thesis now provides a thorough treatment of tidal turbine GBFs. With this information available, the logical next step is to combine the turbine and the support structure in the modeling process, in order to investigate their interaction. As part of such studies, the consideration of an irregular sea state may be of interest. Such conditions are of minor relevance for the foundation design, which is mainly dictated by extreme individual events. However, daily flow conditions including irregular waves are of high interest in the design and configuration of the turbines. Therefore, it may be valuable to extend the methods of this thesis to incorporate irregular sea states for combined turbine-foundation studies. Such an extension pertains to the NWCT of [Chapter 2](#), the VFS reduced modeling approach of [Chapter 4](#), and the experimental filtering method of [Chapter 6](#).

The presented work sets a solid foundation for future developments. It is hoped to provide inspiration for continued research on numerical and experimental modeling of offshore structures. As shown throughout this thesis, the development and application of these models bears enormous potential to unveil substantial technological advancements in the ocean energy sector. In the end, this may be the key to crucial breakthroughs in the development of innovative technologies.



---

# Bibliography

---

- Abdullah, A.J., 1949. Wave motion at the surface of a current which has an exponential distribution of vorticity. *Annals of the New York Academy of Sciences* 51, 425–441.
- Anbarsooz, M., Passandideh-Fard, M., Moghiman, M., 2013. Fully nonlinear viscous wave generation in numerical wave tanks. *Ocean Engineering* 59, 73–85.
- Andre, M., Mier-Torrecilla, M., Wüchner, R., Bletzinger, K.U., 2014. A comparative study of finite element and lattice Boltzmann methods for estimation of dynamic wind loads, in: *The Sixth International Symposium on Computational Wind Engineering*, Hamburg, Germany.
- Apsley, D., Hu, W., 2003. CFD simulation of two-and three-dimensional free-surface flow. *International Journal for Numerical Methods in Fluids* 42, 465–491.
- Aurenhammer, F., 1991. Voronoi diagrams - a survey of a fundamental geometric data structure. *ACM Computing Surveys (CSUR)* 23, 345–405.
- Bahaj, A., Molland, A., Chaplin, J., Batten, W., 2007. Power and thrust measurements of marine current turbines under various hydrodynamic flow conditions in a cavitation tunnel and a towing tank. *Renewable Energy* 32, 407–426.

- Bai, G., Li, J., Fan, P., Li, G., 2013. Numerical investigations of the effects of different arrays on power extractions of horizontal axis tidal current turbines. *Renewable Energy* 53, 180–186.
- Barltrop, N., Varyani, K., Grant, A., Clelland, D., Pham, X., 2007. Investigation into wave-current interactions in marine current turbines. *Proceedings of the Institution of Mechanical Engineers, Part A: Journal of Power and Energy* 221, 233–242.
- Barltrop, N.D., Adams, A.J., Hallam, M., 1991. *Dynamics of fixed marine structures*. Butterworth-Heinemann, Oxford, UK.
- Batchelor, G., 1968. *An introduction to fluid mechanics*. Cambridge University Press, Cambridge, UK.
- Batten, W., Bahaj, A., Molland, A., Chaplin, J., 2006. Hydrodynamics of marine current turbines. *Renewable Energy* 31, 249–256.
- Batten, W., Bahaj, A., Molland, A., Chaplin, J., 2008. The prediction of the hydrodynamic performance of marine current turbines. *Renewable Energy* 33, 1085–1096.
- Batten, W.M., Harrison, M., Bahaj, A., 2013. Accuracy of the actuator disc-RANS approach for predicting the performance and wake of tidal turbines. *Philosophical Transactions of the Royal Society A: Mathematical, Physical and Engineering Sciences* 371.
- Bayraktar, E., Mierka, O., Turek, S., 2012. Benchmark computations of 3D laminar flow around a cylinder with CFX, OpenFOAM and FeatFlow. *International Journal of Computational Science and Engineering* 7, 253–266.
- Besnard, E., Schmitz, A., Hefazi, H., Shinde, R., 2007. Constructive neural networks and their application to ship multidisciplinary design optimization. *Journal of Ship Research* 51, 297–312.
- Bidoae, R., Ciobotaru, R.M., Raad, P.E., 2003. An Eulerian-Lagrangian Marker and Micro Cell Method for Simulating Fluid Interaction with Solid/Porous Bodies, in: *IUTAM Symposium on Integrated Modeling of Fully Coupled Fluid Structure Interactions Using Analysis, Computations and Experiments*, New Jersey, USA, pp. 439–452.

- Birk, L., 2009. Application of constrained multi-objective optimization to the design of offshore structure hulls. *Journal of Offshore Mechanics and Arctic Engineering* 131.
- Bishop, J.R., 1981. Experience with scour at the Christchurch Bay tower. Technical Report. National Maritime Institute.
- Blanchfield, J., Garrett, C., Wild, P., Rowe, A., 2008. The extractable power from a channel linking a bay to the open ocean. *Proceedings of the Institution of Mechanical Engineers, Part A: Journal of Power and Energy* 222, 289–297.
- Blunden, L., Bahaj, A., 2007. Tidal energy resource assessment for tidal stream generators. *Proceedings of the Institution of Mechanical Engineers, Part A: Journal of Power and Energy* 221, 137–146.
- Blunden, L.S., 2009. New approach to tidal stream energy analysis at sites in the English Channel. Ph.D. thesis. University of Southampton, Southampton, UK.
- Bonnans, J.F., Gilbert, J.C., Lemaréchal, C., Sagastizabal, C., 2003. *Numerical Optimization*. Springer, Berlin Heidelberg, Germany.
- Bredmose, H., Jacobsen, N.G., 2011. Vertical wave impacts on offshore wind turbine inspection platforms, in: *The Thirtieth International Conference on Ocean, Offshore and Arctic Engineering*, Rotterdam, Netherlands, pp. 645–654.
- Breton, S.P., Moe, G., 2009. Status, plans and technologies for offshore wind turbines in Europe and North America. *Renewable Energy* 34, 646–654.
- Breuer, M., 2002. *Direkte Numerische Simulation und Large-Eddy Simulation turbulenter Strömungen auf Hochleistungsrechnern*. Shaker Verlag, Aachen, Germany.
- Campana, E., Peri, D., Rossetti, M., 1999. Ships of the optimum shape by direct numerical optimization, in: *SIAM Conference on Optimization*, Atlanta, Georgia.
- Campana, E.F., Peri, D., Tahara, Y., Stern, F., 2006. Shape optimization in ship hydrodynamics using computational fluid dynamics. *Computer Methods in Applied Mechanics and Engineering* 196, 634–651.

- Chakrabarti, S.K., Naftzger, R.A., 1976. Wave interaction with a submerged open-bottom structure, in: Offshore Technology Conference, Houston, TX, USA, pp. 109–124.
- Chamorro, L., Hill, C., Morton, S., Ellis, C., Arndt, R., Sotiropoulos, F., 2013. On the interaction between a turbulent open channel flow and an axial-flow turbine. *Journal of Fluid Mechanics* 716, 658–670.
- Chanson, H., Trevethan, M., Koch, C., 2007. Discussion of “Turbulence measurements with acoustic Doppler velocimeters”. *Journal of Hydraulic Engineering* 133, 1283–1286.
- Chapman, D.C., 1985. Numerical treatment of cross-shelf open boundaries in a barotropic coastal ocean model. *Journal of Physical Oceanography* 15, 1060–1075.
- Chella, M.A., Tørum, A., Myrhaug, D., 2012. An overview of wave impact forces on offshore wind turbine substructures. *Energy Procedia* 20, 217–226.
- Chen, A., Ye, J., 2009. Research on four-layer back propagation neural network for the computation of ship resistance, in: International Conference on Mechatronics and Automation, Changchun, China, pp. 2537–2541.
- Chen, H.C., 2013. CFD Simulation of Directional Short-Crested Waves on a Jack-up Structure. *International Journal of Offshore and Polar Engineering* 23, 38–45.
- Chen, S., Johnson, D.B., Raad, P.E., Fadda, D., 1997. The surface marker and micro cell method. *International Journal for Numerical Methods in Fluids* 25, 749–778.
- Choi, J., Yoon, S.B., 2009. Numerical simulations using momentum source wave-maker applied to RANS equation model. *Coastal Engineering* 56, 1043–1060.
- Christensen, E.D., Deigaard, R., 2001. Large eddy simulation of breaking waves. *Coastal Engineering* 42, 53–86.
- Clayton, V., Andre, G., 1997. *GSLIB - Geostatistical software library and user’s guide*. Oxford University Press, Oxford, UK.

- Clément, A., 1996. Coupling of two absorbing boundary conditions for 2D time-domain simulations of free surface gravity waves. *Journal of Computational Physics* 126, 139–151.
- Cressie, N., 1985. Fitting variogram models by weighted least squares. *Journal of the International Association for Mathematical Geology* 17, 563–586.
- Cressie, N., 1992. Statistics for spatial data. *Terra Nova* 4, 613–617.
- Crombecq, K., Couckuyt, I., Gorissen, D., Dhaene, T., 2009a. Space-filling sequential design strategies for adaptive surrogate modelling, in: *The First International Conference on Soft Computing Technology in Civil, Structural and Environmental Engineering*, Funchal, Madeira, Portugal.
- Crombecq, K., De Tommasi, L., Gorissen, D., Dhaene, T., 2009b. A novel sequential design strategy for global surrogate modeling, in: *Winter Simulation Conference*, Austin, TX, USA, pp. 731–742.
- Crombecq, K., Dhaene, T., 2010. Generating sequential space-filling designs using genetic algorithms and monte carlo methods, in: *Simulated Evolution and Learning*. Springer, Berlin Heidelberg, Germany, pp. 80–84.
- Crombecq, K., Gorissen, D., Deschrijver, D., Dhaene, T., 2011. A novel hybrid sequential design strategy for global surrogate modeling of computer experiments. *SIAM Journal on Scientific Computing* 33, 1948–1974.
- Dalrymple, R.A., 1977. A numerical model for periodic finite amplitude waves on a rotational fluid. *Journal of Computational Physics* 24, 29–42.
- Daus, P., Sepri, M., Biskup, F., Arlitt, R., 2011. Methoden zur ermittlung und bewertung von standortdaten für die nutzung der zeitenströmungsenergie. *Dresdner Wasserbauliche Mitteilungen* 45, 347–359.
- Davies, P., Germain, G., Gaurier, B., Boisseau, A., Perreux, D., 2013. Evaluation of the durability of composite tidal turbine blades. *Philosophical Transactions of the Royal Society A: Mathematical, Physical and Engineering Sciences* 371, 1–15.

- Davis, J.C., Sampson, R.J., 2002. Statistics and data analysis in geology. volume 3. Wiley, New York, NY, USA.
- Dean, R., 1965. Stream function representation of nonlinear ocean waves. *Journal of Geophysical Research* 70, 4561–4572.
- Dean, R.G., 1974. Evaluation and development of water wave theories for engineering application. US Coastal Engineering Research Center, Fort Belvoir, VA, USA.
- Dejhalla, R., Mrša, Z., Vuković, S., 2002. A genetic algorithm approach to the problem of minimum ship wave resistance. *Marine Technology* 39, 187–195.
- Demirbilek, Z., Vincent, C.L., 2002. Coastal Engineering Manual. Chapter II-1-2. Water Wave Mechanics. Engineer Manual 1110-2-1100. US Army Corps of Engineers , II-1-1–121.
- Dennis, S., Chang, G.Z., 1970. Numerical solutions for steady flow past a circular cylinder at Reynolds numbers up to 100. *Journal of Fluid Mechanics* 42, 471–489.
- Edgar, T., Himmelblau, D., Lasdon, L., 2001. Optimization of chemical processes. McGraw-Hill, New York, NY, USA.
- Eleni, D.C., Athanasios, T.I., Dionissios, M.P., 2012. Evaluation of the turbulence models for the simulation of the flow over a National Advisory Committee for Aeronautics (NACA) 0012 airfoil. *Journal of Mechanical Engineering Research* 4, 100–111.
- Engquist, B., Majda, A., 1977. Absorbing boundary conditions for numerical simulation of waves. *Proceedings of the National Academy of Sciences* 74, 1765–1766.
- Evans, E., 1987. Tidal stream energy. Ph.D. thesis. University of Plymouth, Plymouth, UK.
- Faez Hassan, H., El-Shafie, A., Karim, O.A., 2012. Tidal current turbines glance at the past and look into future prospects in Malaysia. *Renewable and Sustainable Energy Reviews* 16, 5707–5717.
- Faudot, C., Dahlhaug, O.G., 2012. Prediction of wave loads on tidal turbine blades. *Energy Procedia* 20, 116–133.



- Fenton, J., 1979. A high-order cnoidal wave theory. *Journal of Fluid Mechanics* 94, 129–161.
- Fenton, J., 1988. The numerical solution of steady water wave problems. *Computers & Geosciences* 14, 357–368.
- Fenton, J., McKee, W., 1990. On calculating the lengths of water waves. *Coastal Engineering* 14, 499–513.
- Fenton, J.D., 1985. A fifth-order Stokes theory for steady waves. *Journal of Waterway, Port, Coastal, and Ocean Engineering* 111, 216–234.
- Ferziger, J.H., Perić, M., 2002. Computational methods for fluid dynamics. volume 3. Springer, Berlin Heidelberg, Germany.
- Finnegan, W., Meere, M., Goggins, J., 2013. The wave excitation forces on a truncated vertical cylinder in water of infinite depth. *Journal of Fluids and Structures* 40, 201–213.
- Flood, I., Kartam, N., 1994. Neural networks in civil engineering. I: Principles and understanding. *Journal of Computing in Civil Engineering* 8, 131–148.
- Freitas, C., 1995. Perspective: selected benchmarks from commercial CFD codes. *Journal of Fluids Engineering* 117, 208–218.
- Funke, S.W., Farrell, P.E., Piggott, M., 2014. Tidal turbine array optimisation using the adjoint approach. *Renewable Energy* 63, 658–673.
- Galloway, P., Myers, L., Bahaj, A., 2010. Studies of a scale tidal turbine in close proximity to waves, in: *The Third International Conference on Ocean Energy*, Bilbao, Spain.
- Gant, S., Stallard, T., 2008. Modelling a tidal turbine in unsteady flow, in: *The Eighteenth International Offshore and Polar Engineering Conference*, Vancouver, Canada, pp. 473–480.
- García, C.M., Cantero, M.I., Niño, Y., García, M.H., 2005. Turbulence measurements with acoustic Doppler velocimeters. *Journal of Hydraulic Engineering* 131, 1062–1073.
- García, J., Oñate, E., 2003. An unstructured finite element solver for ship hydrodynamics problems. *Journal of Applied Mechanics* 70, 18–26.

- Garrett, C., Cummins, P., 2004. Generating power from tidal currents. *Journal of Waterway, Port, Coastal, and Ocean engineering* 130, 114–118.
- Garrett, C., Cummins, P., 2005. The power potential of tidal currents in channels. *Proceedings of the Royal Society A: Mathematical, Physical and Engineering Science* 461, 2563–2572.
- Garrloch, S., Baliga, B., 2006. A PLIC volume tracking method for the simulation of two-fluid flows. *International Journal for Numerical Methods in Fluids* 52, 1093–1134.
- Garrison, C., Snider, R., 1970. Wave Forces on Large Submerged Tanks. Technical Report. Coastal and Ocean Engineering Division, Texas A&M University, Report No. 117-COE.
- Givoli, D., 1991. Non-reflecting boundary conditions. *Journal of Computational Physics* 94, 1–29.
- Givoli, D., 2004. High-order local non-reflecting boundary conditions: a review. *Wave Motion* 39, 319–326.
- Glover, F., 1999. Scatter Search and Path Relinking, in: *New Ideas in Optimization*. McGraw-Hill Ltd., Maidenhead, UK, England, pp. 297–316.
- Goring, D.G., Nikora, V.I., 2002. Despiking acoustic Doppler velocimeter data. *Journal of Hydraulic Engineering* 128, 117–126.
- Gorissen, D., Couckuyt, I., Demeester, P., Dhaene, T., Crombecq, K., 2010. A surrogate modeling and adaptive sampling toolbox for computer based design. *The Journal of Machine Learning Research* 11, 2051–2055.
- Grabbe, M., Lalander, E., Lundin, S., Leijon, M., 2009. A review of the tidal current energy resource in Norway. *Renewable and Sustainable Energy Reviews* 13, 1898–1909.
- Graham, J., 1993. Report on the session comparing computation of flow past circular cylinders with experimental data, in: *Bluff-Body Wakes, Dynamics and Instabilities*. Springer, pp. 317–323.
- Gresho, P.M., 1991. Incompressible fluid dynamics: some fundamental formulation issues. *Annual Review of Fluid Mechanics* 23, 413–453.

- Grigoropoulos, G.J., Chalkias, D.S., 2010. Hull-form optimization in calm and rough water. *Computer-Aided Design* 42, 977–984.
- Grilli, S.T., Voropayev, S.I., Testik, F.Y., Fernando, H.J.S., 2003. Numerical modeling and experiments of wave shoaling over semi-buried cylinders in sandy bottom, in: *The Thirteenth International Offshore and Polar Engineering Conference*, Honolulu, HI, USA.
- Griva, I., Nash, S.G., Sofer, A., 2009. *Linear and nonlinear optimization*. Siam, Philadelphia, PA, USA.
- Gueyffier, D., Li, J., Nadim, A., Scardovelli, R., Zaleski, S., 1999. Volume-of-fluid interface tracking with smoothed surface stress methods for three-dimensional flows. *Journal of Computational Physics* 152, 423–456.
- Guilcher, P., Brosset, L., Couty, N., Le Touzé, D., 2012. Simulations of Breaking Wave Impacts On a Rigid Wall At Two Different Scales With a Two Phase Fluid Compressible SPH Model., in: *The Twenty-second International Offshore and Polar Engineering Conference*, Rhodes, Greece, pp. 460–472.
- Ha, T., Lin, P., Cho, Y.S., 2013. Generation of 3D regular and irregular waves using Navier–Stokes equations model with an internal wave maker. *Coastal Engineering* 76, 55–67.
- Hafsia, Z., Hadj, M.B., Lamloumi, H., Maalel, K., 2009. Internal inlet for wave generation and absorption treatment. *Coastal Engineering* 56, 951–959.
- Halvorsen, M., Carlson, T., Copping, A., 2011. Effects of tidal turbine noise on fish. Technical Report. Pacific Northwest National Laboratory, Sequim, WA, USA, PNNL Report-20787.
- Harding, S.F., Bryden, I.G., 2012. Development of Fixed Hydrodynamic Lifting Surfaces to Stabilise Anchoring Structures in Energetic Tidal Flows, in: *The Thirty-first International Conference on Ocean, Offshore and Arctic Engineering*, Rio de Janeiro, Brazil, pp. 343–351.
- Harlow, F., Amsden, A., Nix, J., 1976. Relativistic fluid dynamics calculations with the particle-in-cell technique. *Journal of Computational Physics* 20, 119–129.

- Harlow, F.H., Welch, J.E., 1965. Numerical calculation of time-dependent viscous incompressible flow of fluid with free surface. *Physics of Fluids* 8, 2182–2189.
- Hart, C.G., Vlahopoulos, N., 2010. An integrated multidisciplinary particle swarm optimization approach to conceptual ship design. *Structural and Multidisciplinary Optimization* 41, 481–494.
- Hassoun, M.H., 1995. *Fundamentals of artificial neural networks*. MIT Press, Cambridge, MA, USA.
- Haupt, S.E., Zajaczkowski, F.J., Peltier, L.J., 2011. Detached eddy simulation of atmospheric flow about a surface mounted cube at high Reynolds number. *Journal of Fluids Engineering* 133, 1–8.
- Hazra, S.B., 2009. *Large-scale PDE-constrained Optimization in Applications*. volume 49. Springer, Berlin Heidelberg, Germany.
- Hendriks, I.E., van Duren, L.A., Herman, P.M., 2006. Turbulence levels in a flume compared to the field: implications for larval settlement studies. *Journal of Sea Research* 55, 15–29.
- Heronimus, W., Margarella, P., McPherson, R., Ewing, D., 1974. On the extraction of kinetic energy from oceanic and tidal river currents, in: *MacArthur workshop on the feasibility of extracting usable energy from the Florida current*, Palm Beach Shores, FL, USA.
- Hirsch, C., 2007. *Numerical Computation of Internal and External Flows: The Fundamentals of Computational Fluid Dynamics*. volume 1. Butterworth-Heinemann, Oxford, UK.
- Hirt, C., Nichols, B., Romero, N., 1975. *SOLA: A Numerical Solution Algorithm for Transient Fluid Flows*. National Technical Information Service, Los Alamos Scientific Lab, NM, USA.
- Hirt, C.W., Nichols, B.D., 1981. Volume of fluid (VOF) method for the dynamics of free boundaries. *Journal of Computational Physics* 39, 201–225.
- Hojjat, M., Stavropoulou, E., Bletzinger, K.U., 2014. The vertex morphing method for node-based shape optimization. *Computer Methods in Applied Mechanics and Engineering* 268, 494–513.

- Hölscher, N., Niemann, H.J., 1998. Towards quality assurance for wind tunnel tests: A comparative testing program of the Windtechnologische Gesellschaft. *Journal of Wind Engineering and Industrial Aerodynamics* 74, 599–608.
- Iafrati, A., Babanin, A., Onorato, M., 2014. Modeling of ocean–atmosphere interaction phenomena during the breaking of modulated wave trains. *Journal of Computational Physics* 271, 151–171.
- Idelsohn, S.R., Oñate, E., Sacco, C., 1999. Finite element solution of free-surface ship-wave problems. *International Journal for Numerical Methods in Engineering* 45, 503–528.
- Israeli, M., Orszag, S.A., 1981. Approximation of radiation boundary conditions. *Journal of Computational Physics* 41, 115–135.
- Issa, R.I., 1986. Solution of the implicitly discretised fluid flow equations by operator-splitting. *Journal of Computational Physics* 62, 40–65.
- Janson, C., Larsson, L., 1996. A method for the optimization of ship hulls from a resistance point of view, in: *The Twenty-first Symposium on Naval Hydrodynamics*, Trondheim, Norway.
- Jasak, H., 1996. Error analysis and estimation for the finite volume method with applications to fluid flows. Ph.D. thesis. Imperial College London (University of London), London, UK.
- de Jesus Henriques, T., Tedds, S., Botsari, A., Najafian, H., Sutcliffe, C., Owen, I., Poole, R., 2013. The Effects of Wave-Current Interactions on the Performance of a Model Horizontal Axis Tidal, in: *The Tenth European Wave and Tidal Energy Conference*, Aalborg, Denmark.
- Kamath, A., Bihs, H., Arntsen, Ø.A., 2013. Evaluation of Hydrodynamic Efficiency of an Oscillating Water Column Device through CFD Simulation, in: *The Twenty-third International Offshore and Polar Engineering Conference*, Anchorage, Alaska, USA, pp. 960–968.
- Kandasamy, M., Peri, D., Ooi, S.K., Carrica, P., Stern, F., Campana, E.F., Osborne, P., Cote, J., Macdonald, N., de Waal, N., 2011. Multi-fidelity optimization of a high-speed foil-assisted semi-planing catamaran for low wake. *Journal of Marine Science and Technology* 16, 143–156.

- Karsten, R., McMillan, J., Lickley, M., Haynes, R., 2008. Assessment of tidal current energy in the Minas Passage, Bay of Fundy. *Proceedings of the Institution of Mechanical Engineers, Part A: Journal of Power and Energy* 222, 493–507.
- Khorsandi, B., Mydlarski, L., Gaskin, S., 2012. Noise in turbulence measurements using acoustic doppler velocimetry. *Journal of Hydraulic Engineering* 138, 829–838.
- Kim, H., Jeong, S., Yang, C., Noblesse, F., 2011. Hull form design exploration based on response surface method, in: *The Twenty-first International Offshore and Polar Engineering Conference*, Maui, HI, USA, pp. 816–825.
- Kim, M., Niedzwecki, J., Roesset, J., Park, J., Hong, S., Tavassoli, A., 2001. Fully nonlinear multidirectional waves by a 3-D viscous numerical wave tank. *Journal of Offshore Mechanics and Arctic Engineering* 123, 124–133.
- Kofoed, J.P., Frigaard, P., Friis-Madsen, E., Sørensen, H.C., 2006. Prototype testing of the wave energy converter wave dragon. *Renewable Energy* 31, 181–189.
- Korteweg, D., de Vries, G., 1895. On the change of form of long waves advancing in a rectangular canal, and on a new type of long stationary waves. *Philosophical Magazine* 39, 422–433.
- Kosmas, O., Vlachos, D., 2012. Simulated annealing for optimal ship routing. *Computers & Operations Research* 39, 576–581.
- Kulkarni, V., Sahoo, N., Chavan, S.D., 2011. Simulation of honeycomb–screen combinations for turbulence management in a subsonic wind tunnel. *Journal of Wind Engineering and Industrial Aerodynamics* 99, 37–45.
- Lal, A., Elangovan, M., 2008. CFD simulation and validation of flap type wave-maker. *World Academy of Sciences, Engineering and Technology* 46, 76–82.
- Lam, N.S.N., 1983. Spatial interpolation methods: a review. *The American Cartographer* 10, 129–150.
- Larsen, J., Dancy, H., 1983. Open boundaries in short wave simulations—a new approach. *Coastal Engineering* 7, 285–297.

- Lauder, B.E., Spalding, D., 1974. The numerical computation of turbulent flows. *Computer Methods in Applied Mechanics and Engineering* 3, 269–289.
- Laws, E., Livesey, J., 1978. Flow through screens. *Annual Review of Fluid Mechanics* 10, 247–266.
- Le Mehaute, B., Divoky, D., Lin, A., 1968. Shallow water waves a comparison of theories and experiments. *Coastal Engineering Proceedings* 11, 86–108.
- Lee, C., Cho, Y.S., Yum, K., 2001. Internal generation of waves for extended Boussinesq equations. *Coastal Engineering* 42, 155–162.
- Lee, C., Suh, K.D., 1998. Internal generation of waves for time-dependent mild-slope equations. *Coastal Engineering* 34, 35–57.
- Li, B., Fleming, C.A., 2001. Three-dimensional model of Navier-Stokes equations for water waves. *Journal of Waterway, Port, Coastal, and Ocean Engineering* 127, 16–25.
- Li, Y., Lin, M., 2010. Wave-body interactions for a surface-piercing body in water of finite depth. *Journal of Hydrodynamics, Ser. B* 22, 745–752.
- Lighthill, J., 1986. Fundamentals concerning wave loading on offshore structures. *Journal of Fluid Mechanics* 173, 667–681.
- Lin, P., Karunarathna, S., 2007. Numerical study of solitary wave interaction with porous breakwaters. *Journal of Waterway, Port, Coastal, and Ocean Engineering* 133, 352–363.
- Lin, P., Liu, P.L.F., 1998. A numerical study of breaking waves in the surf zone. *Journal of Fluid Mechanics* 359, 239–264.
- Lin, P., Liu, P.L.F., 1999. Internal wave-maker for Navier-Stokes equations models. *Journal of Waterway, Port, Coastal, and Ocean Engineering* 125, 207–215.
- Lissamen, P., Radkey, R., 1979. Coriolis program: a review of the status of the ocean turbine energy system, in: *OCEANS'79*, San Diego, CA, USA, pp. 559–565.

- Liu, D., Lin, P., 2008. A numerical study of three-dimensional liquid sloshing in tanks. *Journal of Computational Physics* 227, 3921–3939.
- Liu, Z., Lin, Z., Liao, S., 2012. Nonlinear interaction between shear current and multiple waves, in: *The Twenty-second International Offshore and Polar Engineering Conference*, Rhodes, Greece, pp. 17–22.
- Marklund, J., 2013. Under-body and Diffuser Flows of Passenger Vehicles. Ph.D. thesis. Chalmers University of Technology, Gothenburg, Sweden.
- Markus, D., 2009. A Code Based Methodology to Account for Wave Loading in the Design of Offshore Structures. Diploma Thesis. Universität Stuttgart, Stuttgart, Germany.
- Markus, D., Arnold, M., Wüchner, R., Bletzinger, K.U., 2013a. A Reduced Modeling Methodology for Efficient Ocean Wave CFD Simulation of Fully Submerged Structures, in: *The Thirty-second International Conference on Ocean, Offshore and Arctic Engineering*, Nantes, France.
- Markus, D., Arnold, M., Wüchner, R., Bletzinger, K.U., 2014a. A Virtual Free Surface (VFS) model for efficient wave–current CFD simulation of fully submerged structures. *Coastal Engineering* 89, 85–98.
- Markus, D., Bletzinger, K.U., 2013. Optimal Shape Design of Offshore Foundations Subjected to Wave and Current Loading, in: *The Tenth European Wave and Tidal Energy Conference*, Aalborg, Denmark.
- Markus, D., Ferri, F., Wüchner, R., Frigaard, P., Bletzinger, K.U., 2015a. Complementary numerical-experimental benchmarking for shape optimization and validation of structures subjected to wave and current forces. *Computers & Fluids* 118, 69–88.
- Markus, D., Hojjat, M., Wüchner, R., Bletzinger, K., 2012. A Numerical Wave Channel for the Design of Offshore Structures with Consideration of Wave-Current Interaction, in: *The Twenty-second International Offshore and Polar Engineering Conference*, Rhodes, Greece, pp. 695–702.



- Markus, D., Hojjat, M., Wüchner, R., Bletzinger, K.U., 2013b. A CFD Approach to Modeling Wave-Current Interaction. *International Journal of Offshore and Polar Engineering* 23, 29–32.
- Markus, D., Jakobsen, M., Bletzinger, K.U., Frigaard, P., 2015b. Damping of Unwanted Turbulence in Wave-Current Experiments. *Coastal Engineering* 96, 38–48.
- Markus, D., Kelder, A., Wüchner, R., Bletzinger, K.U., 2014b. Lift Force Optimization of Gravity Base Offshore Foundations using CFD, in: *The Twenty-fourth International Offshore and Polar Engineering Conference*, Busan, Korea, pp. 624–631.
- Markus, D., Kelder, A., Wüchner, R., Bletzinger, K.U., 2015c. Lift Force Reduction by Means of a Diffuser for Gravity Base Foundations in Waves and Currents. *International Journal of Offshore and Polar Engineering* 25, 127–133.
- Markus, D., Wüchner, R., Bletzinger, K.U., 2013c. A numerical investigation of combined wave-current loads on tidal stream generators. *Ocean Engineering* 72, 416–428.
- Markus, D., Wüchner, R., Röhm, J., Bletzinger, K.U., 2011. Gründungen von Meeresströmungskraftwerken - Herausforderungen und Maßnahmen zur numerischen Simulation und Optimierung von umströmten Schwergewichtsfundamenten. *Dresdner Wasserbauliche Mitteilungen* 45, 369–378.
- Masters, I., Malki, R., Williams, A.J., Croft, T.N., 2013. The influence of flow acceleration on tidal stream turbine wake dynamics: A numerical study using a coupled BEM-CFD model. *Applied Mathematical Modelling* 37, 7905–7918.
- McCann, G., 2007. Tidal current turbine fatigue loading sensitivity to waves and turbulence - a parametric study, in: *The Seventh European Wave and Tidal Energy Conference*, Porto, Portugal.
- McCann, G., Thomson, M., Hitchcock, S., 2008. Implications of site-specific conditions on the prediction of loading and power performance of a tidal stream device, in: *The Second International Conference on Ocean Energy*, Brest, France.

- McCombes, T., Johnstone, C., Holmes, B., Myers, L., Bahaj, A., Heller, V., Kofoed, J., Finn, J., Bittencourt, C., 2010. Assessment of current practice for tank testing of small marine energy devices. Technical Report. EquiMar Deliverable D3.3.
- McCroskey, W., 1987. A critical assessment of wind tunnel results for the NACA 0012 airfoil. Technical Report. DTIC Document.
- Menter, F.R., 1993. Zonal two equation  $k-\omega$  turbulence models for aerodynamic flows. *AIAA Journal* 2906.
- Meroney, R., Letchford, C., Sarkar, P., 2002. Comparison of numerical and wind tunnel simulation of wind loads on smooth, rough and dual domes immersed in a boundary layer. *Wind and Structures* 5, 347–358.
- Mikhailova, N., Repik, E., Sosedko, Y.P., 1994. Optimal control of free-stream turbulence intensity by means of honeycombs. *Fluid Dynamics* 29, 429–437.
- Milne, I.A., Day, A., Sharma, R.N., Flay, R.G., Bickerton, S., 2011. Tidal turbine blade load experiments for oscillatory motion, in: Ninth European Wave and Tidal Energy Conference, Southampton, UK.
- Moens, F., Wervaecke, C., 2013. Multi-point optimization of shapes and settings of high-lift system by means of evolutionary algorithm and Navier-Stokes equations. *Engineering Computations* 30, 601–622.
- Mohammadi, B., Pironneau, O., Mohammadi, B., Pironneau, O., 2001. Applied shape optimization for fluids. volume 28. Oxford University Press, Oxford, UK.
- Moin, P., 2002. Advances in large eddy simulation methodology for complex flows. *International Journal of Heat and Fluid Flow* 23, 710–720.
- Mori, N., Suzuki, T., Kakuno, S., 2007. Noise of acoustic Doppler velocimeter data in bubbly flows. *Journal of Engineering Mechanics* 133, 122–125.
- Morison, J., Johnson, J., Schaaf, S., 1950. The force exerted by surface waves on piles. *Journal of Petroleum Technology* 2, 149–154.

- Myers, L., Galloway, P., 2011. Operational issues surrounding the use of towing tanks for performance quantification of marine current energy converters, in: The Ninth European Wave and Tidal Energy Conference, Southampton, UK.
- Nakamura, Y., Ohya, Y., 1984. The effects of turbulence on the mean flow past two-dimensional rectangular cylinders. *Journal of Fluid Mechanics* 149, 255–273.
- Nichols, B., 1975. Methods for calculating multidimensional, transient free surface flows past bodies. Technical Report. NASA STI/Recon.
- Nichols, B., Hirt, C., 1971. Improved free surface boundary conditions for numerical incompressible-flow calculations. *Journal of Computational Physics* 8, 434–448.
- Nichols, B., Hirt, C., 1973. Calculating three-dimensional free surface flows in the vicinity of submerged and exposed structures. *Journal of Computational Physics* 12, 234–246.
- Norberg, C., 1993. Flow around rectangular cylinders: pressure forces and wake frequencies. *Journal of Wind Engineering and Industrial Aerodynamics* 49, 187–196.
- Nowell, A.R., Jumars, P.A., 1987. Flumes - theoretical and experimental considerations for simulation of benthic environments. *Oceanography and Marine Biology* 25, 91–112.
- O'Doherty, T., Egarr, D., Mason-Jones, A., O'Doherty, D., 2009. An assessment of axial loading on a five-turbine array. *Proceedings of the ICE-Energy* 162, 57–65.
- Orlanski, I., 1976. A simple boundary condition for unbounded hyperbolic flows. *Journal of Computational Physics* 21, 251–269.
- Osher, S., Sethian, J.A., 1988. Fronts propagating with curvature-dependent speed: algorithms based on Hamilton-Jacobi formulations. *Journal of Computational Physics* 79, 12–49.
- Owen, A., 2007. The application of low aspect ratio hydrofoils to the secure positioning of static equipment in tidal streams. Ph.D. thesis. The Robert Gordon University, Aberdeen, Scotland.

- Owen, A., Bryden, I., 2005. Prototype support structure for seabed mounted tidal current turbines. *Proceedings of the Institution of Mechanical Engineers, Part M: Journal of Engineering for the Maritime Environment* 219, 173–183.
- Ozmen-Cagatay, H., Kocaman, S., 2011. Dam-break flow in the presence of obstacle: experiment and CFD simulation. *Engineering Applications of Computational Fluid Mechanics* 5, 541–552.
- Paparone, L., Tognaccini, R., 2003. Computational fluid dynamics-based drag prediction and decomposition. *AIAA Journal* 41, 1647–1657.
- Percival, S., Hendrix, D., Noblesse, F., 2001. Hydrodynamic optimization of ship hull forms. *Applied Ocean Research* 23, 337–355.
- Peri, D., Rossetti, M., Campana, E.F., 2001. Design optimization of ship hulls via CFD techniques. *Journal of Ship Research* 45, 140–149.
- Pilliod Jr, J.E., Puckett, E.G., 2004. Second-order accurate volume-of-fluid algorithms for tracking material interfaces. *Journal of Computational Physics* 199, 465–502.
- Pinto, A., Peri, D., Campana, E.F., 2007. Multiobjective optimization of a containership using deterministic particle swarm optimization. *Journal of Ship Research* 51, 217–228.
- Poinsot, T.J., Lelef, S., 1992. Boundary conditions for direct simulations of compressible viscous flows. *Journal of Computational Physics* 101, 104–129.
- Pope, S.B., 2000. *Turbulent Flows*. Cambridge University Press, Cambridge, UK.
- Popinet, S., Zaleski, S., 2002. Bubble collapse near a solid boundary: a numerical study of the influence of viscosity. *Journal of Fluid Mechanics* 464, 137–163.
- Richards, P., Hoxey, R., Short, L., 2001. Wind pressures on a 6 m cube. *Journal of Wind Engineering and Industrial Aerodynamics* 89, 1553–1564.
- Rider, W.J., Kothe, D.B., 1998. Reconstructing volume tracking. *Journal of Computational Physics* 141, 112–152.

- Rienecker, M., Fenton, J., 1981. A Fourier approximation method for steady water waves. *Journal of Fluid Mechanics* 104, 119–137.
- Rojas, R., 1996. *Neutral Networks: A Systematic Introduction*. Springer, Berlin Heidelberg, Germany.
- Roshko, A., 1961. Experiments on the flow past a circular cylinder at very high Reynolds number. *Journal of Fluid Mechanics* 10, 345–356.
- Rudman, M., 1998. A volume-tracking method for incompressible multifluid flows with large density variations. *International Journal for Numerical Methods in Fluids* 28, 357–378.
- Rumelhart, D.E., McClelland, J.L., Group, P.R., et al., 1995. *Parallel Distributed Processing*. volume 1. MIT Press, Cambridge, MA, USA.
- Rung, T., Stück, A., Kröger, J., 2012. A Hybrid Adjoint Approach to Hydrodynamic Shape Optimisation of Ship Hulls, in: *ECCOMAS 2012 - Mini Symposium 651 on Optimisation and Control for Aerodynamic Design*, Vienna, Austria.
- Ruopp, A., Ruprecht, A., R.S., 2011. Automatic Blade Optimisation of Tidal Current Turbines Using OpenFOAM, in: *The Ninth European Wave and Tidal Energy Conference*, Southampton, UK.
- Rusche, H., 2002. Computational fluid dynamics of dispersed two-phase flows at high phase fractions. Ph.D. thesis. Imperial College of Science, London, UK.
- Salas, M.D., Hefner, J.N., Sakell, L., 1999. Modeling complex turbulent flows. volume 7. Springer, Berlin Heidelberg, Germany.
- Salih, A., Moulic, S.G., 2013. A Mass Conservation Scheme for Level Set Method Applied to Multiphase Incompressible Flows. *International Journal for Computational Methods in Engineering Science and Mechanics* 14, 271–289.
- Sanchez, S.E.O., 2013. Development of an experimental methodology for appraising the dynamic response of tethered tidal turbines. Ph.D. thesis. University of Strathclyde, Glasgow, Scotland.
- Saripilli, J., Joga, R., Dhavalikar, S., Kar, A., 2014. Simulation of Numerical Wave Tanks for Generating Irregular Waves and Forward Speed Effects, in: *The Twenty-fourth International Offshore and Polar Engineering Conference*, Busan, Korea, pp. 536–542.

- Sarpkaya, T., 2010. *Wave Forces on Offshore Structures*. Cambridge University Press, New York, NY, USA.
- Scheiman, J., Brooks, J., 1981. Comparison of experimental and theoretical turbulence reduction from screens, honeycomb, and honeycomb-screen combinations. *Journal of Aircraft* 18, 638–643.
- Schmitz, R., 1987. *Beitrag zur Hydrodynamik von Flachgründungen*. Ph.D. thesis. Technische Hochschule zu Berlin, Berlin, Germany.
- Schoefs, F., 2002. Sensitivity and Uncertainty Studies for the Modelling of Marine Growth Effect on Offshore Structures Loading, in: *The Twenty-second International Conference on Offshore Mechanics and Arctic Engineering*, Oslo, Norway, pp. 275–281.
- Schoefs, F., Boukinda, M., et al., 2004. Modelling of Marine Growth Effect on Offshore Structures Loading Using Kinematics Field of Water Particle, in: *The Fourteenth International Offshore and Polar Engineering Conference*, Toulon, France, pp. 419–427.
- Schumann, U., 1975. Subgrid scale model for finite difference simulations of turbulent flows in plane channels and annuli. *Journal of Computational Physics* 18, 376–404.
- Seidell, D.A., Bennett, R.M., 1991. Experimental flutter boundaries with unsteady pressure distributions for the NACA 0012 benchmark model. *AIAA Journal* 91-1010-CP, 697–703.
- Sethian, J.A., 1999. *Level set methods and fast marching methods: evolving interfaces in computational geometry, fluid mechanics, computer vision, and materials science*. volume 3. Cambridge Univ Press.
- Shi, W., Park, H.C., Baek, J.H., Kim, C.W., Kim, Y.C., Shin, H.K., 2012. Study on the marine growth effect on the dynamic response of offshore wind turbines. *International Journal of Precision Engineering and Manufacturing* 13, 1167–1176.
- Singh, P., Deschrijver, D., Dhaene, T., 2013. A Balanced Sequential Design Strategy for Global Surrogate Modeling, in: *Winter Simulation Conference*, Washington, DC, USA, pp. 2172–2179.

- Spagnoli, G., Weixler, L., 2013. Drilling Technologies for Offshore Foundation Engineering, in: The Thirty-second International Conference on Ocean, Offshore and Arctic Engineering, Nantes, France.
- Stein, M.L., 1999. Interpolation of spatial data: some theory for kriging. Springer, Berlin Heidelberg, Germany.
- Stokes, G.G., 1847. On the theory of oscillatory waves. Transactions of the Cambridge Philosophical Society 8, 441–473.
- Stück, A., Rung, T., 2011. Adjoint RANS with filtered shape derivatives for hydrodynamic optimisation. Computers & Fluids 47, 22–32.
- Sumer, B.M., Fredsøe, J., 2006. Hydrodynamics around cylindrical structures. World Scientific, Singapore.
- Sun, W., Yuan, Y.X., 2006. Optimization theory and methods: nonlinear programming. volume 1. Springer, Berlin Heidelberg, Germany.
- Sun, X., Huang, D., Wu, G., 2012. The current state of offshore wind energy technology development. Energy 41, 298–312.
- Tahara, Y., Himeno, Y., 1998. An application of computational fluid dynamics to tanker hull form optimization problem, in: The Third Osaka Colloquium on Advanced CFD Applications to Ship Flow and Hull Form Design, Osaka, Japan, pp. 515–531.
- Tahara, Y., Peri, D., Campana, E.F., Stern, F., 2008. Computational fluid dynamics-based multiobjective optimization of a surface combatant using a global optimization method. Journal of Marine Science and Technology 13, 95–116.
- Tahara, Y., Peri, D., Campana, E.F., Stern, F., 2011. Single-and multiobjective design optimization of a fast multihull ship: numerical and experimental results. Journal of Marine Science and Technology 16, 412–433.
- Tahara, Y., Stern, F., Himeno, Y., 2004. Computational Fluid Dynamics-Based Optimization of a Surface Combatant. Journal of Ship Research 48, 273–287.

- Tan, Y., Van Cauwenberghe, A., 1999. Neural-network-based d-step-ahead predictors for nonlinear systems with time delay. *Engineering Applications of Artificial Intelligence* 12, 21–35.
- Tedds, S., Owen, I., Poole, R., 2014. Near-wake characteristics of a model horizontal axis tidal stream turbine. *Renewable Energy* 63, 222–235.
- Thévenin, D., Janiga, G., 2008. *Optimization and Computational Fluid Dynamics*. Springer, Berlin Heidelberg, Germany.
- Thomas, G., 1990. Wave–current interactions: an experimental and numerical study. Part 2. Nonlinear waves. *Journal of Fluid Mechanics* 216, 505–536.
- Tu, J., Yeoh, G.H., Liu, C., 2007. *Computational fluid dynamics: a practical approach*. Butterworth-Heinemann, Oxford, UK.
- Turek, S., Hron, J., 2006. Proposal for numerical benchmarking of fluid–structure interaction between an elastic object and laminar incompressible flow. Springer, Berlin Heidelberg, Germany.
- Turek, S., Hron, J., Razzaq, M., Wobker, H., Schäfer, M., 2010. Numerical Benchmarking of Fluid-Structure Interaction: A comparison of different discretization and solution approaches. Springer, Berlin Heidelberg, Germany.
- Turnock, S.R., Phillips, A.B., Banks, J., Nicholls-Lee, R., 2011. Modelling tidal current turbine wakes using a coupled RANS-BEMT approach as a tool for analysing power capture of arrays of turbines. *Ocean Engineering* 38, 1300–1307.
- Ugray, Z., Lasdon, L., Plummer, J., Glover, F., Kelly, J., Martí, R., 2007. Scatter search and local NLP solvers: A multistart framework for global optimization. *INFORMS Journal on Computing* 19, 328–340.
- Uzawa, K., Kageyama, K., Murayama, H., Ohsawa, I., Kanai, M., Nishiyama, T., Shichiri, A., 2008. Study of the characteristic and possibility for applying composite materials to the blades of tidal power generation, in: *The Twenty-seventh International Conference on Offshore Mechanics and Arctic Engineering*, Estoril, Portugal, pp. 721–728.



- Vanderplaats, G.N., 1984. Numerical optimization techniques for engineering design: with applications. volume 1. McGraw-Hill, New York, NY, USA.
- Vengatesan, V., Varyani, K., Barltrop, N., 1999. Wave-current forces on rectangular cylinder at low KC numbers, in: The Ninth International Offshore and Polar Engineering Conference, Brest, France, pp. 469–477.
- Vengatesan, V., Varyani, K., Barltrop, N., 2000. An experimental investigation of hydrodynamic coefficients for a vertical truncated rectangular cylinder due to regular and random waves. *Ocean Engineering* 27, 291–313.
- Vennell, R., 2012. The energetics of large tidal turbine arrays. *Renewable Energy* 48, 210–219.
- Venugopal, V., Varyani, K., Westlake, P., 2009. Drag and inertia coefficients for horizontally submerged rectangular cylinders in waves and currents. *Proceedings of the Institution of Mechanical Engineers, Part M: Journal of Engineering for the Maritime Environment* 223, 121–136.
- Versteeg, H.K., Malalasekera, W., 2007. An introduction to computational fluid dynamics: the finite volume method. Pearson Education, Harlow, UK.
- Vogl, T.P., Mangis, J., Rigler, A., Zink, W., Alkon, D., 1988. Accelerating the convergence of the back-propagation method. *Biological Cybernetics* 59, 257–263.
- Vølund, P., 2005. Concrete is the future for offshore foundations. *Wind Engineering* 29, 531–539.
- Voulgaris, G., Trowbridge, J.H., 1998. Evaluation of the Acoustic Doppler Velocimeter (ADV) for Turbulence Measurements. *Journal of Atmospheric and Oceanic Technology* 15, 272–289.
- Wahl, T.L., 2003. Discussion of “Despiking acoustic doppler velocimeter data” by Derek G. Goring and Vladimir I. Nikora. *Journal of Hydraulic Engineering* 129, 484–487.

- Wang, D., Atlar, M., Sampson, R., 2007. An experimental investigation on cavitation, noise, and slipstream characteristics of ocean stream turbines. *Proceedings of the Institution of Mechanical Engineers, Part A: Journal of Power and Energy* 221, 219–231.
- Welch, S.W., Wilson, J., 2000. A volume of fluid based method for fluid flows with phase change. *Journal of Computational Physics* 160, 662–682.
- Werner, H., Wengle, H., 1993. Large-eddy simulation of turbulent flow over and around a cube in a plate channel, in: *Turbulent Shear Flows* 8. Springer, Berlin Heidelberg, Germany, pp. 155–168.
- Whelan, J., Graham, J., Peiro, J., 2009. A free-surface and blockage correction for tidal turbines. *Journal of Fluid Mechanics* 624, 281–291.
- Whelan, J., Thomson, M., Graham, J., Peiro, J., 2007. Modelling of free surface proximity and wave induced velocities around a horizontal axis tidal stream turbine, in: *The Seventh European Wave and Tidal Energy Conference*, Porto, Portugal.
- Wilcox, D.C., 1988. Reassessment of the scale-determining equation for advanced turbulence models. *AIAA Journal* 26, 1299–1310.
- Wilcox, D.C., 1998. *Turbulence modeling for CFD. volume 2*. DCW industries, La Cañada Flintridge, CA, USA.
- Wolfram, J., Theophanatos, A., et al., 1985. The effects of marine fouling on the fluid loading of cylinders: some experimental results, in: *Offshore Technology Conference*, Houston, TX, USA.
- Wu, C.s., Zhu, D.x., Gu, M., 2008. Computation of hydrodynamic forces for a ship in regular heading waves by a viscous numerical wave tank. *Journal of Ship Mechanics* 12, 168–179.
- Wyatt, D.C., Chang, P.A., 1994. Development and assessment of a total resistance optimized bow for the AE 36. *Marine Technology* 31, 149–160.
- Yang, Z., Wang, T., Copping, A.E., 2013. Modeling tidal stream energy extraction and its effects on transport processes in a tidal channel and bay system using a three-dimensional coastal ocean model. *Renewable Energy* 50, 605–613.

- Zaaijer, M.B., 2003. Comparison of monopile, tripod, suction bucket and gravity base design for a 6 MW turbine, in: *Offshore Wind Energy in Mediterranean and Other European Seas Conference*, Naples, Italy.
- Zakerdoost, H., Ghassemi, H., Ghiasi, M., 2013. Ship hull form optimization by evolutionary algorithm in order to diminish the drag. *Journal of Marine Science and Application* 12, 170–179.
- Zhang, Y., Zou, Q.P., Greaves, D., 2012. Air–water two-phase flow modelling of hydrodynamic performance of an oscillating water column device. *Renewable Energy* 41, 159–170.
- Zhao, X.Z., Hu, C.H., Sun, Z.C., 2010. Numerical simulation of extreme wave generation using VOF method. *Journal of Hydrodynamics, Ser. B* 22, 466–477.